Multiscale approach to predict the lifetime of EB-PVD thermal barrier coatings

Julien Frachon

Collège doctoral

ED n° 432: Science des Métiers de l'Ingénieur

THÈSE

pour obtenir le grade de
Docteur de l'Ecole Nationale Supérieure des Mines de Paris
Spécialité Sciences et Génie des Matériaux

présentée et soutenue publiquement par

Julien Frachon

le 14 Décembre 2009

MULTISCALE APPROACH TO PREDICT THE LIFETIME OF EB-PVD THERMAL BARRIER COATINGS
-
APPROCHE MULTI ECHELLE POUR PREDIRE LA DUREE DE VIE DES BARRIERES THERMIQUES DEPOSEES PAR EB-PVD

Directeurs de thèse : ***Esteban P. BUSSO***
Vincent MAUREL

Jury

M.	J.L. CHABOCHE	Rapporteur	ONERA, France
M.	A. SUIKER	Rapporteur	Delft, University of Technology, Netherland
M.	H.E. EVANS	Examinateur	University of Birmingham, England
M	D. MONCEAU	Examinateur	ENSIACET, Toulouse, France
M.	A. TASSELLI	Examinateur	SIEMENS, Lincoln, England
M.	E.P. BUSSO	Directeur de thèse	Ecole des Mines-Paristech, France
M.	V. MAUREL	Directeur de thèse	Ecole des Mines-Paristech, France
M.	J. BESSON	Invité	Ecole des Mines-Paristech, France

Remerciements

La rédaction de cette thèse a commencé dans un chalet des Alpes en juillet 2009. Le défi consistait à cueillir entre amis du génépi (mais pas trop car c'est une plante protégée) et rédiger une thèse! Elle s'achève par ces remerciements en Juillet 2011 au bord d'une rivière du Québec. La soutenance ayant eu lieu en décembre 2009, il aura donc fallu 18 mois pour aboutir à ces remerciements en français tandis que 4 mois auront suffi pour la partie technique en anglais. Cela peut illustrer : soit le courage, la motivation et le soutient moral qu'il faut pour vivre et rédiger une thèse au complet, soit l'absolue nécessité de boire du génépi (plante inexistante au Québec) pour finir la rédaction une thèse.

L'absence de génépi au Québec n'est pas la seule excuse à ce long retard. Il faut aussi se rendre à l'évidence que les remerciements d'une thèse sont souvent les pages les plus lues d'un manuscrit. A ce titre, il est normal de leur consacrer le temps et la réflexion nécessaire. Enfin, écrire des remerciements représente un défi bien plus délicat que d'aligner les équations et les hypothèses. On vous pardonnera volontiers d'oublier de référencer un auteur et son article, mais certainement pas d'oublier de remercier un(e) ami(e)…

Merci à M^{r} Jean-Louis Chaboche et M^{r} Akke Suiker qui ont accepté d'être les rapporteurs du manuscrit et pour leur participation au Jury. Ils ont contribué par leurs nombreuses remarques et suggestions à améliorer la qualité de travail. Je remercie aussi M^{r} H. E. Evans et M^{r} Daniel Monceau qui m'ont fait l'honneur de participer au Jury de la soutenance.

Un grand et sincère remerciement à toutes les personnes travaillant au Centre des Matériaux (CdM) Mines-ParisTech. Coincé entre l'A6, la N104 et la SNECMA, le CdM est un petit village (gaulois) d'irréductibles chercheur(e)s où se succède avec passion et zizanie : les conseils du village, les bagarres pour les clusters, le développement de la potion magique ZeBuLoN...et les banquets à l'arrière de l'atelier.

Merci aux 3 co-directeurs de thèse : Mr Jacques Besson pour sa rigueur scientifique, son honnêteté intellectuelle, son humour un brin intellectuel, et les heures passées à débugger ZeBuLoN. Merci à Mr Vincent Maurel qui malgré 6 mois passés à Amsterdam, un virus tenace, une famille nombreuse, a réussi à apporter toute son expérience sur le sujet et à remettre en question toutes nos hypothèses. Merci pour son soutien dans les moments critiques, pour tous ces joyeux moments passés en conférence téléphonique et ces voyages à Lincoln sous le crachin anglais. Merci à Mr Esteban Busso pour avoir tenté de concilier le travail d'encadrant de thèse et directeur d'un village de recherche gaulois ! Merci pour votre rigueur lors de la rédaction et pour le temps passé en Angleterre chez nos partenaires. Merci enfin à la société SIEMENS en Angleterre et tout particulièrement à M^{r} Andrea Tasselli, pour son esprit critique et son humour décalé.

Je tenais à remercier également tous les « personnages » du CdM : l'atelier et leurs ami(e)s : Maria et Nicole, Cindy, Bertrand, Jojo et son vélo, Michel, J.P. et ses bières, Julien, Franck, René, Abdennour, Mathieu, Sylvain, Jo. Merci pour tous les moments un peu fous et décalés au fond de l'atelier, pour les nombreux BBQ improvisés, les séances nocturnes dans l'atelier…merci à Mr Franck N'Guyen, notre barde Assurancetourix dont le rire «discret» occasionne des troubles auditifs, ce qui lui vaut d'être mis à l'écart lors des banquets! Merci aussi à Christophe, Steve et la grande Julie pour leur présence, toujours souriants et tellement réconfortants.

Merci au bureau B104, seul hutte du village où l'on peut trouver : Alexandre le grand, une Mama camerounaise et sa plante verte Josette, un Blung, un haltérophile-prestidigitateur russe, une Spice Girl, un sac à main pour homme, des bracelets brésiliens et un vautour !

Merci à Greg et Olivier, capable de faire fonctionner le réseau informatique et ZeBuLoN dans ce village de fou. Merci à Nikolay, Farida, Laurent, Stéphane et Djamel, à toutes les personnes de l'administratif du CdM : Anne, Sajo et ses maudits rapports trimestriels ;), Dolorès, Véro et Véro, Konaly sans qui ces remerciements n'existeraient pas, un merci tout particulier à Liliane pour avoir rendu agréables les éternels retards du directeur! Merci à Odile et sa bibliothèque grâce à qui les bibliographies de nos thèses ne sont pas uniquement composées d'articles du XXIème siècle.

Merci à tous les autres étudiant(e)s : l'équipe thermique (Christophe, Marc), les Spice girls, Florence, Delphine, Cédric le marseillais, Clara, Yoann, Vlad le gentil, Jianqiang, Huaidong, Barham l'iranien chantant, l'aile C : Marion, Olivier A., Guillaume, Joao, nOnO, Thomas, Laurent. Et oui, le CdM ressemble vraiment à un village «gaulois» moderne où plus de 20 nationalités se mélangent. Merci au footeux, aux squatteurs du bocal, au RER D pour toutes ses heures passées avec Tony sur les quais. Merci aux chercheurs du CdM : Samuel Forest (constamment sous l'effet de la potion magique), Mr

Pineau (le druide du laboratoire toujours prêt, de jours comme de nuit, à nous narrer des petites histoires de l'Histoire), Mr Boussuge et ses blagues, Loïc Nazé, Jérôme Crépin. David Ryckelynck…

Merci à tous les autres, qui m'ont supporté pendant 3 ans en dehors de la thèse : Tony, les colloc' temporaires du 7ème ciel au 12 rue Michel Chasles : Jim, Tomtom, Flavoun, Doumé, la voisine sourde du dessous, le caviste d'en bas, la colloque du 29 Popincourts (C.M. miss Ricard), le marché d'Aligre, P'ti Ben, Brice et Aude, Caro, la colloque Wissoussienne, Loulou et son frère, Amélie la fofolle, Ayman, Bibou, Steph et sa colloque, Lucho et la Famille Milhaud, les fatc' de Chichounne, Hélène&Piwi, Tarpé, la Fermiette en Picardie, le Réal Délirium, Maryline, le Pantalon, la Gueuze, les Touaregs de Djanet, Dr Sarrazin et enfin Ludivine, la Kiné bavarde, pour m'avoir réappris à marcher !

Merci aux membres du DGM et du LMT de l'ENS Cachan, pour m'avoir mené tranquillement sur les chemins de la recherche : Danielle, Christine, JPP, Mr Neau et ses cravates, Pan^2, François Louf, Eric Florentin, David Néron. Merci pour les 3 années passées ensemble, autour d'un BBQ, d'un verre de Vouvray …

Merci à tous ceux qui m'ont accompagné sur ces chemins sinueux et intenses : le BdA avec Tony, Nico, Lu^2, Hélène, Tom^2, Stef, Thibo, Ayman, Tom, Blung, Mathias, Sami, Piwi, Bellette, Pinouille, Loulou, Flavoun, tous les gens du dimanche soir : le Track'n'Art, PPFC, YAPA, Joke, Les Ouich Lorène, Kwak, les punks…et bien sûr les Skaliers de Secours : Rico le sautillant, Sami, Rno, Hélène, Tarpé, Blung, Nico, Lu^2, Ramsès le pilier de comptoir, Pinouille, nOnO l'ingé-son et le fan club des Skaliers (Olive le bio, Cousin)…merci au squat d'Igny : Jose, Lulu, la famille Mazière, Nanou, le 3G, l'équipe Gala (Pat le D2), le WeiSpirit…Merci à tous les B123, 3B1 et 3B3 : en particulier à Jimbo le déglingo, Brice, Sarah ma binôme, Max, Raph, Martin, Jojo, Xavi, Toinou, Flavien, Marion, Gilou…merci aux inclassables : Amélie, Anaïs, Aline, Mac10, Kazio, Wilou, les [pot] du mardi soir, la Kokarde, les crocs' à la Clavière, la Kfet, la Kro (avec modération bien entendu), la BdaMobile de Burtal, la Koinche, les squatteurs du Bat F, les sous terrains de l'ENS, la burtunade….Merci aux habitants d'Aotearoa, aux maoris, aux punks Pinouille et Burtal, à Pépé Lopez, aux Nicky(s) et la bande de Day street.

Merci aux profs de la PT Cachan, ceux qui m'ont donné ma chance et appris que l'on pouvait « faire les choses sérieusement sans se prendre au sérieux » : M^{me} Bergeron, M^{me} Aspeel, M^r Machu et son cirque, M^r Perrin et ses jeux de mot, M^r Herstain et son homogénéité, M^r Fouraison, M^r Mohan, M^r Bertrand et bien sûr M^r Salangro pour son épicurisme. Voici pour le côté sérieux de cette prépa, passons au côté moins sérieux : Mac10 mon mentor, G8 et son «one&half », Kaza&Erez mes binômes de Kôle, Poisseux pour l'ensemble de son œuvre, Stock, Thomas, les 5/2, l'ATT (Agence Tout Trip) : Christelle, P'ti Ben, Nico, Martin, Manu, Lazik, les fondeurs-tuners : Chaps et sa mère, Vinc', Del Soc, Max, Nico…GG et sa golf rouge, Mourad, l'assiette du Trappeur, le carafon, le camping de Normandie, le GDI, le CROUS…

Merci à celles et ceux qui ont tracé leur chemin à côté du mien depuis plus de 20 ans : Jennifer, Émilie, Mélanie, Cécile la chasseuse de marmotte, Antoine le chilien, p'ti Fab' et Grand Chef. Merci à toute ma famille mosaïque : ma maman et son éternel optimisme sur la recherche, mon papa malgré tout, mes sœurs : Aude qui a enfin compris le phénomène d'oxydation, Lysou (et sa maman), merci aux nouveaux venus qui ont apporté beaucoup de stabilité : Gis' le breton d'origine indienne et Lilian, à mon frère Stéphane et tous ses projets fous, aux nièces et neveux : Maylisse, Alisée, Kilian, Dylan et la dernière venue Lilou. Merci à ma cousine Mireille et sa spiritualité, à ma belle famille Marie-Christine et Lionel pour être toujours là en cas de problème, à Polo le rigolo, la famille Coisel, Noëlle, la bande de Saint Cyp (Francis, Marco et sa maman, Annie et Henri, Mouly et sa maman) et Manou, par qui tout commença.

Pour conclure, s'il faut un peu de courage et un soupçon de génépi pour arriver à terminer une thèse, il faut surtout à la fois une intarissable source de motivation et une étoile qui guide vos pas. Ma source et mon étoile viennent de celle qui depuis l'adolescence est l'unique raison de se lever les matins difficiles (soit 8 jours sur 7, le dimanche compte double), «celle qui tous les jours partage mon cassoulet», celle qui permet d'apprécier les amis(e)s et la famille. Merci à Carine, avec un C svp ;)

« Salut à toi » lecteur !

Abstract

Thermal barrier coatings (TBCs) are used to protect hot components from combustion gases in gas turbines. One of the most widely used TBC systems is that applied by an electron beam-physical vapour deposition (EB-PVD) onto a Ni-base intermediate or bond coat. The resulting top zirconia based thermal insulator exhibits a characteristic columnar morphology. During service, the combination of severe thermal loads and high temperatures leads to the selective oxidation of the intermediate metallic coating, to TBC degradation and, eventually, to the development of microcracks. This may, in turn, be followed by spalling of the top coating, which constitutes the life limiting event for the component. Different approaches have been proposed to predict these phenomena, generally based on macroscopic TBC stresses as the driving force for TBC failure or on fracture mechanics approaches to predict interfacial or cohesive failure. However, no previous work integrates local interface damage and macroscopic stresses or stored strain energy in the prediction of TBC spallation. The objective of this thesis is to develop a multi-scale life predictive approach for TBC life which accounts for the evolution of local interface damage, and its effect on the fracture resistance relevant to the dominant failure mode, such as oxide interface spallation. Even though the study focuses on an EB-PVD TBC system, the proposed approach is generic and can be adapted to other types of TBCs.

The lifetime assessment and the modelling of TBCs require an understanding of individual material properties and interface morphologies, and their in-service evolution. In this thesis, the evolution of each TBCs constituent microstructure has been investigated using scanning electron micrograph, energy-dispersive spectroscopy techniques and image-processing analyses. Based on the understanding gained from the experimental study, a multi-scale and multi-physics approach is proposed which incorporates (i) the kinetics of oxide growth, (ii) the growth strains associated with bond coat oxidation, (iii) realistic (2D and 3D) oxide morphologies, and (iv) the morphological evolution of the oxide and top coat. The approach has been implemented into the finite element method and used to predict the local stress and strain fields driving the evolution of observed interfacial local damage (i.e. porosities, microcracks) through a local continuous damage variable. Through this numerical approach, it is also possible to take into account the time-evolution of the TBC′s morphology (sintering of columnar top coat layer, oxide thickness and roughness), and microcracking under both constant and cyclic temperature histories.

The proposed approach relies on the value of the interface fracture resistance, linked to the current level of interface damage, and on the global stored elastic strain energy to account for the evolution towards a critical state. The latter is assumed to be attained when the stored energy reaches the realevant fracture resistance. The time evolutions of the stored energies and the fracture resistance are inferred from simulations results and TBC life data. The approach can be easily adapted to predict TBC lifetime for long in-service conditions.

Résumé

Le développement d′une nouvelle génération de revêtements thermiques réalisée par voie physique EB-PVD (electron beam-physical vapour deposition) permet d′augmenter la température en service tout en protégeant les aubes monocristallines. Ces systèmes barrières thermiques comprennent une couche isolante composée de zircone stablisée à l′yttrium déposée sur une sous-couche intermédiaire (NiCoCrAlY) protégeant de l′oxydation

le superalliage. A ces températures, l′oxygène oxyde la sous-couche formant ainsi une fine couche d′alumine à l′interface avec la zircone. Des microfissures et des porosités germent dans cette zone critique sous contrainte, diminuant la résistance à l'écaillage des barrières thermiques et entrainant la ruine du système lorsque l′énergie élastique stockée est suffisante. Si de nombreuses approches numériques existent pour prédire les champs de contraintes proches de l'oxyde, aucune ne fait pour l′instant le lien entre les phénomènes microscopiques (contrainte et endommagement interfacial) et les phénomènes macroscopiques (adhésion des interfaces/énergie stockée).

L′objectif est de développé un modèle de durée de vie des barrières thermiques en prenant en compte (i) la relation entre les mécanismes d′endommagement interfacial et la diminution de la résistance à l′écaillage et (ii) l′évolution des propriétés mécaniques des différent composants du systèmes, soumis à des chargements très sévères. L′approche proposés a aussi pour but d′être générique et donc adaptable à d′autre types de barrières thermiques.

La mise en place d′un modèle de durée de vie des barrières thermiques nécessite la connaissance des propriétés thermo-mécaniques et de la morphologie de chacun des composants du système. L′analyse d'images, obtenues par microscopie électronique, a permis d′étudier l′évolution en fonction du temps et de la température de la microstructure colonnaire de la céramique, la composition chimique de la sous-couche et de la morphologie de l′oxyde. Basé sur ces observations expérimentales, un modèle incluant (i) la croissance de l′oxyde, (ii) l′expansion volumique associée à l′oxydation de la sous-couche et (iii) la morphologie réelle de l′oxyde a été établi. Cette approche a été implémenté dans un code élément finis afin de prédire les champs de contraintes et les rélier ces résultats à la modélisation de la germination et de la croissance de porositées et de microfissures proche de l'oxyde. Combiné à l′évolution de la morphology du système barrière thermiques (frittage de la céramique, croissance de l'oxyde), ce modèle permet de prendre en compte les paramètres influenĂğant la durée de vie des barrières thermiques. Une étude paramétrique a été réalisé dans le but d′étudier l′influence de paramètres caractérisant le comportement mécanique et la morphologie des composants ainsi que le chargement thermique, et ce afin d′améliorer la compréhension et donc la modélisation des barrières thermiques.

En reliant l'évolution de la résistance à l'écaillage de l'oxyde, liée à l'endommagement interfacial local, et celle de l'énergie élastique stockée, liée au forte contrainte dans le plan générées lors du refroidissement, il est possible de prédire la durée de vie des barrières thermiques. Cette approche couplant travaux expériementaux et numériques est parfaitement adapté au durée de vie des barrières thermiques utilisées sur les turbine terrestres (40,000h).

Notations

Tensors

Type	Notation	Example
Scalar	a	Poisson's coefficient ν
Vector	$\underline{\boldsymbol{a}}$	Normal vector $\underline{\boldsymbol{n}}$
Second order tensor	$\underset{\sim}{\boldsymbol{a}}$	Stress tensor $\underset{\sim}{\boldsymbol{\sigma}}$
Fourth order tensor	$\underset{\approx}{\boldsymbol{A}}$	Elastic compliance tensor $\underset{\approx}{\boldsymbol{S}}$

Product

Notation	Formulation
$x = \underline{\boldsymbol{a}} . \underline{\boldsymbol{b}}$	$x = a_i b_i$ (scalar product)
$\underline{\boldsymbol{x}} = \underset{\sim}{\boldsymbol{a}} . \underline{\boldsymbol{b}}$	$x_i = a_{ij} . b_j$
$\underset{\sim}{\boldsymbol{x}} = \underset{\sim}{\boldsymbol{a}} . \underset{\sim}{\boldsymbol{b}}$	$x_{ij} = a_{ik} b_{kj}$
$x = \underset{\sim}{\boldsymbol{a}} : \underset{\sim}{\boldsymbol{b}}$	$x = a_{ij} b_{ij}$
$\underset{\sim}{\boldsymbol{x}} = \underset{\approx}{\boldsymbol{A}} : \underset{\sim}{\boldsymbol{b}}$	$x_{ij} = A_{ijkl} b_{kl}$
$\underset{\approx}{\boldsymbol{X}} = \underset{\approx}{\boldsymbol{A}} : \underset{\approx}{\boldsymbol{B}}$	$X_{ijkl} = A_{ijpq} B_{pqkl}$

Normal stress, traction and shear

Notation	Formulation
Normal stress $\underline{\boldsymbol{t}}$	$\underline{\boldsymbol{t}} = \underset{\sim}{\boldsymbol{\sigma}} . \underline{\boldsymbol{n}}$
Traction σ_{nn}	$\sigma_{nn} = \underline{\boldsymbol{n}} . \underset{\sim}{\boldsymbol{\sigma}} . \underline{\boldsymbol{n}}$
Shear σ_{tt}	$\sigma_{tt}^2 = \underline{\boldsymbol{t}} . \underline{\boldsymbol{t}} - \sigma_{nn}^2$

Abbreviations

APS	Air Plasma Sprayed
BC	Bond Coat
CMAS	Calcium Magnesium Aluminium Silicium
CTE	Coefficient of Thermal Expansion
DOF	Degrees of Freedom
EB-PVD	Electron Beam-Physical Vapor Deposition
ERL	Elementary Representative Length
evp	Elasto-visco-plastic
HVOF	High Velocity Oxygen Fuel
PBR	Pilling Bedworth Ratio
SEM	Scanning Electron Microscopy
TBC	Thermal Barrier Coating
TC	Top Coat
TEM	Transmission Electron Microscopy
ve	Visco-elastic
VPS	Vacuum Plasma Spraying
YSZ	Yttrium Stabilised Zirconia

Contents

Chapter -I-

Introduction

Contents

In spite of the drive to substitute fossil fuels (coal, gas, oil) by renewable energies, natural gas is still a major source of electricity generation through the use of gas turbines. Its production has increased from 12 TWh to 19 TWh during the last fifteen years (French Institute of Petroleum). According to some forecasts, electricity generation based on gas sources could reach to 34 TWh in 2030, which will correspond to 20% of the world electricty production. Being a cleaner fuel is a motivation for the use of natural gas, especially for electricity generation. It burns more cleanly than other fossil fuels and releases less carbon dioxide per unit energy producted. For an equivalent production of energy, using natural gas reduces of 30% and 45% the carbon dioxide released when compared to oil and coal, respectively. Gas resources are also spread all around the word, are easly extracted and can supply the world comsumption for the next 70 years. Electricity production by gas turbine is also more flexible than the nuclear energy production to the demand variation.

The environmental concern and the increasing energy demand provide good reasons for engine manufacturers to improve gas turbine efficiency. Among the ways to satisfy this challenge, the turbine temperature has been increasing. Indeed, accepting some assumptions, the thermodynamic efficiency of a turbine, ρ the proportion of the thermal energy converted to mechanical power, is given by:

$$\rho = 1 - \frac{\theta_{out} - \theta_{in}}{\theta_{turb} - \theta_{comp}}, \tag{I.1}$$

where θ_{in} and θ_{out} are the ambient and final temperatures, θ_{comp} is the temperature after compression and θ_{turb} is the turbine operating temperature. It can be seen that the higher is the turbine operation temperature, the greater is the potentially available efficiency. Nowadays, gas turbine efficiencies are around 40% in single-cycle and 60% in combined-cycle (SIEMENS) but the mechanical strength of the turbine components limits the temperature increase. The quest for higher temperatures is dominated by materials and process developments.

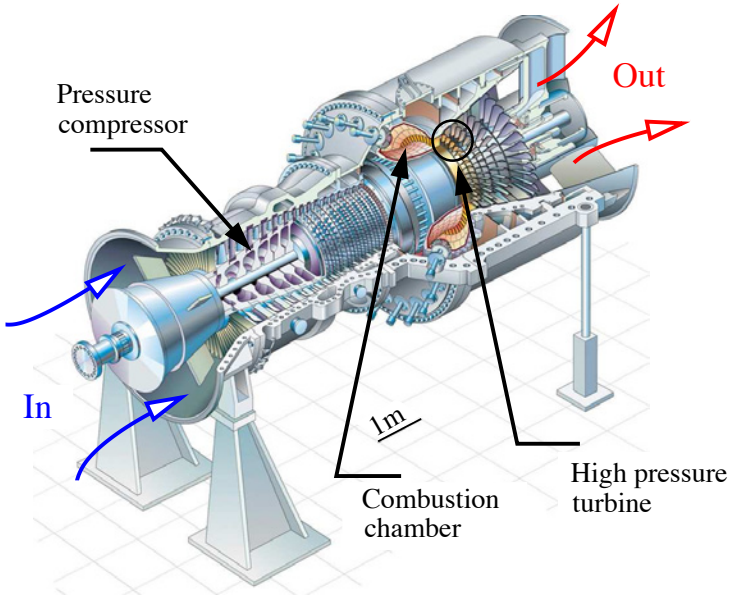

Figure I.1 : Schematic showing a land based gas turbine with a capacity of 287 Megawatts (*SIEMENS*).

I.1 Historical overview

Requiring high performance at elevated temperatures, *superalloy* turbine blades were been developed in the earlier 1950's. The cooling system of turbine blades in the 1960's and the alloy microstructure improvements (directional solidification and single-crystal) have significantly contributed to increase upper service temperatures. Associated to thermo-insulator coatings, the objectives were to protect the superalloy substrate of high temperatures and the hurtful consequences. Ceramic protective coatings for turbine applications have been considered since the late 1940's (Harrison et al., 1947, Garrett and Gyornak, 1953). Thermal barrier coatings (TBCs) are typically formed of ceramic materials deposited by air plasma spraying (APS), flame spraying or physical vapor deposition (PVD) techniques. APS-TBCs are produced with a plasma spray gun, where the powder is injected into a plasma gas which is melt rapidly. This method is one of the lowest cost alternatives but yields low strain-tolerant microstructures. In the hottest areas of gas turbine engines, TBCs are more often deposited by *electron beam-physical vapor deposition* (EB-PVD), which yields a strain-tolerant columnar grain structure (see Fig. I.2) which limit the magnitude if the stress responsible for TBC spallation.

I.2 Composition, morphology and properties of TBC systems

The two main functions of TBC systems consist of (i) **lowering the temperature** and (ii) **protecting** the Ni-based superalloy substrate from detrimental oxidation. The requirement to lower the substrate temperature has been justified previously. The in-service conditions also mean severe oxidation. TBCs should protect the superalloy substrate to severe environmental conditions which can modify its chemical composition and impaired its mechanical properties. Thermal barrier coating systems are composed of three constituents, as shown in Fig. I.2. The *top coat* (TC) provides thermal insulation to the substrate. This low-thermal conductivity layer consists of a ceramic which is deposited onto a bond coat. It is almost transparent to oxygen and does not therefore provide any oxidation resistance. The *bond coat* (BC) has two functionalities: firstly, it ensures a good adherence between the substrate and the thermally insulating layer (ceramic) and secondly, it preserves the substrate chemical composition. Indeed, the bond coat constitutes a reservoir of aluminium reacting with the oxygen allowing the formation of a protective alumina layer at the bond coat-ceramic interface, the so-called *thermally grown oxide* (TGO).

I.2.1 Top coat insulator layer

Thermal barrier coatings comprise thermally insulating materials which have sufficient thickness and durability to sustain a large temperature gradient between the substrate and the top coat surface, around 80 to 150°C. Few methods are used to deposit thermal insulators. In our case, the top coat consists of a 135 μm thick layer of yttria partially stabilised zirconia (YSZ), ZrO_2-8%Y_2O_3 and in the case of an EB-PVD type exhibits a columnar microstructure (Fig. I.2). This process allows to deposit a thin film of material on a substrate, according to the following sequence:

1. the deposited material is converted into vapor by physical means,

2. the vapor is transported across a region of low pressure from its source to the substrate,

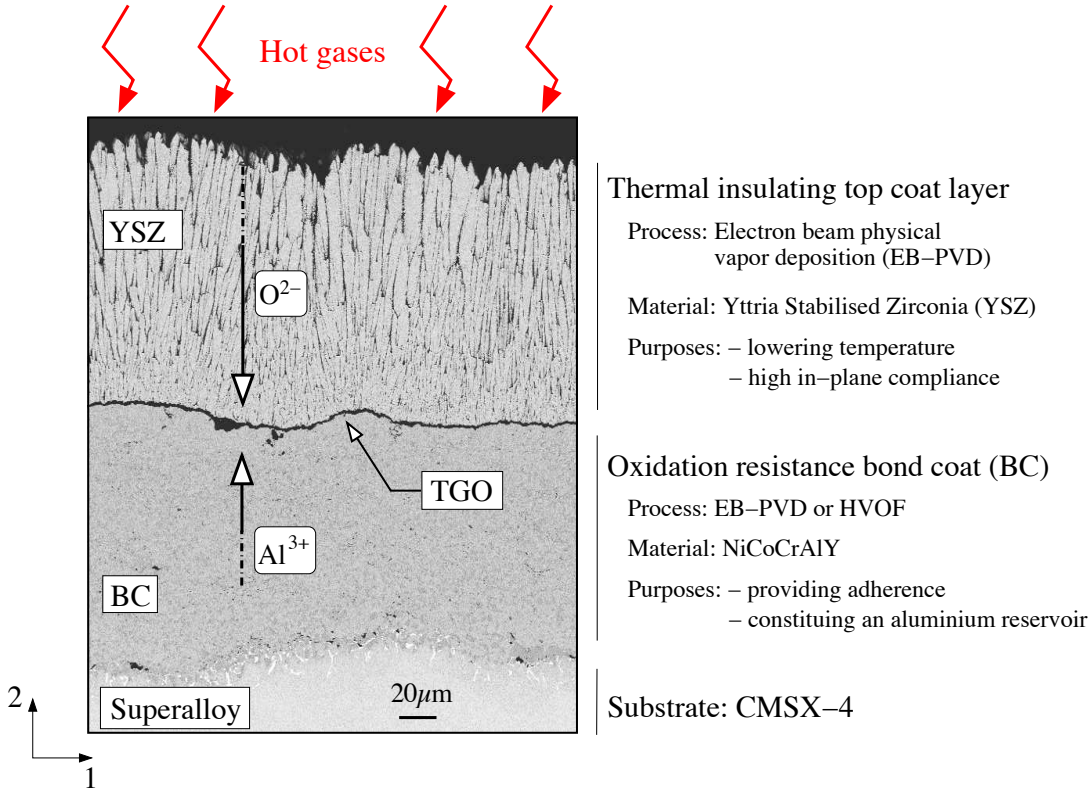

Figure I.2 : Scanning electron micrograph of the layered EB-PVD TBC system showing the three TBC components: the thermal insulator (YSZ), the thermally grown oxide (TGO) and the bond coat (BC) and their respectively functions to protect the superalloy substrate.

3. the vapor undergoes condensation on the substrate to form the columnar layer.

In this work, an EB-PVD YSZ coating has been selected for the following reasons: (i) its low thermal conductivity (2 W/m^{2}K) with minimal temperature sensitivity, (ii) its relatively high coefficient of thermal expansion compared to many other ceramics, reducing the thermal expansion mismatch with the substrate, (iii) its good resistance to the entrainment of high velocity particles in the engine gases (erosion) (Mercer et al., 2005) and (iv) its high planar compliance due to the columnar microstructure. The in-plane direction is parallel to the macroscopic ceramic-bond coat interface and correspond to direction X_1 in Fig. I.2.

I.2.2 Thermally grown oxide

The thermally grown oxide (TGO) is a chemical reaction product which forms at high temperatures in air due to the mechanism of outward and inward diffusion of the respective bond coat metal cations and oxygen anions, as illustrated in Fig. I.2. TGOs, such as alumina (α-Al_2O_3), act as **protective oxides** in oxidising environments and are used to protect the substrate from detrimental oxidation. If the oxidation principle is well understood, the reality is more complex because numerous criteria are required to provide good protective properties to the oxide layer: to cover the substrate uniformly, to be strongly adherent to the bond coat, to consume as less as possible the bond coat, to be stable, to be resistant at several environment (stress, temperature...). Some of these criteria are difficult to control for a simple reason: mechanisms governing the bond coat oxidation are most of the time not

well understood. Nevertheless, the understanding of the bond coat oxidation is fundamental because damage can occur in this zone of TBC systems.

The initial TGO thickness is around 0.5 μm after the YSZ top coat deposition-process and increases with oxidation time. Even if the TGO layer thickness is greatly lower in comparison with the ceramic layer and bond coat, the oxide growth plays a major role in TBCs lifetime. This study takes particularly care on the thermo-mechanical phenomena which are or could be influenced by oxide growth. In the present multi-scale approach, the objective will be to model the complex time-evolution of the oxide layer properties: its morphology, thickness growth, associated growth strains and its mechanical and thermal properties.

I.2.3 Bond coat

Bond coats aim to provide (i) **sufficient adhesion resistance** between the top coat and the substrate and (ii) **good oxidation resistance** to TBC systems. Furthermore, other requirements of the bond coat are:

- to reduce oxide growth and to improve its interfaces toughness, furthermore the TGO microstructure depend on the bond coat chemical composition,
- to provide a strain compliance at high temperatures thanks to its high creep behaviour. This point will be investigated in Chapter III, in particular the creep and plastic bond coat behaviour influence on local stress and strain fields close to the TGO.

Two different types of bond coats are considered to be the best alternative composition regards their objectives: Pt-modified aluminide and $NiCoCrAlY$. The production process for overlay coatings based on $NiCoCrAlY$ alloy system are EB-PVD, High Velocity Oxygen Fuel (HVOF), Vacuum Plasma Spraying (VPS) and Air Plasma Spraying (APS). In particular, HVOF and APS processes provide good compromise between performance, easy monitoring and processing cost. The deposition process and chemical composition of bond coats mainly influence their microstructures and properties.

I.3 Damage mechanisms in TBC systems

In addition to provide low thermal conductivity and oxidation resistance, TBCs used on gas turbine components are required to withstand damage. For turbine manufacturers, damage leads to the partial lost of thermal insulating properties. Several damage mechanisms can occur simultaneously, such as *erosion* due to foreign particles, *infiltration* of atmosphere particles and *spallation* of the ceramic layer.

I.3.1 Erosion: impact damage

Damage generated by the entrainment of high velocity particles through the gas engine can be in the form of erosive wear (generally cause by smaller particles, lower particle velocities, and/or lower impingement angles), see Fig. I.3(a), and impact spallation (generally caused by larger particles with greater particle velocities, and/or greater impingement angles), see Fig. I.3(b). As a consequence, the thickness of the top coat decreases and thermal insulation is not longer assured (Evans et al., 2006). A solution is to process a coating with an outer portion covering the initial ceramic layer so as to enhance impact resistance.

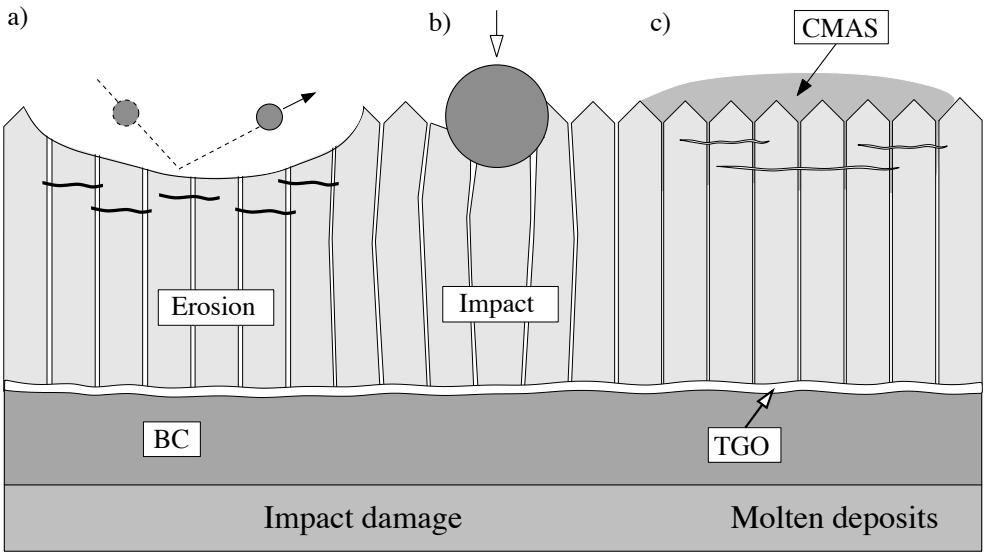

Figure I.3 : Illustration of damage mechanisms that can occur in TBCs due to foreign objects: (a) erosion by small particles, (b) impact of large particles and (c) CMAS infiltration (Evans et al., 2008).

I.3.2 Molten deposits: calcium-magnesium-alumino-silicate infiltration

Calcium-magnesium-alumino-silicate (CMAS) are common particles that are ingested into turbines and can form a molten layer at high temperatures. For engines operating in sandy environments, it has been observed that CMAS rapidly penetrate the open structure of the EB-PVD YSZ coating as soon as melting occurs (Mercer et al., 2005, Chen, 2006, Kraemer et al., 2008). There are many implications: (i) a decrease of the top coat strain compliance at low temperatures, (ii) an increase of the thermal conductivity and then higher local bond coat temperatures that can accelerate the oxide growth and (iii) a modification of the chemical composition of the YSZ ceramic layer. CMAS induce horizontal cracks in the top coat, as illustrated in Fig. I.3(c) (Evans and Hutchinson, 2007).

I.3.3 Top coat spallation

Observations made on engine components removed from service have indicated that, when TBC systems are subjected to critical thermal histories, the coatings are susceptible to spalling. TBCs exhibit multiple failure mechanisms which depend on their multiple structures (APS or EB-PVD top coats, $NiCoCrAlY$ or $(Pt, Ni)Al$ bond coats) or on the thermal loads. Most of the time, damage initiates close to the TGO layer, and when damage at one of the TGO interfaces or in the TGO itself become large enough, delamination is triggered leading to spallation. Figure I.4 illustrates a particular TBCs spallation mechanism, by buckling of the top coat due to interfacial damage at the TGO-BC interface. The top coat spallation is driven by the stored elastic strain energy per unit area (linked to the high level of compressive in-plane stress) in the top coat and oxide layer.

Two conditions have to be fulfilled to induce the top coat spallation: (i) **micro-damage** should be present at the future delaminated interface and (ii) the **stored elastic strain energy** per unit area has to reach the **interface toughness**. The stored energy is relaxed during top coat spallation. The interface toughness decreases with thermal exposure time because interfacial damage extension can proceed either by ductile void growth

(Dalgleish et al., 1989) or by microcrack growth induced by normal traction at the oxide interface (Reimanis et al., 1990, Reimanis et al., 1991). A major difficulty in a TBC study is that, interfacial damage and spallation mechanism are specific to each TBC system and the lifetime prediction should be adapted to the specific failure mechanism of the system to be predictive. Another difficulty is to bring together the numerous phenomena influencing the TBC lifetime which most of the time is controlled by events happening at different scales.

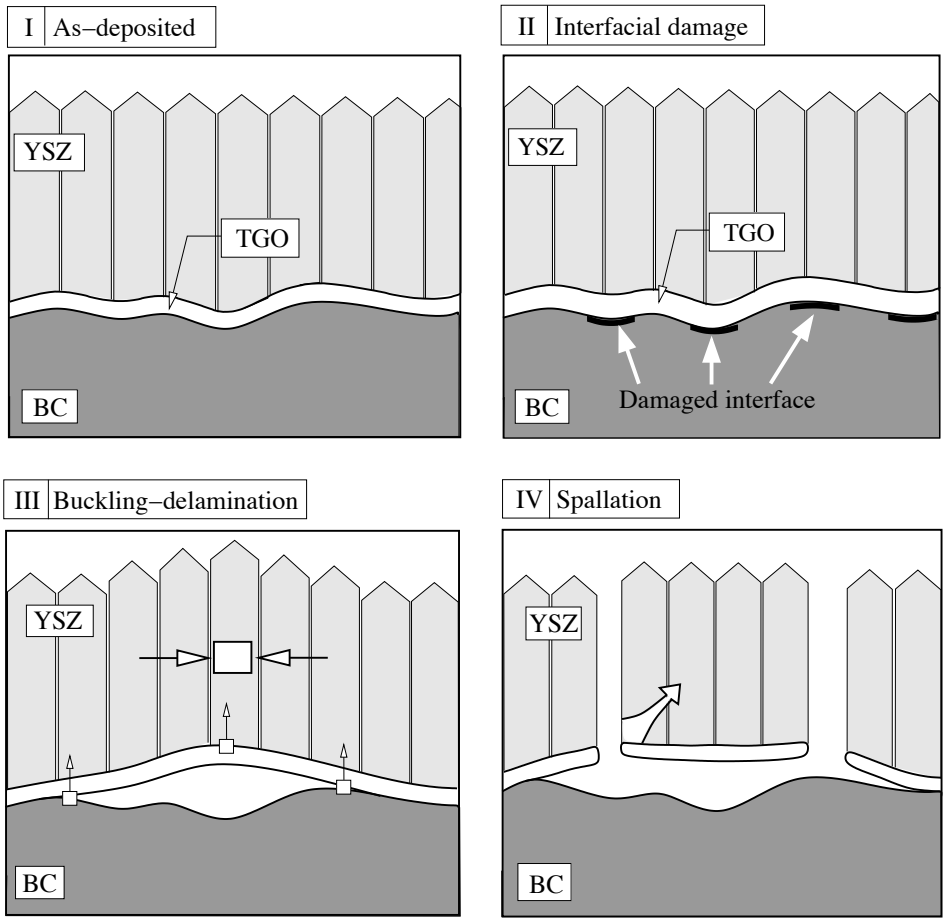

Figure I.4 : Schematics showing one of the TBC system spallation mechanism: (I) safe TBC system, (II) TGO interfacial damage, (III) buckling-delamination and (IV): top coat spallation.

I.4 Outline of thesis

Lifetime assessment of TBC systems requires a preliminary work based on the knowledge of the morphology and microstructure time-evolution of each constituent of the TBC system. The thesis is structured as follows: the Chapter II describes the investigation of (i) the typical microstructure of the porous columnar top coat ceramic, processed by EB-PVD using image-processing tools, (ii) the bond coat multiphase microstructure and (iii) the thin thermally grown oxide which develops at the bond coat-ceramic interface during high temperatures exposure. Based on previous observations and literature data, appropriate models to describe each individual material property of the TBC constituents are proposed. Finally, time-evolution of both oxide interface morphology is studied using image-processing and Fourier analysis. A representative elementary profile of the TGO layer is identified and a simulation of this profile is performed.

Motivated by the conclusions of the previous chapter, simulation and analysis of stress/strain fields occurring in EB-PVD TBC systems and their relationship with the observed macroscopic and microscopic damage are addressed in Chapter II. To reach this goal, the methodology to model oxide growth and to determine stress fields close to the moving TGO interface are presented. A parametric study dealing with the influence of the parameters characterising (i) the mechanical behaviour of each TBC constituent, (ii) the TGO morphology and (iii) the thermal loading on stress and strain fields is presented. Due to the main influence of the oxide roughness on the local stress fields close to the TGO, a realistic and complex simulation of the TGO morphology is performed using Fourier analysis. Stress and strain fields predicted with this latter approach and with a 3D sinusoidal simulation of the TGO profile will be compared to a simple 2D sinusoidal simulation of the TGO morphology.

Chapter IV constitutes the keystone of this thesis as it examines the failure mechanisms of the studied TBC. To achieve this aim, samples tested under isothermal loading conditions are analysed and observed follow by discussions of the dominant EB-PVD TBC failure mechanisms. A distinction is made between macroscopic top coat spallation mechanisms and microscopic oxide interfacial damage. This latter is assumed to be responsible for the TGO-BC interface toughness decrease.

Finally, in Chapter V, motivated by the TBC microstructure analysis, identification of failure mechanisms and numerical simulation of the local stress/strain fields close to the oxide, a relevant multi-scale predictive model of the EB-PVD TBC system lifetime is proposed. This model is based on an energetic approach taking into account the combined effects of time-evolution of the stored elastic strain energy per unit area (due to high level of in-plane stress) and the TGO-BC interface toughness evolution. Oxide interfacial damage, responsible for the oxide interface toughness decrease will be defined as a function of the stress/strain fields close to the oxide interfaces using a model previously developed by Lemaitre (1992). The lifetime model parameters will be calibrated using literature data and validated by the experimental database presented in Chapter IV.

References

Chen, X. (2006). CMAS delamination mechanisms in EB-PVD TBCs. *Surface and Coating Technology*, 200:3418–3427.

Dalgleish, B., Trumble, K., and Evans, A. (1989). The strength and fracture of alumina bonded with aluminium alloys. *Acta Materialia*, 37:1923–1931.

Evans, A., Clarke, D., and Levi, C. (2008). The influence of oxides on the performance of advanced gas turbines. *Journal of European Ceramic Society*, 28:1405–1419.

Evans, A., Fleck, N., Faulhaber, S., Vermaak, N., Maloney, M., and Darolia, R. (2006). Scaling laws governing the erosion and impact resistance of thermal barrier coatings. *WEAR*, 260:886–894.

Evans, A. and Hutchinson, J. (2007). The mechanisms of coatings delamination in thermal gradients. *Surface and Coating Technology*, 201:7905–7916.

Garrett, F. and Gyornak, C. (1953). *NACA*, RM-E 53 A:19.

Harrison, W., Moore, D., and Richmond, J. (1947). *NACA*, TN-1186.

Kraemer, S., Yang, J., and Levi, C. (2008). Infiltration-inhibiting reaction of gadolinium zirconate thermal barrier coatings with CMAS melts. *Journal of American Ceramic Society*, 91:576–583.

Mercer, C., Faulhaber, S., Evans, A., and Dariola, R. (2005). A delamination mechanism for barrier coatings subject to calcium-magnesium-alumino-silicate (CMAS) infiltration. *Acta Materialia*, 53:1029–1039.

Reimanis, I., Dalgleish, B., Brahy, M., Rühle, M., and Evans, A. (1990). Effects of plasticity on the crack-propagation resistance of metal-ceramic. *Acta Metallurgica Materialia*, 38:2645–2652.

Reimanis, I., Dalgleish, B., and Evans, A. (1991). The fracture-resistance of a model metal/ceramic interface. *Acta Metallurgica Materialia*, 39:3133–3141.

Chapter -II-

EB-PVD TBC system characterisation

Contents

II.1 Introduction

In a land based turbine engine, thermal barrier coating systems covering the blades are submitted to severe conditions in terms of temperature gradients and mechanical loading. According to experimental and in-service feedback data, thermo-mechanical loading affects the microstructure of TBC constituents and its interface morphologies (Evans et al., 2001). Due to the combined effect of high temperatures and stresses in turbine blades, several time-dependent phenomena can occur: (i) sintering of the porous ceramic top coat (Lu et al., 2001, Renteria and Saruhan, 2006), (ii) diffusion mechanisms through the bond coat and the superalloy substrate, modifying of the bond coat chemical composition and its microstructure (Nicholls, 2003, Müller and Neuschütz, 2003), (iii) the oxide thickness growth associated with the bond coat oxidation at the YSZ ceramic-bond coat interface, and (iv) evolution of the oxide morphology (Tolpygo and Clarke, 1998, Panat et al., 2003).

Lifetime assessment of TBC systems requires a preliminary work based on the knowledge of each individual constituent material properties and the interface morphology of the multilayer EB-PVD thermal barrier coating system. This chapter investigates:

- the time-evolution of EB-PVD TBC morphology and the parameters defining the microstructure,
- the relationship between microstructure and mechanical/thermal behaviour,
- constitutive material model of each individual TBC constituent.

In Section II.2, time-dependent phenomena occurring in each TBC constituent and their consequences on the microstructure evolution is investigated. Firstly, the typical microstructure of the porous columnar ceramic, processed by EB-PVD, and its evolution due to sintering is presented. In particular, intercolumnar porosity, characterising the YSZ microstructure is analysed using image-processing tools. Secondly, investigations of the bond coat microstructure are focused on the development of different multiphase layers in the bond coat due to interdiffusion with the substrate. The thin thermally grown oxide (TGO) layer is also studied, in particular its (i) kinetic oxide growth, (ii) phase composition, (iii) microstructure and (iv) growth strains associated with the bond coat oxidation. In Section II.3, the constitutive material model of each TBC constituent, at different scales is proposed. Based on previous observations and literature data, these models take into account the effects of extended thermal exposure on the mechanical behaviour. Finally, in Section II.4, the TGO morphology is studied using image-processing analysis. The time-evolution of the TGO interfaces roughness is also quantified. At the same time, a representative elementary profile of the oxide morphology is identified and a model of this profile is developed based on Fourier analyses. These studies are preliminary steps for the models of the TGO morphology proposed in Chapter III.

II.2 Characterisation of the TBC constituents microstructure

II.2.1 EB-PVD YSZ top coating

Ceramic coatings are used to protect hot constituents from the combustion gases. Their deposition is done using EB-PVD technology which requires complex and expensive equipments but provides superior coatings properties than those resulting from other processes, such as APS or HVOF (Beele et al., 1999). The main enhancement consists of its strain-tolerance, improved due to its typical columnar microstructure (An et al., 1999). Mechanical properties, as well as thermal conductivity depend on the texture and microstructure of the top coat (Zhua et al., 2001). The most critical feature is porosity for an EB-PVD YSZ top coating. A relevant model of such microstructure behaviour should be based on macro and microscopic description of the porous ceramic. The influence of thermal exposure times on the porosity spatial distribution along the ceramic layer, and more generally the sintering effects on the ceramic microstructure, are investigated in this section.

II.2.1.1 Observations and descriptions of the microstructure

Yttria stabilised zirconia (YSZ) top coat produced by EB-PVD contains individual columns which grow in a preferred crystallographic direction by adding molecules from the vapor phase (Schulz and Schmücker, 2000, Kato et al., 2005, Jang and Matsubara, 2006). SEM micrographs shown in Figure II.1 illustrate a typical columnar microstructure of the YSZ EB-PVD top coat after heat treatment (isothermal test during 13,500 h at 870°C). The top coating morphology exhibits elongated intercolumnar pores that become predominantly aligned perpendicular to the plane of the coating as its thickness increases, see Fig. II.1(a). The elongated intercolumnar porosity, noted ρ_e, increases the coating compliance, and leads to an improved lifetime of the TBC. Nevertheless, close to the TGO, the ceramic does not exhibit the typical vertical columnar microstructure seen elsewhere, inducing a low strain tolerance in comparison with the ceramic top part, see Fig. II.2(a).

A finer distribution of intracolumnar pores present inside the column also exists (Lughi et al., 2004). These nanopores, whose size is under 100 nm, constitute the internal porosity, ρ_i, as shown in Figs. II.1(b) and (c). Thermal conductivity is governed by the spatial distribution, the size and the morphologies of these nanopores (Jung et al., 2003). At a lower scale, texture of YSZ top coat consists of non-transformable metastable tetragonal θ' phase (Schulz et al., 1996). It could evolve at high temperatures (Lughi and Clarke, 2005) but these nano-scale considerations are not taken into account in our approach because they are difficult to model and are not adapted to the scale of the present study.

II.2.1.2 Sintering of the YSZ EB-PVD top coat

Sintering occurs in the YSZ ceramic after long exposure times at high temperatures, which is typical of land based gas turbine. The EB-PVD YSZ columns develop pronounced smoothing of their surfaces and coalesce together (Lu et al., 2001, Renteria and Saruhan, 2006). As shown in Figure II.1(c), *bridges* or *necks* form between columns. As a consequence, the strain compliance of the top coat decreases and driving spallation in-plane stresses increase. The densification of the columns themselves could also occur after long exposure times which increases the intrinsic Young's modulus of the columns. The surface column smoothing is one of the observed consequences of the intracolumnar pores distribution and

size time-evolution (Leyens et al., 1999, Lu et al., 2001). Sintering affects the mechanical and conductivity properties and should be taken into consideration in a lifetime predictive model (Azzopardi et al., 2004, Renteria et al., 2006, Ratzer-Scheibe and Schulz, 2007).

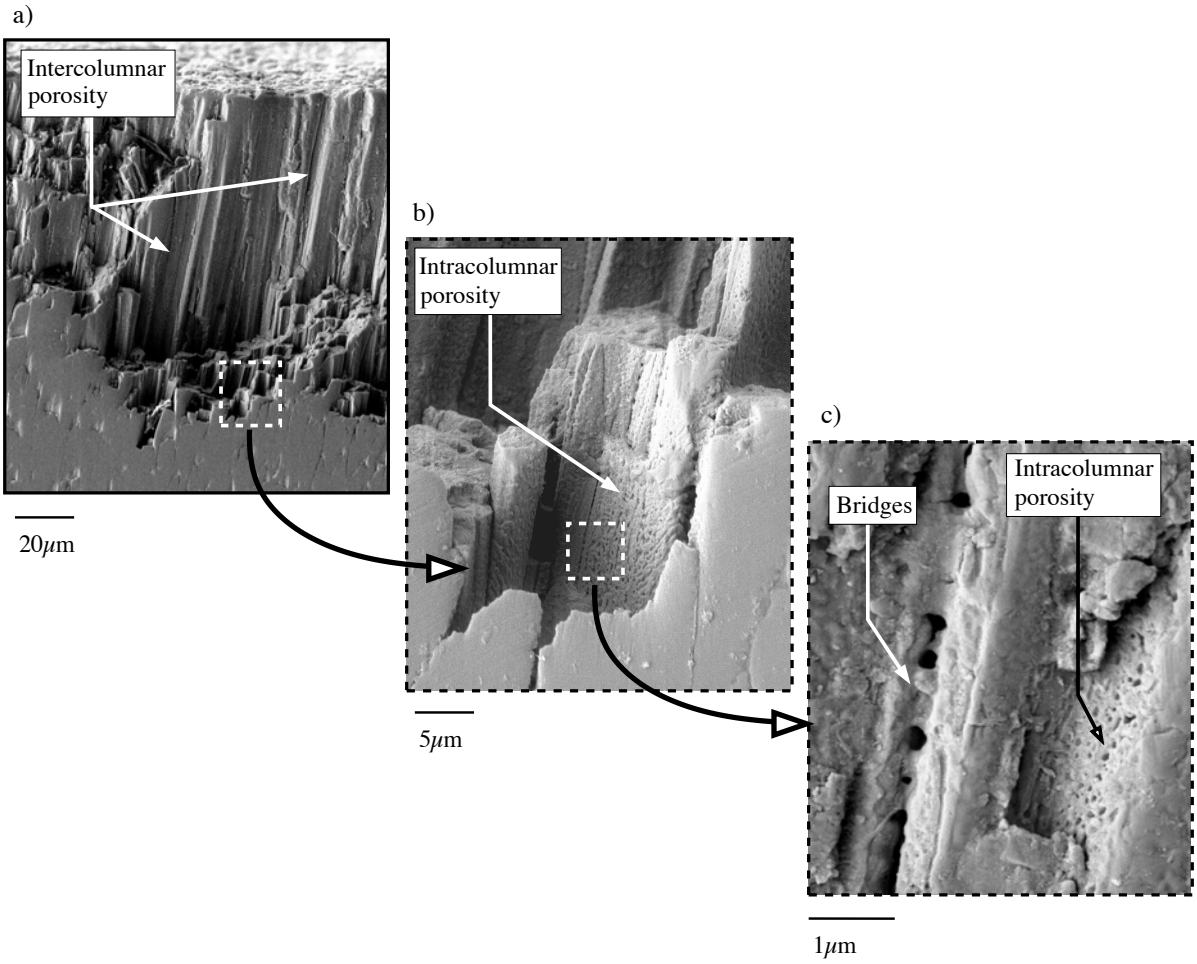

Figure II.1 : SEM micrographs showing the porous morphology of an EB-PVD YSZ coating at different scales, after 13,500 h at 870°C: (a) columnar microstructure and intercolumnar pores, ρ_e, (b) intracolumnar pores, ρ_i, and (c) bridges occurring between columns due to sintering.

II.2.1.3 External porosity evaluation along the top coat by image-processing analysis

The objective of this part of the work is to characterise the YSZ ceramic microstructure and in particular the intercolumnar porosity. The spatial distribution of the external porosity ρ_e along the YSZ layer is investigated for different time-temperature thermal histories. SEM micrographs have been obtained from samples tested under isothermal loading at different temperatures ranging from 930 to 1050°C and exposure times from 0 to 1000 h. The methodology to quantify external porosity is presented and the results for the different samples are analysed.

a) Methodology

The first step of this method consists of extracting the external porosity from SEM micrographs. We assume that pixels with weak luminance in the ceramic layer can be regarded as pores. The initial picture of the SEM micrograph of Fig. II.2(a) is encoded by pixels which are characterised by a grey level value ranging from 0 (dark) to 255 (white) (8 bits format). To extract black pixels corresponding to pores, a binary picture of the initial SEM micrograph is required and is obtained by the following procedure: all the pixels of the initial micrograph whose grey values range from 0 to 10 are amended as black pixels. The other pixels became white. The binary picture of the initial micrograph is given in Fig. II.2(b). This first step requires the use of equivalent grey level histogram for each SEM micrograph. This condition can be respected during the SEM micrograph capture. Note that in addition to the black pixels corresponding to the external pore, black pixels belonging to the internal porosity inside the columns themselves are also extracted. A special numerical tool is used to identify only the external porosity, see Fig. II.2(c). To that purpose, all the isolated porosities whose size were under 100 nm have been considered to be internal porosities and not retained.

The second step of the procedure to analyse the top coat morphology consists of the external porosity evaluation of the ceramic layer. The image-processing relies on the scanning procedure as shown in Figs. II.2(d) and (e). A 4 μm-width scanning band moves along the YSZ layer. For each position of this band, a mean value of the external porosity is obtained. The intercolumnar porosity is represented as a fraction of the whole image area. The influence of the scanning band width has been evaluated. A 4 μm-width band provides an adequate ratio between precision and processing time.

b) Results

The evaluation spatial distribution of intercolumnar porosity from the bottom to the top of the YSZ ceramic layer is discussed here. The measurements for different samples tested under different exposure times and temperatures are given in Figs. II.3 (930°C) and II.4 (990°C). Before any thermal exposure (0 h), the external porosity ranges from a low value (2%) close to the oxide layer, to a maximal value close to the top of the ceramic layer. The low porosity close to the TGO layer indicates that the ceramic is rather compact there. This result is consistent with the preliminary observations of EB-PVD micrographs, see Fig. II.2(a). Due to the EB-PVD process, a few microns are necessary to generate vertical columns and since columns are forming, external porosity is very low. Close to the oxide layer, the external porosity is similar for all the samples, see Figs. II.3 and II.4.

Close to the top of the ceramic layer, the external porosity is quasi-constant and depends on the time-temperature thermal loading, as expected. On the top surface of EB-PVD YSZ ceramic, the external porosity decreases with increasing exposure times and temperatures. At 930°C, ρ_e is equal to 16%, 14% and 10.4% after 120 h, 300 h and 1000 h, respectively. At 990°C, for the same thermal exposure times, the values of ρ_e are 13.5%, 12.4% and 10.5%. These values should be compared to the initial external porosity on the top surface of the YSZ layer before any thermal exposure, namely 16.6%. These measurements agree with those reported at the top of the ceramic layer before and after 24 h of exposure at 1500°C, namely 12% and 9%, respectively, (Wellman and Nicholls, 2005).

Figure II.5 shows the temperature influence on the spatial porosity distribution along the ceramic layer after 300 h at 930°C, 990°C and 1050°C. It can be seen that sintering is responsible for a sharp decrease of the external porosity at 1050°C. At this temperature, the porosity increases linearly through the ceramic layer thickness. Due to the complete

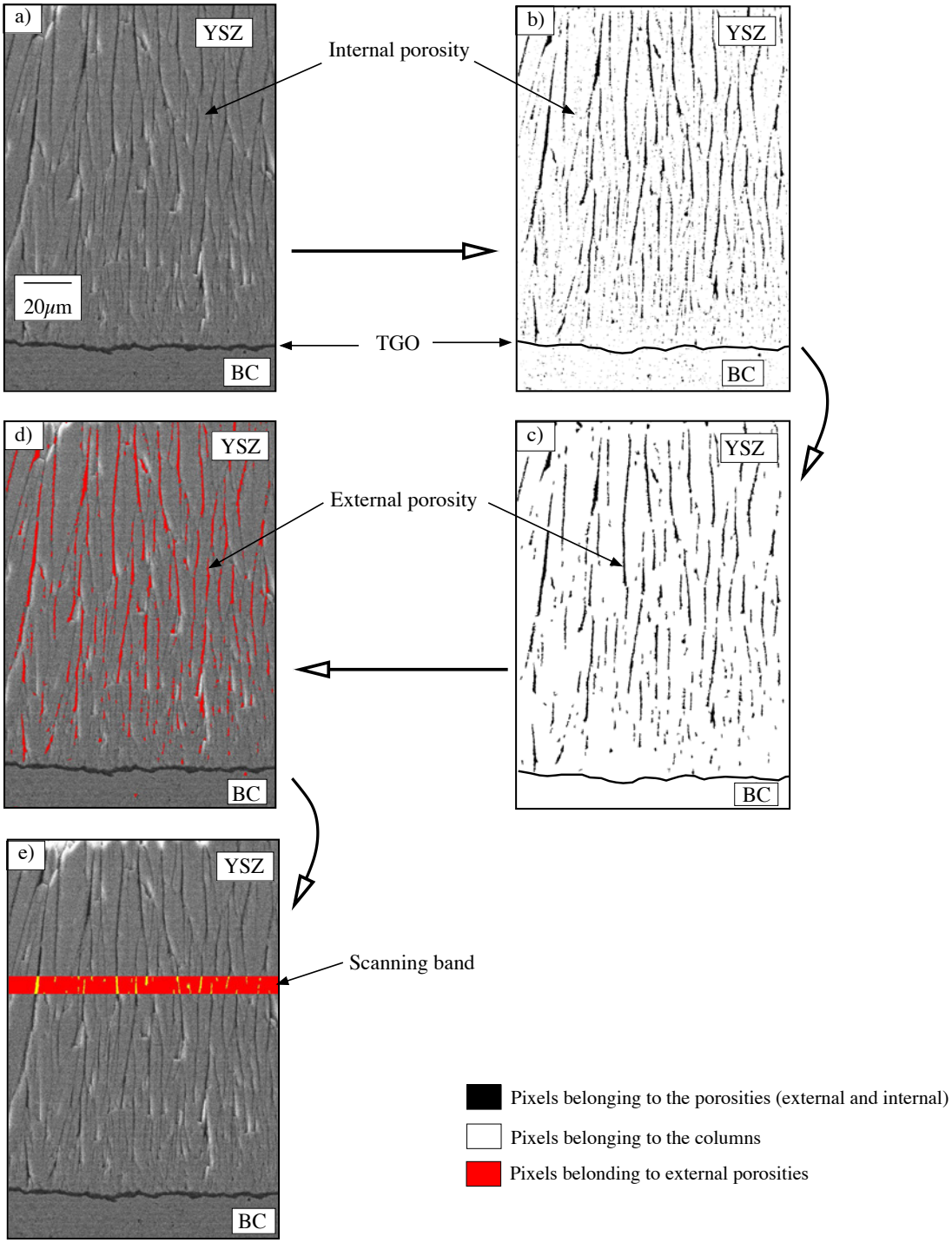

Figure II.2 : (a) Initial SEM micrograph of the EB-PVD TBC cross section, (b) binary picture with external and internal porosities, (c) binary picture showing only the extracted external porosity, (d) external porosity reported in the initial SEM micrograph and (e) evaluation of the external porosity percentage along a 4 μm-wide scanning band.

spallation of specimens tested after 300 h at 1050°C, it was not possible to obtain similar measurements for times up to 300 h.

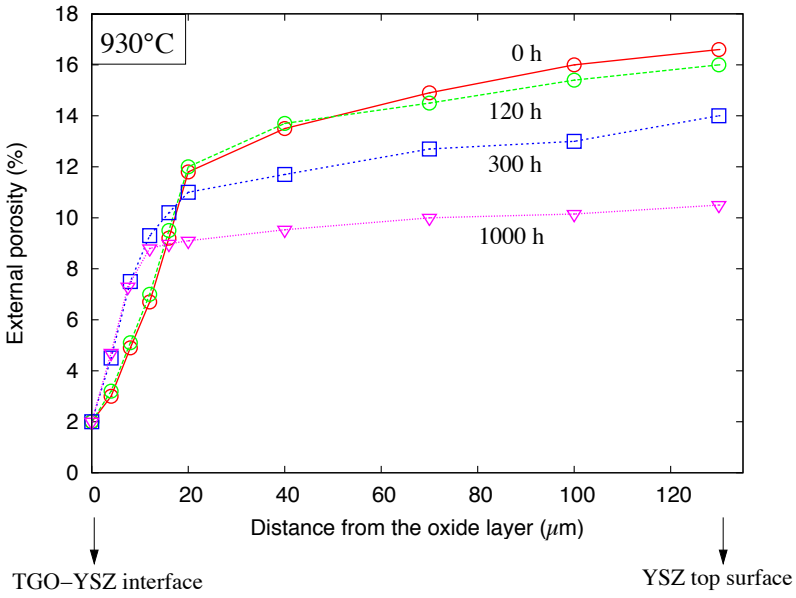

Figure II.3 : Percentage of external porosity along a 4 μm-wide scanning band, as a function of the distance from the oxide layer after 0 h, 120 h, 300 h and 1000 h exposure 930°C.

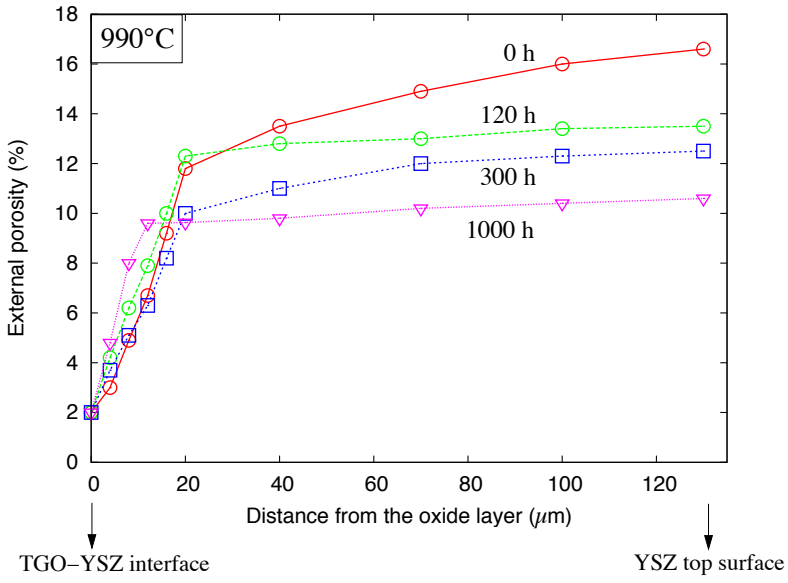

Figure II.4 : Percentage of external porosity along a 4 μm-wide scanning band, as a function of the distance from the oxide layer after 0 h, 120 h, 300 h and 1000 h exposure at 990°C.

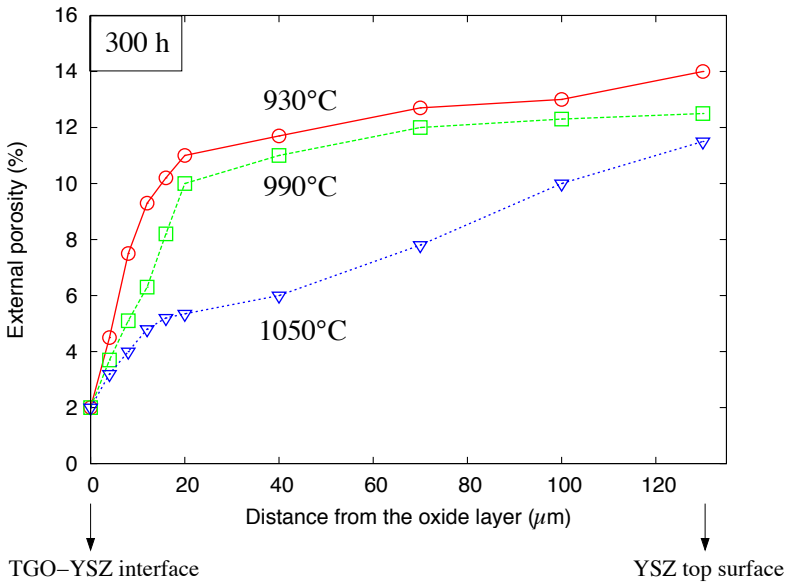

Figure II.5 : Percentage of external porosity along a 4 μm-wide scanning band, as a function of the distance from the oxide layer after 300 h at 930°C, 990°C and 1050°C exposure time.

II.2.1.4 Discussions

The present investigation has provided quantitative and qualitative information about the evolution of top coat EB-PVD microstructure at different temperatures and exposure times. SEM micrographs observation and analysis of the external porosity spatial distribution have shown that: (i) high temperatures typical of industrial practice induces changes in the microstructure (sintering effects) and (ii) intercolumnar porosity varies strongly through the ceramic layer. The external porosity spatial distribution also depends on the deposition process (Terry et al., 1999, Jang and Matsubara, 2004). According to Jang and Matsubara (2004), the total external porosity (pores whose size > 100 nm) increases with the substrate rotation speed and ranges from 5 to 18% for 0 to 20 rpm, respectively. Our approach provides an improvement in the quantification of the external porosity spatial distribution through the top coat and provides more available information than the mean external porosity measured on the top surface of the ceramic layer (Wellman and Nicholls, 2005).

If the need to model the sintering effect on the YSZ top coat morphology is clear from the high level of porosity in a major part of the layer, it might not be required in the region close to the TGO where intercolumnar porosity is lower. Likewise, the columnar microstructure of the ceramic is inhomogeneous across the YSZ top coat thickness. Accordingly, the model to be proposed to describe the top coat mechanical behaviour will not be the same for the ceramic part close to the TGO as for the rest of the YSZ layer. The internal porosity spatial distribution has been also investigated. Nevertheless, the image-processing analysis does not provide interesting results, principally because the criterion to characterise a nano-porosity (<100 nm) required a high level of resolution of SEM micrographs.

II.2.2 Thermally grown oxide

As previously discussed, the thin oxide layer which develops at the bond coat-ceramic interface, provides good oxidation resistance to TBC systems. Despite the thin nature of the TGO in comparison to the bond coat and YSZ ceramic layer, it plays a crucial role in the lifetime of TBC systems. Actually, damage develops close to the TGO and is responsible for a decrease of the interface toughness (Vasinonta and Beuth, 2001, Guo et al., 2005). Furthermore, the oxide thickness growth increases the stored elastic strain energy per unit area which is responsible for TBC spallation.

Mechanisms occurring during alumina growth are more complex than for other oxides (Levi et al., 1986, Monceau et al., 2000, Chevalier, 2007) and have to be described specifically. The objective of this section is to characterise the following TGO properties: (i) oxide thickness evolution (oxidation kinetics), (ii) chemical composition, (iii) microstructure and (iv) growth strains associated with the bond coat oxidation. The oxide morphology and its corresponding roughness will be presented in detail in the next section (II.4).

II.2.2.1 TGO growth: oxidation kinetics

Oxide growth kinetics have been determined at 950°C, 1050°C and 1150°C, for times up to 1000 h by the University of Birmingham (Taylor et al., 2006) for TBC systems provided by SIEMENS. The measured oxide thickness evolution is shown in Fig. II.6. TGO thickness measurements were made in a cross section normal to the bond coat-YSZ ceramic interface. Only the specimens with no damage close to the oxide have been analysed. Kinetics equation that describes the mean TGO is:

$$h_{ox} = h_0 + (k_n t)^{\frac{1}{n}}, \tag{II.1}$$

where h_0 is the oxide thickness of the as-received specimen, t is the oxidation time and k_n and n are material parameters which depend on temperature. These data are required for the numerical approach to be presented in Chapter III.

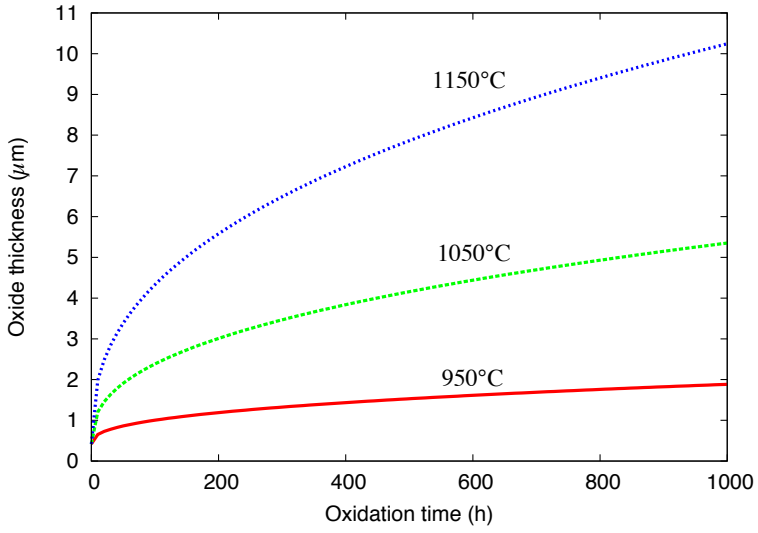

Figure II.6 : Oxide thickness time-evolution for a $NiCoCrAlY$ bond coat at three different temperatures: 950°C, 1050°C and 1150°C (Taylor et al., 2006).

II.2.2.2 Investigation of the TGO chemical composition

The purpose of this section is to carry out a detailed assessment of the chemical composition of the TGO phases. An appreciation of the TGO chemistry will be of assistance to (i) the overall understanding of TGO evolution during thermal exposure and (ii) to model its mechanical behaviour. In order to analyse the TGO metallographic composition, a cross section of a specimen, exposed at 870°C during 13,500 h, was examined by Scanning Electron Microscopy (SEM) and Energy-Dispersive Spectroscopy (EDS) techniques.

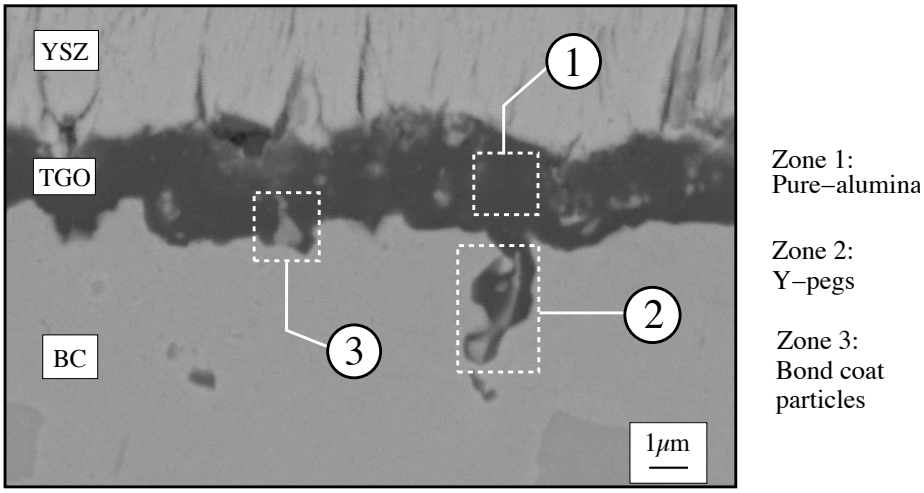

Figure II.7 : SEM micrograph of the TGO layer, showing (1) α-alumina phase, (2) Y-pegs and (3) bond coat particles trapped within the oxide.

a) Observations

Cross-section observations of the TGO revealed an inhomogeneous composition. In Figure II.7, three different areas can be distinguished:

Zone 1: this is the principal zone of the oxide. Its composition is shown in Fig. II.8(a) and Table II.1. EDS revealed that the grains within the regular TGO region are composed of almost pure Al_2O_3 phase, as expected.

Zone 2: many pegs have been observed in the TGO and more precisely at the TGO-BC interface. The pegs thicknesses typically range from 5 to 8 μm, whereas the average TGO thickness is around 3 μm. There is no visible porosity within the pegs themselves. The qualitative and quantitative composition of this pegs are, respectively, given in Fig. II.8(b) and Table II.1.

Zone 3: according to the EDS spectrum, Fig. II.8(c) and Table II.1, this region corresponds to the elements of the bond coat trapped within the TGO.

b) Discussions

The thermally grown oxide in the studied TBC system presents a complex morphology and microstructure. It consists primarily of three constituents: (1) α-alumina, (2) a distribution of oxide pegs rich in yttrium and (3) $NiCoCrAlY$ bond coat particles trapped within the TGO. The formation of these Y-rich particles is likely to be due to one of two mechanisms.

Table II.1 : Quantitative results of the chemical composition for 1: α-alumina phase, 2: Y-pegs and 3: bond coat particles in Fig. II.7

	1: α-alumina phase		**2: Y-pegs**		**3: Bond coat particles**	
Element	**Weight (%)**	**At. (%)**	**W (%)**	**At. (%)**	**W(%)**	**At.(%)**
O	46.48	60.09	19.66	41.98	28.41	50.56
Al	51.40	39.41	20.13	25.48	32.29	34.08
Cr			14.84	9.75	7.66	4.20
Co			13.17	7.63	6.99	3.38
Ni			14.08	8.19	6.97	3.38
Y	2.12	0.49	18.13	6.97	7.01	2.24

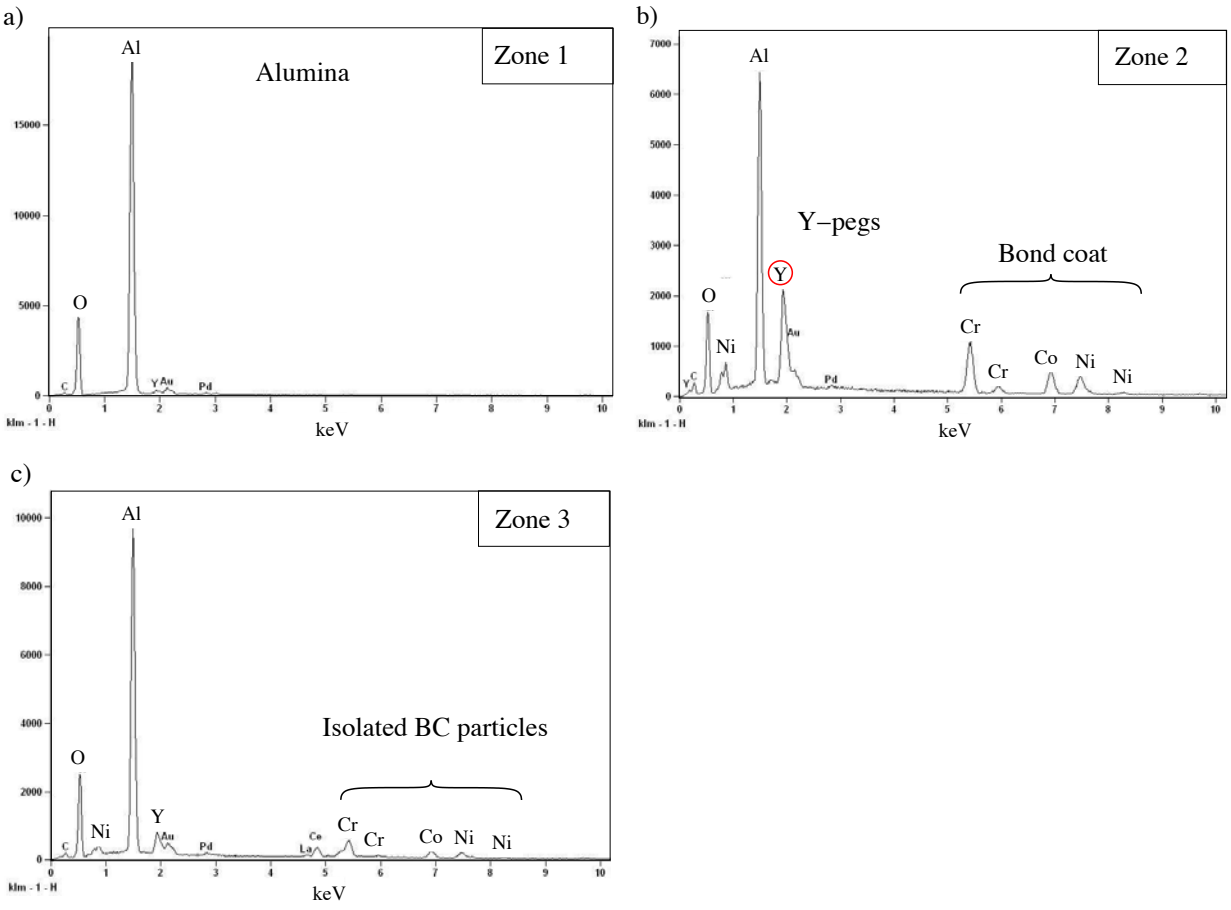

Figure II.8 : EDS spectrum from the zone (a) 1 α-alumina, (b) 2 Y-rich oxide pegs and (c) 3 trapped bond coat particles.

The first, is diffusion of yttrium ions into the TGO during thermal cycling from either the bond coat or substrate. The second mechanism is caused by the entrapment of bond coat regions rich in yttrium by the advancing oxidation front during oxide growth, followed by oxidation (Mercer et al., 2006). These pegs induce numerous thickness heterogeneities and might be at the origin of micro-damage nucleation and growth.

Observations of cross-section micrographs of a TBC sample ($NiCoCrAlY$ bond coat and EB−PVD top coat) after 14,000 h of service in an aero-engine also show relatively uniform TGO with occasional yttrium pegs, bond coat particles trapped in the TGO and small-scale porosities (Xu et al., 2004). Y-pegs and micro porosities are also supposed to be preferential sites to crack nucleation or extension close to the oxide.

II.2.2.3 Microstructural description

Bond coat oxidation creates firstly unstable γ, δ and θ-alumina phases that transform in a stable α-alumina (Pint et al., 1995, Tolpygo and Clarke, 2000a). According to the literature, such phase transformation can induce a volumetric decrease of 14% (Prescott and Graham, 1992). Once the phase-transformation is completed, oxide grain growth mechanisms are mainly influenced by temperature, oxygen pressure and bond coat chemical composition (Monceau et al., 2000). Observations of alumina cross-sections show a duplex alumina scale made up of a columnar layer near the BC-TGO interface and a thin equiaxed layer close to the outer surface, see Fig. II.9 (Clarke, 2003). The duplex morphology of the alumina layer is related to both cationic and anionic diffusion mechanisms associated with alumina growth.

The outward diffusion of Al^{3+} cations leads to an outer equiaxed thin layer and the inward diffusion of oxygen leads to an inner columnar layer (Grabke, 1997, Tolpygo, 1999), as represented in Fig. II.9. The thickness ratio between inner and outer oxide layers is governed by the difference between the diffusion rates of anions and cations in the TGO.

A comparison of experimental results obtained for synthetic compacted and thermally grown alumina shows substantial differences (Balmain et al., 1997, Chevalier et al., 2005). The diffusion of oxygen and aluminium ions is not the same in both systems. Nevertheless, there is a point for which the results agree: alumina formation is strongly dependent in reactive elements such as yttrium (Choquet and Mevrel, 1989, Pint et al., 1993, Mennicke et al., 1998). The diffusion of oxygen ions at alumina grain boundaries becomes predominant in the presence of yttrium. This leads to an enhancement of oxidation at the BC-TGO interface (the so-called internal interface) and the columnar grain structure. Due to the presence of yttrium in the bond coat and the TGO columnar microstructure generally observed in $NiCoCrAlY$ bond coat, we will assume that the oxide layer growth close to the BC-TGO interface is controlled by the diffusion of oxygen ions through the alumina grain boundaries. It is assumed that the TGO growth does not occur in the entire layer and is not function of its thickness time-evolution, as reported by Balint and Hutchinson (2005).

II.2.2.4 Growth strains due to TGO formation

Alumina formation process occurs as illustrated in Fig. II.10. Here, the columnar grain structure beneath an equiaxed initial layer supports the understanding that the new TGO forms primarily at the bond coat interface. This is believed to happen because oxygen diffusivity along TGO grain boundaries exceeds that of Al^{3+} cations, *i.e.* $J^{Al_{3+}} \ll J_{O^{2-}}$. A volumetric expansion, representing the volume increase which accompanies

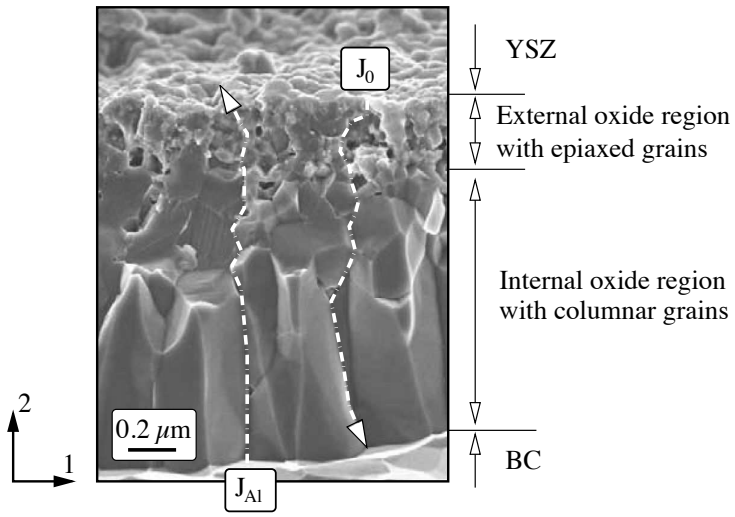

Figure II.9 : Transmission electron micrograph (TEM) showing the inner columnar alumina layer and the outer layer with little epiaxed grains (Clarke, 2003). The respective inward and outward diffusion of oxygen and aluminium are also shown.

the bond coat transformation to alumina at the TGO-BC interface, is associated with the oxidation phenomena. This mechanism is one of the main stress sources (around 1 GPa) at high temperatures in TBC systems (Evans et al., 2001, Karlsson and Evans, 2001, Nychka et al., 2004). How does the oxide volumetric expansion occur?

From a macroscopic point of view, it has been observed that, for the constrained strain conditions as TGO is submitted, growth strains do not develop isotropically. Instead, they develop preferentially along the direction offering the lowest resistance to that expansion, here direction X_2 in Figs. II.9 and II.10. This direction is also the preferred orientation of the oxide grain. Nevertheless, it is not well understood whether locally the growth strains are also anisotropic. Indeed, in an unconstrained system, the volumetric expansion can be isotropic (Evans et al., 2001, Hille, 2009). As mentioned in the literature, growth strains accompanying the TGO formation could also be influenced by (i) the existence of in-plane compressive stresses (direction X_1), (ii) the TGO columnar microstructure (Karlsson et al., 2003) and (iii) dislocation climb (Clarke, 2003).

In our model, we will consider the relationship between the local growth strains occurring at the micro-scale and the global growth strains found at the grain scale. Consider a columnar oxide grain, 0.5 μm thick, the possible locations of new oxide nucleation are the top (zone 1), the bottom (zone 2) and the grain boundaries of the oxide scale (zone 3), as illustrated in Fig. II.10. For diffusion-controlled oxidation reaction, it is assumed that the plan of reaction is oriented so that it is everywhere normal to the flux of reactants and so to the local interfaces (Rhines, 1940, Darken, 1942, Rhines and Wolf, 1970). Rhines and Wolf (1970) assumed that, if the oxide grows only by complete inward or outward diffusion of oxygen and aluminium ions respectively, no transversal strains are generated at it is illustrated by Cases 1 and 2 in Fig. II.10. Only an oxide reaction occurring at TGO grain boundaries (Case 3) could induce in-plane stresses.

According to the initial definition of the Pilling Bedworth Ratio (PBR), π is the volume expansion associated with the oxidation reaction of an $NiAl$ material:

$$NiAl + \frac{1}{2}O_2 \longrightarrow \frac{1}{3}Ni_3Al + \frac{1}{3}Al_2O_3, \tag{II.2}$$

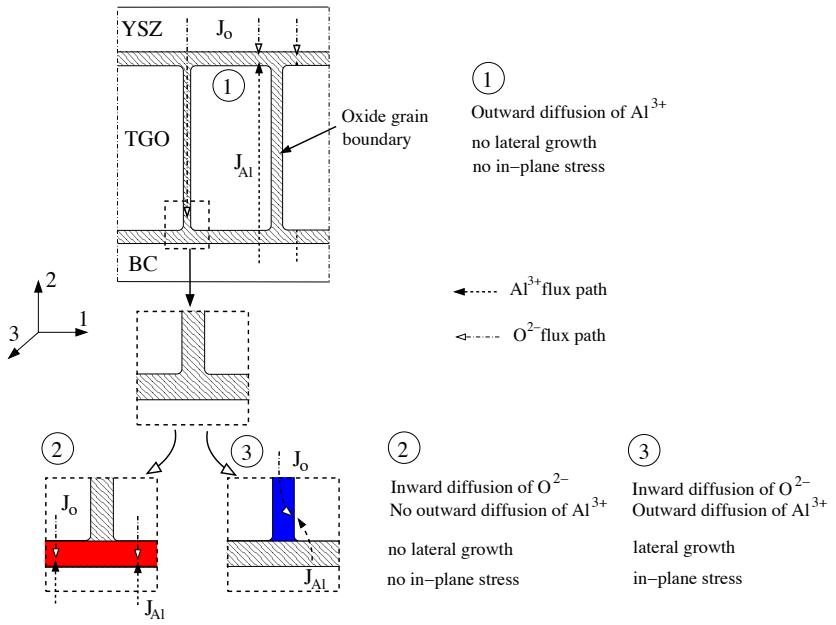

Figure II.10 : Schematic illustration showing the new oxide associated with inward and outward diffusion of O^{2-} and Al^{3+} ions. With or without outward oxygen diffusion, new oxide is generated respectively parallel to the BC-YSZ interface (Cases 1 and 2) inducing normal growth strain or in grain boundary (Case 3) and gives rise to transversal growth strain responsible for high in-plane stresses.

Using this approach, (Pilling and Bedworth, 1927), π is obtained from the ratio between the molar volume (m^3/mol) of the Al_2O_3 produced, $V_m^{Al_2O_3}$, and that before oxidation, $V_{Al-[cons]}^m$:

$$\pi = \frac{V_m^{oxide-produced}}{V_m^{Al-consumed}} = \frac{V_m^{Al_2O_3}}{V_m^{Al-[cons]}}, \tag{II.3}$$

with $V_m^{Al-[cons]}$ being the difference between the initial atomic volume of Al in the $NiAl$, noted $V_m^{Al-[NiAl]}$ and the final atomic volume of Al in the Ni_3Al, noted $V_m^{Al-[Ni_3Al]}$:

$$V_m^{Al-[cons]} = 3V_m^{Al-[NiAl]} - V_m^{Al-[Ni_3Al]}, \tag{II.4}$$

$V_m^{Al-[NiAl]}$ and $V_m^{Al-[Ni_3Al]}$ can be calculated knowing (i) the number of molecules per unit cell, Z of Al and Ni for the $NiAl$ and Ni_3Al, (ii) the molar volume of a unit cell corresponding to $NiAl$ and Ni_3Al (m^3/mol), respectively noted V_m^{NiAl} and $V_m^{Ni_3Al}$:

$$V_m^{Al-[NiAl]} = \frac{Z_{Al}}{Z_{NiAl}} V_m^{NiAl} = \frac{1}{2} V_m^{NiAl}, \tag{II.5}$$

$$V_m^{Al-[Ni_3Al]} = \frac{Z_{Al}}{Z_{Ni_3Al}} V_m^{Ni_3Al} = \frac{1}{4} V_m^{Ni_3Al}. \tag{II.6}$$

Note that the crystal structure is not the same for the Ni_3Al and $NiAl$. Finally, the atomic volume of the components $V_m^{Al_2O_3}$, $V_m^{Ni_3Al}$ and V_m^{NiAl} can be calculated from:

$$V_m = \frac{N_a a^3}{Z}, \tag{II.7}$$

where N_a is the Avogadro's number (6.02 10^{23} at/mol), a^3 is the volume of an unit cell (m^3/at) and Z is the number of molecules per unit cell. Using the data available in the literature (Xu and Gao, 2000), $V_m^{Al_2O_3}, V_m^{Ni_3Al}$ and V_m^{NiAl} take, respectively, the following values: 2.56^{-5} m^3/mol, 2.72^{-5} m^3/mol and 1.44 10^{-5} m^3/mol. Finally, the value of π associated with the Eq. II.3 is:

$$\pi = 1.73 \tag{II.8}$$

This result shows that the PBR calculated for $NiCoCrAlY$ oxidation is different from that calculated for pure Al ($\pi = 1.29$). This high value of growth strain will generate high stress levels during bond coat oxidation. To compare these PBR values, our reasoning should also take into account the volumetric reduction due to β-$NiAl$ phase transformation in the bond coat. The estimated magnitude of the volume decrease associated with the bond coat phase transformation is around 0.62 (Tolpygo and Clarke, 2000b) and offsets partially the high dilatation associated with alumina formation, as illustrated Fig. II.11. This preliminary work illustrates that the PBR approach based on its historical definition, is not the most relevant one.

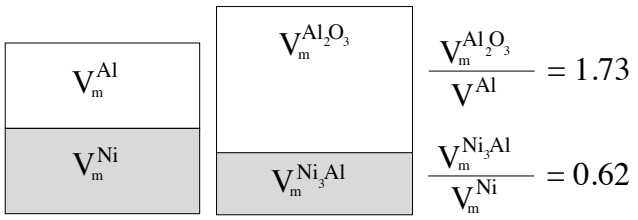

$$\frac{V_m^{Al_2O_3} + V_m^{Ni_3Al}}{3V_m^{NiAl}} = 1.22$$

Figure II.11 : Illustration of the volumetric expansions associated with the $NiCoCrAlY$ bond coat oxidation, Eq. II.2.

Another approach consists of defining the volume expansion associated with the $NiCoCrAlY$ bond coat oxidation (Eq. II.2) as the ratio, $\pi^\star$, between the atomic volume of the produced metal/oxide, $V_m^{metal/oxide-produced}$, and that before, $V_m^{metal-consumed}$. It can be formulated as follows,

$$\pi^\star = \frac{V_m^{metal/oxide-produced}}{V_m^{metal-consumed}} = \frac{V_m^{Al_2O_3} + V_m^{Ni_3Al}}{3V_m^{NiAl}}. \tag{II.9}$$

Here, $V_m^{Al_2O_3}, V_m^{Ni_3Al}$ and V_m^{NiAl} have been calculated previously. Finally, the value of $\pi^\star$ related to the Eq. II.9 is:

$$\pi^\star = 1.22 \tag{II.10}$$

Based on this result, the value related to the bond coat volumetric reduction is similar to that found by Tolpygo and Clarke (2000), namely 0.62. Also, $\pi^\star$ has a value close to that for the oxidation of pure aluminium ($\pi = 1.29$), discussed above. This value also indicates that the volume increase associated with alumina formation cannot be neglected in the model.

The approach based on the Pilling Bedworth Ratio is considered sometimes too simplistic as it does not provide any answers about the mechanisms occurring during oxidation. Nevertheless, it has the advantage to assure that mass conservation is preserved (Eq. II.9).

Each molar volume of the bond coat changed into oxide induces a volumetric expansion where, oxidation takes place, at the grain boundaries or at both oxide interfaces.

Before defining the oxide growth strains, the following assumptions should be born in mind:

- oxide growth occurs at the TGO-BC interface due to the presence of yttrium in the oxide grain boundaries, slow down the diffusion of aluminium: $J_{Al_{3+}} \ll J_{O^{2-}}$,
- the TGO microstructure is composed of columnar grains close to the TGO-BC interface,
- growth strains are normal to the oxide grain interfaces, and points out the predominant role of the TGO microstructure on oxide growth which induces anisotropic growth strains,
- the volumetric expansion associated with the bond coat oxidation, $\pi^\star$, has to be considered at the grain scale.

The relationship between $\pi^\star$ and the growth strain components is given by the following equation:

$$\pi^\star = \frac{V_f}{V_0} = (1+\varepsilon_1)(1+\varepsilon_2)(1+\varepsilon_3), \tag{II.11}$$

where V_f and V_0 are the respective values of the oxidised and unoxidised volume of bond coat. Also, ε_1, ε_2 and ε_3 correspond to the growth strains in the directions X_1, X_2 and X_3 illustrated in Fig. II.10. Assuming the lower values of the growth strains, one finds:

$$\pi^\star = \frac{V_f}{V_0} \approx 1 + \varepsilon_1 + \varepsilon_2 + \varepsilon_3. \tag{II.12}$$

Locally, the respect of the mass conservation implies that the oxide growth strain tensor associated with oxidation occurring normal to the YSZ-BC interface, $\underset{\sim}{\boldsymbol{\varepsilon}}_\phi^{l1}$ (Case 2 in Fig. II.10), is defined as:

$$\underset{\sim}{\boldsymbol{\varepsilon}}_\phi^{l1} = \begin{bmatrix} \varepsilon_1 & 0 & 0 \\ 0 & \varepsilon_2 & 0 \\ 0 & 0 & \varepsilon_3 \end{bmatrix} = \begin{bmatrix} 0 & 0 & 0 \\ 0 & \pi^\star - 1 & 0 \\ 0 & 0 & 0 \end{bmatrix} \tag{II.13}$$

In the present case, $\varepsilon_1 = \varepsilon_3 = 0$ and according to Eq. II.12, $\varepsilon_2 = \pi^\star - 1$. The oxide growth strain tensors at the oxide grain boundaries close to the TGO-BC interface (Case 3) are $\underset{\sim}{\boldsymbol{\varepsilon}}_\phi^{l2}$ and $\underset{\sim}{\boldsymbol{\varepsilon}}_\phi^{l3}$ for the directions X_1 and X_3 respectively:

$$\underset{\sim}{\boldsymbol{\varepsilon}}_\phi^{l2} = \begin{bmatrix} \pi^\star - 1 & 0 & 0 \\ 0 & 0 & 0 \\ 0 & 0 & 0 \end{bmatrix} \tag{II.14}$$

$$\underset{\sim}{\boldsymbol{\varepsilon}}_\phi^{l3} = \begin{bmatrix} 0 & 0 & 0 \\ 0 & 0 & 0 \\ 0 & 0 & \pi^\star - 1 \end{bmatrix} \tag{II.15}$$

At this scale, the grain growth accompanying the oxidation can be defined by a normal and transversal to the bond coat-ceramic interface strain growth components, ε_N and ε_T, respectively. The normal and transversal directions correspond to the direction X_1 and X_2, respectively.

$$\underset{\sim}{\varepsilon}^g_\phi = \begin{bmatrix} \varepsilon_T & 0 & 0 \\ 0 & \varepsilon_N & 0 \\ 0 & 0 & \varepsilon_T \end{bmatrix} \tag{II.16}$$

The global anisotropic growth strain $\underset{\sim}{\varepsilon}^g_\phi$ is a function of the ratio between the number of oxidation reactions at the TGO-BC interface (N_1) or at grain boundaries (N_2 and N_3), illustrated respectively in Cases 2 and 3 in Fig. II.10. N_T is the total number of reactions (Eq. II.18):

$$\underset{\sim}{\varepsilon}^g_\phi = \sum_{i=1}^{n=3} \frac{N_i}{N_T} \underset{\sim}{\varepsilon}^{li}_\phi, \tag{II.17}$$

$$N_T = N_1 + N_2 + N_3. \tag{II.18}$$

Mass conservation is respected locally and at the grain scale, one finds:

$$Tr(\underset{\sim}{\varepsilon}^l_\phi) = Tr(\underset{\sim}{\varepsilon}^g_\phi) = \pi^\star - 1. \tag{II.19}$$

The ratio between normal and transversal strain components characterises the relative weight of each diffusion mechanism. Equation II.11 implies that the phase transformation strain tensor (Eq. II.16) associated with the inward oxidation reaction can be fully described knowing the volume evolution $\pi^\star$ and the ratio between ε_N and ε_T. In this work, the ratio between the normal and the transversal strain components (Eq. II.20) is taken to be that inferred from experiments done for oxidised Ni (Huntz et al., 2002). For a $NiCrAlY$ bond coat, experimental work should be carried out to determine in the same way the ratio between the transversal and normal growth strains.

$$\varepsilon_N = 87\varepsilon_T \tag{II.20}$$

Note that, even if the growth strains at the oxidation temperature are not completely elucidated, our approach is based on a microscopic analysis of the TGO microstructure and physical phenomena. Finally, the transversal growth strain values ($\varepsilon_T = 0.24\%$) is of the same order of magnitude than that reported in the literature (Caliez et al., 2002, He et al., 2003, Hille, 2009), 0.25%, 0.2% and 0.3%. Most of the time, these values are introduced to match the measured growth stress or strain experimentaly obtained, and are not based on the understanding of the mechanistic or physical phenomena (mass conservation).

II.2.2.5 Discussions

The understanding of oxide growth in a $NiCoCrAlY$ TBC system was required because TGO has a critical role on TBC damage. First, oxidation kinetics will be usefull in the numerical simulation of oxide growth. Second, the study of the chemical composition provides us information (i) to model the oxide mechanical properties, to be presented next in Section II.3 and (ii) the time-evolution of the oxide microstructure. The presence of yttrium enhances inward oxidation at the TGO-BC interface and influences mainly the TGO microstructure. Third, the growth strains associated with the bond coat oxidation has been investigated. Growth strains which develop at the TGO grain boundaries induce stresses and is one of the driving forces to generate damage at high temperatures close to the TGO and leading to the subsequent TBCs spallation.

II.2.3 Bond coat

II.2.3.1 Observations

This section attempts to identify the bond coat microstructure as a preliminary step to model the bond coat mechanical behaviour and its time-evolution. The bond coat of interest is made primarily of five constituents: nickel, cobalt, chrome, aluminium and yttrium, Ni 22Co 17Cr 12.5Al 0.6Y (wt%). It is deposited by EB-PVD on a CMSX-4 Ni-based superalloy substrate. The sample corresponds to the same one used to analyse the TGO chemical composition, exposed to 870°C during 13,500 h. As it can be observed in Fig. II.12(a), the bond coat microstructure could be decomposed into three different layers: (i) a 10 μm thick layer close to the TGO, (ii) a principal layer and (iii) a 20 μm thick layer close to the substrate. The chemical composition and the distribution of each layer in the bond coat is investigated next.

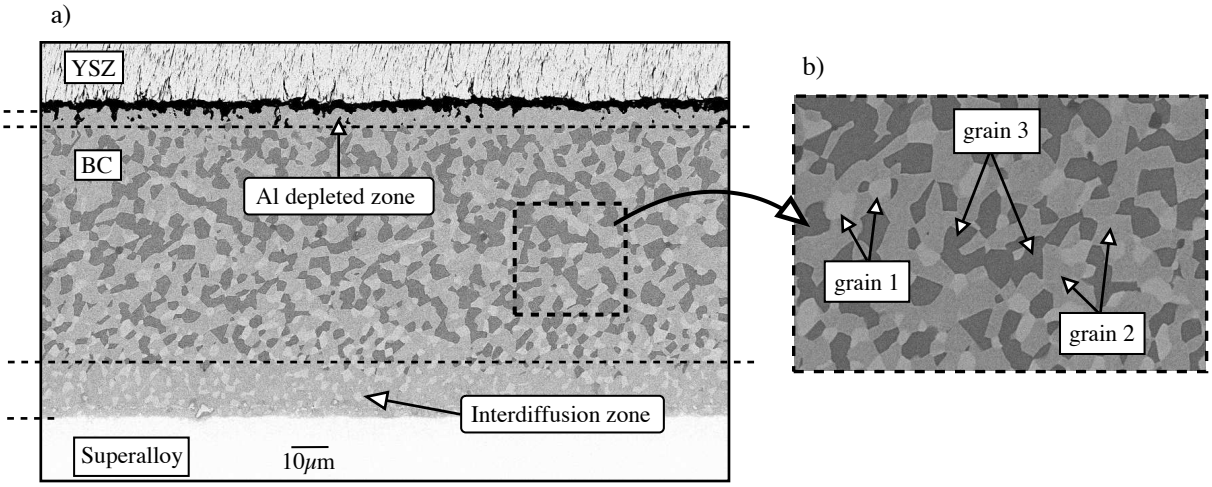

Figure II.12 : SEM micrograph of the bond coat (a) showing the three different layers of the bond coat and (b) a close-up view of the principal layer and the 3 grains: (1) mixed of γ-Ni and α-Cr, (2) γ-Ni and (3) mixed of β-NiAl and γ'-Ni_3Al.

Grain 1 is mostly composed of chrome (60 atom %), cobalt (27 atom %) and nickel (13 atom %), see Table II.2. This grain is present in all the bond coat but its concentration is greater close to the bond coat-superalloy interface.

Grain 2 is composed of Ni, Cr and Co, with similar concentrations (around 30 atom %). The chemical composition and the dispersion of each phase in the bond coat are summarised in Table II.2. This grain is present in all the bond coat.

Grain 3 is composed of Al (34 atom %) and Ni (53 atom %). This grain is the single one containing aluminium and there is a depletion of this phase close to the BC-superalloy and TGO-BC interfaces.

II.2.3.2 Phase identification

In order to determine the most likely phase composition of these grains, an Al-Cr-Ni ternary phase diagram at 850°C is used, see Fig. II.14. It is assumed that (i) phases are stable during the temperature range and (ii) cobalt has similar properties to nickel. Indeed, in the chemical elements periodic table, the position of cobalt and nickel are close and their

Table II.2 : Quantitative results of the chemical composition for the grains 1, 2 and 3 of Fig. II.12.

	Grain 1		**Grain 2**		**Grain 3**	
Element	**Weight %**	**Atome %**	**Weight %**	**Atome %**	**Weight %**	**Atome %**
Al	0.3	0.6	2.4	4.9	19.2	34.0
Cr	57.3	60.1	29.1	30.9	4.8	4.3
Co	29.6	27.4	31.8	29.7	10.5	8.5
Ni	12.8	11.9	36.7	34.5	65.5	53.2

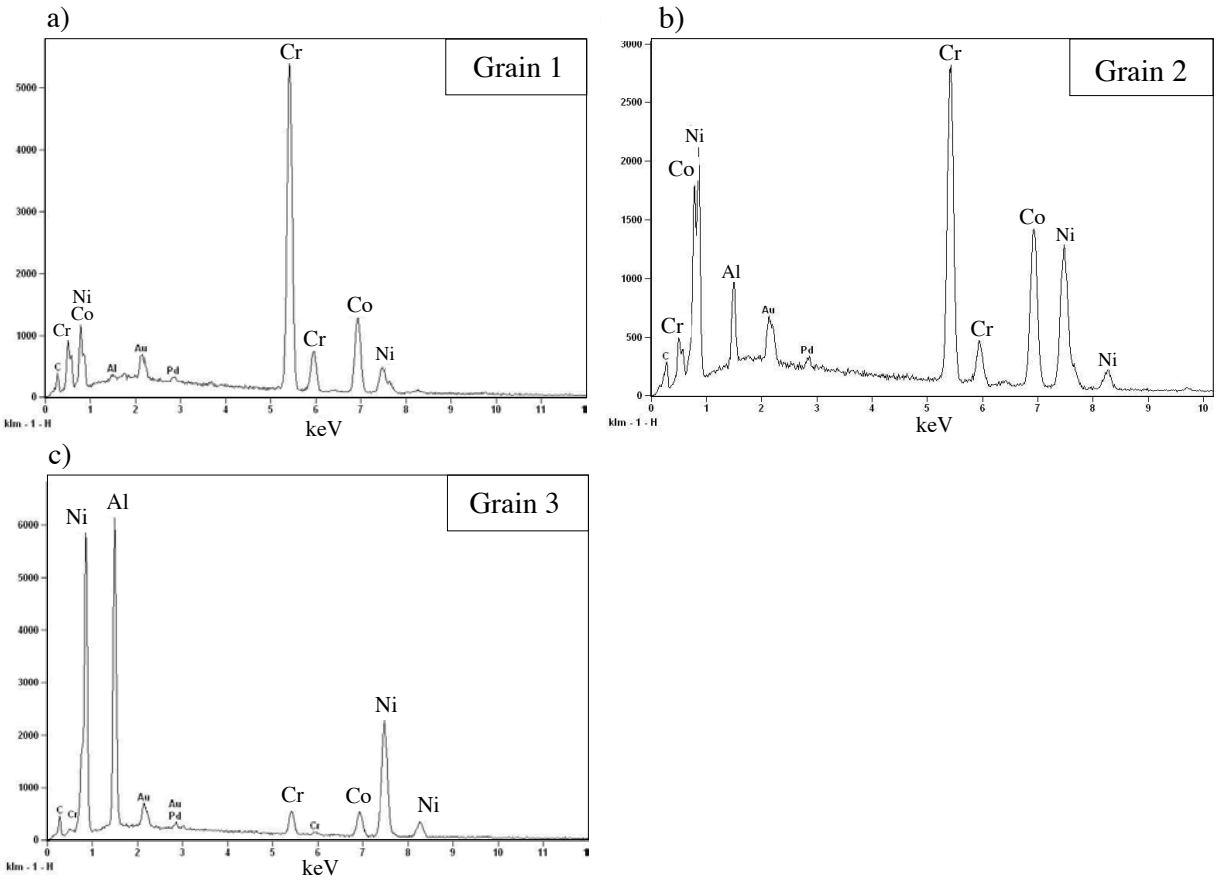

Figure II.13 : SED spectrum from the grain (a) 1 mixture of α-Cr/γ-Ni, (b) 2 γ-Ni and (c) 3 mixture of β-NiAl/γ'-Ni_3Al.

chemical structures are the same up to 500°C (cubic face-centred). Therefore, the chemical composition (atom %) of the three grains changed. Close inspection of the ternary diagram yields three possibilities regarding the compositional nature of the various grains within the bond coat. Grain 1: mixed phase of α-Cr/γ-Ni, 2: γ-Ni and 3: β-NiAl/γ'-Ni_3Al.

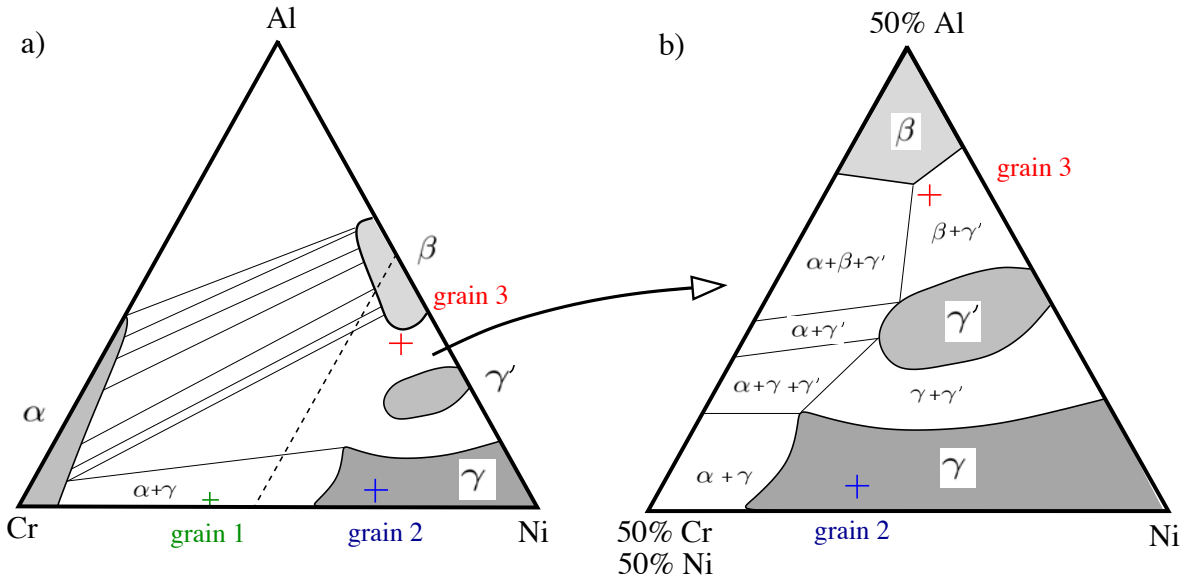

Figure II.14 : (a) Complete and (b) partial *Al-Ni-Cr* ternary phase diagram at 850°C showing the relative position of the three bond coat grains and α-*Cr*, β-*NiAl*, γ-*Ni* and γ'-Ni_3Al phases (Petzow and Effenberg, 1988).

II.2.3.3 Discussions

SEM and SED observations and analyses reveal that the *NiCoCrAlY* bond coat is not a two-phase microstructure of β-NiAl and γ-Ni phases but is considerably more complex. *Cr*-rich phase precipitates were observed to be abundant in the *NiCoCrAlY* bond coat. The chemical composition of grain 3 (mixed of β-NiAl/γ'-Ni_3Al β-*NiAl* phases) could be evaluated with the oxidising time and the γ'-Ni_3Al phase may increase. According to the literature, γ'-Ni_3Al is not an equilibrium phase at high temperatures but forms on cooling below a temperature of 750°C (Lapin, 1997, Czeppe and Wierzbinski, 2000). The generation of this phase is governed by the primary oxidation reaction of the β-*NiAl* (Eq. II.2).

The mechanism of outward diffusion of metal cations consists in *Al* diffusing through the bond coat depletes this latter of this element close to the substrate. The TGO formation associated with the bond coat oxidation also leads to a depleted zone close to the TGO-BC interface and a lack of β-*NiAl* phase. Similar observations have been made and explained (Kim et al., 2002). The Al-depleted zone is not observed in as-prepared specimens.

Extensive microstructural characterisation carried out on the diffusion aluminide bond coats and it has shown to undergo a martensitic transformation, with an associated volume change, on cooling from high temperatures (Darzens et al., 2003, Karlsson, 2003). For the *NiCoCrAlY* bond coats, it has been demonstrated that martensitic transformation should not give rise to a significant volume change and does not play a significant role in the mechanical stability of TBCs (Mendis and Hemker, 2008).

II.3 Mechanical and thermal behaviour model of TBC constituents

Simulation of TBC systems behaviour under in-service thermal loading requires an understanding of the relationship between the microstructure of each TBC constituent and its associated mechanical behaviour. The influence of ageing on EB-PVD TBC microstructure has been presented in Section II.2. For the ceramic top coat, sintering effects have been observed through the evolution of the ceramic layer morphology. Bond coat oxidation generates interdiffusion with the substrate, leads to various phase evolution and creates an *Al*-depleted zone close to the TGO layer. For the latter, oxidation leads to an evolution of its thickness and to growth strains. The bond coat chemical composition influences mainly the TGO microstructure (reactive elements such as yttrium). Motivated by the observations and analyses of the TBC constituents, this section deals with the mechanical and thermal behaviour model of each layer constituting the TBC system.

II.3.1 EB-PVD YSZ top coating

According to the literature, SEM micrograph observation and image-processing analysis, YSZ top coat deposited by EB-PVD has a complex microstructure. The top coat mechanical behaviour model has to consider: the columnar microstructure, the spatial distribution of intercolumnar porosity and ageing effects. To achieve these tasks, two different zones are distinguished: (i) a major part of the ceramic layer with a porous columnar microstructure, see zone 1 in Fig. II.15 and (ii) a thin layer of ceramic close to the TGO, where external porosity is low and microstructure is clearly non-columnar (zone 2). For each zone, the YSZ top coat mechanical behaviour is modelled differently. The relevance of each model will be discussed later in Section III.4.1.3.

II.3.1.1 Material properties of the transversely YSZ isotropic ceramic

According to experimental tests, the YSZ top coat columnar microstructure exhibits anisotropic elastic properties (Johnson et al., 1998, Lugscheider et al., 2001). Following the morphology of typical YSZ top coat microstructures, the orientation of columns will be assumed to be vertical (direction X_2) in the YSZ top coat located in Zone 1. In an elastic transversely isotropic material, symmetry considerations imply that:

$$E_1 = E_3, \quad G_{12} = G_{23}, \tag{II.21}$$

$$\nu_{13} = \nu_{31}, \quad \nu_{13} = \nu_{32}, \quad \nu_{21} = \nu_{23}, \tag{II.22}$$

$$\frac{\nu_{21}}{E_2} = \frac{\nu_{12}}{E_1}, \quad G_i = \frac{E_i}{2(1+\nu_i)}. \tag{II.23}$$

In Zone 1, columns are normal to the macroscopic top coat-bond coat interface and oriented along direction X_2 (general basis). In Zone 2, columns are normal to the rough YSZ-TGO interface (local basis). Nevertheless, the general basis is used in both cases to define the anisotropic top coat microstructure. The local orientation of the columns is not directly modelled in the present study as it has been done by Busso *et al.* (2006). Nevertheless, it is taken into account via the anisotropic model of the YSZ mechanical behaviour. Finally, for both zones, the transversely isotropic material can be described in terms of five independent

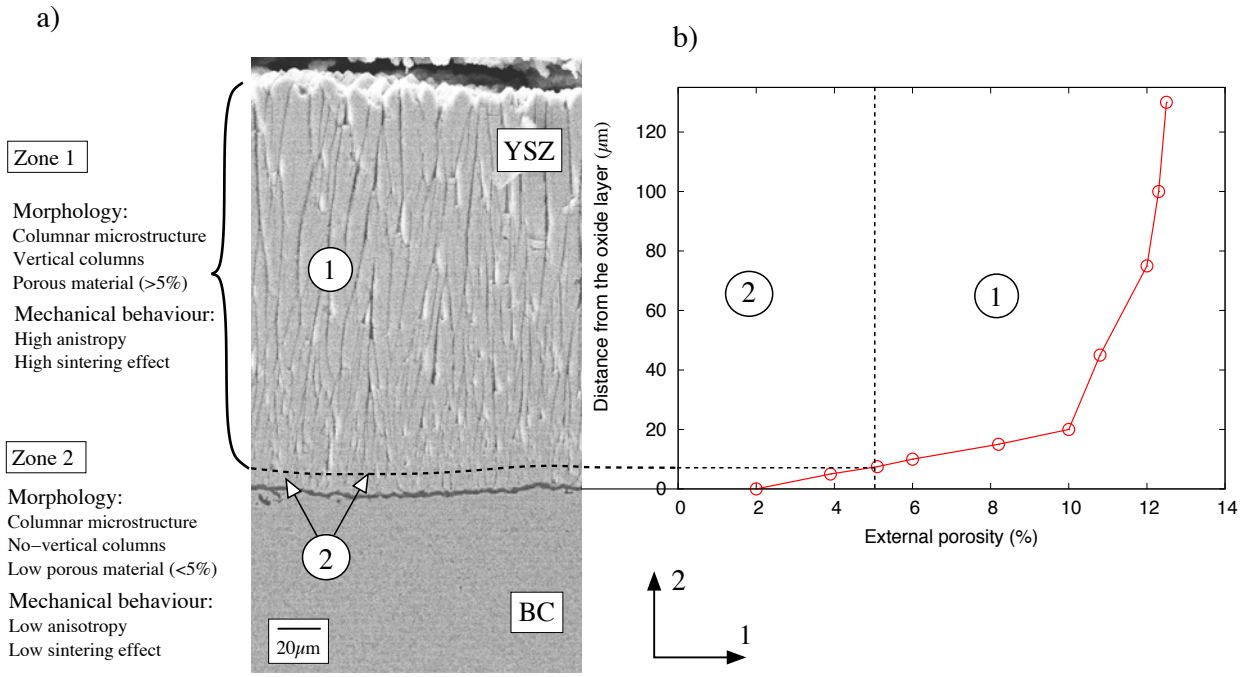

Figure II.15 : After 300 h at 990°C, (a) SEM micrograph showing two zones with different microstructures and the associated mechanical characteristics: (1) with vertical columns and high level of external porosity ($\rho_e > 5\%$) and (2) with non-vertical columns and low porosity ($\rho_e < 5\%$), and (b) spatial distribution of the intercolumnar porosity showing the criterion distinguishing the two zones ($\rho_e = 5\%$).

elastic constants, namely E_1, E_2, ν_1, ν_{21} and G_2. Using Voigt notations, the elastic compliance tensor $\underset{\sim}{\boldsymbol{S}}$ becomes:

$$\underset{\sim}{\boldsymbol{S}} = \begin{bmatrix} 1/E_1 & -\nu_{21}/E_2 & -\nu_1/E_1 & 0 & 0 & 0 \\ -\nu_{12}/E_1 & 1/E_2 & -\nu_{12}/E_1 & 0 & 0 & 0 \\ -\nu_1/E_1 & -\nu_{21}/E_2 & 1/E_1 & 0 & 0 & 0 \\ 0 & 0 & 0 & 1/G_2 & 0 & 0 \\ 0 & 0 & 0 & 0 & 1/G_1 & 0 \\ 0 & 0 & 0 & 0 & 0 & 1/G_2 \end{bmatrix} \tag{II.24}$$

II.3.1.2 Determination of top coat mechanical properties by nanoindentation

For both zones, the five independent elastic constants for the transversaly isotropic elastic YSZ material were determined as follows. The in-plane Poisson's ratio ν_1 is taken to be 0.1 (Chen et al., 1998). It is assumed that $\nu_{21} = \nu_1$ which allows to obtain ν_{21}, Eq. II.23. G_2 is approximated by $G_2 = (E_2/E_1)G_1$ (Busso and Qian, 2006).

The in-plane and out-of-plane Young's moduli identifications for YSZ EB-PVD coatings have been determined by nanoindentation tests (Jang and Matsubara, 2005, Guo and Kagawa, 2006). Whether the out-of-plane Young's modulus E_2 is not affected by ageing or porosity evolution, the in-plane Young's modulus E_1 is strongly dependent on the time spent at high temperatures. Actually, due to sintering effects, the changes in the top coat microstructure described above lead to an increase of the in-plane Young's modulus.

Time and temperature influences on mechanical and thermal properties evolution of EB-PVD YSZ top coat have been observed to show the sintering effect (Bouzakis et al., 2003, Guo and Kagawa, 2006).

Porosity influence on the measured Young's moduli has been also investigated, see Fig. II.16 (Jang and Matsubara, 2005). According to Jang and Matsubara, in-plane Young's modulus has a significant dependence on the porosity, amount of the external, ρ_e, and internal, ρ_i, porosities. The ratio between in-plane and out-of-plane Young's modulus decreases when porosity decreases.

II.3.1.3 Determination of top coat Young's moduli using image-analysis

If the mechanical behaviour of the entire top coat (Zones 1 and 2) can be modelled as a transversely isotropic material, the ratio between the in-plane and out of plane Young's moduli is inhomogeneous along the ceramic layer. In Zone 1, far away from the TGO layer in-plane Young's modulus is low and evolves with exposure time. In contrast, close to the TGO layer (Zone 2) where external porosity is low ($< 5\%$), the top coat is lightly affected by sintering and is less anisotropic due to the local orientation of the columns. The different assumptions chosen for each zone are summarized in Fig. II.15(a).

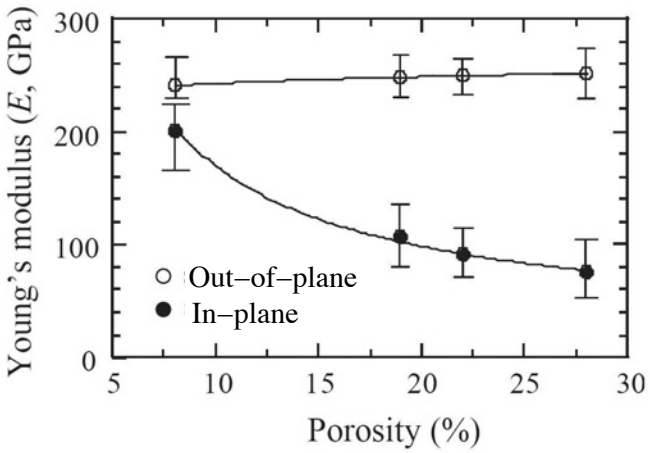

Figure II.16 : In-plane and out-of-plane Young's moduli as a function of porosity for EB-PVD YSZ coatings (Jang and Matsubara, 2005).

The out-of-plane Young's modulus corresponding to Zone 1 is taken as 200 GPa. According to the image-processing analysis performed in Section II.2.1.3, for as-prepared YSZ, the internal and external porosities on the top surface of the ceramic layer are assumed to be around 10% and 17% respectively. For these values, the ratio between E_1 and E_2 is taken as 0.3, see Fig. II.16, and E_1 is taken as 60 GPa. Due to sintering effect, external porosity on the top surface of the YSZ layer ranges from 17% to 10%, depending on the exposure time and temperature. The internal porosity is assumed to be constant ($\rho_i = 10\%$). Based on the data reported by Jang and Matsubara (2005) and using the results obtained by the image-processing analysis, the in-plane Young's modulus time-evolution on the top surface of the ceramic layer has been determined for temperatures ranging from 930 to 1050°C between 0 to 1000 h, see Fig. II.17. The values obtained are in agreement with those proposed in the literature (Jang and Matsubara, 2005, Guo and Kagawa, 2006, Zhao et al., 2006).

Concerning the top coat close to the TGO with a low external porosity, Zone 2 in Fig.

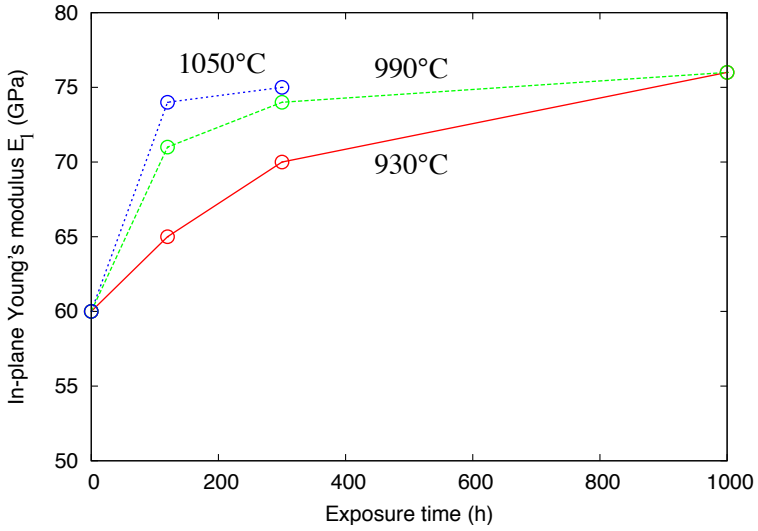

Figure II.17 : In-plane Young's modulus on the top surface of the EB-PVD YSZ coatings as a function of exposure time using the external porosity provided by image-processing analysis performed on the YSZ layer and data from Jang and Matsubara (2005).

II.15, the time-temperature dependence of the in-plane Young's modulus is low. Indeed, the external porosity is similar in all the tested sample, around 2%. Using the same approach as that previously discussed, the in-plane Young's modulus has been determined. E_1 is assumed to be independent of exposure times and temperatures and is taken as 100 GPa close to the TGO layer ($\rho_e = 3\%$).

Creep and sintering effects on the YSZ top coat mechanical behaviour are not presented here. Indeed, close to the TGO where we are interested to predict local stresses, it is assumed that they does not occur for such a low external porosity ($\rho < 5\%$) and low temperatures ($< 1100°C$). Furthermore, according to the model commonly used to describe the sintering deformation $\underset{\sim}{\boldsymbol{\epsilon}}^s$, Eqs. II.25 and II.26, high level of stress is required to induce sintering (Besson and Abouf, 1992, Busso and Qian, 2006). Then:

$$\dot{\underset{\sim}{\boldsymbol{\epsilon}}}^s = \frac{A}{T} exp\left(- \frac{Q}{RT} \right) \left(\frac{L_0}{L} \right)^z \hat{b} \, (\sigma_m - \sigma_s) \underset{\sim}{1}, \tag{II.25}$$

where L is the average grain size, σ_m is the mean pressure and σ_s is the sintering potential, defined as:

$$\sigma_s = \frac{6\,\gamma}{L} \, \rho_e^2 \, \left(\frac{2\rho_e - \rho_0}{1 - \rho_0} \right). \tag{II.26}$$

Here γ is the surface free energy per unit area. For $\rho_e \approx 1$, as observed close to the TGO layer, the sintering potential σ_s is too high to induce sintering. These assumptions will be discussed and the influence of the top coat mechanical behaviour on the local stress/strain fields close to the TGO layer will be studied in Section III.4.1.3.

II.3.2 Thermally grown oxide

II.3.2.1 TGO elastic properties

The elastic properties of stabilized α-alumina are commonly considered to be isotropic, even if at the grain scale the oxide microstructure is anisotropic. These elastic parameters have been measured for alumina (Chung and Simmons, 1968, Jaminet et al., 1992, Fukuhara and Yamauchi, 1993, Wachtman, 1996), see Table II.3.

Table II.3 : Comparison of the Young's modulus and Poisson′s ratio for α-alumina from the literature (Chung and Simmons, 1968, Jaminet et al., 1992, Fukuhara and Yamauchi, 1993, Wachtman, 1996). (Temperature in Kelvin).

Reference	**E (GPa)**	ν
(Chung and Simmons, 1968)	417-0.052T	0.23-2.10^{-5}T
(Jaminet et al., 1992)	406-0.014T	-
(Fukuhara and Yamauchi, 1993)	410-0.023T	-
(Wachtman, 1996)	407-0.075T	0.23-2.10^{-5}T

According to Table II.3, the TGO Young's modulus ranges from 385 to 467 GPa at 20°C and from 296 to 452 GPa at 1200°C. Finally, the Young's modulus is taken as the mean value of the experimental data from Chung and Simmons (1968), Jaminet *et al.* (1992), Fukuhara and Yamauchi (1993) and Watchman (1996). It could be represented by the following interpolation formula:

$$\boxed{E(GPa) = 410 - 0.041T \text{ T in Kelvin}}$$

As for the Young's modulus, the mean value of the Poisson's ratio has been determined using experimental data from Chung and Simmons (1968) and Watchman (1996). The value decreases with temperature and the following relation was found:

$$\boxed{\nu = 0.23 - 2\,10^{-5}T \text{ T in Kelvin}}$$

The TGO elastic properties as a function of temperature are summarised in Table II.6 and the thermal properties in Table II.7.

II.3.2.2 TGO creep properties

The lifetime of a material constituent operating at high temperatures may be limited by the long-term creep characteristics of the material. TGO such as alumina generally exhibit a

temperature and stress-dependent steady-state creep behaviour which can be described by a power law relation of the form:

$$\dot{e}^{vp} = A \exp\left(\frac{-Q}{RT}\right)\left(\frac{\sigma_{eq}}{\sigma_0}\right)^n, \tag{II.27}$$

$$\sigma_{eq} = \left(\frac{3}{2}\underset{\sim}{\boldsymbol{\sigma}}_D : \underset{\sim}{\boldsymbol{\sigma}}_D\right)^{\frac{1}{2}}, \tag{II.28}$$

where $A(s^{-1})$ is the creep constant, n is the stress exponent, Q is the activation energy, R is the fundamental molar gas constant (8.314 J/mol) and σ_0 (MPa) is a scale parameters fixed and equal to 100 MPa. The material constants A, n and Q are determined from experimental data, obtained for compacted alumina. Also, $\underset{\sim}{\boldsymbol{\sigma}}_D$ is the deviatoric stress tensor and σ_{eq} the corresponding von Mises equivalent stress.

According to previous observations, the TGO is essentially alumina even through it also contains increasing amounts of other oxides, distinguishable by phase contrast, and which also seemed to form pegs into the bond coat, see Fig. II.7. According to our metallographic analyses, these pegs are yttrium-rich. A minor addition of reactive element such as yttrium changes the oxide growth mechanisms and microstructure (Pint et al., 1998, Nakagawa et al., 2007, Pint and More, 2009). It has been also shown that dopant addition can significantly improve the creep resistance of polycrystalline alumina, see Fig. II.18 (Johnson et al., 1984, French et al., 1994, Cho et al., 1997). Table II.4 lists the main experimental results for pure and doped alumina.

Table II.4 : Reported values of the creep parameters (A, Q and n), see Eq. II.27, for alumina (Johnson et al., 1984, French et al., 1994, Cho et al., 1997).

Material	**Q (kJ/mol)**	**A (s^{-1})**	**n**	**Authors**
Pure alumina	453	3.4 10^{10}	1.8	(French et al., 1994)
Y-doped alumina	698	2.3 10^{17}	1.7	
70 wt % Al_2O_3 , 30 wt % Y_2O_3	695	1.1 10^{16}	2.6	
Mgo-doped alumina	480	1.4 10^{11}	2.0	(Johnson et al., 1984)
Y-doped alumina	685	1.3 10^{16}	2.0	(Cho et al., 1997)
Pure alumina	467	4.0 10^{10}	1.7	

In the numerical approach to be presented next, the alumina creep behaviour is described by Eq. II.27. Creep parameters are taken as the average values of those experimentally obtained for Y-doped alumina by French *et al.* (1994) and Cho *et al.* (1997):

The creep stress exponent value $n = 1.85$ implies a vacancy diffusion controlled by creep mechanism in alumina. The role of vacancies, concentrated at the grain boundaries

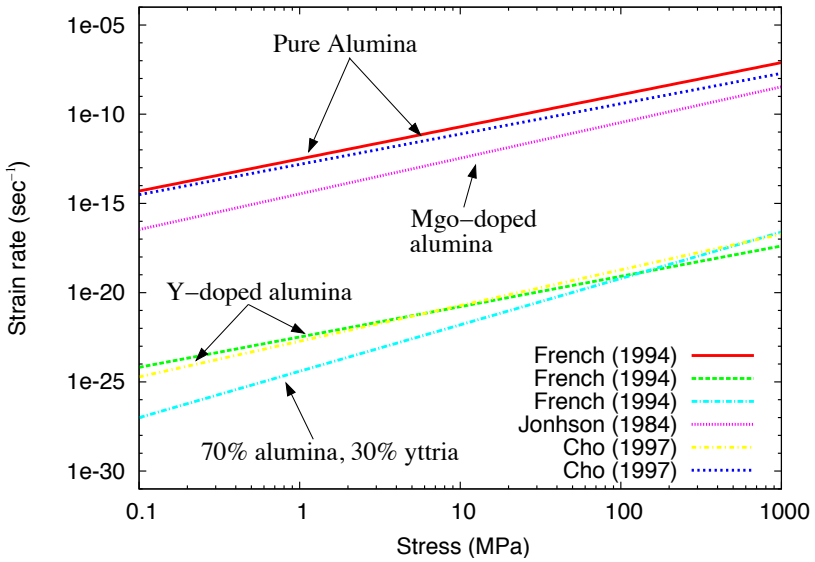

Figure II.18 : Creep properties of alumina at 1100°C showing the influence of dopant components (Y, MgO) according to different authors (Johnson et al., 1984, French et al., 1994, Cho et al., 1997).

n = 1.85
Q = 690 kJ/mol
A = 5.1 10^{16}
σ_0 = 100 MPa

(Coble, 1961), on TGO growth strains and on the TGO creep behaviour has been investigated by Clarke (2003). Alumina is assumed to be only visco-elastic and no plastic strain occurs.

II.3.3 Bond coat

The ability of the top coat to resist to spallation can be greatly influenced by the bond coat creep and plastic properties. Indeed, bond coats are weak in creep and allow for greater stress relaxation. According to our observations, $NiCoCrAlY$ bond coat is a multiphase material with a microstructure which evolves with oxidation time. Nevertheless, the mechanical properties of the Al-depleted zone, generated by interdiffusion in the bond coat, are assumed to be independent of time. To describe the bond coat microstructure close to the oxide, the bond coat is modelled as a γ'-Ni_3Al and β-NiAl isotropic material. The elastic mechanical properties are presented in Tables II.6 and the thermal ones in Tables II.7. To determine creep properties, an homogenisation method of the multiphase $NiCoCrAlY$ bond coat has been proposed (Busso et al., 2001a) based on results obtained experimentally (Vandervoort et al., 1966, Frost and Ashby, 1979). Experimental results have been provided by the University of Birmingham (Taylor et al., 2007) and by Lapin (1997) and listed in Table II.5.

In the numerical approach presented in Chapter III, the bond coat creep behaviour is described by Eq. II.27. Creep parameters are taken as the average value of those reported by Lapin (1997) and Busso *et al.* (2001):

Table II.5 : Reported values of the creep parameters (A, Q and n), see Eq. II.27, for $NiCoCrAlY$ bond coats (Lapin, 1997, Busso et al., 2001a, Taylor et al., 2007).

Q (kJ/mol)	**A (s^{-1})**	**n**	**Authors**
301	$3.2\ 10^{7}$	4.1	(Lapin, 1997)
263	$2.1\ 10^{9}$	4.1	(Busso et al., 2001a)
929	$2.9\ 10^{17}$	12.5	(Taylor et al., 2007)

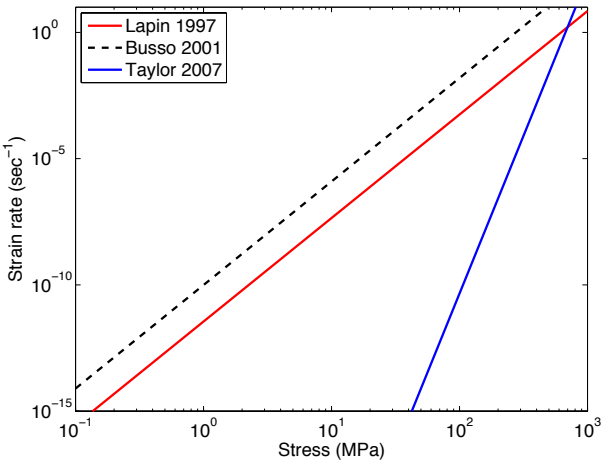

Figure II.19 : Creep properties of the bond coat at 1100°C according to different authors (Lapin, 1997, Busso et al., 2001a, Taylor et al., 2007).

n = 4.1
Q = 282 kJ/mol
A = $1.1\ 10^{8}$
σ_0 = 100 MPa

The inelastic behaviour of the bond coat is assumed to have, in addition to the rate-dependent behaviour, a rate-independent perfectly-plastic component. The temperature dependence of the bond coat rate-independent yield stress, taken from Cheng *et al.* (1998), is presented in Table II.6.

Table II.6 : Elastic and plastic properties of the bond coat (Lapin, 1997, Busso et al., 2001a) and the thermally grown oxide (Chung and Simmons, 1968, Jaminet et al., 1992, Fukuhara and Yamauchi, 1993, Wachtman, 1996).

T(°C)	**Material**				
	Bond coat			**Oxide**	
	E (GPa)	ν	σ_Y (Nm^{-2})	E (GPa)	ν
25	117	0.24	420	404	0.23
600	104	↓	360	370	0.22
800	99		260	355	0.21
1000	94		190	325	0.20
1100	92		120	320	0.20

Table II.7 : Thermal properties α $(10^{-6}\,°C)$ of the top coat (Chen et al., 1998), the TGO (Chen et al., 1998), the bond coat (Panat et al., 2003) and of the CMSX-4 superalloy substrate.

T(°C)	**Material**			
	Top coat	**Bond coat**	**TGO**	**Substrate**
25	9.7	12.3	8.0	13.9
600	9.9	15.2	8.7	14.0
800	10.0	16.3	9.0	14.5
1000	10.1	17.2	9.3	16.0
1100	10.1	17.7	9.5	16.1

II.4 Simulation of the TGO morphology

Top coat spallation resistance is limited by one of the oxide interfaces toughness. Many analyses have pointed out the role of the oxide type on the adhesion resistance (Tolpygo and Clarke, 2000b, Tolpygo et al., 2004). It has been observed that locally a minor variation in the TGO morphology can result in a difference in stress field close to the oxide and so increase the probability for damage to nucleate and growth. However, a rough oxide interface inhibits the damage to propagate hence increasing the TGO interface toughness (Pint et al., 1998) and TBC lifetime (Spitsberg et al., 2005). The complex influence of the oxide roughness on TBC lifetime is a good illustration of the need to take into account micro and macroscopic phenomena occurring in EB-PVD TBC systems. This section attempts to characterise and to model the TGO morphology after 13,500 h at 870°C and to provide preliminary information for the simulation of stress and strain fields close to the oxide layer.

II.4.1 Oxide interface roughness

II.4.1.1 Image-processing analysis

a) TGO morphology characterisation: methodology

The first step to obtain a realistic simulation of the oxide morphology is to characterise the TGO roughness. Image-processing tools have been developed to analyse the oxide morphology along a 800 μm long profile. The length of this window has been chosen to be wide enough to be representative of the global specimen. Furthermore, its length should not be too large so as to validate the assumption that thermo-mechanical loading is homogeneous along this small part of the sample.

The method consists of extracting the TGO layer from a SEM micrograph. As for the extraction of the top coat ceramic external porosity, Section II.2.1.3, an initial picture of a SEM micrograph, Fig. II.20(a), is encoded by pixels in a 8 bits format. To extract the black pixels belonging to the TGO layer, a binary picture of the initial SEM is required and is obtained by a binairisation procedure, Fig. II.20(b). The black pixels belonging to the external porosity in the YSZ layer and to the β-NiAl phase of the bond coat have been also extracted. For that reason, only the oxide layer needs to be extracted from the binary picture using a geometrical percolation procedure. Only black pixels belonging to the TGO percolate from the right to the left of the binary picture, Fig. II.20(c). There are still black pixels that belong to the top coat external porosity. To resolve this problem, the oxide layer is smoothed. A close-up view of the final binary picture of the TGO layer is represented in Fig. II.20(d).

b) Oxide roughness criteria

Prior to obtain a signal corresponding to the TGO morphology, the TGO thickness is required. A numerical analysis has been conducted to determine the average oxide thickness and its associated distribution, from the final extracted oxide layer along a 800 μm long window, illustrated in Fig. II.20(c). Knowing the oxide thickness, a numerical procedure gives the oxide mean position (vertical position) as a function of the horizontal position along the TGO layer. The oxide mean profile is represented by a white curve, see Fig. II.20(e). As shown in Fig. II.20(e), the YSZ-TGO and BC-TGO interface profiles are also extracted using image-processing.

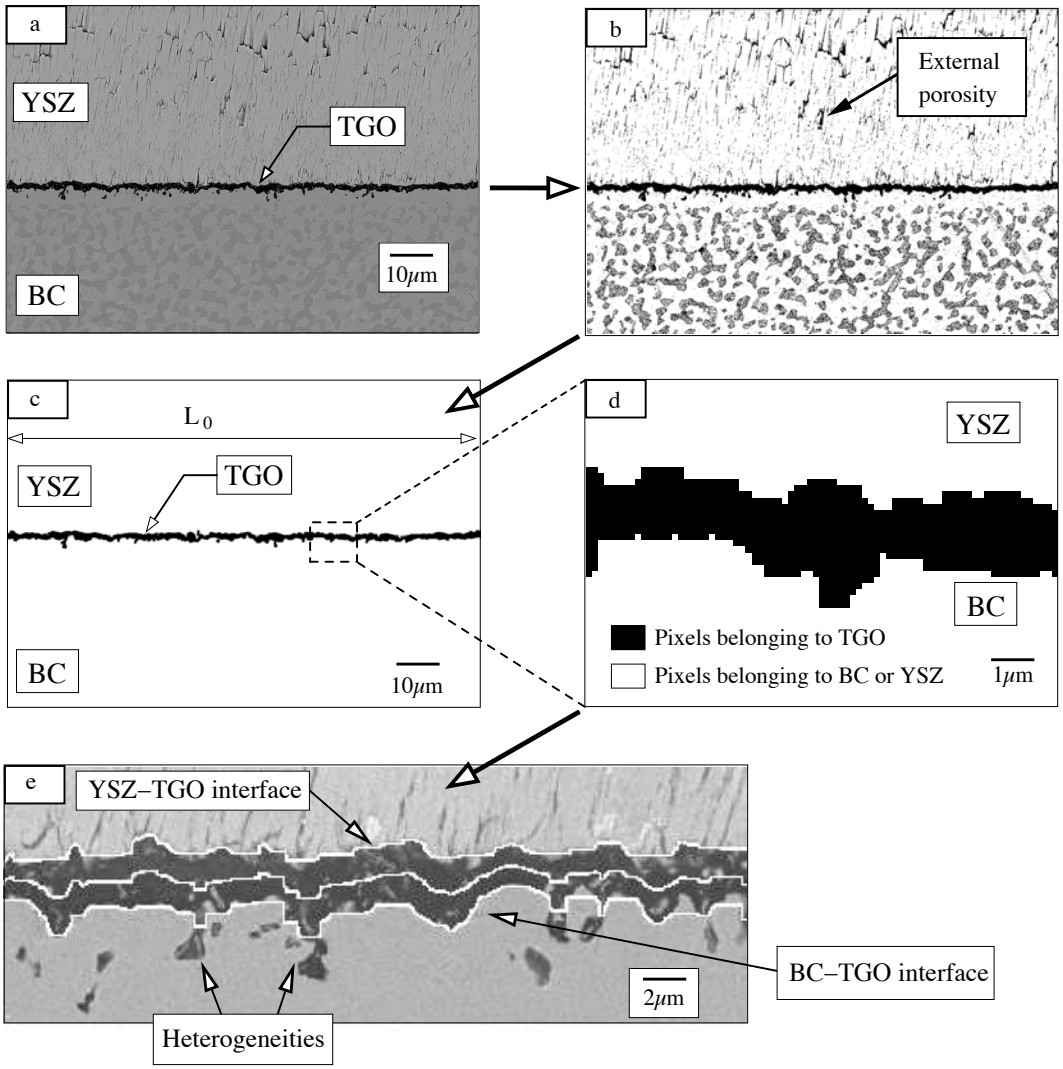

Figure II.20 : (a) Initial SEM micrograph of the EB-PVD TBC cross section, (b) binary representation of the micrograph, (c) extraction by a percolation method of the dark TGO pixels and smoothing of the obtained TGO layer, (d) close-up view of the smoothed extracted TGO layer and (e) the two TGO interfaces profiles (YSZ-TGO and BC-TGO) and oxide mean profile.

In this work, we have chosen two classical roughness criteria to characterise the TGO morphology. The absolute roughness, R_a, is defined by:

$$R_a = \frac{1}{L_0} \int_{L_0} |f(x)|\, dx, \tag{II.29}$$

where $f(x)$ is a function describing the profile and L_0 the observation window's length (here 800 μm). The lineal roughness (tortuosity), R_l, is defined as the ratio between the profile length, L, and, L_0 (see Eq. II.30):

$$R_l = \frac{L}{L_0}. \tag{II.30}$$

c) Analysis of a sinusoidal profile

Using R_a and R_l, three profiles roughness been determined for the 800 μm long micrograph of the EB-PVD TBC specimen, see Table II.8. It is observed that the TGO-YSZ interface roughness is the lowest one. It is assumed that the TGO-YSZ interface roughness remains unchanged with oxidation time and is equal to the TGO-BC interface roughness before any exposure time. In contrast, the TGO internal interface roughness R_l increases with exposure time, from 1.036 to 1.086.

Knowing the TGO mean roughness, it is necessary to calibrate the amplitude, a, and the wavelength, w, of a sinusoidal profile commonly used to characterise the oxide morphology. The objective behind this part of the work is to perform and optimise a finite element mesh representative of the TGO morphology. From the image-processing analysis, the mean wavelength is determined for the oxide mean profile, namely 11.72 μm. To determine the mean amplitude, we have applied both roughness criteria to a sinusoidal profile. The result obtained from the absolute roughness R_a is independent on the signal amplitude. For this reason, the equivalent amplitude has been obtained using the lineal roughness, R_l:

$$f(x) = a.cos\left(\frac{2\pi x}{w}\right), \tag{II.31}$$

$$L = \int_{x=0}^{x=L_0} \sqrt{1 + [f'(x)]^2}dx. \tag{II.32}$$

To solve the problem numerically a mean amplitude of 0.864 μm associated with the given wavelength w is obtained, see Table II.8.

Table II.8 : TGO interfaces and oxide mean profiles roughness in terms of the absolute R_a and lineal R_l roughness criteria. The equivalent sinusoidal amplitude a is also presented ($w = 11.27$ μm). L_{int} and L_{sup} are the YSZ-TGO and BC-TGO profile lengths.

Profile	R_a (μm)	R_l	a (μm)
TGO-YSZ interface	0.71	$\frac{L_{sup}}{L} = 1.036$	0.715
Mean	0.74	$\frac{L_{mean}}{L} = 1.052$	0.864
TGO-BC interface	0.99	$\frac{L_{int}}{L} = 1.086$	1.127

According to the literature, the TGO presents a roughness (R_a) of the order of 1 μm (Ibégazène-Ouali et al., 2000, Wen et al., 2006, Balint et al., 2006) which can increase with exposure time (Tolpygo and Clarke, 2004b, Tolpygo and Clarke, 2004c). For $(Pt, Ni)Al$ bond coats, a *rumpling* mechanism can occur due to the martensitic phase transformation induced by the cyclic thermal loading (Karlsson, 2003, Zhang et al., 2003, Balint and Hutchinson, 2003, Poulain et al., 2006).

This phenomenon is not observed in $NiCoCrAlY$ systems (Hemker et al., 2008). Nevertheless, roughness could also increase due to the (i) oxide growth (Karlsson et al., 2002, Balint and Hutchinson, 2005), (ii) bond coat plastic/creep strains (Panat et al., 2003), (iii) bond coat multiphase composition generating zones where diffusion is greater (boundary

grain) and (iv) bond coat volume change associated with to the β-γ' phase transformation (Darzens et al., 2003).

II.4.2 Representative elementary length of the TBC system studied

To determine representative of oxide roughness, it is necessary to analyse micrograph along a sufficiently long section (800 μm). However this is incompatible with a reasonable calculation time. Image-processing analysis enables a representative elementary length (REL) of the global micrograph to be determined based on the covariance C of the oxide layer. The covariance is a scalar function defining the covering ratio between an initial picture X and the same picture translated X_{+h} by a vector h, as illustrated in Fig. II.21. For a group of pixels X and for a given vector h, the covariance $C(X, h)$ is defined as:

$$C(X, h) = X \cap X_{+h} \tag{II.33}$$

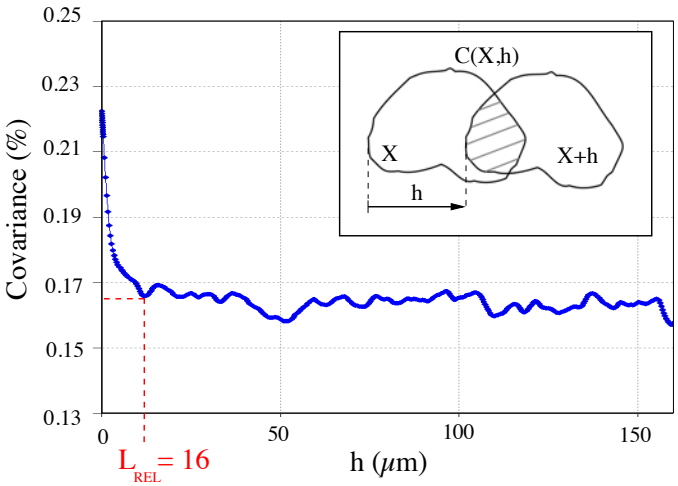

Figure II.21 : Illustration and graph of the covariance C of the EB-PVD TBC sample and value of the representative elementary length, $L_{REL} = 16$ μm.

The covariance of the pixel group belonging to the TGO has been determined, see Fig. II.21. Its value decreases from 22% ($h = 0$ μm) to 16% (corresponding to $h = 800$ μm). According to the literature (Serra, 1988), a value of the representative elementary length corresponds to the critical point at the end of the significant decrease, as shown by the dotted line in Fig. II.21. For this EB-PVD TBC sample, 16 μm is chosen for the corresponding REL value. In other words, the TGO morphology could be modelled by a 16 μm long length, without significant lost of information. Note that this value is close to the mean wavelength previously obtained for a sinusoidal profile, namely $w = 11.72$ μm.

II.4.3 Model of a realistic TGO morphology

A preliminary model of the TGO morphology based on a simply 2D sinusoidal simulation might provide a relevant compromise between local precision of mechanical fields and CPU time. With this type of approach, we assume that an elementary unit cell could be representative of the entire TBC system. Nevertheless we have observed many heterogeneities along the TGO-BC interface which might be critical regions where porosities or microcracks can nucleate and grow.

II.4.3.1 Generation of a 2D FE mesh representative of the realistic TGO morphology

a) Fourier analysis of the TGO morphology

The objective of this section is to model the oxide morphology using a realistic finite element mesh. The approach consists of transforming the oxide mean profile given by the image-processing analysis, Fig. II.20(e), into Fourier series. A 16 μm long region of the global profile, having the same roughness ($R_l = 1.052$), was extracted to apply a Fourier analysis. This REL is periodic, continuum and representative of the global TGO layer. First, the signal of the oxide mean profile, $P(x)$, is transformed in a discrete Fourier transform, $F(x)$, where x is the horizontal position along the oxide:

$$P(x) = F(x) = \frac{a_0}{2} + \sum_{k}^{\infty} a_k cos\left(k\frac{2\pi x}{L_0}\right) + b_k sin\left(k\frac{2\pi x}{L_0}\right) \tag{II.34}$$

It has been chosen to decompose the signal in 512 frequencies. Then, $P(x)$ is formulated as:

$$P(x) \approx F_1(x) = \frac{a_0}{2} + \sum_{k}^{512} a_k cos\left(k\frac{2\pi x}{L_0}\right) + b_k sin\left(k\frac{2\pi x}{L_0}\right). \tag{II.35}$$

For the developed numerical tool, the spatial frequency spectrum of the oxide mean profile is required and is shown in Fig. II.22 (only the first hundred frequencies). The weight of each spatial frequency is given. It appears that six frequencies have more influence than the others.

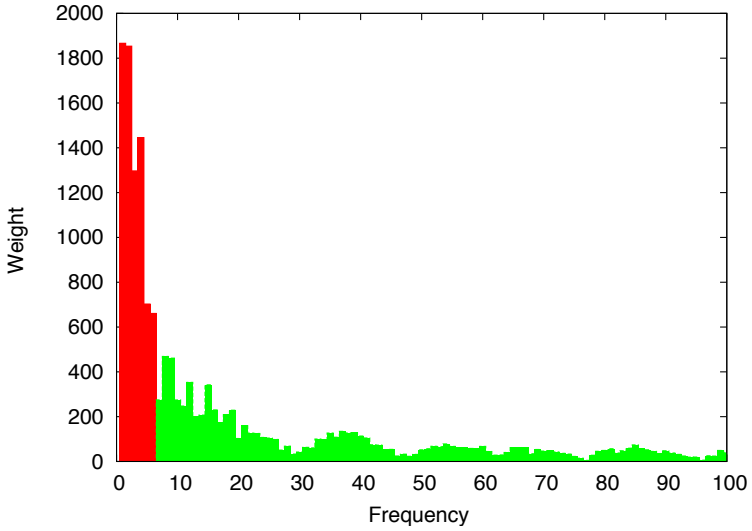

Figure II.22 : Spatial frequency spectrum of the TGO mean profile and the six frequencies having the higher weight.

b) Reconstitution of the TGO mean profile by Fourier analysis

In order to simplify the Fourier series which defined the oxide mean profile, only six spatial frequencies (Fig. II.22) are kept: $\frac{k}{L_0}$, for $k = [1-6]$. These six frequencies correspond to the six frequencies which have the most important weights. It means that all the yttrium

heterogeneities in the TGO are taken into account but not the default induced by the numerical procedure used to extract the oxide mean profile, Section II.4.1.1. The TGO mean profile can be then defined by the twelve parameters (a_k, b_k) and the six frequencies which are related to the Fourier series (Table II.9).

$$P(x) \approx F_2(x) = \frac{a_0}{2} + \sum_{k}^{6} a_k cos(k\frac{2\pi x}{L}) + b_k sin(k\frac{2\pi x}{L}). \quad \text{(II.36)}$$

Table II.9 : The six associated spatial frequencies and associated Fourier's coefficients (a_k, b_k) of the TGO mean profile.

$\mathbf{f}_k$	$\mathbf{a}_k$	$\mathbf{b}_k$
$\frac{1}{L}$	-0.25	-0.03
$\frac{2}{L}$	-0.016	-0.25
$\frac{3}{L}$	0.04	-0.17
$\frac{4}{L}$	0.2	-0.12
$\frac{5}{L}$	0.01	-0.09
$\frac{6}{L}$	-0.03	0.05

A comparison between the oxide mean profiles from the processing-image method and its Fourier transform is represented in Fig. II.23. It can be seen that a good correlation is founds between the two curves. The profile obtained by Fourier transform takes into account the observed heterogeneities.

c) FE meshing of a representative oxide morphology

A numerical tool has been developed to generate automatically a realistic FE mesh simulating the TGO morphology. The 16 μm-long domain modelled is representative of the irregular oxide geometry, Fig. II.24(a). Using the previous Fourier decomposition, an initial regular finite element mesh, Fig. II.24(b), has been distorted into a mesh consistent with the TGO morphology, Fig. II.24(c). In order to simulate the TGO-BC interface roughness increase, as it occurs during oxidation, the procedure was improved. The roughness evolution has been implemented and is assumed to increase as a linear function of the vertical position ranging from the YSZ-TGO to the final BC-TGO interface, 1.036 and 1.086 μm, respectively.

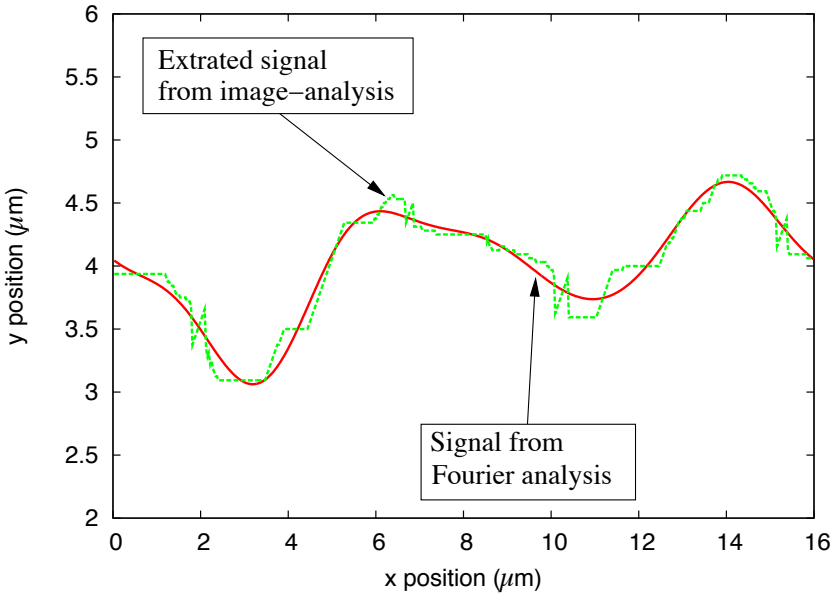

Figure II.23 : Comparison between the oxide mean profiles from the image-processing analysis and its Fourier transform.

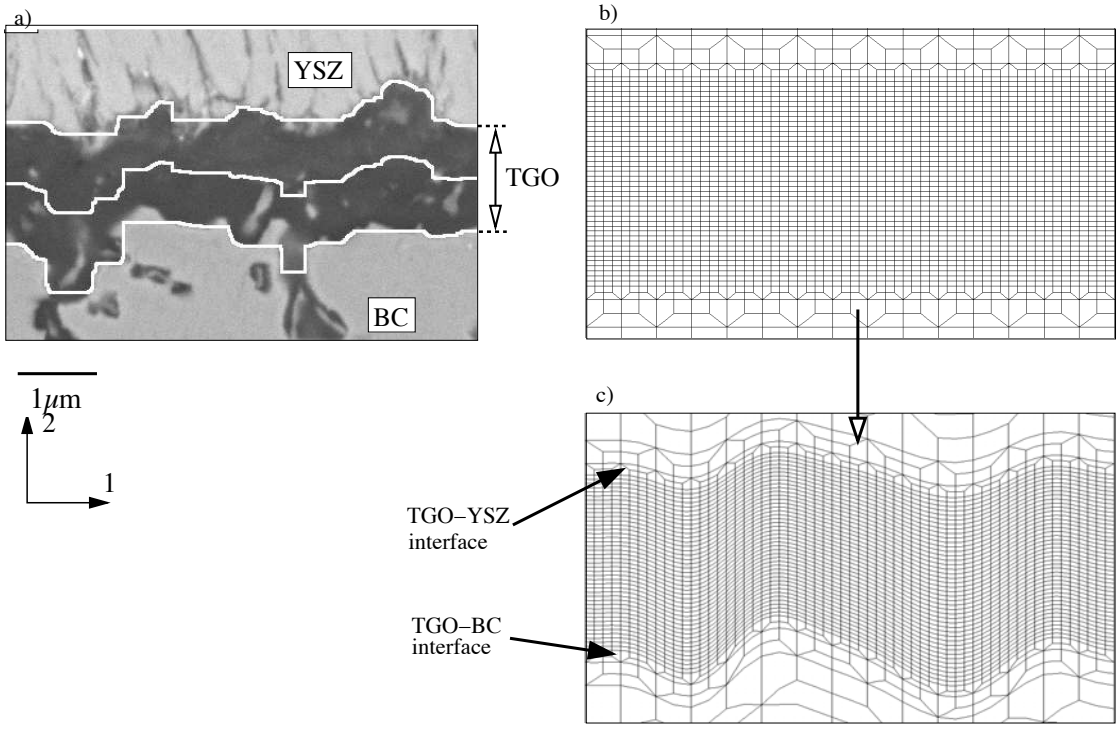

Figure II.24 : (a) A typical EB-PVD TBC micrograph, (b) the initial undistorted FE mesh and (c) the compliant or distorted FE mesh representative of the initial micrograph.

II.5 Concluding remarks

The individual study of each TBC constituent morphology has shown that their microstructures and mechanical/thermal behaviour are strongly time dependent. Using image-processing analysis, the columnar microstructure of the EB-PVD YSZ top coat has been investigated. The intercolumnar porosity spatial distribution is influenced by the EB-PVD deposition process and affected by the thermal exposure time. The top coat microstructure is non-homogeneous along its thickness, close to the TGO, the top coat is a a very low porous material ($< 5\%$) and might not be concerned by sintering effects. In contrast, most of the ceramic close to the top surface can be affected by sintering. Based on these considerations, the mechanical behaviour associated with the top coat is differentiated between the ceramic part close to the TGO and the remaining part of this layer.

In the TBC system of our interest, the $NiCoCrAlY$ bond coat has a complex multiphase microstructure. Associated to the oxide growth and diffusion phenomena, an Al-depleted area appears close to the TGO. An evaluation of the β-$NiAl$ volume fraction as a function of the oxidation time should be addressed to study the strong effect of exposure time on the bond coat microstructure.

The bond coat has also a great influence on the TGO time-evolution. Due to the presence of reactive element such as yttrium, the TGO grows by inward oxidation ($J_{Al^{3+}} \ll J_{0^{2-}}$), yttrium heterogeneities are observed at the BC-TGO interface and the TGO has columnar microstructure. The growth strains associated with the bond coat oxidation reaction is assumed to be anisotropic, influenced by the TGO microstructure and the boundary conditions.

The investigation of the TGO morphology is predominant because it is expected that the TGO may have a great influence on the local stress/strain fields and on the critical oxide interface toughness. To model the TGO morphology, its roughness has been simulated by a sinusoidal profile. The mean wavelength ($w = 11.72\ \mu$m) and amplitude ($a = 0.864\ \mu$m) have been obtained by image-processing analysis. A representative elementary length has also been determined ($L_{REL} = 16\ \mu$m) and has been simulated using Fourier analysis.

Reference

An, K., Ravichandran, K., Dutton, R., and Semiatin, S. (1999). Microstructure, texture, and thermal conductivity of single-layer and multilayer TBCs of Y_2O_3-stabilized ZrO_2 and Al_2O_3 made by physical vapor deposition. *Journal of American Ceramic Society*, 82:399–406.

Azzopardi, A., Mévrel, R., Saint-Ramond, B., Olson, E., and Stiller, K. (2004). Influence of aging on structure and thermal conductivity of Y-PSZ and Y-FSZ EB-PVD coatings. *Surface and Coating Technology*, 177-178:131–139.

Balint, D. and Hutchinson, J. (2003). Undulation instability of a compressed elastic film on a nonlinear creeping substrate. *Acta Materialia*, 51:3965–3983.

Balint, D. and Hutchinson, J. (2005). An analytical model of rumpling in thermal barrier coatings. *Journal Mechanics and Physic Solids*, 53:949–973.

Balint, D., Xu, T., Hutchinson, J., and Evans, A. (2006). Influence of bond coat thickness on the cyclic rumpling of thermally grown oxides. *Acta Materialia*, 54:1815–1820.

Balmain, J., Huntz, A., and Philibert, J. (1997). Atomic transport properties in alumina scales and calculation of the oxidation parabolic rate constant. *Defect and Diffusion Forum*, 143-147:1189.

Beele, W., Marijnissen, G., and van Lieshout, A. (1999). The evolution of thermal barrier coatings-status and upcoming solutions for today's key issues. *Surface and Coatings Technology*, 120-121:61–67.

Besson, J. and Abouf, M. (1992). Rheology of porous aluminia and simulation of isostatic pressing. *Journal of American Ceramic Society*, 75:2165–2172.

Bouzakis, K., Lontos, A., Michailidis, N., Knotek, O., Lugscheider, E., Bobzin, K., and Etzkorn, A. (2003). Determination of mechanical properties of EB-PVD TBC's by means of nanoindentation and impact testing. *Surface and Coating Technology*, 163-164:75–80.

Busso, E., Lin, J., Sakurai, S., and Nakamaya, M. (2001a). A mechanistic study of oxydation-induced degradation in a plasma-sprayed thermal barrier coating system. Part I: model formulation. *Acta Materialia*, 49:1515–1528.

Busso, E. and Qian, Z. (2006). Mechanistic study of microcracking in transversely isotropic ceramic-metal systems. *Acta Materialia*, 54:325–338.

Caliez, M., Feyel, F., Kruch, S., and Chaboche, J. (2002). Oxidation induced stress fields in an EB-PVD thermal barrier coatings. *Surface and Coating Technology*, 157:103–110.

Chen, M., Jordan, H., Gell, M., and Barber, B. (1998). Thermal residual stress in an electron beam-physical vapor deposited thermal barrier coating system. *Acta Materialia*, 46:5839–5850.

Chevalier, S. (2007). *Traitements de surface et nouveaux materiaux*. Université de Dijon.

Chevalier, S., Lesage, B., Legros, C., Borchardt, G., Strehl, G., and Kilo, M. (2005). Oxygen diffusion in alumina. Application to synthetic and thermally grown Al_2O_3. *Defect and Diffusion Forum*, 237-240:899.

Cho, J., Harmer, M., Chan, H., Rickman, J., and Thompson, A. (1997). Effect of yttrium and lanthanum on the tensile creep behavior of aluminium oxide. *Journal of American Ceramic Society*, 80:1013–1017.

Choquet, P. and Mevrel, R. (1989). Microstructure of alumina scales formed on NiCoCrAlY alloys with and without yttrium. *Materials Science Engineering A*, 120:153–159.

Chung, D. and Simmons, G. (1968). Pressure and temperature dependences of the isotropic elastic moduli of polycrystalline alumina. *Journal of Applied Physics*, 39:5316–5326.

Clarke, D. (2003). The lateral growth strain accompanying the formation of a thermally grown oxide. *Acta Materialia*, 51:1393–1407.

Coble, R. (1961). Sintering crystalline solids I and II. *Journal of Applied Physics*, 32:787–799.

Czeppe, T. and Wierzbinski, S. (2000). Structure and mechanical properties of NiAl and Ni_3Al-based alloys. *International Journal of Mechanical Sciences*, 42:1499–1518.

Darken, L. (1942). *AIME Trans.*, 150:157–71.

Darzens, S., Mumm, D., Clarke, D., and Evans, A. (2003). Observations and analysis of the influence of phases transformations on the instability of the thermally grown oxide in a thermal barrier system. *Mettalurgical and Materials Transactions*, 34A:511–522.

Evans, A., Mumm, D., Hutchinson, J., Meier, G., and Pettit, F. (2001). Mechanisms controlling the durability of TBCs. *Progressive Material Science*, 46:505–553.

French, J., Zhao, J., Harmer, M., Chan, H., and Miller, G. (1994). Creep of duplex microstructures. *Journal of American Ceramic Society*, 77:2857–2865.

Frost, H. and Ashby, M. (1979). *Creep Mechanisms Maps.*

Fukuhara, M. and Yamauchi, I. (1993). Temperature-dependence of the elastic-moduli, dilational and shear internal frictions and acoustic-wave velocity for alumina, (Y)TZP and β-SiAl on ceramics. *Journal Materials Sciences*, 28:4681–4688.

Grabke, H. (1997). Oxidation of aluminides. *Materials Science Forum*, 251-252:149–162.

Guo, S. and Kagawa, Y. (2006). Effect of thermal exposure on hardness and Young's modulus of EB-PVD YSZ TBC's. *Ceramic International*, 32:263–270.

Guo, S., Mumm, D., Karlsson, A., and Kagawa, Y. (2005). Measurement of interface shear mechanical properties in TBC systems by a Barb pullout method. *Scripta Materialia*, 53:1043–1048.

He, M., Hutchinson, J., and Evans, A. (2003). Simulation of stress and delamination in plasma-spayed TBC system upon thermal barrier cycling. *Materials Science Engineering A*, 178:172–178.

Hemker, K., Mendis, B., and Eberl, C. (2008). Characterizing the microstructure and mechanical behavior of two-phase NiCoCrAlY bond coat for thermal barrier system. *Materials Science Engineering A*, 483-484:727–730.

Hille, T. (2009). *Lifetime Modeling of Thermal Barrier Coating.* PhD thesis.

Huntz, A., Evans, H., and Cailletaud, G. (2002). Comparison of oxide growth stress in NiO film measured by deflection and calculated using creep analysis or finite element modeling. *Oxidation of Metals*, 57:499–521.

Ibégazène-Ouali, F., Mévrel, R., Rio, C., and Renollet, Y. (2000). Microstructure evolution and degradation modes in cyclic and isothermal oxidation of an EB-PVD thermal barrier coating. *Materials at High Temperatures*, 17:205–218.

Jaminet, P., Wolfenden, A., and Kinra, V. (1992). *Mechanics and Mechanisms of material Damping*. American Society For Testing and Materials.

Jang, B. and Matsubara, H. (2004). Influence of rotation speed on microstructure and thermal conductivity of nanoporous zirconia layer fabricated by EB-PVD. *Scripta Materialia*, 52:553–558.

Jang, B. and Matsubara, H. (2005). Influence of porosity on hardness and Young's modulus of nanoporous EB-PVD TBCs by nanoindentation. *Materials Letters*, 59:3462–3466.

Jang, B. and Matsubara, H. (2006). Surface roughness and microstructure of yttria stabilized zirconia EB-PVD coatings. *Surface and Coating Technology*, 200:4594–4600.

Johnson, C., J.A. Ruud, R. B., and Wortman, D. (1998). Relationships between residual stress, microstructure and mechanical properties of EB-PVD TBCs. *Surface and Coating Technology*, 108-109:80–85.

Johnson, S., Dalgleish, B., and Evans, A. (1984). High-temperature failure of polycrsystalline alumina: III, failures times. *Journal of American Ceramic Society*, 67:759–63.

Jung, Y., Sasaki, T., Tomimatsu, T., Matsunaga, K., Yamamoto, T., Kagawa, Y., and Ikuhara, Y. (2003). Distribution and structures of nanopores in YSZ-TBC deposited by EB-PVD. 4:571–574.

Karlsson, A. (2003). On the mechanical response in a thermal barrier system due to martensitic phase transformation in the bond coat. *ASME Journal of Engineering Materials and Technology*, 125:346–352.

Karlsson, A. and Evans, A. (2001). A numerical model for the cyclic instability of TGOs in TBC systems. *Acta Materialia*, 49:1793–1804.

Karlsson, A., Hutchinson, J., and Evans, A. (2002). A fundamental model of cyclic instabilities in TBC systems. *Journal of the Mechanics and Physics of Solids*, 50:1565–1589.

Karlsson, A., Hutchinson, J., and Evans, A. (2003). The displacement of the TGO in TBC systems upon temperature cycling. *Materials Science Engineering A*, 351:244–257.

Kato, T., Matsumoto, K., Matsubara, H., Ishimata, Y., Saka, H., Hirayama, T., and Ikuhara, Y. (2005). TEM characterization of the YSZ fabricated by EB-PVD deposition. *Surface and Coating Technology*, 194:16–23.

Kim, G., Yanar, N., Hewitt, E., Pettit, F., and Meier, G. (2002). The effect of the type of thermal exposure on the durability of thermal barrier coatings. *Scripta materialia*, 46:489–495.

Lapin, J. (1997). Effect of ageing on the microstructure and mechanical behaviour of a directionnaly solidified Ni_3Al-based alloy. *Intermettalics*, 5:615–624.

Levi, C., Sommer, E., Terry, S., Cataniou, A., and Rühle, M. (1986). Alumina grown during deposition of thermal barrier coatings on NiCrAlY. *Journal of American Ceramic Society*, 86:676–685.

Leyens, C., Schulz, U., Pint, B., and Wright, I. (1999). Influence of EB-PVD TBC microstructure on TBC system performance under cyclic oxidation conditions. *Surface and Coating Technology*, 120:68–76.

Lu, T., Levi, C., Wadley, H., and Evans, A. (2001). Distributed porosity as a control parameter for oxide thermal barrier made by physical vapor deposition. *Journal of American Ceramic Society*, 84:2937–2946.

Lughi, V. and Clarke, R. (2005). Tansformation of EB-PVD YSZ thermal barrier coating. *Journal of American Ceramic Society*, 88:2552–2558.

Lughi, V., Tolpygo, V., and Clarke, R. (2004). Microstructural aspects of the sintering of thermal barrier coatings. *Materials Science Engineering A*, 368:212–221.

Lugscheider, E., Bobzin, K., Bärwulf, S., and Etzkorn, A. (2001). Mechanical properties of EB-PVD TBC's by nanoindentation. *Surface and Coating Technology*, 138:9–13.

Mendis, B. and Hemker, K. (2008). Thermal stability of microstructural phases in commercial NiCoCrAlY bond coats. *Scripta Materialia*, 58:255–258.

Mennicke, C., Schumann, E., Rühle, M., Hussey, R., Sproule, G., and Graham, M. (1998). The effect of yttrium on the growth process and microstructure of α-Al_2O_3 on FeCrAlY. *Oxidation of metals*, 49:455–466.

Mercer, C., Faulhaber, S., Yao, N., McIlwrath, K., and Fabrichnaya, O. (2006). Investigation of the chemical composition of the thermally grown oxide layer in thermal barrier systems with NiCoCrAlY bond coats. *Surface and Coating Technology*, 201:1495–1502.

Monceau, D., Bouhanek, K., Pieraggi, B., Malie, A., and Pieraggi, B. (2000). Transition in high-temperature oxidation kinetics of Pd-modified aluminide coatings: role of oxygen partial pressure, heating rate, and surface treatment. *Journal of Materials Research*, 15:665–675.

Müller, J. and Neuschütz, D. (2003). Efficiency of α-alumina as diffusion barrier between bond coat and bulk material of gas turbine blades. *Vaccum*, 71:247–251.

Nakagawa, T., Sakaguchi, I., Shibata, N., Matsunaga, K., Mizoguchi, T., Yamamoto, T., Haneda, H., and Ikuhara, Y. (2007). Yttrium doping effect on oxygen grain boundary diffusion in α-Al_2O_3. *Acta Materialia*, 55:6627–6633.

Nicholls, J. (2003). Advances in coatings design for high performance gas turbine. *MRS Bull*, 28:659–670.

Nychka, J., Xu, T., Clarke, D., and Evans, A. (2004). The stresses and distortions caused by formation of a thermally grown alumina: comparison between measurements and simulations. *Acta Materialia*, 52:2561–2568.

Panat, R., Zhang, S., and Hsia, K. J. (2003). Bond coat surface rumpling in thermal barrier coatings. *Acta Materialia*, 51:239–249.

Petzow, G. and Effenberg, G. (1988). *Ternary alloys*, volume 4.

Pilling, N. and Bedworth, R. (1927). *Journal Instit. Matels*, 2:529.

Pint, B., Martin, J., and Hobbs, L. (1993). O/SIMS characterization of the growth mechanism of doped and undoped α-alumina. *Oxidation of metal*, 39:167–195.

Pint, B., Martin, J., and Hobbs, L. (1995). The oxidation mechanisms of the θ-Al_2O_3. *Solid State Ionics*, 78:99–107.

Pint, B. and More, K. (2009). Characterization of alumina interfaces in TBC systems. *Journal of Materials Science*, 44:1676–1686.

Pint, B., Wright, I., Lee, W., Zhang, Y., Prübner, K., and Alexander, K. (1998). Substrate and bond coat compositions: factor affecting alumina scale adhesion. *Materials Science Engineering A*, 245:201–211.

Poulain, M., Dorveaux, J., Mevrel, R., Rio, C., and Ritti, M. (2006). Evolution of the alumina layer/bon coat interface in oxidisied EB-PVD TBCs. *Surface Modification Technologies XVIII*, pages 405–409.

Prescott, R. and Graham, M. (1992). The formation of aluminium-oxide scales on high-temperature alloys. *Oxidation of Metals*, 38:233–254.

Ratzer-Scheibe, H. and Schulz, U. (2007). The effects of heat treatment and gas atmosphere on the thermal conductivity on APS and EB-PVD YSZ TBCs. *Surface and Coating Technology*, 201:7880–7888.

Renteria, A. F. and Saruhan, B. (2006). Effects of ageing on microstructure changes in EB-PVD manufactured standard PYSZ top coat of thermal barrier coatings. *Journal of European Ceramic Society*, 26:2249–2255.

Renteria, A. F., Saruhan, B., Schulz, U., Raetzer-Scheibe, H., Haug, J., and Wiedenmann, A. (2006). Effects of morphology on thermal conductivity of EB-PVD PYSZ TBCs. *Surface and Coating Technology*, 201:2611–2620.

Rhines, F. (1940). *AIME Trans.*, 137:246–286.

Rhines, F. and Wolf, J. (1970). The role of oxide microstructure and growth stress in the high-temperature scaling of nickel. *Metal. Trans.*, 1:1701–1710.

Schulz, U., Oettel, H., and Bunk, W. (1996). Texture of EB-PVD thermal barrier coatings under variable deposition conditions. *Zeitschrift fur Metallkunde*, 87:488–492.

Schulz, U. and Schmücker, M. (2000). Microstructure of $Zr0_2$ thermal barrier coatings applied by EB-PVD. *Materials Science Engineering A*, 276:1–8.

Serra, J. (1988). *Image analysis and mathematical morphology*, volume 1. Theretical advances.

Spitsberg, I., Mumm, D., and Evans, A. (2005). On the failure mechanisms of thermal barrier coatings with diffusion aluminide bond coatings. *Materials Science Engineering A*, 394:176–191.

Taylor, M., Gray, S., and Evans, H. (2006). *Contract Report*. SIEMENS.

Taylor, M., Gray, S., and Evans, H. (2007). *Contract Report*. SIEMENS.

Terry, S., Litty, J., and Levi, C. (1999). Evolution of porosity and texture in thermal barrier coatings grown by EB-PVD. *Elevated Temperature Coatings: Science and Technology III*, pages 13–26.

Tolpygo, V. (1999). The morphology of thermally grown α-Al_2O_3 scales on Fe-Cr-Al alloys. *Oxidation of Metals*, 51:449–477.

Tolpygo, V. and Clarke, D. (1998). Wrinkling of alumina films grown by thermal oxidation. Part I. *Acta Materialia*, 46:5153–5166.

Tolpygo, V. and Clarke, D. (2000a). Microstructural study of the θ-α transformation in alumina scales formed on nickel-aluminides. *Material at High Temperatures*, 17:59–70.

Tolpygo, V. and Clarke, D. (2000b). Surface rumpling of a (Ni,Pt)Al bond coat induced by cyclic oxidation. *Acta Materialia*, 48:3283–3293.

Tolpygo, V. and Clarke, D. (2004b). On the rumpling mechanism in nickel-aluminide coatings. Part I : an experimental assessment. *Acta Materialia*, 52:5115–5127.

Tolpygo, V. and Clarke, D. (2004c). On the rumpling mechanism in nickel-aluminide coatings. Part II : characterization of surface undulations and bond coat swelling. *Acta Materialia*, 52:5129–5141.

Tolpygo, V., Clarke, D., and Murphy, K. (2004). Evaluation of interface degradation during cyclic oxidation of EB-PVD thermal barrier coatings and correlation with TGO luminescence. *Surface and Coating Technology*, 188-189:62–70.

Vandervoort, R., Mukherjee, A., and Dorn, J. (1966). *Trans. Am. Soc. Metals*, 59:930.

Vasinonta, A. and Beuth, J. (2001). Measurement of interfacial toughness in TBC systems by indentation. *Acta Materialia*, 48:843–840.

Wachtman, J. (1996). *Mechanical properties of Ceramics*.

Wellman, R. and Nicholls, J. (2005). On the effects of ageing in the erosion of EB-PVD TBCs. *Surface Coating Technology*, 177:80–88.

Wen, M., Jordan, E., and Gell, M. (2006). Effect of temperature on rumpling and thermally grown oxide stress in an EB-PVD thermal barrier coating. *Surface and Coating Technology*, 201:3289–3298.

Xu, C., Faulhaber, S., Mercer, C., Maloney, M., and Evans, A. (2004). Observations and analyses of failure mechanisms in thermal barrier systems with two phase bond coats based on NiCoCrAlY. *Acta Materialia*, 52:1439–1450.

Xu, C. and Gao, W. (2000). Pilling Billing bedworth ratio for oxidation alloys. *Materials Research Innovations*, 3:231–235.

Zhang, Y., Haynes, J., Pint, B., Wright, I., and Lee, W. (2003). Martensitic transformation in CVD NiAl and (Pt,Ni)Al bond coatings. *Surface and Coating Technology*, 163-164:19–24.

Zhao, X., Wang, X., and Xiao, P. (2006). Sintering and failure behaviour of EB-PVD thermal barrier coating after isothermal treatment. *Surface and Coating Technology*, 200:5946–5955.

Zhua, U., Miller, R., and B.A. Nagarajb, R. B. (2001). Thermal conductivity of EB-PVD thermal barrier coatings evaluated by a steady-state laser heat flux technique. *Surface and Coating Technology*, 138:1–8.

Chapter -III-

Numerical approach to predict stress and strain fields in EB-PVD TBC system

Contents

III.1 Introduction

Thermal barrier coating (TBC) spallation is expected to occur on cooling when the stored elastic strain energy per unit area reaches the toughness of one of the thermally grown oxide (TGO) interfaces. It is reported in the literature that the interface resistance decreases with exposure time at high temperatures and with the number of thermal cycles (Spitsberg et al., 2005). Initiation and growth of micro-damage (porosity, microcrack) close to the TGO can be responsible for the weakening of the oxide interfaces toughness, leading to top coat spallation. One of the aim of the present thesis is to establish a relationship between the local stress/strain fields close to the TGO, the oxide interfacial damage and the decrease of the TGO interfaces toughness.

During service, stresses in TBC are generated (i) on cooling by volumetric expansion due to the thermal expansion mismatch between the superalloy substrate and the others layers (bond coat, TGO and top coat) and (ii) at high temperatures by the growth strains associated with the TGO formation. The mechanical response also depends on the continuous evolution of the TBC constituents microstructure, as explained in Chapter II.

Several numerical studies have shown that the local stresses close to the TGO layer are function of the TBC morphology, TGO growth strains and thermo-mechanical properties of the TBC constituents. Few of them simulate the oxide growth, time-dependent mechanical properties and time-evolution of the TGO roughness as a continuous function of time. Moreover, numerical analyses mostly focus just on the stress field analysis after cooling, arising the growth strains because it does not affect the stress fields at low temperatures (Chen et al., 1998, Bialas, 2008).

In $NiCoCrAlY$ TBC systems, heterogeneities are observed at the TGO-BC interface, which can be sites of local stress concentration and therefore potential sites for damage initiation (Stiger et al., 1999, Xu et al., 2004). For this reason, TGO morphology modelled as a simple 2D sinusoidal profile and which does not take into account the heterogeneities and oxide roughness evolution may not be sufficient. Zhu *et al.*(2005) have published the results of the stress fields close to oxide pegs and have analysed the conditions under which cracks may initiate and growth. Nevertheless, the stress/strain fields were obtained for elastic/perfectly plastic TBC constituents and without continuous model of the oxide growth (Zhu et al., 2005).

In this work, we propose to use a realistic simulation of the TGO morphology and a relevant finite element model to predict the stress/strain fields. It accounts for: (i) oxide growth, (ii) growth strains associated with bond coat oxidation, (iii) 2D and 3D realistic oxide morphology, (iv) oxide roughness increase, (v) bond coat creep and plastic behaviour, (v) TGO creep and (vi) EB-PVD top coat microstructural morphology. In Section III.2, the methodology to model the oxide growth and to determine stress/strain fields close to the moving TGO-BC interface is presented. Then, stress and strain fields resulting from a 2D sinusoidal simulation of the TGO morphology are obtained numerically. The influence of the parameters characterising the mechanical behaviour, TGO morphology and thermal loading on the stress/strain fields is analysed in Section III.4. Section III.5 deals with the need to rely on a realistic and complex simulation of the oxide morphology. To achieve this goal, a more representative model of the oxide morphology based on Fourier analysis of a TBC micrograph has been presented in Section II.4. For the latter case, the stress and strain fields obtained numerically is compared with a 2D and 3D sinusoidal model of the TGO morphology.

III.2 Methodology to model numerically the oxide growth and the stress/strain fields

III.2.1 Oxide growth model

It has been reported that grown alumina is made of a columnar layer and a thin equiaxed layer, respectively, close to the BC-TGO and YSZ-TGO interfaces, see Section II.2.2.3. The duplex morphology of alumina films is related to the fact that alumina growth is ensured by diffusion of aluminium cations and oxygen anions. The columnar grain structure beneath an equiaxed initial layer indicates that new TGO forms primarily at the interface with the bond coat (inward oxidation). This is believed to happen because oxygen diffusivity along TGO grain boundaries exceeds that at Al^{3+} cations. Reactive elements such as yttrium in $NiCoCrAlY$ bond coats segregate at the TGO grain boundaries and suppress outward transport of aluminium along oxide grain boundaries (Haynes et al., 1999, Nychka and Clarke, 2005). For this reason, only the inward oxidation is modelled in the current work. The oxide growth is assumed to occur close to the TGO-BC interface and not in the entire TGO layer, see Section II.2.2.4.

A numerical model of oxide growth requires the knowledge of the TGO oxidation kinetics. The experimental work performed by the University of Birmingham (Taylor et al., 2006) provides data of TGO thickness time-evolution at different temperatures (from 950 to 1150°C), see Section II.2.2.1. The parameters defining the TGO oxidation kinetics (k_n and n) are function of the temperature, see Eq. II.1 and directly input in the procedure. For simplicity, we have chosen to implement directly oxide growth, based on the experimental data. It could have been possible to introduce a diffusion-reaction model, but this approach does not allow to model the oxide roughness time-dependence generated by the complex bond coat or TGO microstructures. Such approach would have required data to describe the complex relationship between stress and diffusion, which are not available. A phase-field approach could certainly provide a way to model this problem (Wu et al., 2004).

III.2.1.1 Methodology

Once the oxidation kinetics is known, the development of a method to drive the motion of the inward oxidation front during oxidation in a FE mesh is required. For the stress and strain fields calculation, it is necessary to know to which TBC constituent each integration point belongs to in the FE mesh so as to associate the appropriate material behaviour to the integration point.

In each finite element, a parameter representing the oxide volume fraction, f_{ox}, defines its belonging to one of the TBC constituents. When $f_{ox} = 0$ the element is not oxidised and belongs to the top coat or the bond coat. When $f_{ox} = 1$, the material is assumed to be fully oxidised, hence it is within the TGO. The TGO-BC interface is modelled by a transition zone corresponding to a FE row, seen in Fig. III.1. When the oxidation front is within a given finite element, its position is defined by the variable f_{ox} which ranges continuously from 0 to 1. The algorithm used to determine the oxide volume fraction is as follow: at each time increment, the position of the oxidation front, y_{ox}, the size of the oxidised FE, h_{ox}, and, N, the numbers of FE already oxidised, are known. Thus it is possible to determine the distance between the actual position of the oxidation front, y_{ox}, and that of the FE which is being cut by the oxidation front, $N.h_{ox}$:

$$h_f = y_{ox} - Nh_{ox}, \tag{III.1}$$

where h_f is the relative position of the oxidation front in the oxidised FE. The expression for the oxide volume fraction, f_{ox}, in the transition FE is defined by the ratio between the relative position of the oxide front in the FE element, h_f, and the FE size, h_{tran}:

$$f_{ox} = \frac{h_f}{h_{tran}}, \tag{III.2}$$

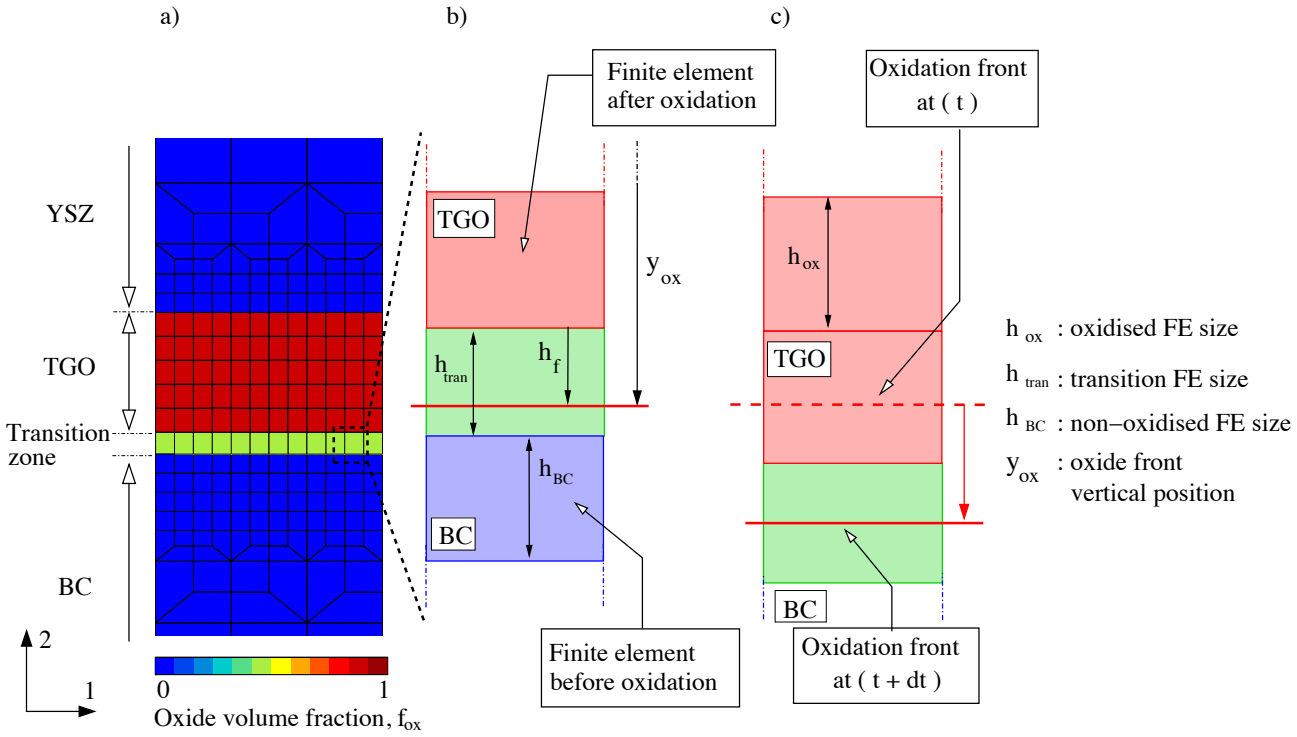

Figure III.1 : (a) Value of the variable f_{ox} representing the oxide volume fraction in a 2D FE mesh, (b) and (c) close-up views of the transition zone corresponding to the TGO-BC interface for two different oxidation times.

Note that f_{ox} is homogeneous within the FE being oxidised, *i.e.* crossed over by the oxidation front, and it depends on the evolution of the transition FE size. As discussed in Section II.2.2.4, the bond coat oxidation induces a volumetric expansion of 22%. The method proposed here to model the TGO front motion has the advantage to be applied to both the inward and the outward oxidation fronts and for any profile chosen to model the TGO morphology, either in 2D or in 3D.

III.2.1.2 Application to a rough TGO profile

In Section II.4, we have proposed to take into consideration the oxide roughness due to its influence on TBC lifetime. The method has been improved to simulate the oxide growth in a FE mesh where the TGO morphology is described by a 2D sinusoidal profile. Its geometry is defined by two parameters: a sinusoidal wavelength, w, and an amplitude, a, see Fig. III.2(a). Here, the FE mesh is generated with chosen values for w and a, and the oxide front motion is adapted to the TGO sinusoidal shape. Figures III.2(a), (b) and (c) show the evolution of the oxide volume fraction, f_{ox}, along the rough oxide for three different oxidation times, namely 500 h, 2000 h and 5000 h at 950°C.

The simplicity of this approach is sufficient for a preliminary study of stress/strain fields in TBC system requiring a reasonable CPU time for its calculation. Nevertheless, it is assumed that the oxide thickness is constant along the oxide layer and the roughnesses of both TGO interfaces are identical and constant with time. The method has been improved to reach a more representative description of the oxide morphology, to be detailed in Section III.5.

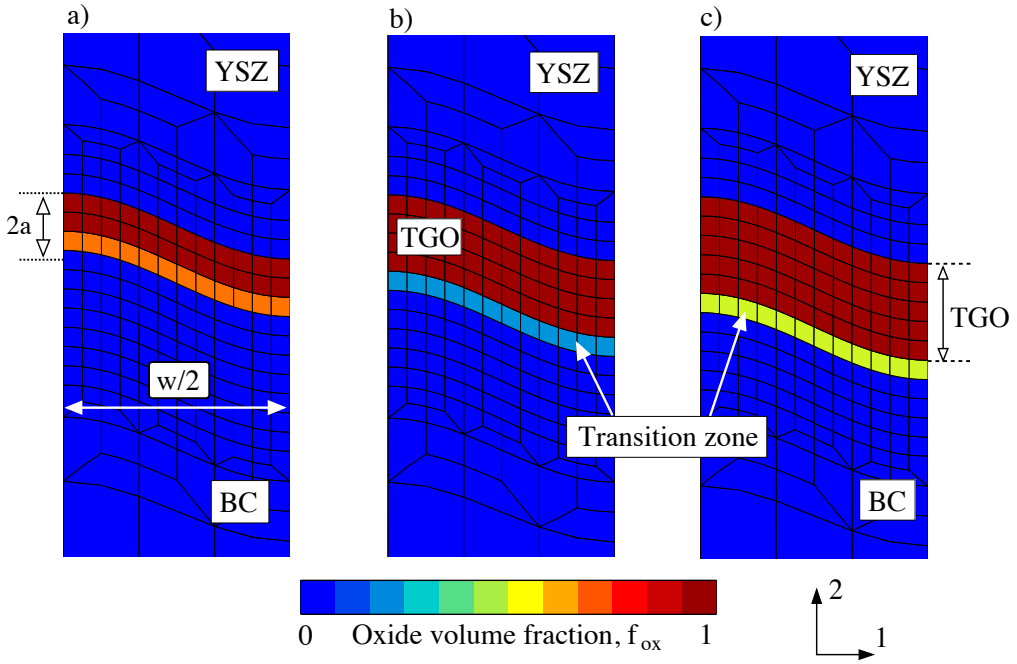

Figure III.2 : Gauss point value plots of the oxide volume fraction, f_{ox}, in a rough FE mesh at different oxidation times: (a) 500 h, (b) 2000 h and (c) 5000 h at 950°C.

III.2.1.3 Growth strains due to TGO formation

The volumetric expansion represents the volume increase upon converting the bond coat to alumina at the TGO-BC interface, which induces compressive stresses at high temperatures. The formulation of the anisotropic growth strain ($\underline{\underline{\varepsilon}}_{\phi}$) has been discussed in Section II.2.2.4. The new oxide grows close to the BC-TGO interface, normally to the YSZ-BC interface and to the oxide grain boundary. This phenomenon induces respectively a normal, ε_N, and a lateral growth strain, ε_T. The ratio between the normal and transversal strain components characterises the weight of the diffusion mechanisms occurring in the TGO layer ($\varepsilon_N/\varepsilon_T = 87$, see Eq. II.20). To respect mass conservation, the volumetric expansion is determined using an approach based on the Pilling Bedworth Ratio, and applied to the oxide scale. In the present study, the direction normal to the YSZ-BC interface is the direction X_2, see Fig. III.2.

III.2.2 Stress determination at the TGO-BC interface

As previously presented in Section I.3.3, the decrease of the oxide interface toughness can be explained by the local high stress level which is found close to the critical TGO-BC interface where micro-damage is observed. This point justifies the need to propose an accurate methodology for stress evaluation. Stresses are generated first during cooling by thermal

properties mismatch between the substrate and the others TBC constituents (BC, TGO and YSZ). At high temperatures, stresses are triggered by the oxide growth strains. The volumetric expansion can be expressed in the form proposed in Eq. III.3. It comprises a component normal to the oxide layer and lateral components, ε_N and ε_T respectively. The high normal growth strain value ($\varepsilon_N = 21.5\%$) in this transition zone requires that a finite strain framework be used. In presence of two materials in the transition zone (BC and TGO), the equivalent behaviour is determined using a Voigt homogenisation.

The first step of the methodology is to determine the global strain gradient tensor in finite strain $\underset{\sim}{\hat{\boldsymbol{F}}}$. This tensor, is the product of the strain gradient tensor due to mechanical effects, $\underset{\sim}{\boldsymbol{F}}_m$, and the oxidation strain gradient tensor, $\underset{\sim}{\boldsymbol{F}}_\phi$, see Eq. III.4. The oxidation strain gradient tensor, $\underset{\sim}{\boldsymbol{F}}_\phi$, is a function of the oxide volume fraction in a finite element, f_{ox}, and of the growth strain tensor, $\underset{\sim}{\boldsymbol{\varepsilon}}_\phi$, Eq. III.5. Finally the stress tensor is determined using the Voigt method (Eq. III.6), where $\underset{\sim}{\boldsymbol{\sigma}}_{TGO}$ and $\underset{\sim}{\boldsymbol{\sigma}}_{BC}$ are the stresses calculated using the material models, respectively, for the TGO and the bond coat. When the oxide volume fraction ranges from 0 and 1, the material behaviour in the transition zone is assumed to be given by that of the homogenised material. Thus,

$$\underset{\sim}{\boldsymbol{\varepsilon}}_\phi = \begin{bmatrix} \varepsilon_T & 0 & 0 \\ 0 & \varepsilon_N & 0 \\ 0 & 0 & \varepsilon_T \end{bmatrix} \tag{III.3}$$

$$\underset{\sim}{\hat{\boldsymbol{F}}} = \underset{\sim}{\boldsymbol{F}}_m . \underset{\sim}{\boldsymbol{F}}_\phi, \tag{III.4}$$

$$\underset{\sim}{\boldsymbol{F}}_\phi = \underset{\sim}{\boldsymbol{I}}_2 + f_{ox}\underset{\sim}{\boldsymbol{\varepsilon}}_\phi, \tag{III.5}$$

$$\underset{\sim}{\boldsymbol{\sigma}} = \underset{\sim}{\boldsymbol{\sigma}}_{TGO} f_{ox} + \underset{\sim}{\boldsymbol{\sigma}}_{BC}(1 - f_{ox}). \tag{III.6}$$

In summary, the material behaviour attached to each Gauss point located in the transition zone is determined using a Voigt approach, in finite strain and takes into account the anisotropic volumetric expansion. Since the growth strains are applied to each Gauss point in a FE during oxidation, f_{ox} has to be homogeneous in all the FEs. Indeed, a discontinuous value of the oxide volume fraction in the same FE might generate high stress gradients incompatible with the element shape functions.

III.2.3 Description of the thermal loading and finite element mesh

III.2.3.1 Thermal loading

The previous FE model is applied to simulate the TBC mechanical response for 200 day-long thermal cycles, typical of land based turbine gas. The initial state of the TBC system is taken to approximate that the $NiCoCrAlY$ bond coat is deposited on the substrate. The bond coat is assumed to be stress-free in the as-processed stated. The EB-PVD top coat elaboration process is modelled by a free stress state at the deposition temperature, step followed by a cooling down to room temperature. The growth of the thin TGO formed during deposition is also simulated ($h_0 = 0.5\ \mu$m). During top coat deposition, the blade, the bond coat and the top coat have the same temperature (400°C). This process temperature is lower than that currently used, but corresponds to industrial data. The influence of the temperature during the EB-PVD process on the stress and strain fields is investigated in Section III.4.3. The top coat deposition process and the cyclic thermal loading are represented in Fig. III.3. In all the simulations carried out in this study, the temperature is assumed to be uniform throughout the layered system.

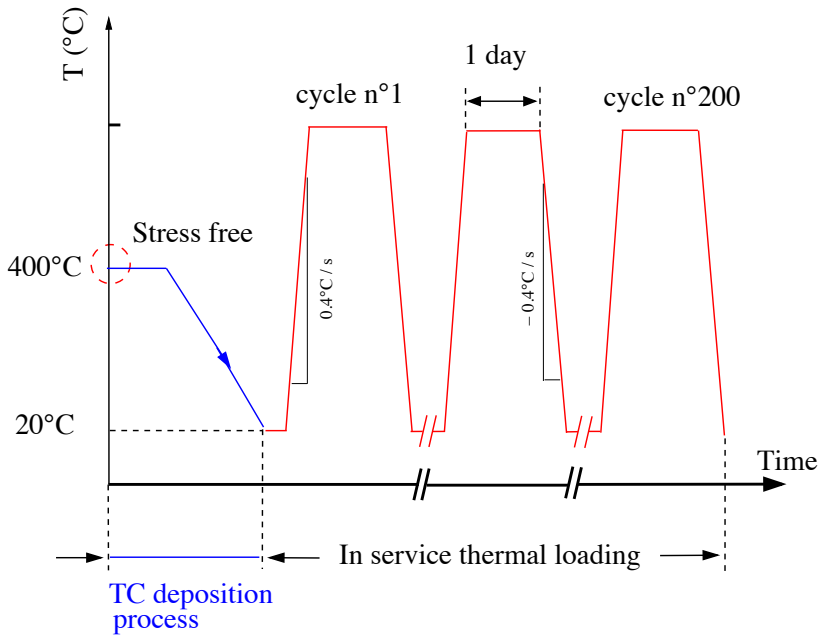

Figure III.3 : Cyclic thermal loading including the top coat deposition process and the in-service thermal loading imposed on the TBC system during the simulation. A cycle consists of a 22 h-40 min period at high temperature and 40 min cooling/heating phases.

III.2.3.2 Finite element mesh

In a preliminary approach and according to the image-processing analysis performed on tested samples, see Section II.4.1.1, the TGO morphology is modelled by a representative sinusoidal profile, as shown in Fig. III.4. It provides the advantages to be a simple and a fast approach, yielding comparable results to those in the literature. The mean wavelength, w, and amplitude, a, of the sinusoidal function has been determined by image-processing given 11.72 μm and 0.864 μm, respectively. The ceramic layer and bond coat are, respectively, 45 μm and 25 μm thick. It is not usefull to model the entire bond coat and ceramic thicknesses because local stresses close to the TGO might not be affected by the top of the YSZ and by the bottom of the bond coat. This point will be discussed in Section III.3.2.1. The superalloy substrate is modelled *via* the relative thermal expansions of each TBC constituent. The FE mesh consists in 12,603 quadratic elements with full integration and 76,184 degrees of freedom (DOF). The FE mesh is subjected to plane-strain and boundary conditions, determined using symmetries and periodicity of the problem, see Fig. III.4. It is assumed that the substrate rigidity and thickness are high enough to impose its own deformation to the other layers during the mechanical and thermal loads. According to an investigation of the size influence of FE crossed over by the oxidation front, the element size in the area prone to oxidation has to be smaller than a critical value of 0.05 μm. The influence of the blade rotational speed and the gas pressure are assumed to be negligible in comparison with the other stress sources.

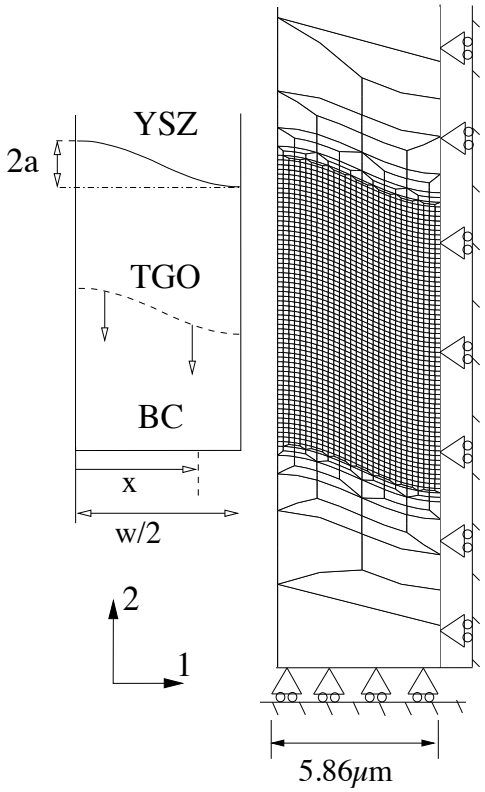

Figure III.4 : Finite element mesh using a 2D sinusoidal TGO morphology and boundary conditions. Wavelenght (w): 11.72 μm and amplitude (a): 0.864 μm.

III.3 Predicted stress and strain fields in TBC system

It is expected that the local strain and stress fields close to the TGO generated at high and low temperatures exert a central influence on the micro-damage initiation or propagation. Thus, one of the objective of the numerical calculations is to obtain estimations of the critical stress conditions responsible for the oxide interfaces damage and hence for the TBC toughness decrease. The results from the FE analyses are presented and discussed in this section. They will include the associated effects of bond coat oxidation, in-service thermal loading and material behaviour of the BC (elasto-visco-plastic), the TGO (elasto-viscous) and the YSZ (elastic transversaly isotropic). The objectives are to study at room (20°C) and peak temperatures, close to the TGO layer the (i) in-plane σ_{11} and out-of plane σ_{22} stresses along the direction X_1 and X_2 due to oxide growth and thermal cycling, (ii) traction (normal to the oxide interface) σ_{nn} and the shear-stress σ_{tt} at the two TGO interfaces,(iii) time-evolution of the normal traction and (iv) accumulated bond coat plastic and creep strains.

III.3.1 In-plane stress field

In a preliminary approach the magnitudes of the in-plane compressive stresses in the TBC constituents at high and low temperatures are analytically and numerically determined. This study is necessary as the stored elastic strain energy per unit area driving to the TBC spallation is directly function of the in-plane compressive stresses.

At low temperatures, in-plane stresses are generated by the thermal expansion mismatch between the superalloy substrate and the others layers constituting the system. Due to its large thickness in comparison with the others TBC constituents, it is assumed that the substrate imposes its own deformation to the other layers during thermal loading, see Fig. III.5. At high temperatures, in-plane stresses are generated by the growth strains associated with the bond coat oxidation.

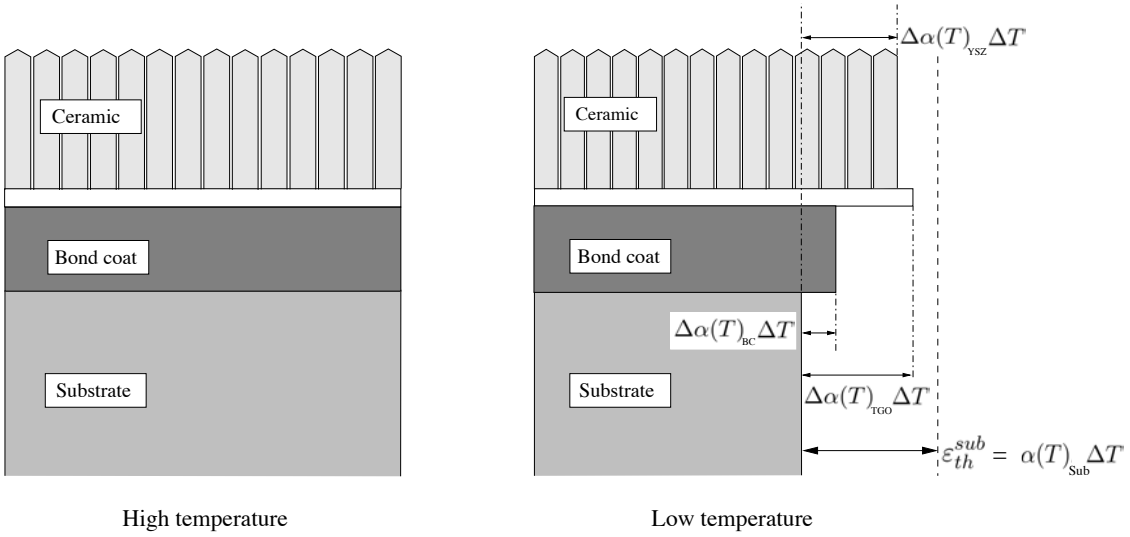

Figure III.5 : Drawing illustrating the thermal expansion mismatch between the superalloy substrate and the others layers constituting the system.

This approach allows to determine the stress order of magnitude inside each TBC layer and to study the influence of each TBC constituent mechanical behaviour. The comparison

between in-plane stress fields obtained numerically and analytically (marked by a star in Table III.1) is also made. In the latter case, each TBC constituent is assumed to be only elastic. Assuming plane strain conditions, in-plane stresses at high temperature in the TGO-BC transition zone can be formulated as follows:

$$\sigma_{11}^{ox} = \frac{\varepsilon_T}{1-\nu} E_1, \tag{III.7}$$

where E_1 is the in-plane Young's modulus and ε_T the the oxide growth strain due to the bond coat oxidation. The in-plane stresses generated by the thermal expansion mismatch are marked by $^{(1)}$ in Table III.1 and expressed as:

$$\sigma_{11}^{th} = \frac{\Delta\varepsilon_{th}}{1-\nu} E_1, \tag{III.8}$$

where$\Delta\ \varepsilon_{th}$ is the relative thermal expansion between each TBC constituent and the substrate, see Fig. III.5 and given by:

$$\Delta\varepsilon_{th}^{i} = \varepsilon_{th}^{i} - \varepsilon_{th}^{sub} = \Delta\alpha^{i}(T)\Delta T, \text{ with } i = \text{YSZ, TGO and BC} \tag{III.9}$$

where$\Delta\ \alpha^i(T)$ the relative coefficient of thermal expansion between each TBC constituent and the substrate.$\Delta\ \alpha^i(T)$ depends on temperature and the considered TBC constituent. Two cases have to be distinguished for the stresses induced by thermal expansion. In Eq. III.8,$\Delta\ T$ could be the relative temperature (ΔT_a) between the EB-PVD deposition and the in-service temperatures, respectively noted T_{dep} and T thus:

$$\sigma_{11}^{th} = \frac{\Delta\alpha^{i}(T)\Delta T_a}{1-\nu_i} E_1^i = \frac{\Delta\alpha^{i}(T)[T-T_{dep}]}{1-\nu_i} E_1^i, \text{ with } i = \text{YSZ and BC} \tag{III.10}$$

This equation could be applied to all the TBC constituents except for the new oxide formed at high temperatures. In this case, marked by $^{(2)}$ in Table III.1,$\Delta\ T$ is the relative temperature, noted$\Delta\ T_b$, between the in-service and peak temperature T_h:

$$\sigma_{11}^{th} = \frac{\Delta\alpha^{i}(T)\Delta T_b}{1-\nu_i} E_1^i = \frac{\Delta\alpha^{i}(T)[T-T_h]}{1-\nu_i} E_1^i, \text{ with } i = \text{TGO}. \tag{III.11}$$

From the analysis of in-plane stresses resulting from the analytical and numerical analyses of a flat mutli-layer TBC system (Table III.1), some points should be stressed:

- according to the numerical simulation, no in-plane stresses develop at high temperatures in the bond coat and the TGO (few MPa). Bond coat and TGO creep behaviour enable stress relaxation. In contrast, the analytical approach based on elastic assumptions, provides high in-plane stresses value at high temperatures, -242 MPa in the bond coat, and -1220 MPa in the oxide layer, due to the high value of the oxide Young's modulus (≈ 400 GPa).

- In the transition zone simulating the TGO-BC interface, the bond coat and TGO creep behaviour enable the stress relaxation and thus explain the lower in-plane stresses obtained numerically (0 to -810 MPa) in comparison with the analytical approach (-242 to -1120 MPa).
- Compressive stresses develop in the YSZ and TGO layers after cooling , -142 MPa and -2736 MPa, respectively. About the in-plane stress in TGO, the difference between the analytical and numerical results is high but is only due to the difference at the peak temperature ($\sigma_{11}^{ox} = -1220$ MPa). The stress induced by the cooling (σ_{11}^{th}) is similar to both models. Note also that creep relaxation is inhibited when the temperature decreases even under high stress levels.

Table III.1 : In-plane stresses (MPa) in the TBC constituents and the TGO-BC transition zone at high (950°C) and low temperatures (20°C) after 200 days of cyclic thermal loading. $^{(*)}$ corresponds to stresses obtain analytically for elastic TBC constituents, $^{(1)}$ for stresses generated at high temperatures due to oxide growth (Eq. III.7) and $^{(2)}$ for the new formed oxide (Eq. III.11).

T(°C)	Material						
	BC		TGO		YSZ	Trans. zone	
	evp	elas.$^{(*)}$	ev	elas.$^{(*)}$	elas.	evp/ep	elas.$^{(*)}$
20	-246	-60	-2736 $^{(2)}$	-3955 $^{(2)}$	-142	/	/
950	5	-242	3 $^{(1)}$	-1220 $^{(1)}$	280	0 to -810	-242 to -1220 $^{(1)}$

Figure III.6(a) shows the contours of the oxide volume fraction, f_{ox}, and the in-plane stress component, σ_{11}, evaluated at 950°C and 20°C, Figs. III.6(b) and (c), respectively, after 200 day-long cycles at 950°C. At in-service temperatures, a high compressive in-plane stress level is generated by the growth strains associated with bond coat oxidation (around 1 GPa), see Fig. III.6(b). The highest stress is concentrated in the transition zone modelling the TGO-BC interface. At room temperature, the oxide roughness associated with the thermal strain mismatch strongly influences the in-plane stress fields, see Fig. III.6(c). Compressive in-plane stress ranges from 1.8 to 4.5 GPa and illustrates the need to take into account the TGO morphology in the stress fields calculations. Actually, the average in-plane stress for a flat oxide was found to be around 2.7 GPa, see Table III.1. This latter value should be compared to the minimal and maximal in-plane stress values predicted for a rough oxide, 1.8 to 4.5 GPa, respectively.

In conclusion, low stresses occur at high temperatures in TBC system, excepted at the TGO-BC interface due to the oxide expansion linked to the bond coat oxidation (-1 GPa). At low temperatures, the YSZ and TGO layers are under compression (respectively 0.25 and 2.7 GPa). These high values of compressive stresses point out the need to include in-plane stress in a lifetime model, thanks to the stored elastic strain energy per unit area. The comparison between numerical and analytical stress simulations done for a flat TBC system shows the absolute necessity to consider the creep and plastic behaviour of the TGO and bond coat to predict in-plane stress fields, especially at high temperatures. The oxide roughness influence on in-plane stress fields has been also demonstrated.

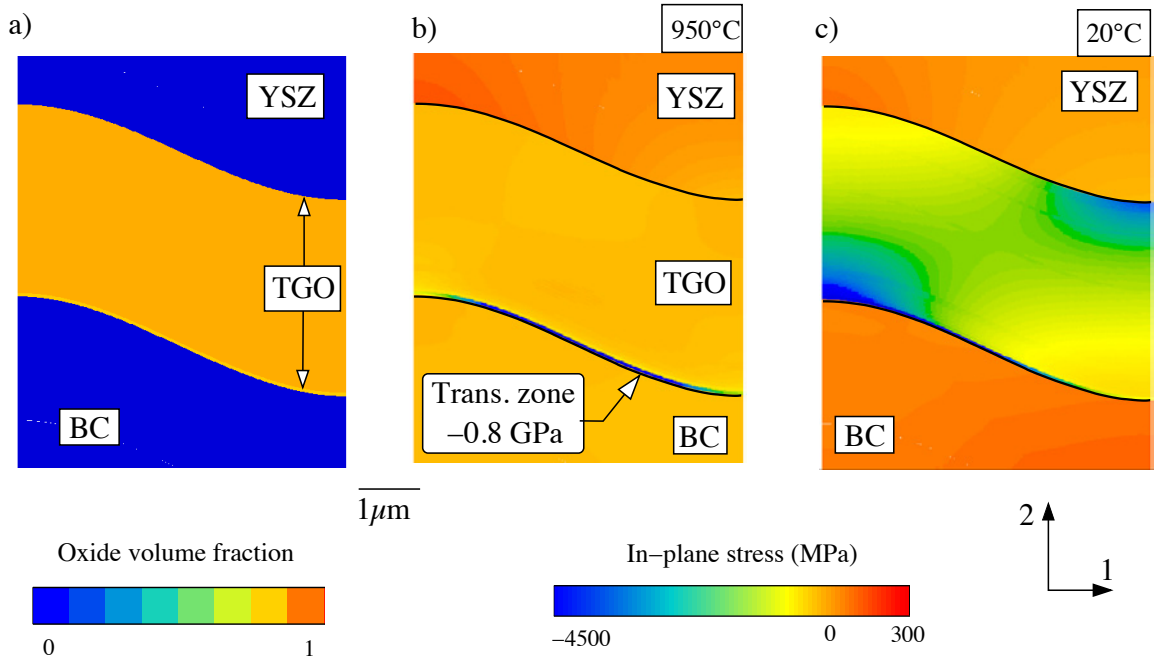

Figure III.6 : (a) Value of the oxide volume fraction f_{ox} and Gauss point plot of in-plane stress component σ_{11} at (b) 950°C and (c) 20°C after 200 day-long cycles at 950°C.

Using photo-stimulated luminescence piezo-spectroscopy (PLPS), developed by Clarke *et al.* (Christensen et al., 1996, Clarke et al., 1997), growth stresses within the TGO have been measured using near-field luminescence and the compressive stress ranges from 0.8 to 1.6 GPa at high temperatures and between 3 to 4 GPa at room temperature (Tomimatsu et al., 2004). The compressive stress level is dictated by the TGO creep strength. In comparison with the predicted stress obtained using our approach, qualitative results are similar. In-plane stresses close to the top coat are lower than that close to the bond coat. This is in agreement with a larger thermal strain mismatch between the TGO and bond coat, as illustrated in Fig. III.5.

To go further in the analysis of the stress induced by the bond coat oxidation (σ_{11}^{ox}) and the associated growth strains, in-plane stress time-evolution in a fixed finite element at the peak temperature crossed over by the oxidation front is plotted in Fig. III.7. For this study, the thermal loading is isothermal at 950°C. Initially the FE belongs to the bond coat (Zone 1) and due to creep relaxation, the in-plane stress is close to zero. When the oxidation front crosses over the chosen FE, the in-plane stress ranges from 12 MPa (the FE belongs to the bond coat) to a maximal value, σ_{max}, Zone 2. Finally, when the FE belongs to TGO, stresses decrease due to the TGO creep relaxation, Zone 3. The maximal compressive in-plane stress value decreases with exposure time. Oxide growth rate decreases with time and allows a greater stress relaxation in the bond coat and the oxide. In following the internal oxide front motion, a high value of in-plane compressive stress $\sigma_{11} = [0.6 - 1.1]$ GPa is induced by the oxide growth strains. The TGO and bond coat creep or plastic deformations enable to limit the stress consequences of the oxide growth strains.

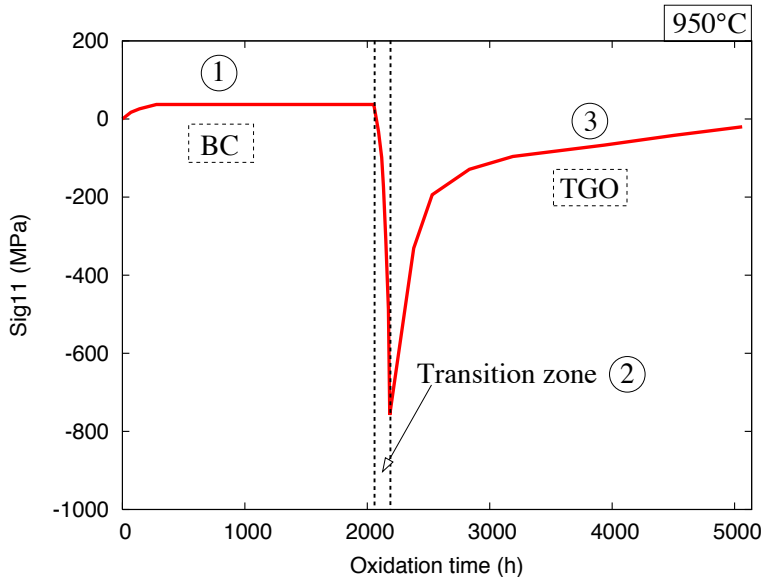

Figure III.7 : Evolution of in-plane stress σ_{11}^{ox} in a given FE that belongs initially to the bond coat and crossed by the oxidation front at 950°C. Zones 1, 2 and 3 define the material of which the FE belongs to, respectively the bond coat, the transition zone and the oxide.

III.3.2 Out-of-plane stress field

The out-of-plane stress is defined to be the stress in the direction X_2, see Fig. III.6. Figure III.8 shows the Gauss point value plot of the out-of-plane stress component, σ_{22}, evaluated before and after cooling after 200 day-long cycles at 950°C. At the peak temperatures, it can be seen that the most highly stressed region is close to the TGO-BC interface (-300 MPa) where bond coat oxidation occurs. Out-of-plane stresses are also observed at the TGO-YSZ interface (100 MPa). The out-of-plane stress magnitude increases during cooling down. At room temperature and at the TGO-BC interface, the peak zone is under tensile stress (512 MPa) while the valley zone is under compression (-325 MPa), see Figs. III.8 (b) and (c). Opposite results are observed at the TGO-YSZ interface, -365 MPa and 275 MPa in the peak and valley zones, respectively. Quantitatively, the out-of-plane stresses are higher close to the TGO-BC interface than at the TGO-YSZ one.

A quantitative stress distribution has been previously determined by many authors (Sfar et al., 2002, Caliez et al., 2002, Bialas, 2008). It has been observed that high tensile stresses occur at the top of the interface (peak zone) and ranges from 200 to 750 MPa. According to Caliez *et al.* (2002), the ratio between stress at high temperature σ_{22} (1100°C) induced by the introduction of 1 GPa of growth stress (simulating the oxide growth) and the maximum stress computed at ambient temperature, σ_{max}, has been found to be $\sigma_{22}/\sigma_{max} = 0.4$. With our approach, the ratio is around 0.6 but the zones where maximal stresses occur at low and high temperatures are not the same and make it difficult to have a relevant comparison.

III.3.2.1 Out-of-plane stresses through the layered TBC system

Out-of plane stresses through the three layers of the TBC system close to the TGO-BC (A-A view) and TGO-YSZ (B-B view) interfaces have been investigated. Figures III.9(a) and (b) show the out-of-plane stress profile at 20°C after 200 thermal day-long cycles at

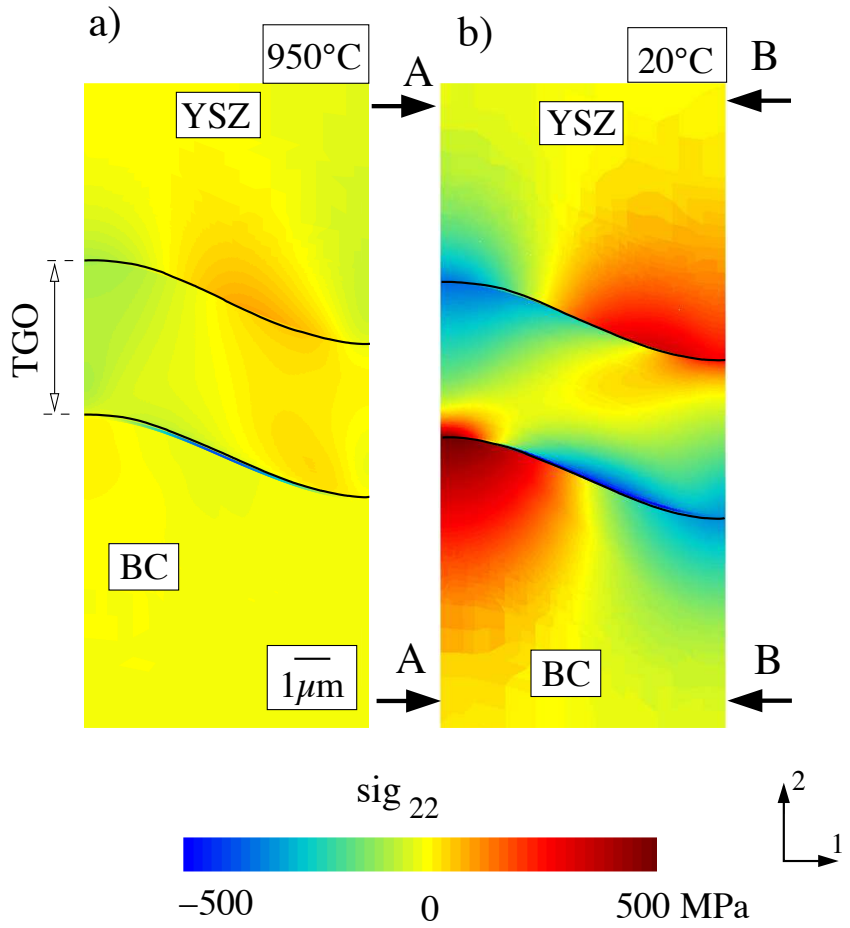

Figure III.8 : Gauss point value plot of the out-of-plane stress component σ_{22} at (a) 950°C and (b) 20°C after 200 day-long cycles at 950°C. The peak and valley regions are marked by the arrows, A-A and B-B, respectively.

950°C on both sides of the TGO interface in the peak and valley zones, *i.e.* A-A and B-B. The out-of-plane stress field at room temperature is also illustrated in Fig. III.9(c). As observed in Fig. III.8(b), stress fields extracted at 20°C in the peak and valley zones have an opposite distribution. Close to both interfaces, out-of-plane stresses strongly reach to maximum values. Due to the high stress gradient observed close to both oxide interfaces, it is difficult to extract a relevant value for the oxide interface normal traction. Moreover, the stress value is extracted in the Gauss's point and not exactly at the oxide interfaces. The FE size has also an influence on the interface stress fields. These points show the difficulty to define a microscale criterion for micro-damage initiation.

From the type of results shows in Fig. III.9, it can also be observed that at 3 μm away from each oxide interface, the out-of-plane stress is equal to zero. This is in agreement with the fact that the out-of-plane stress close to the oxide is only due to the TGO roughness. For this configuration of parameters, the influence of the top coat and bond coat thicknesses has been analysed. The latter point was addressed in the following manner: the normal traction

in the peak zone at the TGO-BC interface, which is equal to σ_{22}, has been extracted from a FE mesh built with the thickness reference values for the top coat and bond coat, 135 μm and 90 μm respectively. Then, the top coat and bond coat thicknesses were progressively and proportionally decreased and the obtained normal tractions in the peak zone were compared to the reference one. According to this analysis, it is sufficient to model only 45 μm and 25 μm of the ceramic layer and bond coat, respectively. Then, the difference between the normal traction obtained with an entire TBC system model are found to be less than 2%. We can conclude that: (i) out-of-plane stresses may not be affected by the mechanical phenomena which takes place far away from the TGO such as top coat sintering and (ii) it is sufficient for a representative FE model to include only a part of the bond coat and the YSZ thickness.

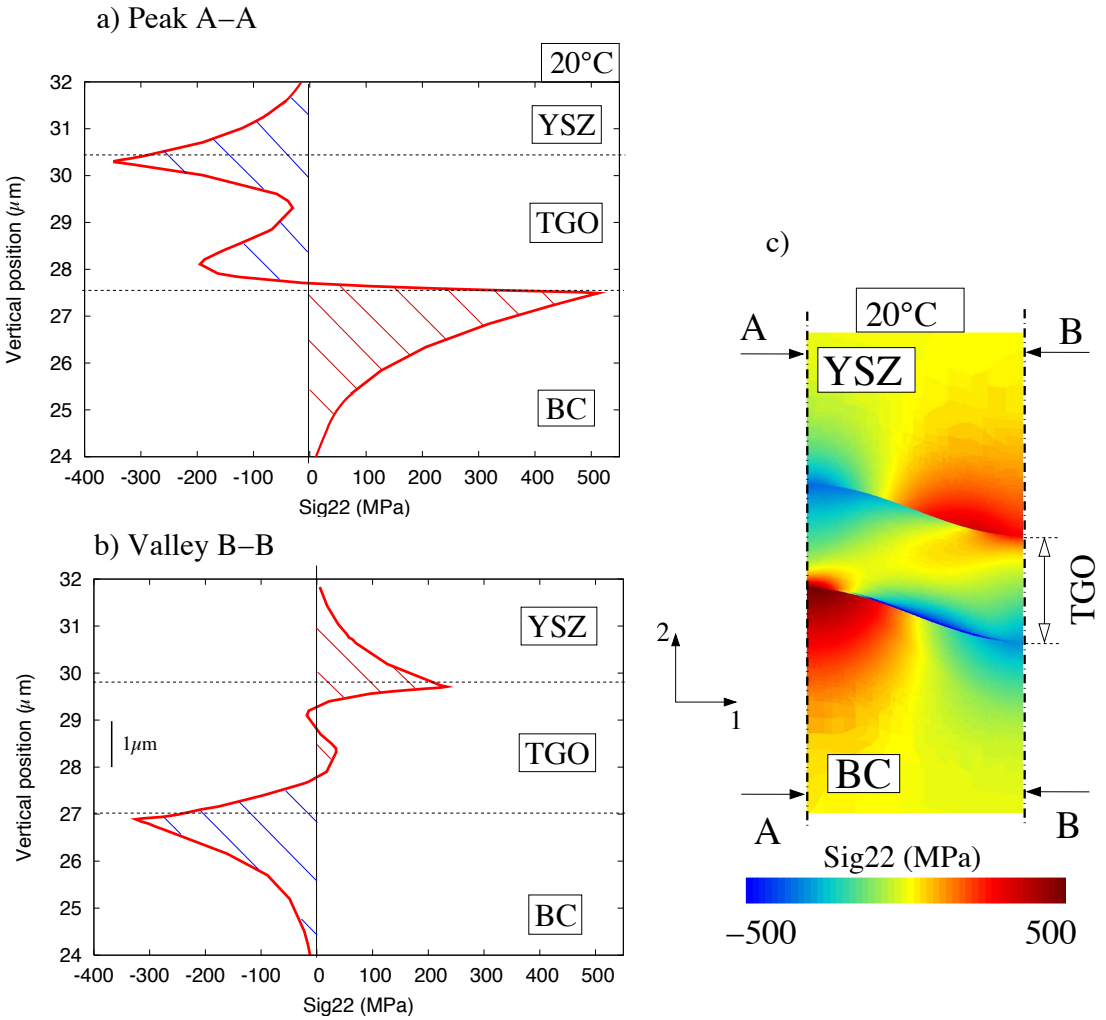

Figure III.9 : Out-of-plane stress through the TBC system (a) in the peak (A-A) and (b) in the valley regions (B-B) at 20°C after 200 day-long thermal cycles at 950°C. Gauss point value plot of σ_{22} at ambient temperature.

III.3.3 Normal tractions along the TGO interfaces

To understand micro-damage initiation and growth, one of the principal focus is on the normal tractions at the TGO interfaces because they govern crack growth parallel to the oxide interfaces. The normal traction at the TGO interfaces, σ_{nn}, is a scalar resulting from the stress tensor $\underset{\sim}{\boldsymbol{\sigma}}$ and of the interface normal vector $\vec{n}$. Corresponding normal tractions are

evaluated as a function of the relative position ($2x/w$) along the two TGO interfaces at 20°C and 950°C (noted LT and HT, respectively), see Fig. III.10.

Normal traction is higher at ambient temperature than before cooling, and follows the in-plane stress time-evolution, see Fig. III.9. After cooling at 20°C, the two normal traction distributions at the two TGO interfaces are inversed, as mentioned previously. It can be seen that the maximum tensile traction at the internal TGO-BC interface occurs in the peak region (482 MPa), while the maximum tensile traction along the TGO-YSZ interface is found at the valley region (274 MPa). These maximum values are lightly inferior than the maximal ones observed in Fig. III.10 (respectively 512 MPa and 275 MPa). Indeed, these latter values have not been exactly extracted at the TGO-BC interface, see Fig. III.9.

At the peak temperature, due to the bond coat creep/plastic behaviour, normal tractions are close to zero at the BC-TGO interface, whereas it ranges from -79 to 45 MPa at the YSZ-TGO interface. The influence of the top coat mechanical behaviour on normal traction at the external oxide interface will be investigated in Section III.4.1.3.

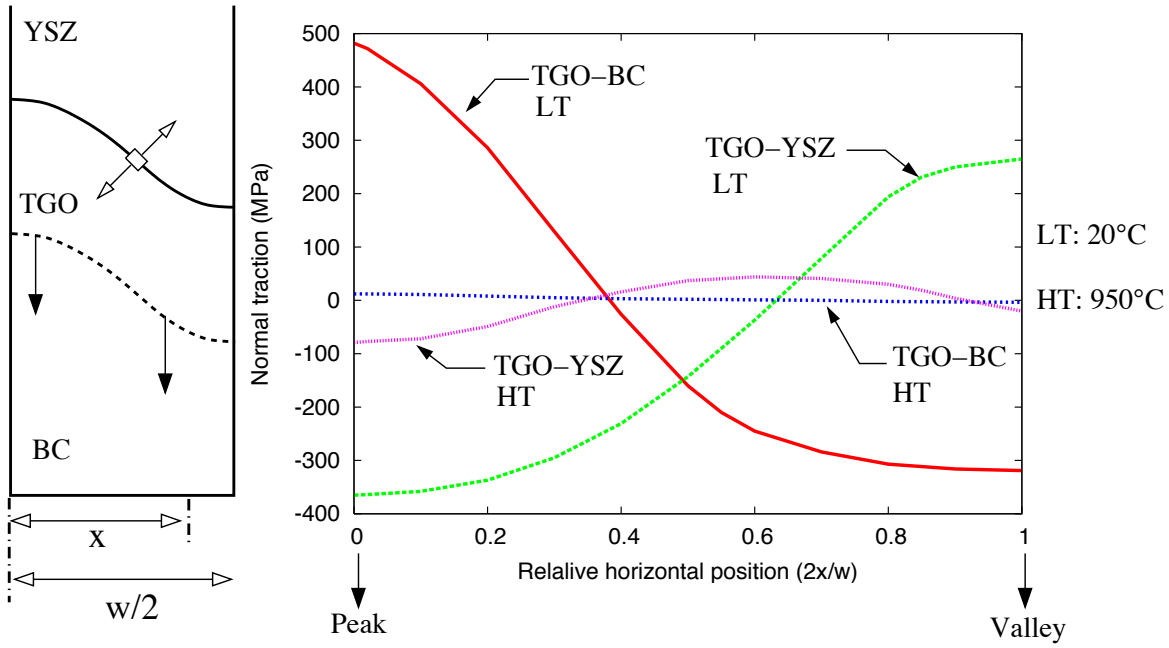

Figure III.10 : Normal traction, σ_{nn}, along the two oxide interfaces at high (950°C) and ambient temperature (20°C) as a function of the relative position ($2x/w$) along the oxide interfaces after 200 day-long thermal cycles at 950°C.

In comparison with the values obtained by Busso and Qian (2006 and 2009), our approach gives similar spatial distribution of the normal tractions along both oxide interfaces. At high temperatures, the predicted normal traction σ_{nn} ranges from -20 to 10 MPa at both oxide interfaces.

III.3.3.1 Time-evolution of normal tractions

The time evolution of the maximum normal traction in the peak zone, point A, at the TGO-BC interface is represented in Fig. III.11. The point A position follows the oxidation front motion through the FE mesh, as illustrated in Fig. III.11. The normal stress increases with exposure time in the first thousand hours from 370 to 460 MPa and then slowly

converges to an asymptotic regime (σ_{nn} = 480 MPa). After long times characterising blade in-service conditions, at the TGO-BC interface, σ_{nn}, one of the driving force for micro-damage initiation or propagation, is constant. Identical observation has been done for other numerical simulations (Xu et al., 2004).

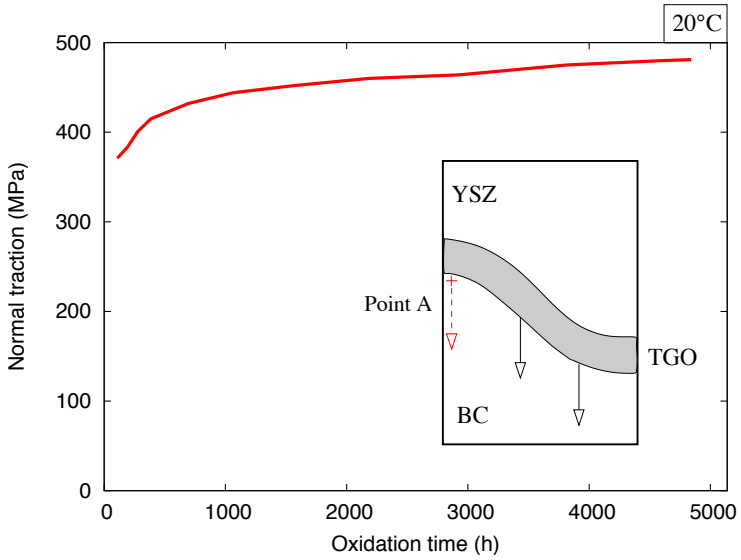

Figure III.11 : Normal traction in the peak zone (point A) at the moving TGO-BC interface at low temperature (20°C) as a function of the oxidation time after 200 day-long thermal cycles at 950°C.

These investigations suggest that TBC failure would have initiated at the TGO-BC interface close to the peak region or at the TGO-YSZ interface close to the valley region. However, since it was not possible to ascertain from the results whether TBC failure was initiated in this manner, our predictions can only provide an insight into the local driving forces for interfacial failure. For instance, the fact that even if the largest tensile traction was found close to the peak region at the TGO-BC interface after cooling should not rule out the possibility that failure of the TGO-YSZ interface or elsewhere at the TGO-BC interface may occur first at high temperatures. Furthermore, the predicted normal tractions are constant after thousand hours and do not increase with exposure time.

III.3.4 Shear stress along the oxide interfaces

Normal traction is not the only driving force which generates damage. Shear stress can be considered as another parameter influencing TBC system lifetime. The difference of thermal expansion coefficient between the TBC constituents induces shear stress at the two oxide interfaces. Figure III.12 represents the shear component, σ_{tt}, of the normal stress $\underline{\underline{t}}$ along both TGO interfaces at 20°C (LT) and 950°C (HT) after 200 day-long thermal cycles.

At both temperatures, the significant shear stress occurring at the TGO-YSZ and TGO-BC interfaces are concentrated between the peak and valley zones, contrary to the maximal normal tractions present in there zones. The maximum shear stress at room temperature at the TGO-YSZ and TGO-BC interfaces ranges from 0 in the peak and valley zones to 530 MPa and 433 MPa, respectively. At high temperatures, the shear stress is higher at the TGO-BC interface (from -30 to 133 MPa) than at the TGO-YSZ one (from -31 to 41 MPa), due ti the growth strains at the TGO-BC interface. The simulated high shear-stress value suggests

that, combined with elasto-visco-plastic bond coat and elasto-viscous TGO behaviours, it could generate creep and plastic strains close to the BC-TGO interface. These predicted shear stresses might be also employed for lifetime prediction, especially to understand damage evolution at high temperatures.

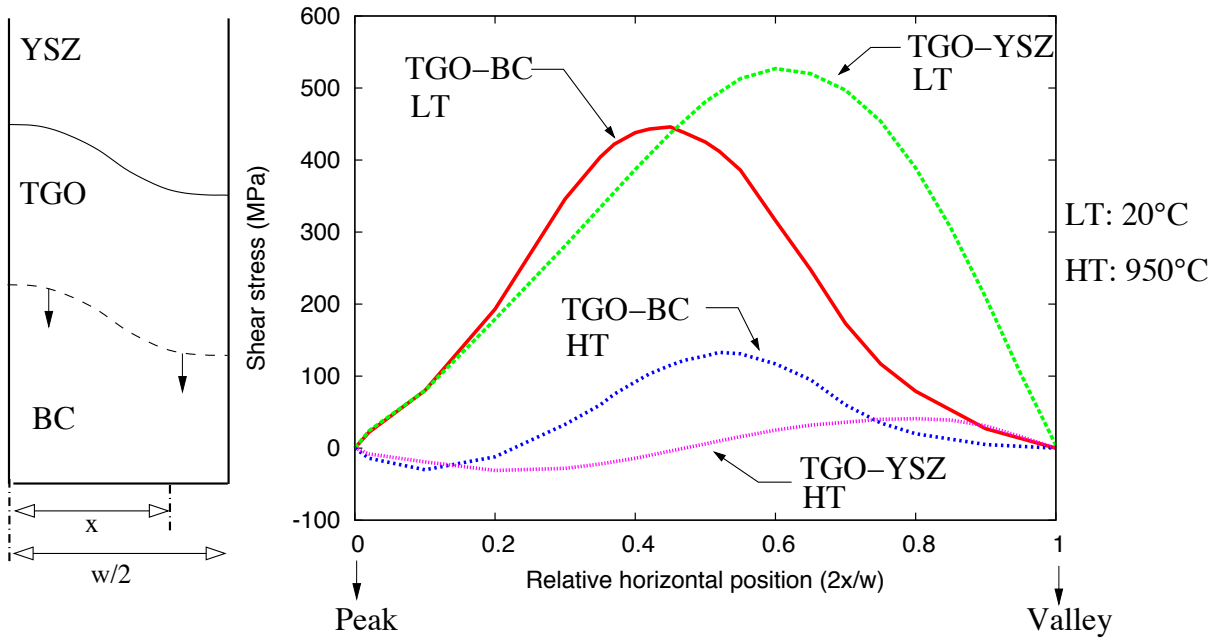

Figure III.12 : Shear stress component, σ_{tt}, at the TGO-YSZ and TGO-BC interfaces at 20°C (LT) and 950°C (HT) after 200 day-long thermal cycles at 950°C.

III.3.5 Bond coat accumulated creep and plastic strains

The bond coat is a layer with several functionalities: from a chemical point of view, it constitutes a reservoir of aluminium cations, necessary to protect the substrate. From a mechanical point of view, bond coat guarantees the good adherence properties between the top coat and the substrate. Owing to its creep and plastic behaviour, it also relaxes stresses associated with the oxide growth and the cyclic thermal loading as previously detailed in Section III.3.1. This point is often mentioned in the literature (Evans et al., 2001) but the following results are going to give more information on the key role of the bond coat creep and plastic behaviour in relaxing the stresses close to the BC-TGO interface. The accumulated irreversible strain, ε^i_{acc}, is defined using the irreversible strain rate, $\dot{\varepsilon}^i$, for the creep and plastic strains and formulated as:

$$\dot{\varepsilon}^i = \left(\frac{2}{3} \underset{\sim}{\dot{\varepsilon}}^i : \underset{\sim}{\dot{\varepsilon}}^i \right)^{\frac{1}{2}} \text{ with } i = \text{creep or plastic}, \tag{III.12}$$

where $\underset{\sim}{\varepsilon}^i$ is the irreversible strain tensor. The plastic and creep strain rate tensors are distinguished and noted $\underset{\sim}{\dot{\varepsilon}}^p$ and $\underset{\sim}{\dot{\varepsilon}}^c$, respectively.

The predicted bond coat accumulated creep (ε^c_{acc}) and plastic (ε^p_{acc}) strains close to the BC-TGO interface are shown in the Fig. III.13 after 10, 100 and 200 day-long thermal cycles at 950°C. The creep and plastic accumulated strains occur in the valley zones during thermal loading due to the high stresses generated by the oxide growth strains and thermal

expansion. A few microns thick long zone of bond coat is affected and follows the oxidation front displacement.

The maximal accumulated plastic strain values are at the same order of magnitude than the accumulated creep strain (around 70%) and the plastic/creep strain fields are similar, see Fig. III.13. Their spatial distributions increase with the number of cycle and oxidation time. After 200 days, accumulated creep strain decreases from 69% close to the TGO-BC interface, relaxing the stress generated by the alumina growth strain, to 1.5% where the bond coat only relaxes its relative thermal expansion with respect to the substrate. The need for the TBC system to have a so large bond coat thickness (90 μm) is not due to mechanical but to chemical reasons: the high level of aluminium provides a sufficient reservoir of scale-forming aluminium over a long period of time without depleting the substrate alloy.

These results are in good agreement with those obtain by Chen *et al.* (1998) for the equivalent plastic strain in the bond coat after cooling (around 2% for 1 cycle) and with the numerical investigation performed by Karlsson and Evans (Karlsson and Evans, 2001). For these authors, accumulated plastic strain in the bond coat after 12 cycles has been determined for different values of the bond coat's Yield strength. Also, ε^p_{acc} was found to approx 8% in the valley zone.

For a given fixed FE located in the valley zone close to the BC-TGO interface, see point B in Figs. III.13 and III.14(b), accumulated plastic and creep strains are presented as a function of exposure time, Fig. III.14(a). As expected and previously shown, accumulated creep and plastic strains have similar evolutions. A close-up view done for a cycle shows that in detail their evolutions are different: the accumulated plastic strain only increases by step due to thermal cycling and the accumulated creep strain increases due to the combination of the oxide growth and thermal cycling. The homogenisation approach used to model the material at the TGO-BC interface explains the low accumulated plastic or creep strains increase when the FE belongs to the transition zone.

The predicted results previously presented are in agreement with those obtained by He (He et al., 2002), which focused only on plastic strain evolution in the bond coat as a consequence of the stresses. Plastic strain is not developed during TGO growth at high temperatures as the study was limited to the plastic strain. The present analysis is able to differentiate the plastic and creep strains which allows to understand the effects of the oxide growth strains at high temperatures.

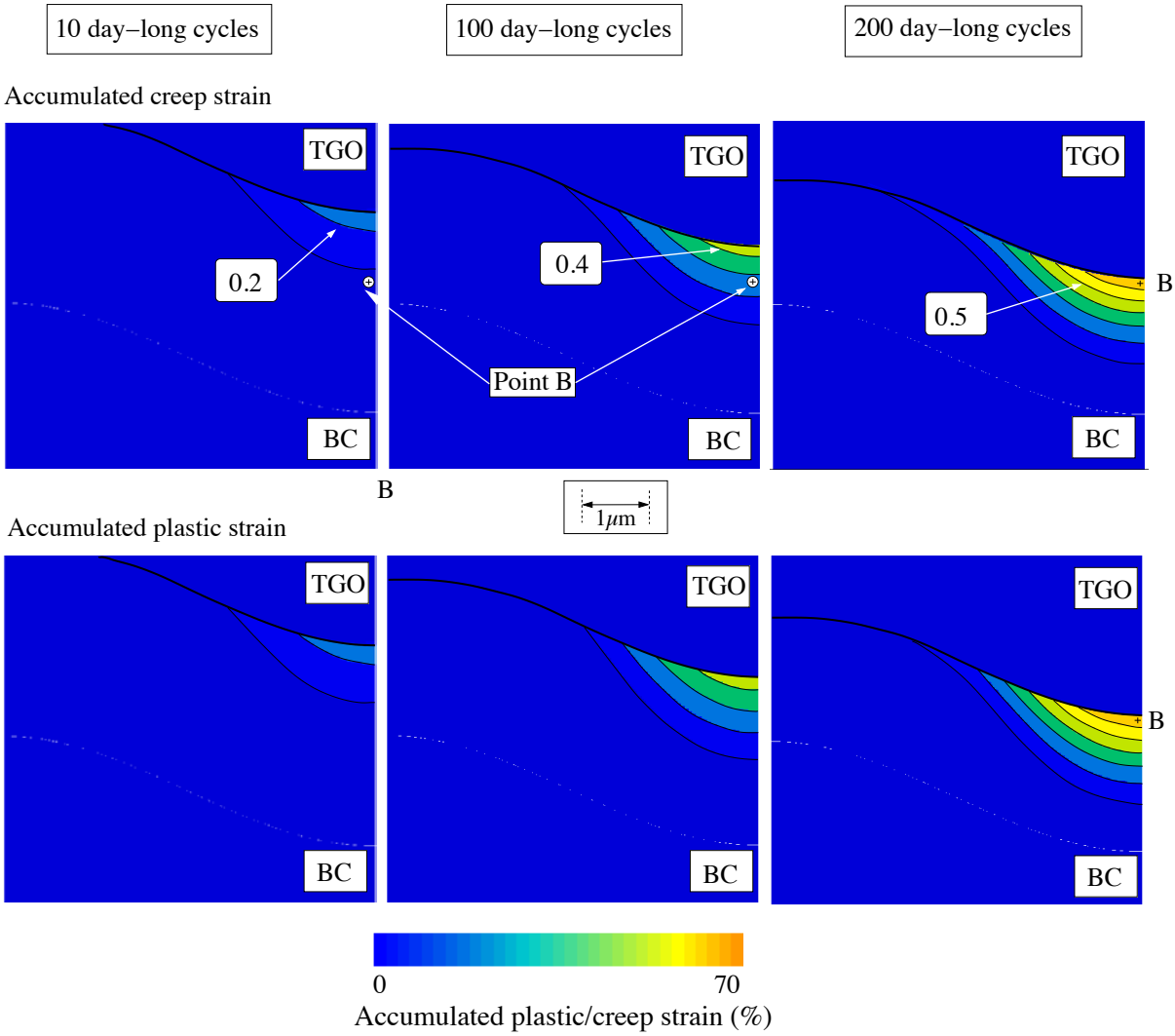

Figure III.13 : Accumulated creep, ε^c_{acc}, and plastic, ε^p_{acc}, strains in the bond coat after 10, 100 and 200 day-long thermal cycles at 950°C.

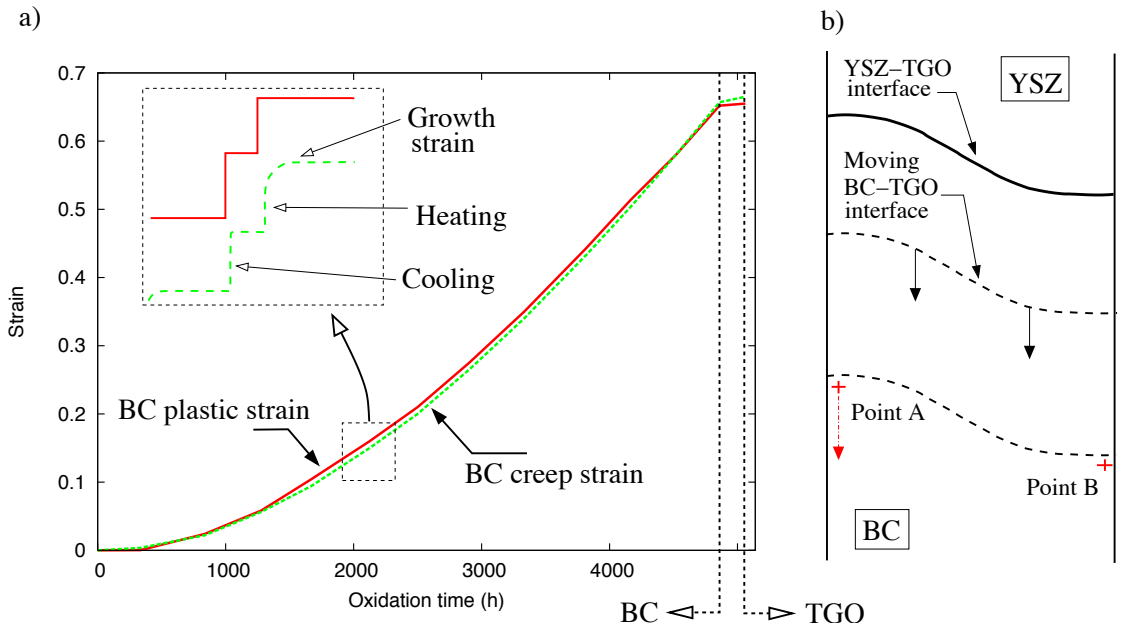

Figure III.14 : For a given FE, point B, which is found initially in the bond coat, and then transforming in oxide, (a) the accumulated creep ε^c_{acc} and plastic ε^p_{acc} strains generated by the oxide front displacement and the thermal cycling, (b) a drawing showing the moving oxide front and the spatial position of the chosen FE (point B).

III.4 Parametric study on stress and strain fields

To improve our knowledge of EB-PVD TBC system behaviour and to predict their lifetime, a parametric study of the influence of material parameters is carried out. In Section III.3.1 a preliminary investigation discussing the influence of the TGO and bond coat creep and plastic behaviour on the in-plane stress fields, has been performed. To go further in this analysis, we now investigate the influence of: (i) the mechanical behaviour of each TBC constituent, (ii) the TGO roughness and (iii) the thermal loading on local stress and strain fields close to the oxide interfaces.

III.4.1 Influence of TBC constituents material parameters

III.4.1.1 Effect of bond coat parameters

Bond coat mechanical functionality has been mentioned previously through a preliminary analysis dealing with the creep and plastic strains role on relaxing stresses. In more detail and in differentiating the bond coat elastic, creep/plastic behaviour, analyses of normal tractions and in-plane stresses close to the TGO are investigated. The TGO is modelled as an elasto-viscous material, see Section II.3.1. Table III.2 summarises the different mechanical behaviour combinations used in this part of the parametric study. In all the simulations carried out in this study, the thermal loading contain slow heat up and cool down period (40 min each) and 200-day long thermal cycles at 950°C.

Table III.2 : Different combinations of the bond coat mechanical behaviour model.

Case	**BC**	**TGO**	**YSZ**
n°1	Elasto-visco-plastic (*evp*)	Elasto-viscous	Iso-transverse elastic
n°2	Visco-elastic (*ev*)	Elasto-viscous	Iso-transverse elastic
n°3	Elastic (*e*)	Elasto-viscous	Iso-transverse elastic

a) Influence of BC parameters on the normal traction at the TGO-BC interface

The objective is to analyse the influence of the bond coat creep and plastic behaviour on the normal tractions along the TGO-BC interface at high (950°C) and low (20°C) temperatures. The results are summarised in Fig. III.15.

At high temperatures, normal traction distributions along the internal oxide interface are almost zero and identical for the Cases n°1 and 2 (*evp* and *ev* bond coat). When bond coat is modelled as an elastic material, high normal traction appears along the TGO-BC interface, from -100 MPa in the peak zone to 200 MPa in the valley zone. As expected, only the creep component in the bond coat mechanical behaviour the relaxes stresses due to growth strains at high temperatures.

At room temperature, normal tractions are lower for an elastic bond coat (Case n°3) than an *evp* or an *ev* bond coat (Cases n°1 and 2). This non-expected result could be explained by the fact that even if the normal tractions increase more when the temperature decreases for

an elastic bond coat (around 530 MPa), at ambient and high temperatures they have opposite distributions. Normal traction at peak temperature (-100 MPa) decreases the normal traction at ambient (430 MPa). Close to the valley zone ($2x/w = 1$), where creep or plastic strains develop in the bond coat, the predicted normal tractions for an *evp* or a *ev* bond coat are different (-310 MPa and -470 MPa). It points out the combined role of the bond coat creep and plastic deformation in stress relaxation during cooling.

Busso and Qian (2006) have investigated the effects of the bond coat properties on normal tractions along the TGO interfaces at 20°C but do not point out the specific role of the bond coat creep behaviour in valley zones. More recently, this point has been studied in more details for different bond coat compositions: $(Ni, Pt)Al$ and $NiCoCrAlY$ (Busso et al., 2008). The conclusions are similar for the normal traction distribution at low temperature.

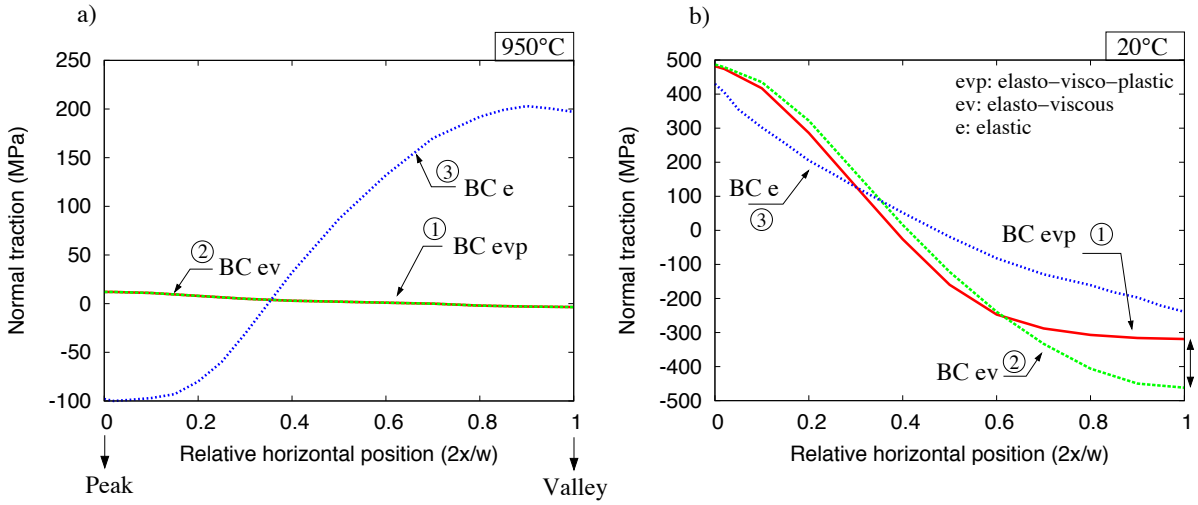

Figure III.15 : Normal tractions at the TGO-BC interface at (a) 950°C and (b) 20°C after 200 days of cyclic thermal loading at 950°C as a function of the relative horizontal position ($2x/w$). Three different combinations of bond coat mechanical behaviour have been tested, Case n°1: elasto-visco-plastic (*evp*), n°2 elasto-viscous (*ev*) and n°3 elastic (*e*). The TGO is modelled as an elasto-viscous material.

b) Influence of the BC parameter on the in-plane stress at high temperatures

Figure III.16 shows the time-evolution at peak temperature (950°C) of the in-plane stresses generated by the oxide growth strains σ_{11}^{ox} in a given FE which belongs initially to the bond coat and is crossed over by the internal oxidation front. The in-plane stress evolutions are similar for an *ev* and *evp* bond coat, showing that plastic deformation is not activated at high temperatures. If the bond coat is modelled as an elastic material (Case n°3), when the element belongs to the bond coat, the in-plane stress increases from 0 to 380 MPa due to the thermal expansion mismatch and then slowly increases, from 380 to 440 MPa due to oxide growth. The stress, generated by both thermal loading and oxide growth strains is not relaxed by the bond coat creep behaviour as it is observed when the chosen bond coat mechanical behaviour is *evp* or *ev*.

When the FE is in the transition zone, the maximal compressive stress is identical for all the cases (760 MPa). Then, the in-plane stress follows the same evolution than for an *evp* bond coat (Case n°1) because the element belongs to the TGO and is not affected by the bond coat behaviour model. Nevertheless, the final compressive in-plane stress value is

greater for an elastic bond coat than for an *evp* or *ev* bond coat. In conclusion, bond coat creep behaviour relaxes stresses at high temperatures when the oxide growth strains generate in-plane stresses and no plastic strains are observed.

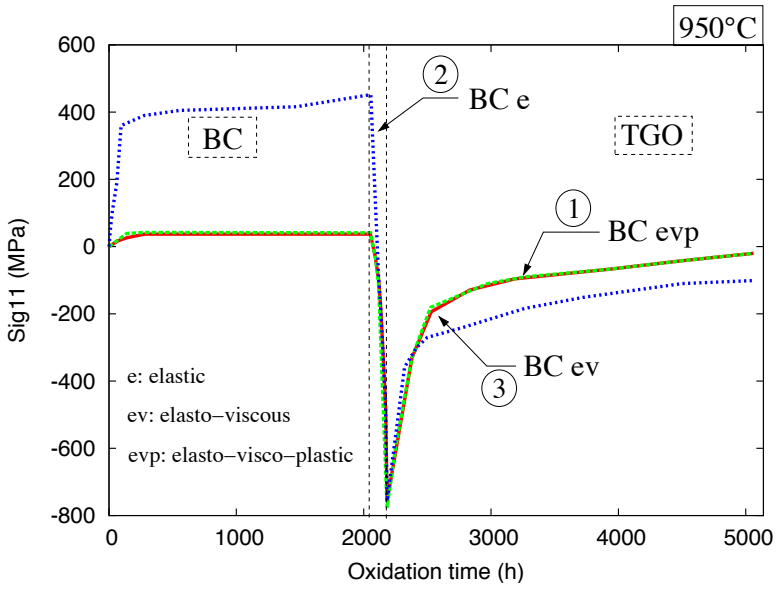

Figure III.16 : Evolution of the in-plane stress σ_{11} at 950°C, in a given element which belongs initially to the bond coat and is the crossed over by the oxidation front. Three different combinations of the bond coat mechanical behaviour are tested. The TGO is modelled as an elasto-viscous material.

III.4.1.2 Effect of TGO behaviour

As previously done for the bond coat, the influence of the TGO creep behaviour is investigated here, especially on the normal traction along the BC-TGO interface after cooling and on the in-plane stresses generated at high temperatures due to the oxide growth strains. The most complete TGO behaviour model, the elasto-viscous Case n°1 is compared to an elastic TGO, Case °4. In the simulations to be shown next, the bond coat is modelled as an elasto-visco-plastic material, see Table III.3.

Table III.3 : Different combinations of the TGO mechanical behaviour model.

Case	BC	TGO	YSZ
n°1	Elasto-visco-plastic	Elasto-viscous (*ev*)	Iso-transverse elastic
n°4	Elasto-visco-plastic	Elastic (*ev*)	Iso-transverse elastic

a) Influence of the TGO parameters on the normal traction

Figure III.17 shows the normal tractions along the TGO-BC interface at 20°C for two different combinations of the TGO mechanical behaviour. The spatial distribution of the normal

tractions are similar and the results show that, as expected, normal tractions are higher in the peak zone (638 MPa for an elastic TGO) and normal traction is higher in the valley zone (-376 MPa for an elastic TGO).

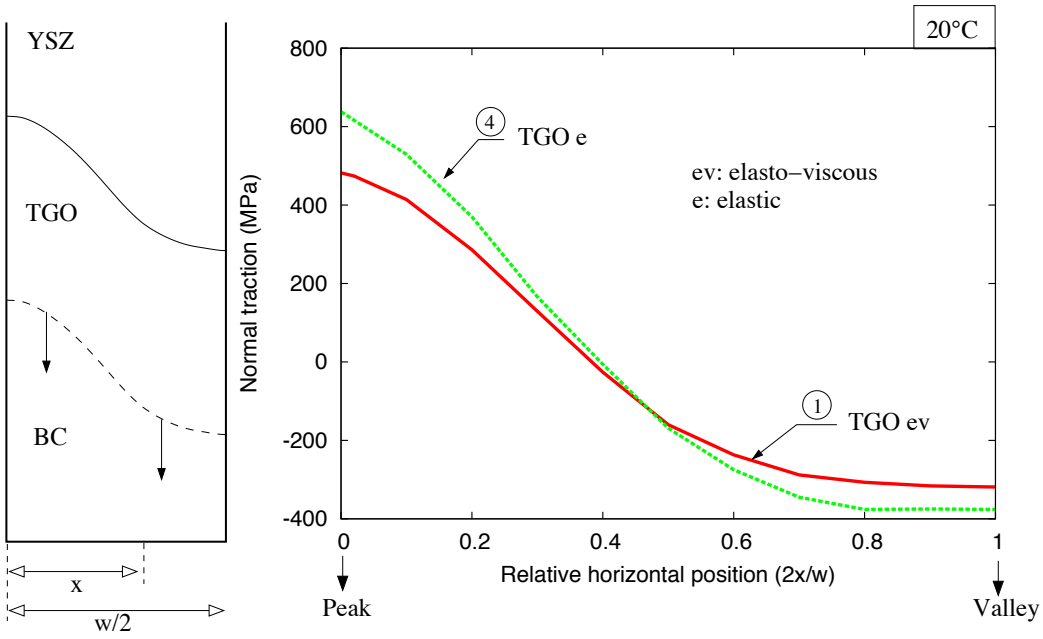

Figure III.17 : Normal traction at 20°C along the TGO-BC interface as a function of the relative horizontal position along the interface. Two different combinations of the TGO mechanical behaviour are tested. Case n°1: elasto-viscous, n°4: elastic. In both cases, the bond coat is modelled as an elasto-visco-plastic material.

b) Influence of the TGO parameters on the in-plane stress at high temperatures

Figure III.18 shows the time-evolution at peak temperature (950°C) of the in-plane stresses generated by the oxide growth strains σ_{11}^{ox} in a given FE which belongs initially to the bond coat and is crossed over by the internal oxidation front. At the peak temperatures, in-plane stress time-evolution is mainly different. When the FE belongs to the bond coat, in-plane stresses are identical. When the oxide front goes through the FE, in-plane compressive stress increases from 0 to 7 GPa. This point also illustrates the influence of the TGO creep behaviour on stress relaxation.

The parameters defining the TGO creep behaviour influence mainly the stress fields at high and low temperatures. Unfortunately, these parameters are difficult to obtain experimentally and do not allow to have an accurate prediction of the stress fields. The TGO creep influence has been investigated in detail by Schwarzer (Schwarzer et al., 2004), for an APS TBC system. That study shows the crucial influence of the oxide creep behaviour on the stress fields at high temperatures, up to 1100°C.

III.4.1.3 Effect of YSZ behaviour

The typical columnar microstructure of the EB-PVD YSZ top coat has already been investigated by image-processing analysis of SEM micrograph in Section II.2.1.3. It shows that the top coat microstructure is non homogeneous. Close to the TGO, external porosity

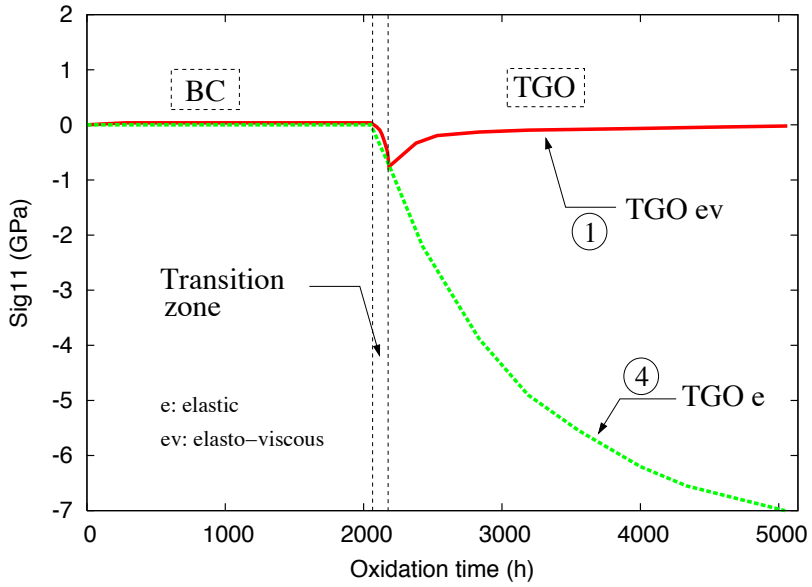

Figure III.18 : Evolution of in-plane stress σ_{11} in a given FE belongs initially to the bond coat and crossed by the oxidation front at 950°C. Two different combinations of the TGO mechanical behaviour (Cases n°1 and 4) are tested. The bond coat is modelled as an elasto-visco-plastic material.

between the columns is low ($\rho_e < 5\%$) and columns are non vertical. The top coat layer has been modelled as a transversaly isotropic material. The ratio between the in-plane and out-of-plane Young's moduli is function of the external porosity, see Section II.3.1.3. Here, the effects of sintering and the YSZ anisotropy on the stresses are investigated. To that purpose, in addition to the behaviour considered thus far, the predicted stress fields are compared for three different models of the EB-PVD top coat mechanical behaviour, presented in Table III.4. The new YSZ materials are modelled as: Case n°5, a fully dense (no porosity, no

Table III.4 : Different combination of YSZ mechanical behaviour model.

Case	BC	TGO	YSZ
n°1	Elasto-visco-plastic	Elasto-viscous	Iso-transverse (no sintering)
n°5	Elasto-visco-plastic	Elasto-viscous	Isotropic (200 GPa)
n°6	Elasto-visco-plastic	Elasto-viscous	Iso-transverse (sintering)

sintering) ceramic with isotropic elastic properties (200 GPa) and Case n°6 a transversaly isotropic ceramic submitted to sintering effects. The ratio E_1/E_2 evolves with oxidation time from 0.3 to 0.4, for the respective values of the external porosity, ρ_e, 17% and 10% after 0 h and 1000 h at 950°C.

When compared with the results given in Section III.3 for a transversaly isotropic material, the top coat mechanical behaviour has no effect on the normal tractions and shear stresses at the TGO-BC interface at 20°C. At the YSZ-TGO interface, normal tractions have similar evolution but stresses are higher for an isotropic (Case n°5) and lower for an isotropic transverse porous top cot ceramic affected by sintering effect (Case n°6) than the reference one

(Case n°1), Fig. III.19. This qualitative conclusion was expected because in-plane Young's modulus does not mainly influence normal tractions. Sintering effects increase of 12% and 15% the normal traction in peak and valley zones at the TGO-YSZ interface, see Fig. III.19(a).

This point has been study by Busso (Busso and Qian, 2006, Busso et al., 2008). If the spatial distribution of the normal traction at the YSZ-TGO interface is similar to the present approach, the quantitative values are different, principally because we have chosen to take into account the low external porosity of the EB-PVD YSZ layer close to the oxide.

Predicted results show that the combined effects of YSZ sintering and anisotropy have a considerable influence on the shear-stress at the outward oxide interface, as it is shown in Fig. III.19(b). In comparison with the Case n°1, the maximal shear stress increases by 30% in the Case n°5 (isotropic) and decreases of 53% in the Case n°6 (porous material submitted to sintering effect).

In conclusion, the model taking into account the top coat sintering effect is a necessity in regard of its influence on the local shear-stress occurring at the YSZ-TGO interface. Nevertheless, sintering does not influence the local stresses at the other TGO interface. Keep in mind that from a macroscopic point of view, sintering effects should be take into account to predict the stored elastic strain energy per unit area.

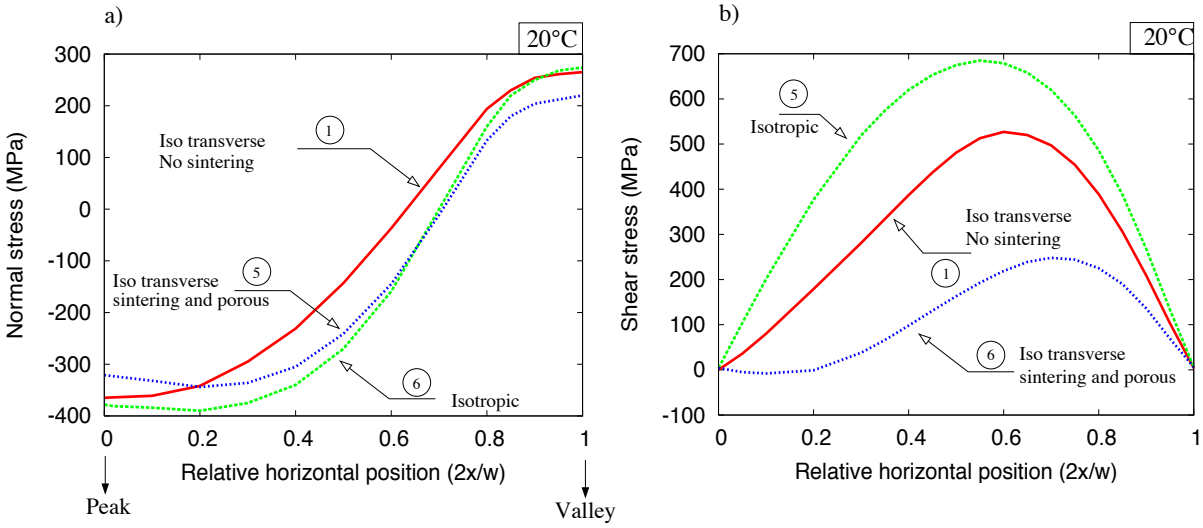

Figure III.19 : (a) Normal tractions and (b) shear-stresses at the TGO-YSZ interface as a function of the relative horizontal position along the interface. Three different combinations of the top coat mechanical behaviour have been tested. Case n°1: transversaly isotropic with no sintering effect, n°5: isotropic (Young's modulus=200 GPa), n°6: transversaly isotropic and porous material submitted to sintering phenomenon ($E_1 = [60-75]$ GPa and $E_2 = 200$ GPa).

Table III.5 summarises the influence of the mechanical behaviour of each TBC constituent. To study the effect of the TGO and bond coat mechanical behaviour influence, the normal traction, σ_{nn}, and the shear-stress, σ_{tt}, are extracted at the TGO-BC interface. Because the top coat ceramic has no influence on stress field at the TGO-BC interface, the values are given at the TGO-YSZ interface and noted by a star in the table, Cases n°5 and 6.

III.4.2 Influence of the TGO morphology

According to the observations presented in Section II.4.1.1 and the literature, TGO morphology evolves with exposure time. Previous investigations have demonstrated a strong

Table III.5 : Influence of the mechanical behaviour of each TBC constituent on the maximal normal traction, σ_{nn}, shear-stress, σ_{tt} at low temperatures and the maximal in-plane stress at peak temperature in the transition zone σ_{11}^{ox} (MPa). In the Cases n°5 and 6, noted by a star, the local stresses have been determined at the TGO-YSZ interface. The Case n°1 is taken as the reference to determine the given comparative values.

Case	**BC**	**TGO**	**YSZ**	σ_{nn} peak	σ_{nn} valley	σ_{tt}max	σ_{11}
n°1	evp	ev	Iso-trans. elas.	482	-319	527	760
n°2	ev	ev	Iso-trans. elas.	487 (+1%)	-462 (+45%)	544 (+3%)	765
n°3	e	ev	Iso-trans. elas.	430 (-11%)	-240 (-25%)	588 (+12%)	772
n°4	evp	e	Iso-trans. elas.	638 (+32%)	-376 (+18%)	7152	7121
n°5*	evp	ev	Iso.(200 GPa)	-378 (+15%)	274 (+??%)	685 (+30%)	-
n°6*	evp	ev	Iso-trans. sint.	-321 (+12%)	220 (+??%)	248 (+53%)	-

dependency of the TGO roughness on the out-of-plane stress field (Caliez et al., 2002). The TGO morphology influence on the in-plane stress field has also been investigated in Section III.3.1. The influence of the internal oxide roughness and its time-evolution on the normal traction along the moving TGO-BC interface is presented for two different models of the oxide morphology: a constant and a time-dependent TGO-BC interface roughness.

III.4.2.1 Time-independent TGO-BC interface roughness

In a preliminary approach, we have considered that the TGO roughness is unchanged with exposure time and that it has been characterised by two sinusoidal parameters, the wavelenght, w, and the amplitude, a. In the simulations to be discussed next, the wavelength is kept constant ($w = 11.72$ μm) and the amplitude ranges from 0.216 to 1.296 μm. Figure III.20 shows the normal traction along the relative horizontal position at the TGO-BC interface for different values of the amplitude on the wavelength ratio ($r = a/w$). Due to the boundary conditions and the geometry of the problem, normal traction is equal to zero if the interface is perfectly flat. Normal tractions increase with the roughness as expected, see Fig. III.20(a). For high values of the ratio r, the normal tractions at the TGO-BC interface reaches a constant value.

The maximum normal tractions after the 200 day-long thermal cycles at 950°, in the peak zone at the TGO-BC interface, noted point A' in Fig. III.20, increases linearly with the roughness for low values of the oxide roughness ($r < 0.07$), see Fig. III.20(b). It ranges from 0 to 482 MPa when the amplitude varies from 0 to 0.864 μm. For high oxide roughnesses ($r > 0.07$), normal traction reaches a maximal value, as previously observed.

The bond coat regions where accumulated plastic and creep strains develop, are unchanged by oxide interface roughness. Nevertheless, the maximal value of accumulated creep/plastic strains in the valley zone (point B in Fig. III.20) is strongly influenced by the TGO roughness. Actually, ε_{acc}^{p} and ε_{acc}^{c} increase with roughness. The results are presented in Table III.6.

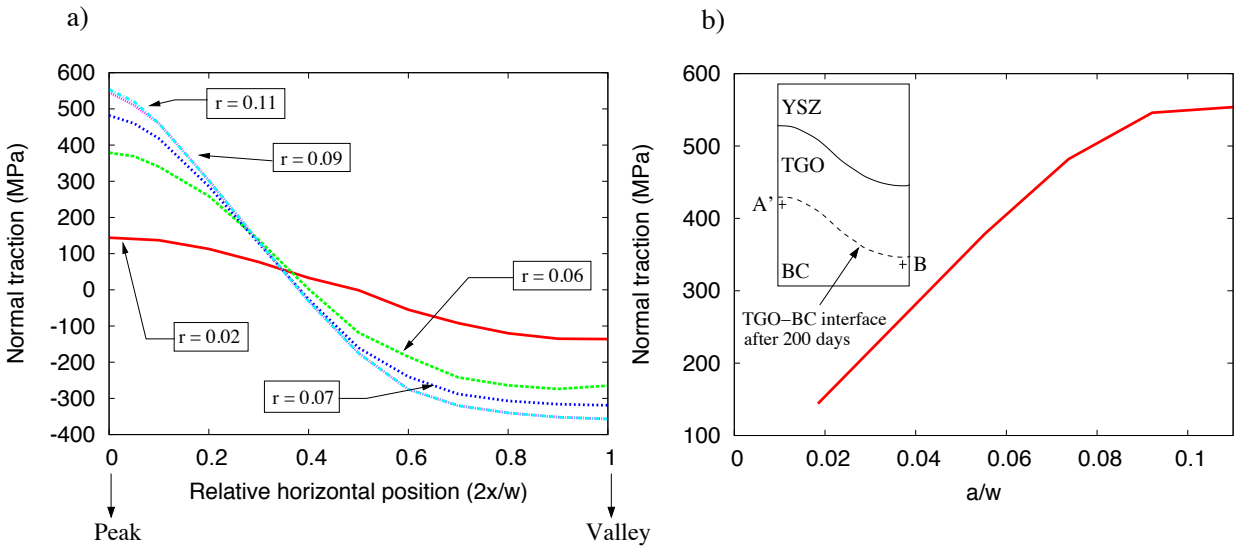

Figure III.20 : Normal traction at (a) the BC-TGO interface and (b) in the peak zone (point A') as a function of the amplitude on the wavelength ratio, $r = a/w$, at 20°C after 200 day-long thermal cycles at 950°C.

Table III.6 : Maximum accumulated creep and plastic strains, ε^c_{acc} and ε^p_{acc}, in the valley zone (point B, see Fig. III.20) as a function of the TGO-BC interface roughness.

Roughness ($r = a/w$)	ε^c_{acc}	ε^p_{acc}
0.02	0.02	0.03
0.06	0.45	0.46
0.07	0.69	0.70
0.09	0.85	0.89
0.11	0.97	1.07

III.4.2.2 Time-dependent TGO interface roughness

In order to simulate the TGO-BC interface roughness evolution, as it occurs during oxidation, the numerical tool implemented to simulate the oxide growth has been improved. Using the standard criterion previously presented to define the TGO roughness ($R_l = L/L_0$ is the ratio between the oxide mean profile and window length), image-processing analysis gives an initial R_l^{ini} and final R_l^{fin} interface roughness after 200 days of exposure time, 1.036 and 1.054 respectively, see Section II.4.

The objective is to follow the time-evolution of the normal tractions at the moving TGO-BC interface when the TGO-BC interface roughness increases. Oxide roughness evolution has been implemented and is assumed to increase as a linear function of the vertical position (direction X_2). The representative FE mesh is shown in Fig. III.21(a). The final interface roughnesses R_l^{fin} are equal for a time-independent and time-dependent TGO-BC interface morphology, namely 1.054.

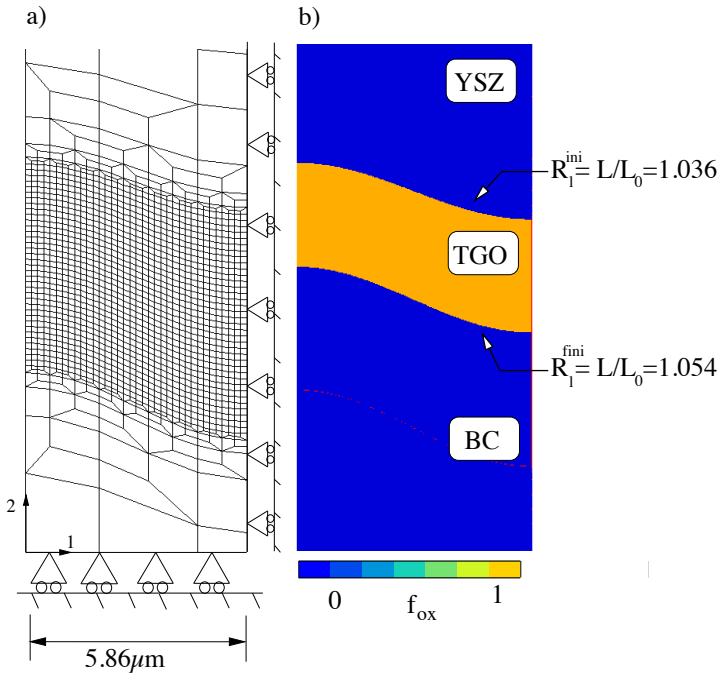

Figure III.21 : (a) Finite element mesh simulating a sinusoidal oxide interface morphology of whose roughness increases with exposure time and (b) the oxide volume fraction f_{ox}. The YSZ-TGO and the final BC-TGO interface roughnesses defined by $R_l = L/L_0$ take the values of 1.036 and 1.054.

In a similar way to that previously used for a constant TGO interface roughness, Fig. III.11, time-evolution of the maximal normal tractions in the peak zone of the moving TGO-BC interface has been predicted in point A, shown in Fig. III.22. It can be seen that the magnitude of σ_{nn} decreases by 5% when the oxide roughness increase is modelled. The convergence of the two curves was expected at the end of the thermal loading when the roughnesses are identical. It concludes on the importance of modelling the time-evolution of the TGO roughness and not only its final value. In the case of $NiCoCrAlY$ bond coats, no rumpling phenomenon occurs, roughness evolution is not substantial and the local stress fields are not affected. The same numerical analysis performed on a rough $(Pt, Ni)Al$ TBC system might give interesting results.

III.4.3 Influence of thermal loading

As for the TBC constituents mechanical behaviour and the TGO morphology, the influence of in-service thermal loading on the stress/strain fields is investigated in this section. For simplicity bond coat chemical composition or YSZ top coat microstructure are assumed to remain unchanged by temperature. Here, a purely mechanical approach is investigated. The influence of four parameters is discussed: the top coat deposition process temperature T_{dep}, the in-service peak temperature (between 950 to 1150°C), the cyclic thermal loading and the temperature gradient during heating up and cooling down.

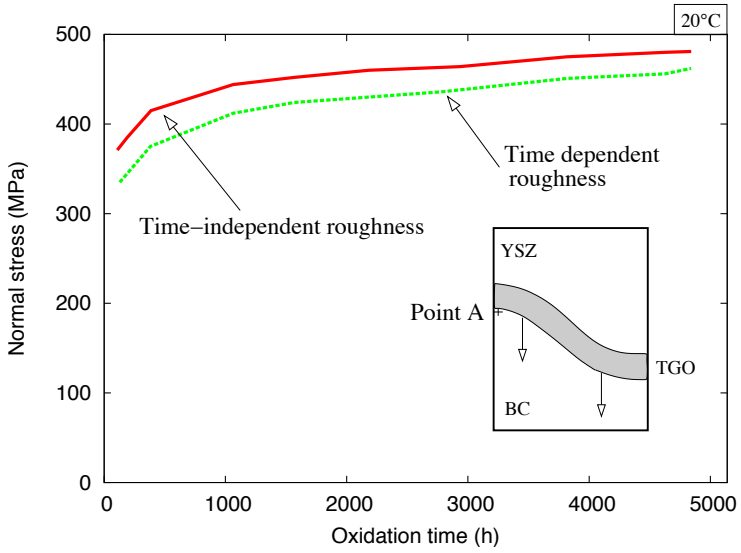

Figure III.22 : Comparison between the normal tractions in the peak region at the moving TGO-BC interface, point A, at ambient temperature (20°C) as a function of oxidation time after 200 day-long thermal cycles at 950°C for a time-independent and a time-dependent TGO-BC interface roughness.

III.4.3.1 Effect of the top coat deposition process temperature

According to the literature, the deposition temperature, T_{dep}, for an EB-PVD top coat could reach 1100°C (Schulz and Schmücker, 2000). If the effects of EB-PVD process on the top coat morphology have been studied experimentally (Kato et al., 2005), these investigations focused only on the effects for the top coat morphology and not on stresses resulting in TBC. This section deals with the influence of this initial condition on the macroscopic in-plane stresses inside each TBC constituent and locally, on the normal traction at both TGO interfaces.

To study the influence of T_{dep} on the macroscopic in-plane stresses, the TBC system is assumed to be flat. As previously presented in Section III.3.1, in-plane stresses occurring inside each TBC constituent are function of the relative temperature ΔTa between the EB-PVD deposition T_{dep} and the in-service temperature, T, as explained previously, see Eq. III.8. For $T_{dep} = 1100$°C, after 200 days, no in-plane stresses occur in the bond coat and TGO layer at high temperatures and the in-plane compressive stresses in the TGO and bond coat are 2.7 GPa and 0.2 GPa, respectively. In the top coat, σ_{11} ranges from -80 to -487 MPa before and after cooling, respectively. These values should be compared to the previous ones obtained for $T_{dep} = 400$°C. For the bond coat and the TGO, the values are similar, for the top coat, σ_{11} ranges from 280 MPa to -142 MPa, respectively after and before cooling. For $T_{dep} = 1100$°C, the ceramic layer is under compressive in-plane stresses at room temperature and the stored strain elastic energy per unit area is higher than that found with $T_{dep} = 400$°C. In conclusion, it is preferable to depose the top coat layer at low temperature to reduce the stored energy.

σ_{nn} and σ_{tt} at the BC-TGO and YSZ-TGO interfaces are not influenced by the deposition process temperature, due to the bond coat and TGO layers ability to relax after few hours the stresses due to the top coat deposition process. To illustrate this point, normal tractions in the peak zone (point A) at the moving TGO-BC interface at room temperature are determined as a function of the oxidation time for $T_{dep} = 400$°C and 1100°C, see Fig. III.23.

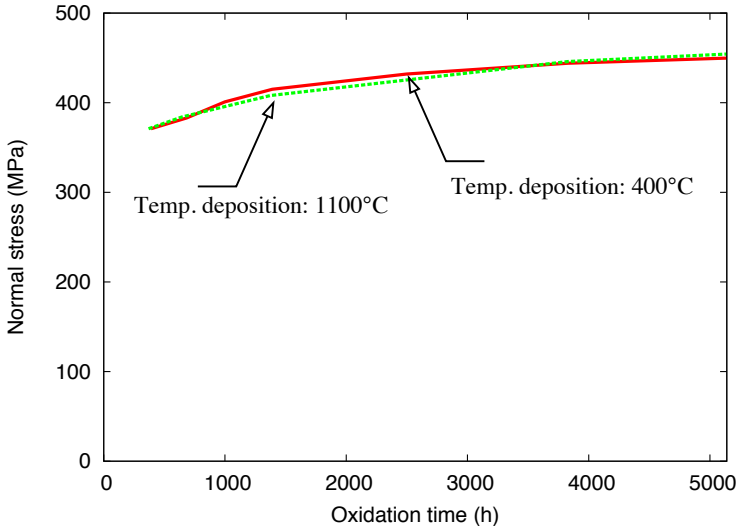

Figure III.23 : Comparison between the normal tractions at the moving TGO-BC interface in the peak zone, point 1 in Fig. III.22, at ambient temperature (20°C) as a function of the oxidation time after 200 day-long thermal cycles at 950°C for an EB-PVD deposition temperature of 400°C and 1100°C.

III.4.3.2 Effect of the in-service temperature

Using the same thermal loading (200 day-long cycles) but for different values of the maximum temperature (1050°C and 1150°C), two additional numerical simulations have been carried out. FE mesh and TBC constituents mechanical behaviours are identical with the previous simulations, only the oxidation kinetics are changed. The results of these simulations are compared to the reference one, simulating a 950°C in-service temperature, see Fig. III.24. When compared with the results given in Section III.3.3 for a low in-service temperature, $T = 950$°C, the results obtained are similar close to the valley regions, due to creep and plastic strains in the TGO and bond coat layers occurring in this part of the FE mesh. In the peak zone, the maximum normal traction increases with in-service temperature: 550 MPa and 605 MPa at 1050°C and 1150°C, respectively.

III.4.3.3 Effect of thermal gradient during cooling and heating transients

To study the influence on the bond coat and TGO creep and plastic strains of the TBC cooling and heating transients, the creep and plastic strains have been determined for thermal loadings comprise a fast and low heating up and cooling down (4 min and 40 min respectively) and cyclic thermal loading includes 1 day exposure at a peak temperature (950°C). For a fast heating up and cooling down, the bond coat ε^c_{acc} and ε^p_{acc} are 75% and 64% and 70% and 69% for a low heat up and cool down, as previously predicted in Section III.3.5.

III.4.3.4 Effect of thermal cycling

According to the previous results, thermal cycling does not play an important role in the normal traction time-evolution at the TGO interfaces, see Section III.3.3.1. Nevertheless, it has been demonstrated that cooling and heating during thermal cycling can induce creep and plastic strains in the bond coat. For two thermal loading simulations, with or without

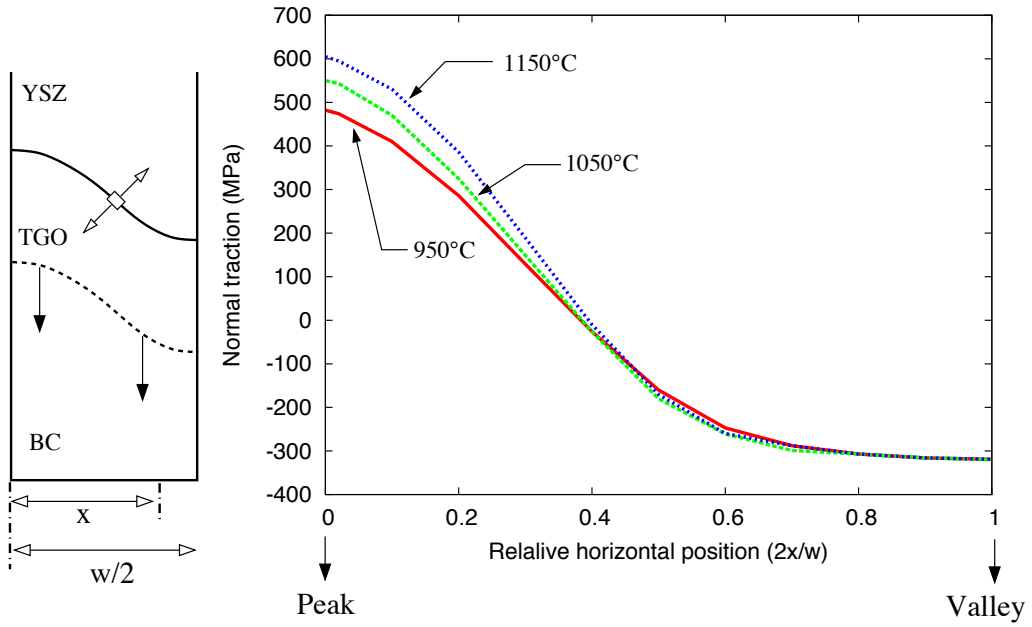

Figure III.24 : Comparison between the normal tractions along the TGO-BC interface at ambient temperature (20°C) after 200 day-long thermal cycles at 950°C, 1050°C and 1150°C.

thermal cycling, the accumulated creep strain fields as a function of the exposure time, are presented in Fig. III.25. The accumulated plastic strain field is not presented because no plastic deformation develops at high temperatures. Creep deformation is predominant for low stresses at high temperatures, inhibiting plastic strain.

The accumulated creep strains in the bond coat remain unchanged during isothermal loading. Also, ε^c_{acc} is greater between the peak and valley zones. Its maximal value is constant $\approx 4\%$. In comparison with the accumulated creep strain obtained for a cyclic thermal loading, the ε^c_{acc} field distribution and is very different, see Fig. III.25(b). ε^c_{acc} was concentrated in the valley regions and increased with exposure time to 70%. This study illustrated that the bond coat creep and plastic strains are not developed in the same area at high and low temperatures, as it might be the case for the damage.

III.4.4 Discussions

EB-PVD TBC system behaviour and their lifetime could be influenced by many parameters, from the bond coat chemical composition to the insulator top coat deposition temperature. At the same time, depending on the in-service thermo-mechanical loading, the mechanical behaviour of each TBC constituent can be affected. The present parametric study attempts to clarify the influence of each mechanical, morphological or thermal loading parameters. It does not take into account all the parameters (bond coat microstructure evolution, interdiffusion in the bond coat, etc...), but it identifies the parameters which are expected to influence locally the stress/strain fields close to the TGO and the in-plane stresses.

The parametric study results are summarised in Table III.7. It shows the influence of each parameter on the macroscopic in-plane stresses, σ^{ox}_{11} (at 950°C) and σ^{th}_{11} (at ambient) and on the local stress/strain fields at ambient temperature. From this table, it can be established that:

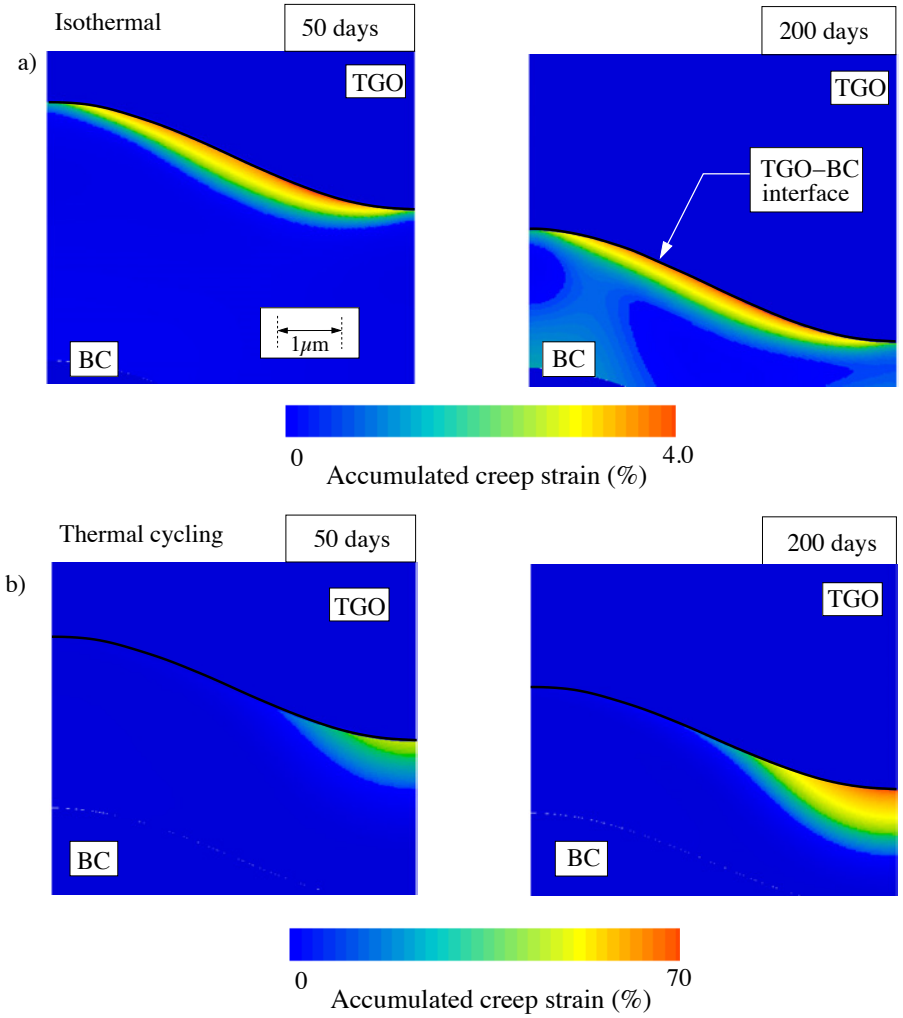

Figure III.25 : Accumulated creep strain ε^c_{acc} in the bond coat after 50 and 200 days of (a) isothermal and (b) cyclic thermal loading at 950°C.

- at high temperatures, in-plane stresses in the TGO are influenced by (i) TGO and bond coat mechanical behaviour (creep strain) and (ii) the in-service temperature,
- at room temperature, in-plane stresses in each TBC constituent are affected by (i) their own mechanical behaviour, as expected, (ii) the oxide roughness and (iii) the top coat deposition process. The latter only effects the compressive in-plane stresses at low temperature and hence the stored strain energy per unit area,
- local stress fields at the TGO-BC interface are mainly influenced by the oxide roughness,
- shear stresses at the YSZ-TGO interface are affected by the YSZ sintering. The latter does not affect the local stress/strain fields close to the TGO-BC interface,
- bond coat creep/plastic strains are function of the oxide roughness and the thermal loading (cycling),
- thermal cycling only influences the creep/plastic strains, and not on the stress fields,
- no plastic deformation are developed for isothermal loading at 950°C,
- the oxide roughness appears as the most critical parameter.

Table III.7 : Summary of the parametric study: σ_{11}^{ox}, in-plane stress at peak temperature in the TGO due to the growth strain, σ_{11}^{th}, in-plane stress due to thermal expansion at room temperature; σ_{nn} and σ_{tt}, normal traction and shear stress at both oxide interfaces at low temperature; $T_{dep.}$ and $T_{ser.}$, are the respective top coat deposition and in-service temperatures. The number of + defines the level of influence of a parameter.

	Mechanical behaviour			**TGO roughness**	**Thermal loading**		
	BC	**TGO**	**YSZ**	$r = a/w$	$T_{dep.}$ (°C)	$T_{ser.}$ (°C)	Cycl.
σ_{11}^{ox}	+	++	0	0	0	0	0
σ_{11}^{th}	+	++	+	++	++	+	0
TGO-BC							
σ_{nn}	+	+	0	+++	0	+	0
σ_{tt}	+	+	0	++	0	+	0
TGO-YSZ							
σ_{nn}	0	0	+	++	0	0	0
σ_{tt}	0	0	++	++	0	0	0
ε_{acc}^{c}, ε_{acc}^{p}	+	0	0	++	0	++	+++

III.5 Investigation of the relative importance of modelling a realistic TGO morphology

The previous numerical study, based on a simply 2D sinusoidal simulation of the TGO morphology, provided a relevant compromise between information on the general TBC system behaviour and CPU time. There, we assumed that an elementary 2D unit cell could be representative of the entire TBC system. Nevertheless, many heterogeneities have been observed along the TGO-BC interface (Section II.2.2) and can be critical regions where porosities or microcracks initiate and grow (Brumm and Grabke, 1993).

This section deals with a numerical simulation of the oxide morphology based on (i) a realistic 2D FE mesh obtained from a representative SEM micrograph and modelled using the Fourier decomposition presented in Section III.5 and (ii) a 3D sinusoidal FE mesh. In both cases, stress fields resulting of these simulations are compared to the preliminary 2D sinusoidal simulation performed in Section III.3.

In all the simulations carried out in this study, the thermal loading comprises a slow heat up and cool down (40 min each) and a 1 day exposure at a peak temperature (950°C). The FE size in the area prone to oxidation is the same as that used previously (0.05 μm). The top coat and bond coat layers have initial thickness of 45 and 25 μm. To compare the results, the TGO-BC interface roughness is assumed identical for all the profiles chosen to model the TGO morphology and to be time-independent.

III.5.1 2D realistic simulation of the TGO morphology

In this section, the stress/strain fields in TBC system close to the TGO layer is obtained for a 2D realistic simulation of the oxide morphology and will be compared with the results obtained for the 2D sinusoidal case. The FE mesh of the realistic oxide morphology is composed of 37,803 quadratic generalised plane strain elements with full integration (227,400 DOF).

III.5.1.1 Oxide growth model

In order to simulate the oxide front motion along a representative FE mesh, the numerical tool implemented to model the oxide growth in Section III.2.1.1 has been improved. Using the standard criterion previously presented to define the interface roughness, ($R_l = L/L_0$ is the ratio between the oxide mean profile and window length), image-processing analysis gives an oxide mean profile roughness of 1.052. Figure III.26 shows the simulation of the TGO growth along the 2D FE mesh.

III.5.1.2 Analysis of the stress/strain fields

a) In-plane stress fields

In-plane stress component, σ_{11}, has been evaluated at 950°C and 20°C, respectively in Figs. III.27(a) and (b). At high temperatures, around 1 GPa of compressive in-plane stresses are generated at the TGO-BC interface due to the growth strains associated with the bond coat oxidation, see Fig. III.27(a). At low temperatures, the oxide roughness associated with the thermal strain mismatch strongly influences the in-plane stress fields, as illustrated in Fig. III.27(b). Compressive in-plane stress ranges from 0.7 to 5.8 GPa and when compared with

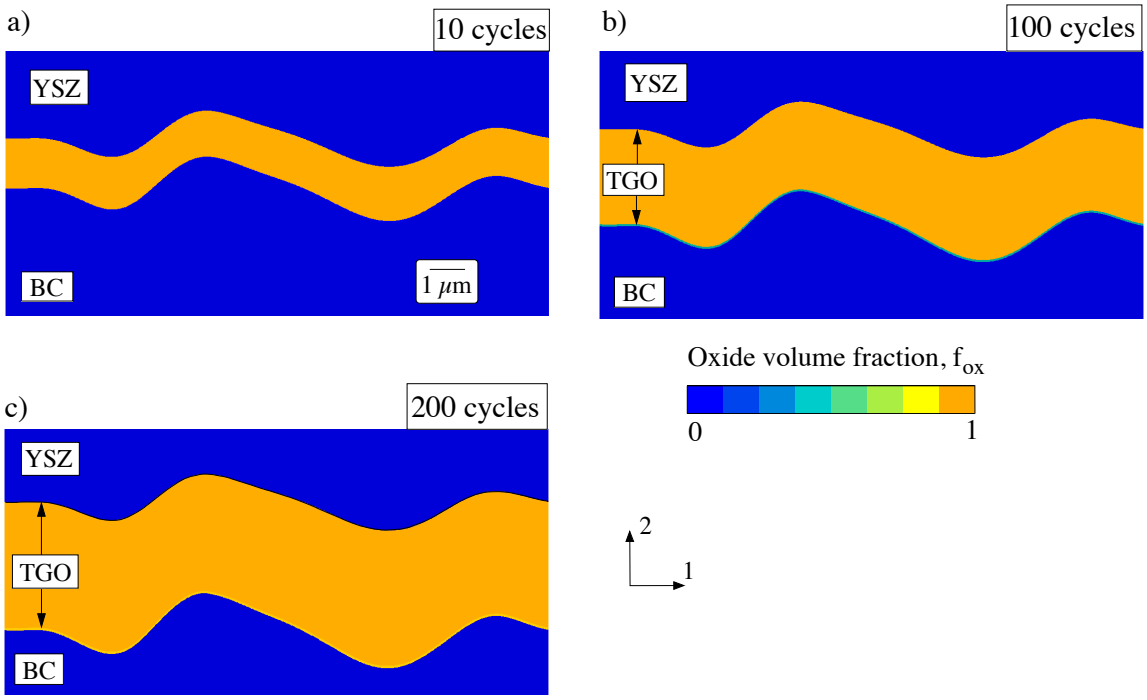

Figure III.26 : Oxide volume fraction f_{ox} at 950°C, after: (a) 10, (b) 100 and (c) 200 day-long cycles.

the results given in Section III.3.1 for a sinusoidal simulation, $\sigma_{11} = [1.8 - 4.5]$, the difference in the maximum in-plane stresses is 30%.

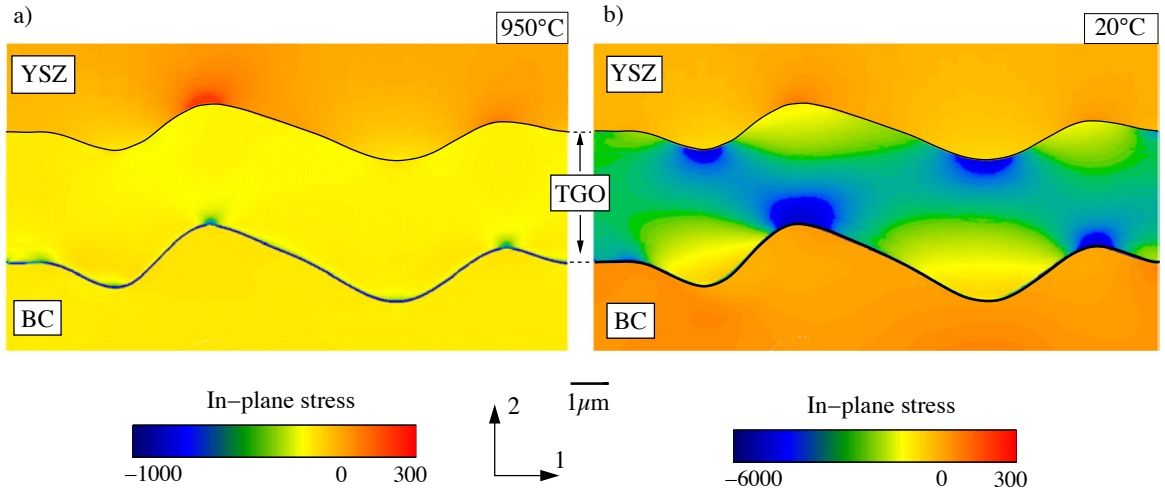

Figure III.27 : Gauss point value plot of the in-plane stress component σ_{11} at (a) 950°C and (b) 20°C after 200 day-long cycles at 950°C.

b) Out-of-plane stress fields

Figure III.28 shows the out-of-plane stress component σ_{22} (direction X_2) evaluated before and after cooling, respectively, at 950°C and 20°C. At high temperatures, it can be seen that the most highly stressed region is close to the TGO-BC interface, points n°2 and 4

in Fig. III.28(a). At room temperature peak zones at the TGO-YSZ interface are under compression (points 6 and 8) and valley zones are subject to tensile stresses (points 5 and 7), see Fig. III.28(b). The opposite stress distribution is observed at the TGO-BC interface, where peak (points 2 and 4) and valley zones (points 1 and 3) are respectively subject to tensile and compressive tractions. The high normal traction gradient close to the peak zone at the TGO-BC interface is still present in this simulation as it has been observed in Section III.3.3. Normal tractions along the TGO-BC interface range from -365 to 572 MPa. The result is 17% greater in the peak zone and 14% in the valley one when compared with the results found for a 2D sinusoidal case. Nevertheless, the present simulation based on the realistic description of the oxide morphology is four times more expensive in CPU time than the sinusoidal profile case.

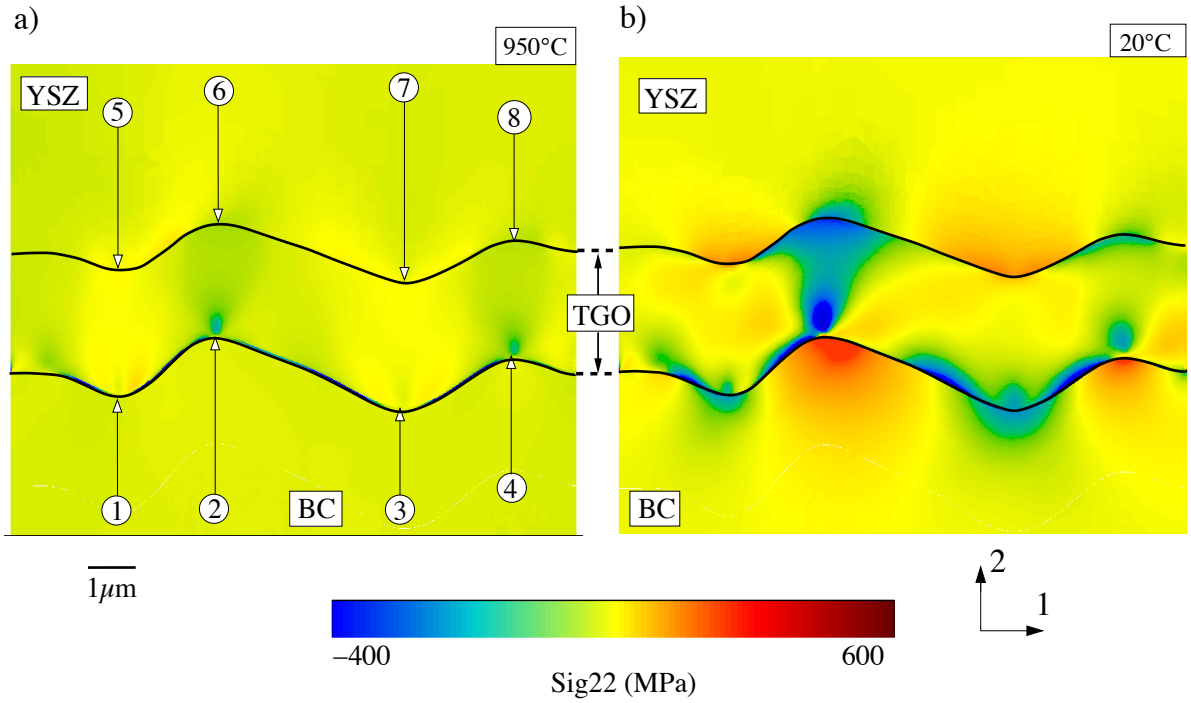

Figure III.28 : Gauss point value plots plot of the out-of-plane stress component σ_{22} at (a) 950°C and (b) 20°C after 200 day-long cycles at 950°C.

III.5.1.3 Accumulated creep and plastic strains

Accumulated creep and plastic strains have been predicted for a realistic representation of the TGO morphology. The predicted values of ε^c_{acc} and ε^p_{acc} are 90%. Nevertheless, the spatial distribution is different. In the sinusoidal case presented in Section III.3.5, accumulated creep and plastic strains only developed in the bond coat close to the valley region. Here, accumulated plastic/creep strains also occur between the valley and peak zones,

III.5.2 3D sinusoidal simulation of the TGO morphology

The 2D simulation of the oxide morphology previously reported in Section III.3, was based on plane-strain conditions. Indeed, due to its rigidity and thickness, the substrate imposes its own deformation to the other layers during mechanical and thermal loading. The in-plane

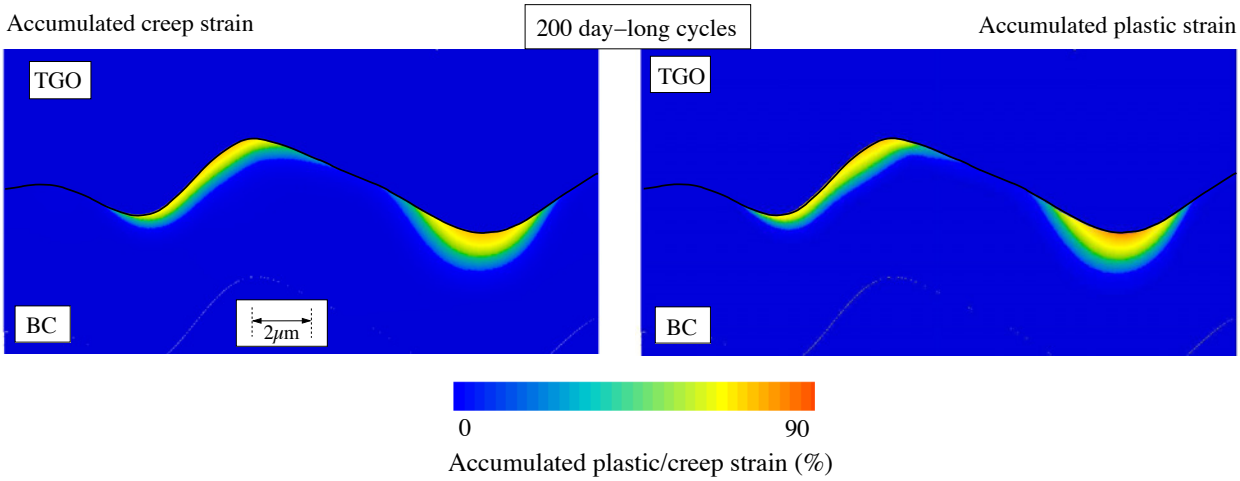

Figure III.29 : Accumulated creep, ε^c_{acc}, and plastic, ε^p_{acc}, strains of the bond coat after 200 days of cycling thermal loading at 950°C.

strain assumption implies that the 2D morphology of the oxide is projected in the direction X_3. Thus, it does not account for the roughness in the direction X_3. A numerical simulation based on a 3D simulation of the TGO morphology is performed in this final part and the results are compared to those obtained for the 2D sinusoidal case.

III.5.2.1 Oxide growth model along a 3D FE mesh

To compare the results obtained for the 2D and 3D simulations of the TGO layer, the oxide interface roughness has to be identical for any chosen model. The standard criterion defining the interface roughness ($R_l = L/L_0$) for a 2D profile is applied to a 3D profile. Here:

$$R_l = \frac{L}{L_0} = \frac{S}{S_0}. \tag{III.13}$$

Using the value of wavelength $w = 11.72$ μm along X_1 and X_2, the amplitude, a, for a 3D simulation of the oxide roughness has been determined. Here, $f(x,z)$ is a function describing the profile with $L_0 = w$.

$$S = \int_{z=0}^{z=L_0} \int_{x=0}^{x=L_0} dS, \tag{III.14}$$

$$S = \int_{z=0}^{z=L_0} \int_{x=0}^{x=L_0} \sqrt{1 + \left[\frac{\partial f(x,z)}{\partial x}\right]^2} \sqrt{1 + \left[\frac{\partial f(x,z)}{\partial z}\right]^2} dxdz, \tag{III.15}$$

$$f(x,z) = a.cos(\frac{2\pi x}{w}) + a.cos(\frac{2\pi z}{w}). \tag{III.16}$$

Based on the amplitude value numerically obtained ($a = 0.604$ μm) associated to w, the sinusoidal 3D FE mesh consists of 23,030 quadratic generalised plane strain elements (302,814 DOF) with full integration, and is subjected to symmetry and periodic boundary conditions, see Fig. III.30(a).

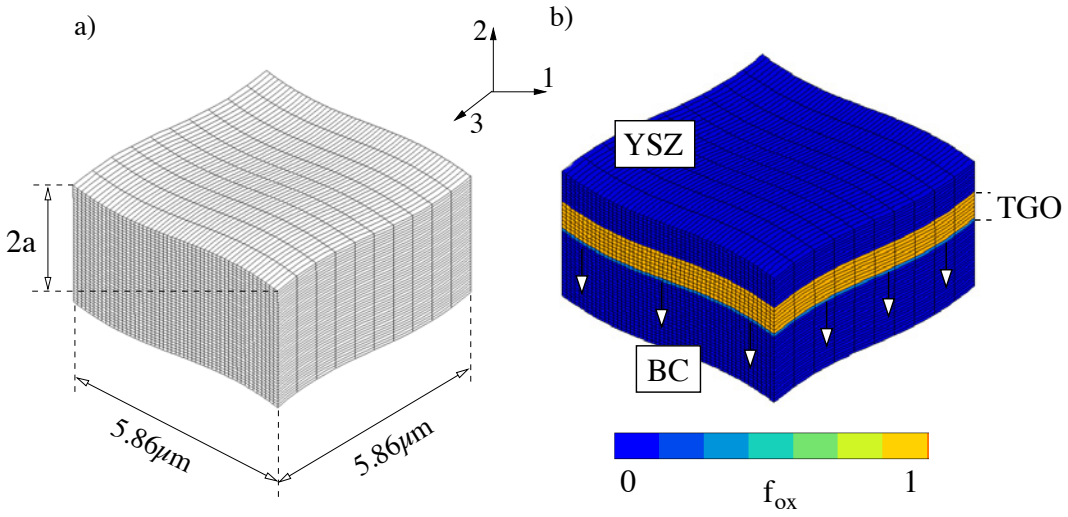

Figure III.30 : (a) Finite element mesh simulating a 3D sinusoidal TGO morphology and (b) the oxide volume fraction f_{ox} after 20 days exposure time at 950°C.

III.5.2.2 Stress/strain fields for a 3D TGO interface morphology

The predicted compressive in-plane stresses along X_1 ranges from 1.2 to 5.0 GPa at room temperature and are similar to those obtained in the 2D sinusoidal case (Section III.3). Figure III.31 shows the contours of the out-of-plane stress component (σ_{22}) evaluated at 20°C after 200 day-long cycles at 950°C. Predicted results show the considerable influence of the 3D simulation of the TGO morphology. It can be seen that the stress field is different that in the 2D case. The most highly stressed region is close to the peak zone. The tensile stress reaches 635 MPa at the TGO-BC interface while the TGO-YSZ interface is under compression (-1170 MPa). In comparison with the results given in Section III.3, the maximal tensile out-of-plane occurs in the same region as that for the sinusoidal case but its value increases by 30%. The compressive out-of-plane stress found close to the peak zone at the TGO-YSZ interface is two times greater for the 3D simulation of the TGO morphology than the 2D case. It is also observed that 6 μm and 7 μm away from the respective TGO-BC and TGO-YSZ interfaces, the out-of-plane stress is equal to zero. These values are two times greater than those previously obtained for a 2D simulation.

Table III.5 summarises the influence of the TGO morphology at low temperature on the maximal normal traction σ_{nn} (MPa) and the maximal in-plane stress in the TGO layer σ_{11}^{th} (GPa).

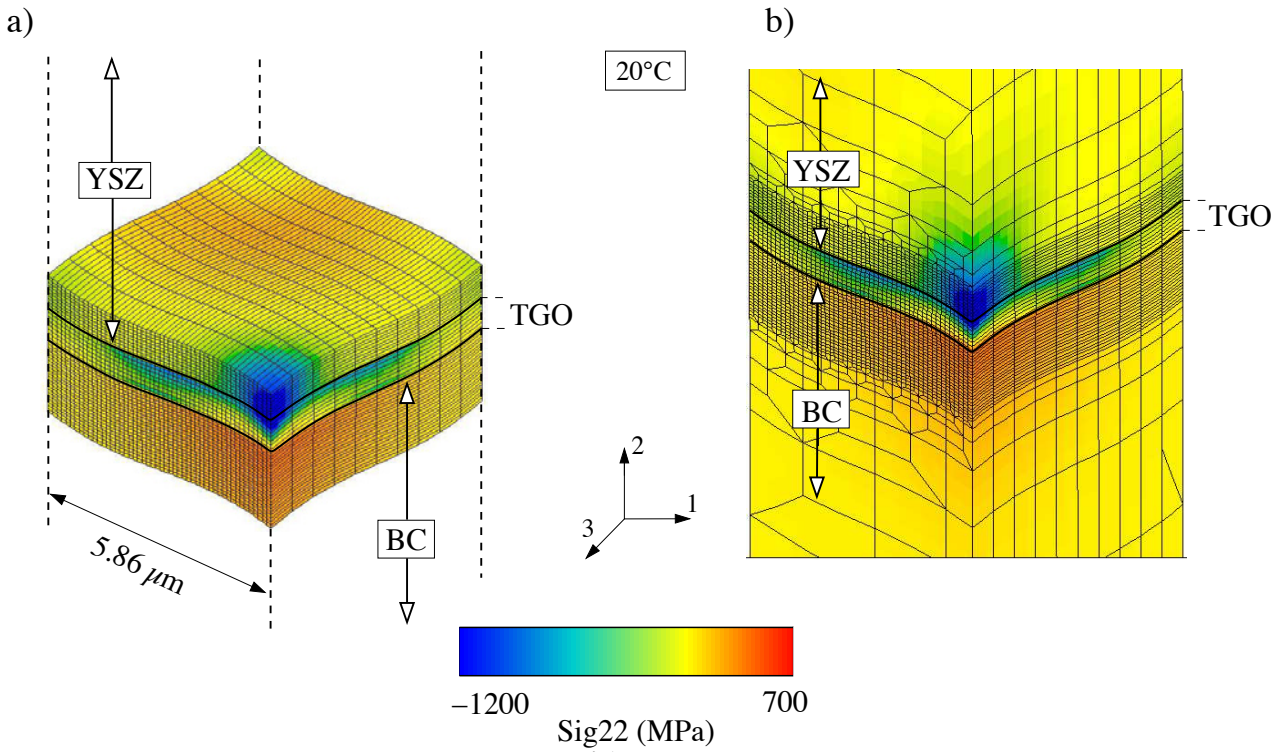

Figure III.31 : Gauss point value plot of the out-of-plane stress component σ_{22} at (a) 950°C and (b) 20°C after 200 day-long cycles at 950°C.

Table III.8 : Influence of the TGO morphology on the simulation of the maximal normal traction σ_{nn} (MPa) and the maximal in-plane stress at low temperature in the TGO σ_{11}^{th} (GPa).

Simulation	σ_{nn} (MPa)	σ_{11} (GPa)
Sinu. 2D	482	4.5
Sinu. 2D progressive	465 (-5%)	4.4 (-2%)
2D Fourier	572 (+17%)	5.8 (+29%)
Sinu. 3D	635 (+35%)	5.0 (+11%)

III.6 Concluding remarks

This chapter has described the methodology and the FE implementation of a numerical tool simulating the TGO growth in an EB-PVD TBC system. The tool has been improved to be applied to any FE mesh simulating the oxide morphology evolution (2D and 3D) and taking into account the TGO roughness increase. To determine the stress field in the critical oxide TGO-BC interface area, the anisotropic growth strains associated with the bond coat oxidation is modelled. The stress and strain fields for a 2D sinusoidal FE mesh simulating the TGO morphology have been obtained. For this configuration of parameters and from the analysis of the results obtained, it points out that:

- at high temperatures, in-plane and out-of-plane stresses in the transition zone simulating the TGO-BC interface develop principally due to the growth strains. At room temperature, the oxide roughness associated with the thermal strain mismatch strongly influences the compressive in-plane stress fields,
- 3 μm away from each TGO interface, the out-of-plane stress drop to zero,
- only a part of the ceramic layer and bond coat have an influence on the local stress field close to the TGO, 45 μm and 25 μm, respectively,
- at room temperature, the maximum traction is found along the TGO-BC interface at the peak region. Normal tractions increase with exposure time in the first thousand hours and then reaches an steady state,
- significant shear-stresses occur at the TGO-YSZ and TGO-BC interfaces, concentrated between the peak and valley zones,
- the bond coat accumulated creep and plastic strains develop during cooling, in the valley regions of the TGO-BC interface.

A parametric study of the different parameters influencing the mechanical behaviour of TBC system has been investigated. The respective role of the creep and plastic strain in the phenomenon of stress relaxation during cooling has been shown. Unfortunately, the TGO creep properties are difficult to obtain experimentally. The YSZ sintering has no influence on the stress/strain fields at the TGO-BC interface but strongly influences the shear-stress at the TGO-YSZ interface. Bond coat accumulated creep/plastic deformations are generated by (i) the thermal gradient during cooling from high temperatures and then develop in the valley regions, and (ii) by the TGO growth strains at high temperature and then develop between the peak and valley regions. Finally, the TGO roughness was also tested and appears as the most critical parameter, see Table III.7.

Previous 2D numerical simulation of the oxide morphology has provided a relevant compromise between information on the general TBC system behaviour and CPU time. To take into account the influence of the TGO roughness, stress/strain fields have been predicted based on a 2D model of the TGO, generated by a numerical tool using SEM micrograph and a Fourier decomposition. This approach allows to simulate the heterogeneities observed at the TGO-BC interface. The same approach has been applied to a 3D sinusoidal profile of the oxide morphology. In comparison with the 2D sinusoidal case, a difference of 17% in the maximal normal traction is predicted. In the case of the 3D sinusoidal simulation of the oxide morphology, the difference reaches 35% and the out-of-plane stress field is rather different.

Reference

Bialas, M. (2008). Finite element analysis of stress distribution in thermal barrier coatings. *Surface and Coating Technology*, 202:6002–6010.

Brumm, M. and Grabke, H. (1993). Oxidation behaviour of NiAl. Cavity formation beneath the oxide scale on NiAl of different stoichiometries. *Corrosion Science*, 34:547–561.

Busso, E. and Qian, Z. (2006). Mechanistic study of microcracking in transversely isotropic ceramic-metal systems. *Acta Materialia*, 54:325–338.

Busso, E., Qian, Z., Taylor, M., and Evans, H. (2008). The influence of bond coat and topcoat mechanical properties on stress development in thermal barrier coating systems. *Acta Materialia*, 57:2349–2361.

Caliez, M., Feyel, F., Kruch, S., and Chaboche, J. (2002). Oxidation induced stress fields in an EB-PVD thermal barrier coatings. *Surface and Coating Technology*, 157:103–110.

Chen, M., Jordan, H., Gell, M., and Barber, B. (1998). Thermal residual stress in an electron beam-physical vapor deposited thermal barrier coating system. *Acta Materialia*, 46:5839–5850.

Christensen, R., Lipkin, D., Clarke, D., and Murphy, K. (1996). Nondestructive evaluation of the oxidation stresses through thermal barrier coatings using Cr^{3+} piezospectroscopy. *Appl. Phys. Lett.*, 69:3754–3756.

Clarke, D., Christensen, R., and Tolpygo, V. (1997). The evolution of the oxidation stresses in zirconia thermal barrier coated superalloy leading to spalling failure. *Surface and Coating Technology*, 94-95:89–93.

Evans, A., Mumm, D., Hutchinson, J., Meier, G., and Pettit, F. (2001). Mechanisms controlling the durability of TBCs. *Progressive Material Science*, 46:505–553.

Haynes, J., Freber, M., Porter, W., and Rigney, E. (1999). Characterization of alumina scales formed during isothermal and cyclic oxidation of plasma-sprayed TBC systems at 1150°C. *Oxid. Metals*, 52:31–76.

He, M., Hutchinson, J., and Evans, A. (2002). Large deformation simulations of cyclic displacement instabilities in thermal barrier systems. *Acta Materialia*, 50:1063–1073.

Karlsson, A. and Evans, A. (2001). A numerical model for the cyclic instability of TGOs in TBC systems. *Acta Materialia*, 49:1793–1804.

Kato, T., Matsumoto, K., Matsubara, H., Ishimata, Y., Saka, H., Hirayama, T., and Ikuhara, Y. (2005). TEM characterization of the YSZ fabricated by EB-PVD deposition. *Surface and Coating Technology*, 194:16–23.

Nychka, J. and Clarke, D. (2005). Quantification of aluminium outward diffusion during oxidation of FeCrAl alloys. *Oxidation of Metals*, 63:325–352.

Schulz, U. and Schmücker, M. (2000). Microstructure of $Zr0_2$ thermal barrier coatings applied by EB-PVD. *Materials Science Engineering A*, 276:1–8.

Schwarzer, J., Löhe, D., and Vöhringer, O. (2004). Influence of the TGO creep behavior on delamination stress development in thermal barrier coatings systems. *Materials Science Engineering A*, 387-389:692–695.

Sfar, K., Aktaa, J., and Munz, D. (2002). Numerical investigation of the residual stress fields and crack behavior in TBC systems. *Materials Science Engineering A*, 333:351–360.

Spitsberg, I., Mumm, D., and Evans, A. (2005). On the failure mechanisms of thermal barrier coatings with diffusion aluminide bond coatings. *Materials Science Engineering A*, 394:176–191.

Stiger, M., Yanar, N., Toppings, M., Pettit, F., and Meier, G. (1999). Thermal barrier coatings for the 21st century. *Z. Metall*, 90:1069–1078.

Taylor, M., Gray, S., and Evans, H. (2006). *Contract Report*. SIEMENS.

Tomimatsu, T., Zhu, S., and Kagawa, Y. (2004). Local stress distribution in thermally-grown-oxide layer by near-field optical microscopy. *Scripta Materialia*, 50:137–141.

Wu, K., Chang, Y., and Wang, Y. (2004). Simulating interdiffusion microstructure in Ni-Al-Cr diffusion couples: a phase field approach coupled with CALPHAD database. *Scripta Materialia*, 50:1145–1150.

Xu, C., Faulhaber, S., Mercer, C., Maloney, M., and Evans, A. (2004). Observations and analyses of failure mechanisms in thermal barrier systems with two phase bond coats based on NiCoCrAlY. *Acta Materialia*, 52:1439–1450.

Zhu, H., Fleck, N., Cocks, A., and Evans, A. (2005). Numerical simulations of crack formations from pegs in thermal barrier systems with NiCoCrAlY bond coats. *Materials Science Engineering A*, 404:26–32.

Chapter -IV-

Observations and analyses of failure mechanisms in an EB-PVD TBC systems

Contents

IV.1 Introduction

The end-life of TBC systems corresponds to the spallation of a visible area of the insulator top coat (few mm^2). Among one of the plausible scenario proposed to explain top coat spallation, the common idea is that planar compressive stresses generated during the system cooling by thermal properties mismatch between the substrate and the others TBC constituents, are responsible for top coat spallation.

According to A.G. Evans *et al.* (1983), if an interfacial crack is already present at a brittle interface, spallation occurs when one of the oxide interface toughness becomes lower than the stored elastic strain energy per unit area (J/m^2). Another approach to explain TBC spallation has been proposed by H.E. Evans (1989). The high compressive stress levels may trigger the propagation of cracks through the top coat and oxide layers. In this case, spallation occurs due to the weak oxide layer and the strong interface toughness. Other models have been proposed to describe the final spallation failure. Nevertheless, they do not model continuous interfacial damage (Siegler, 1993, Tolpygo and Grabke, 1994, Suo, 1995). The understanding of the macroscopic spallation mechanisms does not explain how the TGO interfaces toughness could be affected by the presence of microscopic defects, such as porosities (Dalgleish et al., 1989), microcracks (Reimanis et al., 1990) or heterogeneities along the oxide interfaces. Due to combined high levels of stress and temperature, damage evolution can proceed by porosity growth or brittle microcrack propagation.

Two distinct steps leading to TBC spallation can be identified: (i) micro-damage appears close to the TGO, resulting on the oxide interfaces toughness decrease, following (ii) by macroscopic top coat spallation driving by the high level of stored strain energy per unit area. The relative influence of each mechanism is also crucial to understand TBC systems spallation.

The objective of this chapter is to examine the interfacial micro-damage evolution responsible for the oxide interface toughness decrease and the macroscopic spallation mechanism. In particular, the nature of the micro-damage close to the TGO interfaces is analysed. This study is fundamental to develop a predictive TBC lifetime model, integrating macro and microscopic failure mechanisms. This is fundamental to develop a predictive TBC lifetime model, integrating macro and microscopic failure mechanisms. Observations are made on a TBC consisting in an EB-PVD top coat and a $NiCoCrAlY$ bond coat tested under isothermal conditions.

Section IV.2 introduces the tested samples and the describes the characterisation of the top coat spallation mechanism. The TBC end-life obtained experimentally, as a function of the temperature (from 930 to 1110°C), exposure time (from 24 h to 1000 h) or TGO thickness is presented. In Section IV.3, additional observations are made on cross-section micrographs located close to the TGO where interfacial micro-damage is present. The aim here is to identify the oxide interfacial defects responsible for interface debonding and to understand oxide interface damage evolution. Finally, measurements of the oxide interface toughness for $NiCoCrAlY$ bond coat published in the literature are discussed.

IV.2 Macroscopic failure of an EB-PVD TBC system

IV.2.1 Experimental procedure

Specimens used to characterise failure of EB-PVD TBC systems deposited on samples representative of blades existing in a gas turbine and having different radii of curvature, see Fig. IV.1. The bond coat thickness is approximately 90 μm and has an overall composition of Ni 22Co 17Cr 12.5Al 0.6Y (wt%). The EB-PVD top coat has a nominal thickness of 135 μm. Isothermal loading comprises slow heating and cooling transients (15 min each) and an exposure time at a peak temperature, ranging from 930 to 1110°C. After testing, cross-sections were polished using a precision polishing system to maintain flatness. Micro-cloth with multi-crystalline diamond spray (3, 1 and 0.1 μm) was used for final polishing to preserve the fine structure near the TGO. After sectioning and preparation, the specimens were observed using scanning electron microscopy (SEM).

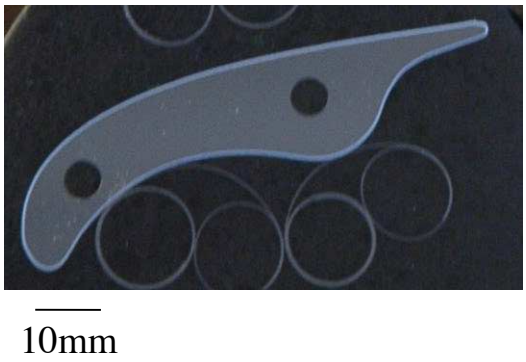

Figure IV.1 : Picture of a sample representative of blades existing in a gas turbine.

IV.2.2 Literature review of top coat spallation mechanisms

First, let us remain the definitions of delamination and spallation terms. **Delamination** consists in a large separation ($>$ 100 μm) of one of the TGO interfaces due to mechanical effects. **Spallation** occurs when an entire zone of a few mm^2 of the top coat is completely peeled off the remaining TBC system. As background to understand the end-life of multilayer systems, final delamination/spallation mechanisms reported in the literature are summarised in Fig. IV.2 (Evans et al., 1983, Evans, 1989).

Spallation mechanisms of thin films could be classified into two categories, depending on whether the interface is more or less brittle than the thin film, top coat spallation will occur by buckling/edge delamination, see Figs. IV.2(a) and (b), or by cracking, see Fig. IV.2(c).

Top coat spallation induced by buckling-delamination occurs when two conditions are fulfilled: (i) a horizontal crack is present at one of the TGO interfaces and (ii) the stored elastic strain energy per unit area is greater than one of the oxide interfacial toughness. Then vertical cracks propagate in the YSZ ceramic layer, leading to its spallation, as illustrated in Fig. IV.2(a). When top coat spallation is induced edge-delamination, a vertical crack is present in the top coat before it spalls and propagates in Mode II along one of the damaged oxide interface, see Fig. IV.2(b). In both cases, top coat spallation relaxes the stored elastic strain energy. When the interface is strong, horizontal microcracks appear in the oxide layer and vertical cracks propagate in the YSZ layer (Yanar et al., 2006). Top coat spallation

occurs when the two cracks coalesce as illustrated Fig. IV.2(c).

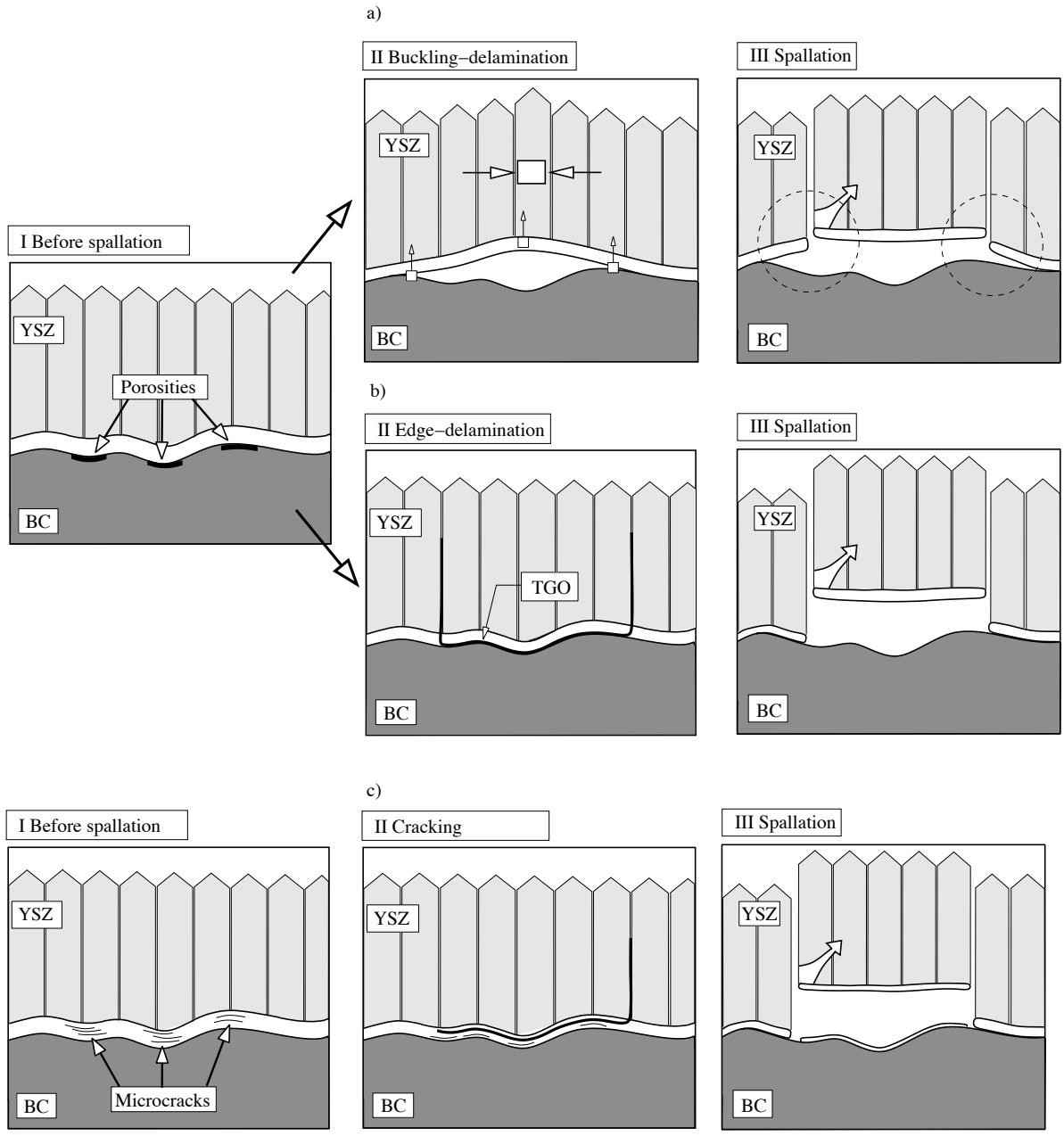

Figure IV.2 : Literature review of EB-PVD TBC spallation mechanisms: when the interface is brittle, (a) buckling or (b) edge delamination (A.G. Evans, 1983) and (c) when the interface is strong, shear crack (H.E. Evans 1989).

IV.2.3 Observation of the studied TBC system

SEM micrograph observation of non-spalled TBC samples shows that no vertical cracks are present in the ceramic or in the bond coat. For this reason, spallation emanating from these vertical cracks, corresponding to the cases illustrated in Figs. IV.2(b) and (c), will not be addressed in the present study.

For the TBC system of interest here, spallation seems to be caused by a buckling

delamination phenomenon. Indeed, the first signs of the TBC spallation after high temperature exposure times (Figs. IV.3 and IV.4) shows clearly a buckling of the top coat. Spallation of a top coat part also leads to the propagation of a large horizontal delamination crack at both TGO interfaces, illustrated in Fig. IV.4 and shown by the dotted circles in Fig. IV.2(a). The influence of buckling on the local stress fields close to the delamination crack tip have been addressed by Choi *et al.* (1999).

Delamination is in our case mostly observed at the TGO-BC interface, see Fig. IV.3. When it occurs at the external oxide interface, it can result from the top coat spallation. Delamination at the YSZ-TGO interface is only observed close to TBC zones which have already spalled off, as shown in Fig. IV.4.

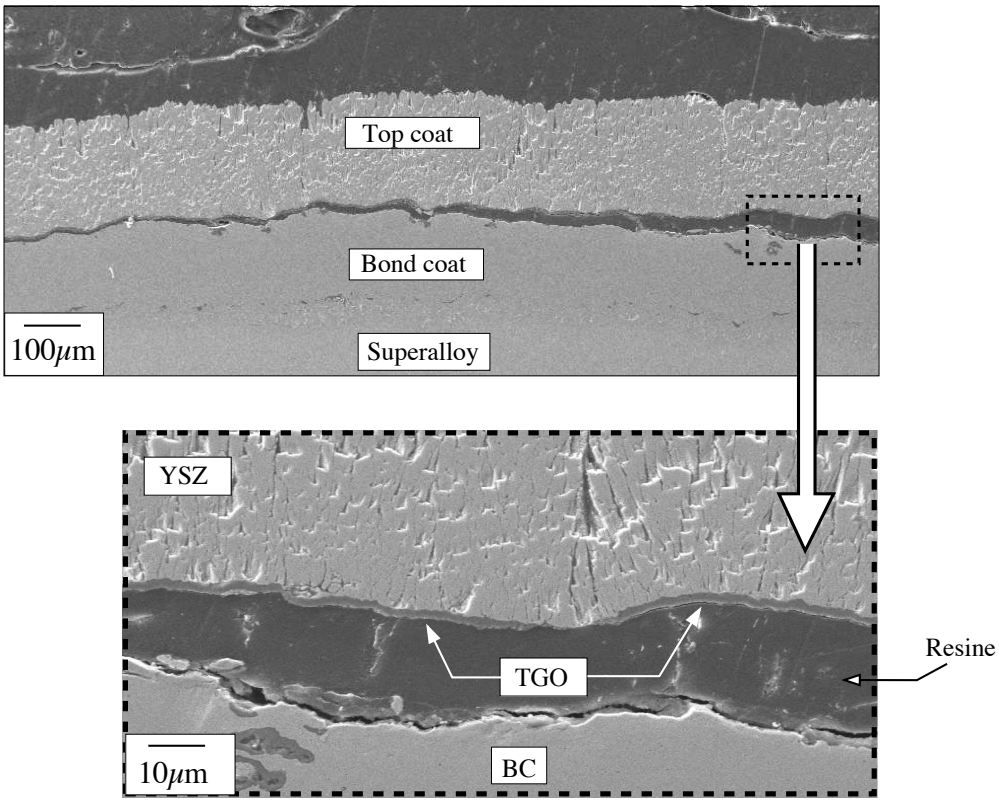

Figure IV.3 : SEM micrographs showing the horizontal delamination and its localisation (at the TGO-BC interface) in an EB-PVD TBC system tested at 1110°C after 24 h of exposure time.

IV.2.4 TBC lifetime experimental results

Before analysing in detail the lifetime experimental results obtained for the present TBC system it is important to understand the relationship between the delamination and spallation stages. From SEM micrographs observations, spallation and delamination mechanisms are observed simultaneously. Furthermore, no bucking delamination has been observed on non-spalled TBC systems. The TBC system is unstable and is defined by two states: 1) non-spalled but with micro-damage close to the TGO layer and 2) spalled with large horizontal delamination close to the TGO, see Fig. IV.3. The delaminated zones are only observed close to spalled top coat zones due to the dynamic nature spallation phenomenon, see Figs. IV.3

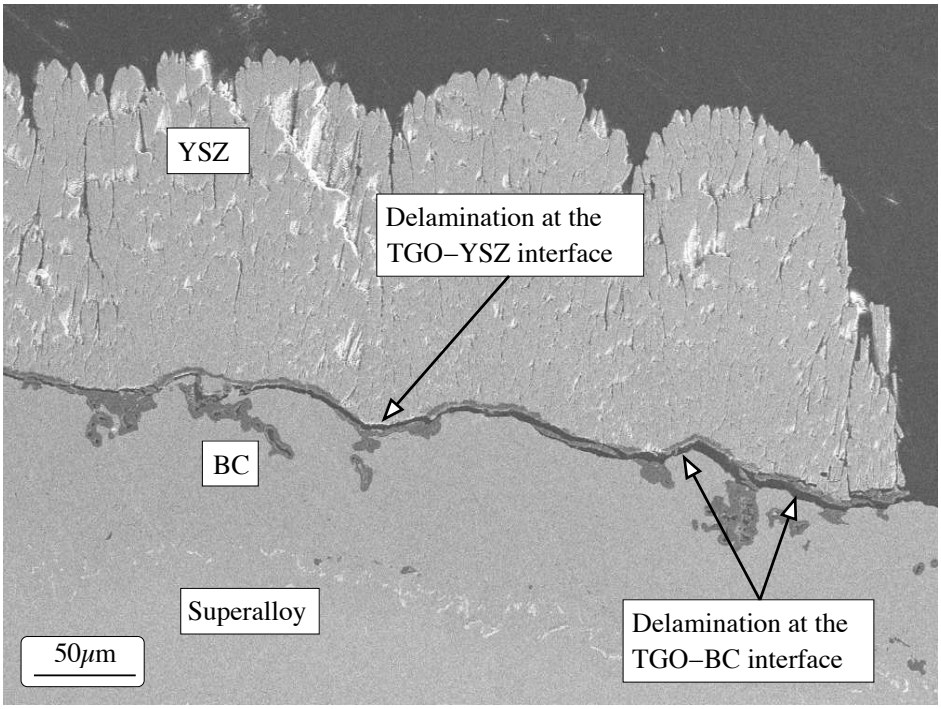

Figure IV.4 : SEM micrograph showing the horizontal delamination at both TGO interfaces induced by to the dynamic nature of the top coat spallation.

and IV.4.

Times at which top coat delamination/spallation was observed experimentally after cooling from the peak temperature (930 to 1110°C) are presented in Figs. IV.5. TBC states (spalled or not spalled) as a function of temperature and exposure time are shown in Fig. IV.5(a). At 930°C no spallation is observed even after 1000 h. At 990°C and 1050°C, the YSZ top coat failed at 1000 h and 300 h respectively. After 24 h of exposure time at 1110°C, top coat spallation is observed.

According to the plot representing the TBC state as a function of temperature and TGO thickness h_{ox}, see Fig. IV.5(b), it is possible to extract a critical TGO thickness value for which the TBC spallation occurs, between 1.92 μm and 2.15 μm. According to the Figure IV.5(b) the TGO thickness is an important parameter in the TBC lifetime, nevertheless it is not relevant to limit a TBC lifetime model to this parameter, especially during thermal cycling.

IV.2.5 Discussions

General observations of delaminated and spalled parts of the TBCs studied, indicate that: (i) even if interface toughness decreases and stored elastic strain energy increases can be continuous mechanisms, when conditions to spall are fulfilled, spallation is a brittle fracture mechanism. In the observed TBC samples, buckling delamination and spallation were seen to be the final events in TBC failure, (ii) spallation and delamination occur simultaneously in a relative short time, and the stage illustrated by the Step II in Fig.IV.2(a) is assumed to be negligible compared to time to reach the critical TGO interface damage leading to spallation. The studied TBC system has been assumed to be defined by a binary state: spalled or not. Due to the different radii of curvature of the sample, a non-spalled TBC

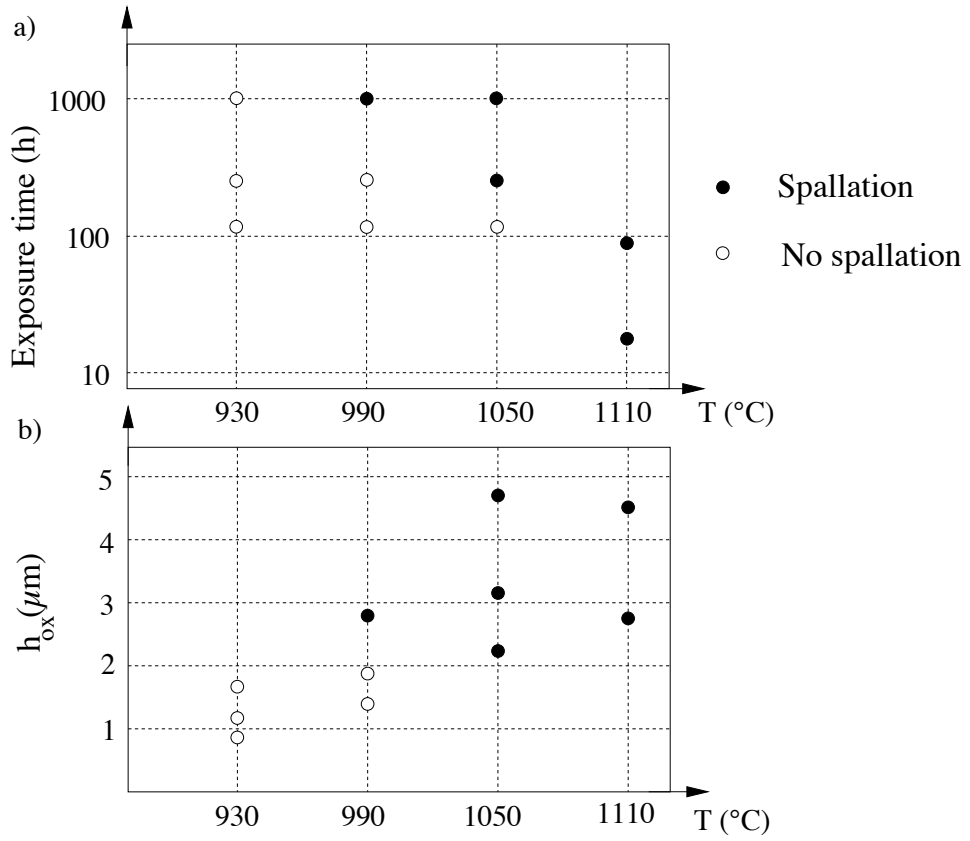

Figure IV.5 : TBC state (spalled or not spalled) as a function of isothermal loading ranging from 930 to 1110°C and (a) exposure time or (b) TGO thickness.

system can be locally damaged, and (iii) the TGO-BC interface is the weaker one. For these reasons, our attention will be focused on the mechanisms involved in the progressive decrease of the TGO-BC interface toughness with thermal exposure.

IV.3 Microscopic interfacial damage close to the TGO layer

The TBC final failure mechanisms (delamination and spallation) previously presented do not explain the oxide interface toughness decrease, induced by interfacial damage. The present section studies the effect of microscopic interfacial damage on the TGO interface fracture resistance or toughness.

IV.3.1 Literature review

For EB-PVD TBC systems, the degradation mechanisms under thermal loading are confined to a zone located between the ceramic and the bond coat. Damage initiation could be induced by several mechanisms, as summarised in Figs. IV.6(a) and (b). In addition to the vertical separation which can be present along the YSZ ceramic columns and out-f-plane cracks in the bond coat, Cases 2 and 5 in Figs. IV.6(a) and (b), damage could also initiate at both oxide interfaces (Cases 1 and 6). Indeed, high normal traction levels generated by the oxide interfaces roughness constitute the driving forces for micro-damage initiation, as discussed in Section III.3.2. The EB-PVD deposition can create voids at the TGO-YSZ interface (Case 3). Interfacial voids or porosities (Case 4) are also observed at the TGO-BC interface and might also appear due to chemical phenomena as vacancy diffusion (Ibégazène-Ouali et al., 2000). When the interface is stronger than the oxide, microcracks appear in the TGO, especially during cyclic thermal loading (Case 7) (Yanar et al., 2006).

Propagation of oxide interfacial damage generally observe close to the TGO is presented in Figs. IV.6(c) and (d). Microcracks could coalesce along the oxide interfaces by propagation (Cases I and V), through the TGO (Mumm and Evans, 2000) or through the top coat (He et al., 2004) (Cases III and IV). A vertical separation in the top coat might coalesce with an interfacial crack (Case II), leading to edge delamination. Finally, damage could increase by the simple growth of interface porosities (Case VI) (Harvey et al., 2008).

Numerous experimental studies dealing with interfacial damage in $(Ni, Al)Pt$ bond coats have been reported in the literature. Most of the time, in-plane cracks nucleate and extend along the TGO-YSZ interface and through the top coat (Newaz et al., 1998, Bi et al., 2000, Spitsberg et al., 2005). TBC systems constituted of a $NiCoCrAlY$ bond coat and EB-PVD top coat have already been studied. Imperfections close to the TGO have been observed by Mumm and Evans (2000). According to these authors, the failed oxide interface has a brittle appearance, micro-fracture progresses along the BC-TGO interface and no void are observed. Microcracks nucleate around morphological imperfections in the TGO. In another study, burner ring specimens have been observed after 14,000 h and in regions where the oxide is thin and uniform, cracks are located at the TGO-BC interface, (Xu et al., 2004). Porosities at the TGO-BC interface have also been observed after 100 cycles at 1000°C (Yang et al., 2001) and at 1100°C (Kim et al., 2002).

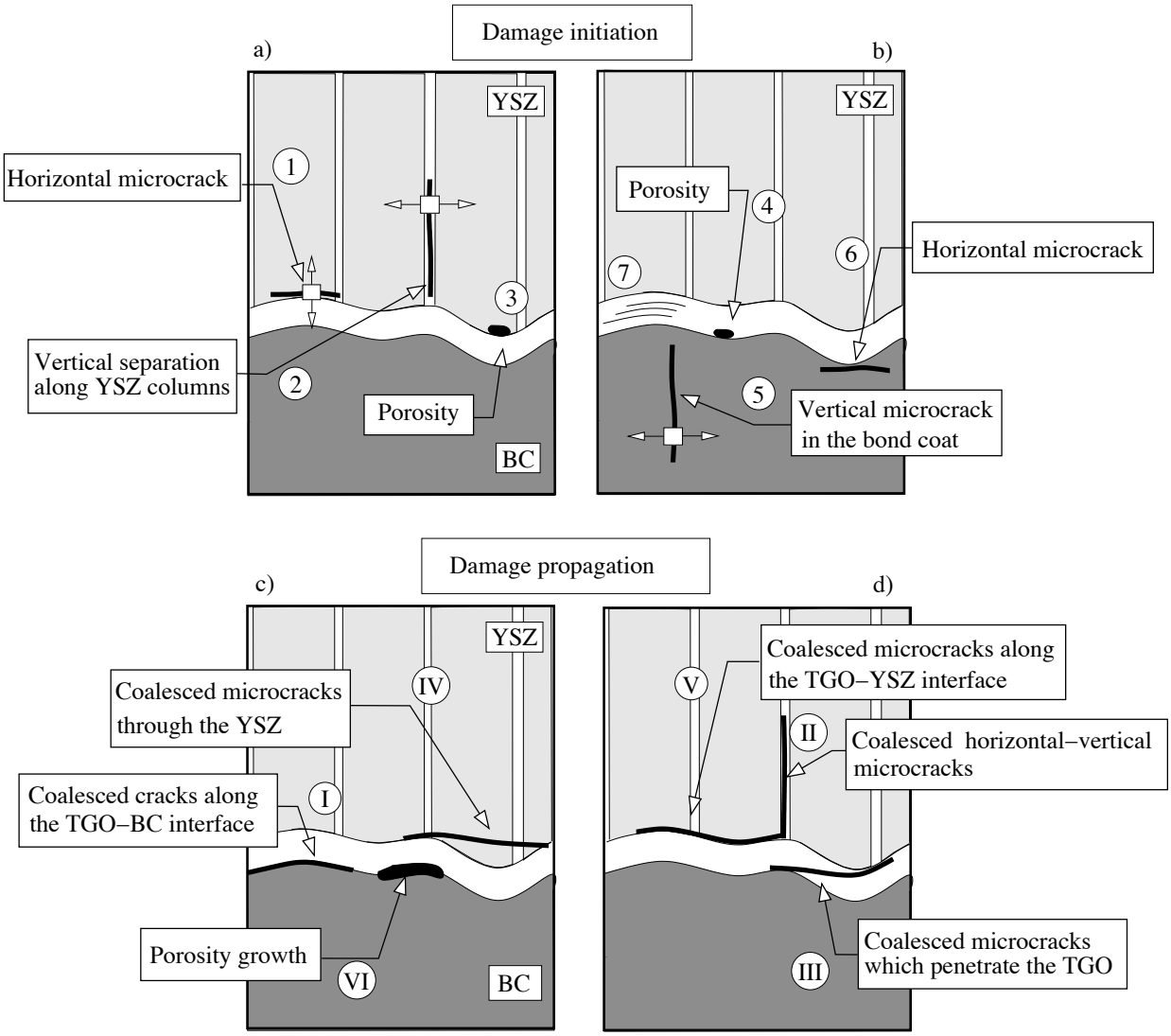

Figure IV.6 : Schematics of possible micro-damage mechanisms in an EB-PVD TBC system: (a, b) initiation and (c, d) propagation.

IV.3.2 Observation of micro-damage on the TBC system

IV.3.2.1 Analysis of SEM micrographs

In order to understand and to characterise interfacial damage evolution, cross-sections of TBC specimens after exposure to high temperature (from 930°C to 1110°) and for 24 to 1000 h were analysed using SEM techniques.

At 930°C, no porosities have been observed, even after 1000 h. At 990°C, porosities whose size is under 3 μm were present after 300 h and seemed to have grown after 1000 h, leading to spallation of a small part of the specimen. The presence of porosities for high temperatures ($>$ 990°C) illustrates the likely relationship between interfacial porosities and interdiffusion in the bond coat due to its oxidation.

After 120 h at 1050°C, porosities whose size is under 3 μm were observed in the non-spalled part of the TBC, see Fig. IV.7(a). In another part of the specimen, the porosity size is $10 - 20$ μm and they were seen to be close to the coalescence stage, see Fig. IV.7(b).

Close to the spalled top coat zone, large voids were observed and were seen to have joined together with interface cracks certainly as a result of the top coat spallation mechanism, see Figs. IV.7(c) and (d). After 300 h, large delamination regions are developed in the whole specimen, and it was not possible to identify the micro-damage mechanisms.

After a short exposure time at high temperatures (24 h at 1110°C), porosities are observed along the entire sample at the TGO-BC interface, see Fig. IV.8. Size voids range from 3 to 30 μm. Since there is no proof of void coalescence, we can assume that large voids (> 3 μm) are the result of void coalescence. Unfortunately, the TBC specimens was seen to have completely spalled on the sample tested after 96 h at 1110°C and does not give us more information.

IV.3.3 Interfacial micro-damage characterisation

In this section, the study of the oxide interfacial damage, limited to the porosities will be carried out. Indeed, for the TBCs studied and for isothermal loading, microcracks were not observed for any oxidation times and temperatures tested. In the case of spalled samples, microcracks have been induced by top coat spallation mechanisms.

The effect of thermal exposure time on interfacial porosity evolution is presented in Figs. IV.9(a) and (b). There are four different types of damaged TBC systems: 1) no oxide interfacial damage, 2) small porosities (< 3 μm), 3) large porosities and 4) total spalled TBC. To establish the relationship with the previous results, the figure representing the TBC states (spalled or not) is also shown, Fig. IV.9(a). It is important to note that, in the same sample, one part of the TBC can be seen to have spalled whereas another was only locally damaged at the TGO-BC interface. This is in correlation with the different radii of curvature of the samples.

Even if no damage was present at 930°C, small porosities were seen to have nucleate at 990°C after 300 h and to have grown after 1000 h. Certainly, due to interdiffusion mechanisms in the bond coat, the higher the temperature, the earlier the porosities appeared to have developed and grown. After 120 h at 1050°C, large porosities were observed and seemed to have seriously damaged the TGO-BC interface. The presence of interfacial porosities might imply that the local damage mechanism is ductile. It also illustrates the progressive damage mechanism of the TGO-BC interface, leading to a decrease of the TGO interface toughness. The nucleation of interface porosities could result from a small interfacial crack (mechanical effect) or from the coalescence of vacancies due to, for instance, interdiffusion. The particular round morphology of the porosities focuses our attention on the chemical effect inducing porosity nucleation and growth.

IV.3.4 Void nucleation and growth

For the analysed isothermal loadings, oxide interfacial damage was seen to be limited to porosity nucleation and growth. The present section proposes physical and mechanical mechanisms explaining the interfacial damage evolution. The relationship between the observations and the model of the local interfacial damage time-evolution presented in Chapter V is addressed.

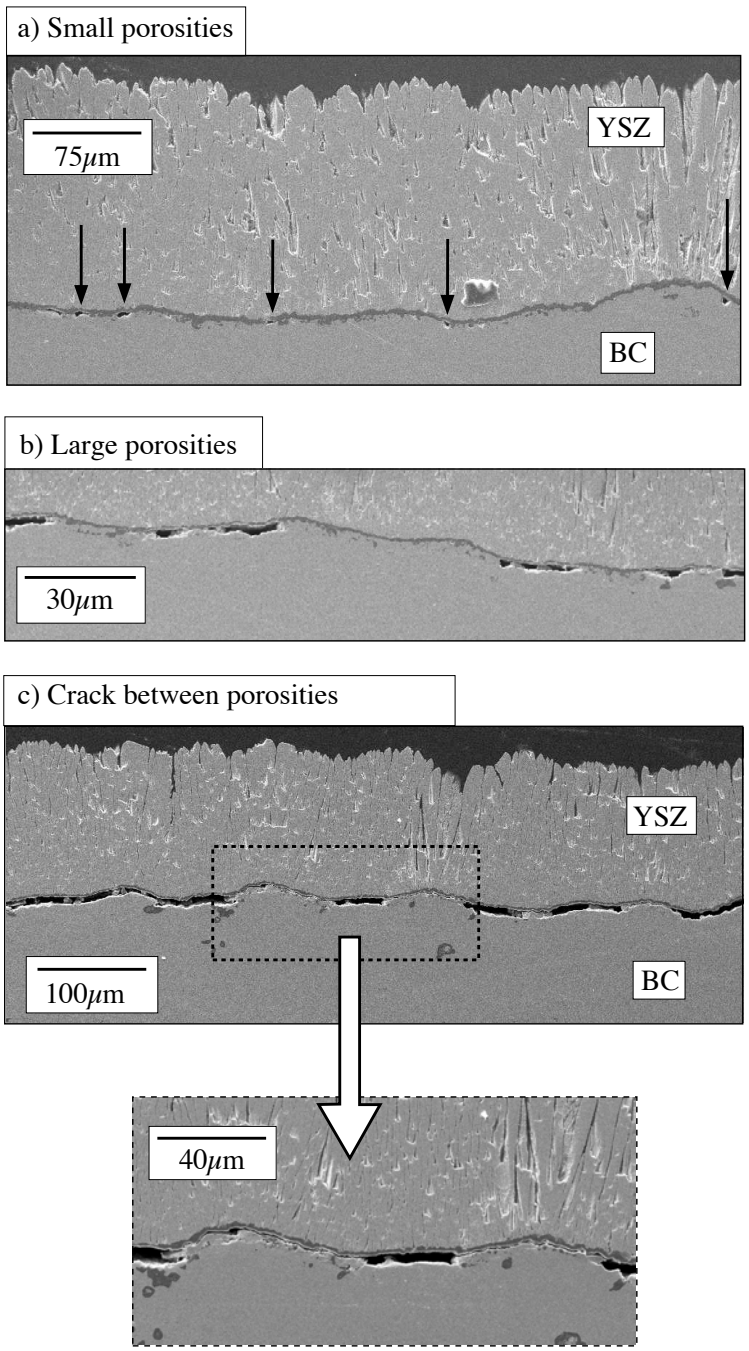

Figure IV.7 : SEM micrographs of an EB-PVD TBC system after 120 h at 1050°C showing: (a) the presence of initial porosities at the TGO-BC interface (marked by arrows), (b) grown porosities and (c) cracks between large porosities near the spalled zone, probably caused by the dynamic mechanism of top coat spallation.

IV.3.4.1 Porosity nucleation: Kirkendall effect

The diffusion processes involved in the bond coat can lead to volume changes, aluminium depletion and phases dissolution, as discussed previously in Section II.2.3. An additional consequence of the inward oxygen diffusion through the TGO is the formation of interfacial porosities which could be explained by the different mobilities of the bond coat constituent

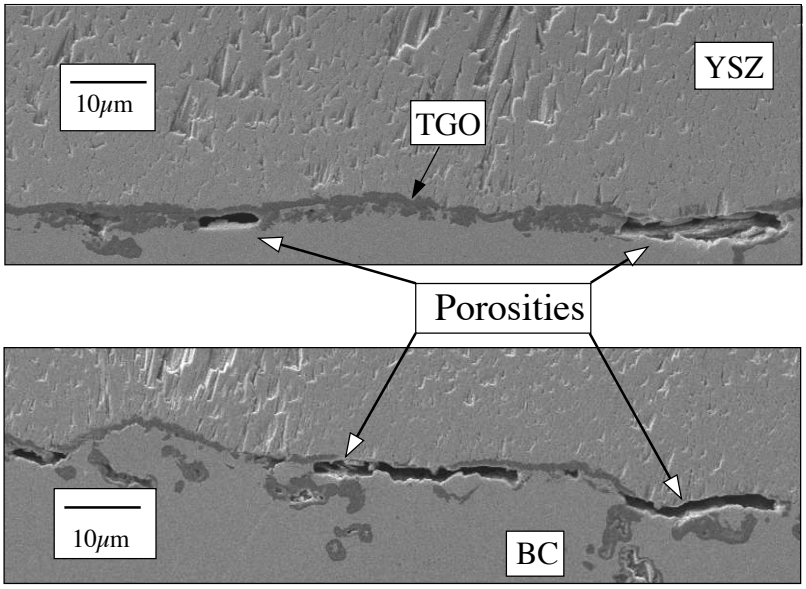

Figure IV.8 : SEM micrograph showing large damaged zones (porosities) at the TGO-BC interface after 24 h oxidation at 1110°C.

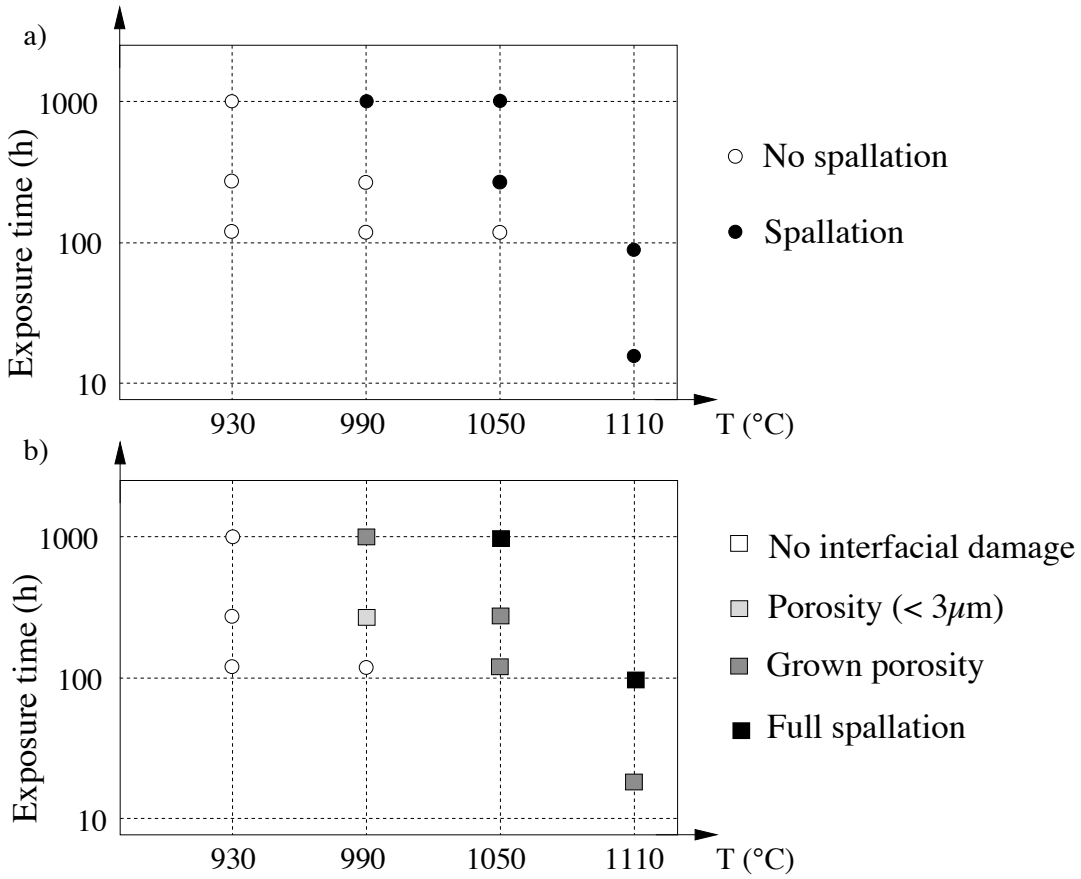

Figure IV.9 : (a) TBC state (spalled or not spalled) and (b) different types of damage at the TGO-BC interface as a function of peak oxidation ranging from 930 to 1110°C and exposure time.

species (Brumm and Grabke, 1993). Indeed, bond coat oxidation is associated with the respective outward and inward diffusion of Ni and Al, Fig. IV.10(a). Since the diffusion of nickel is three times greater than aluminium in nickel-rich $NiAl$ alloy, see Fig. IV.10(b), the vacancy flux induced by the imbalance between J_{Al} and J_{Ni} leads to void formation, see Fig. IV.10(a). The unbalanced material flows is known as the Kirkendall effect. It has been proposed that voids can nucleate by vacancy coalescence (Hindam and Smeltzer, 1980).

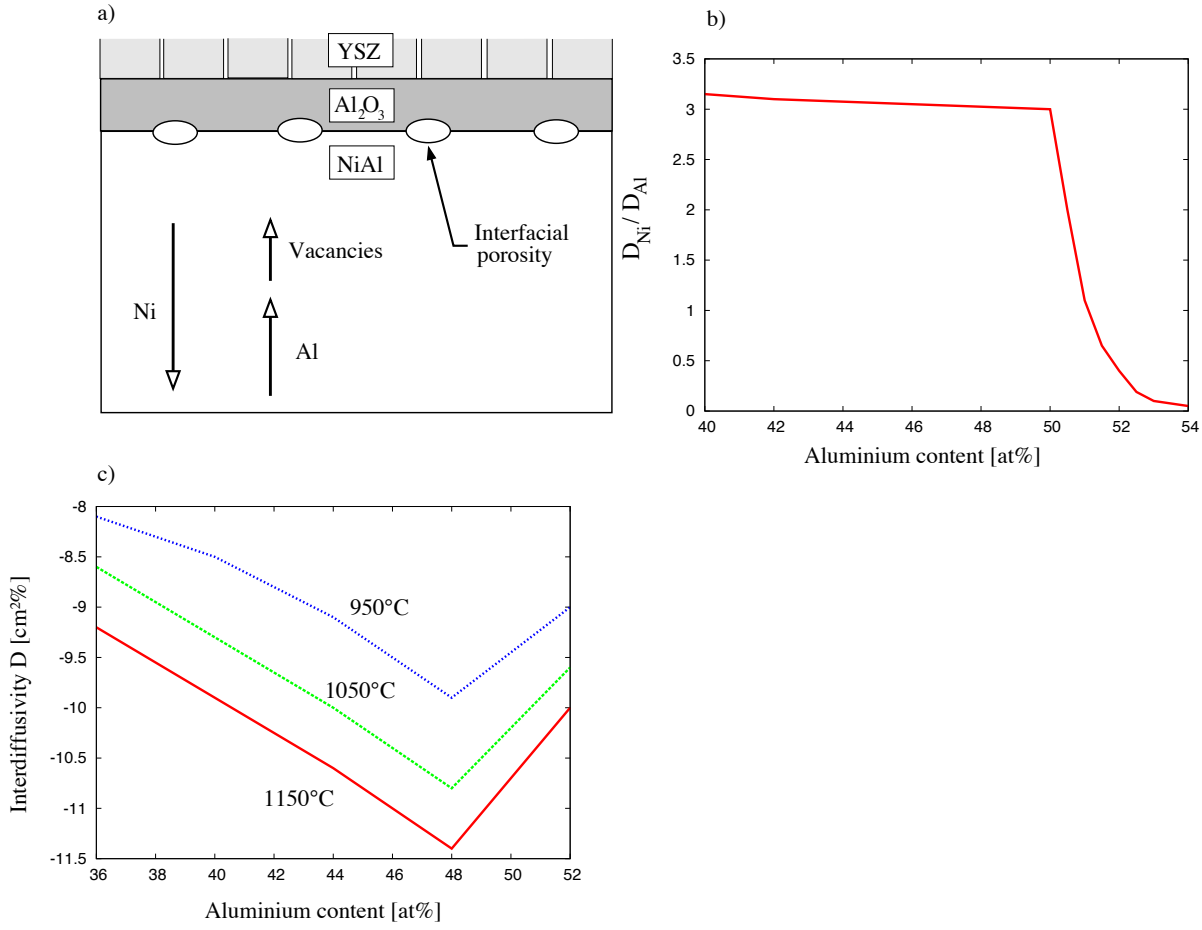

Figure IV.10 : (a) Schematics illustrating the interdiffusion of Ni and Al in the bond coat responsible for porosity nucleation at the TGO-BC interface, (b) ratio between Al and Ni diffusivity in $NiAl$ as a function of the Al concentration and (c) quantitative values of the interdiffusivity as a function of temperature (Kumar et al., 1974).

IV.3.4.2 Porosity growth

In the continuity of this latter approach, porosity growth can be explained by the Figs. IV.10(b) and (c) (Kumar et al., 1974): the decrease of aluminium concentration in the bond coat with oxidation time also induces an increase in the aluminium interdiffusivity in the bond coat and in the ratio J_{Al}/J_{Ni}. The Kirkendall phenomenon is inclined to increase with exposure time and temperature, accelerating the nucleation and growth of porosities. This analysis agrees with the porosity evolution with exposure time and temperature seen in the experimental observations previously discussed, see Fig. IV.9.

How can stress state, thermal loading and the TBC constituents mechanical behaviour explain the particular spherical morphology of the interfacial voids? According to Cocks and

Ashby (1982), voids at a grain boundary could grow either by boundary, surface diffusion or by power-law creep. A combination of these three mechanisms is also possible. The voids grow on grain boundaries when diffusion is involved and within the grain as well when power-creep law is dominant. The same explanation could be employed to model TGO-BC interfacial void growth. If void growth is controlled by a boundary diffusion mechanism, voids should remain spherical, see Fig. IV.11(a), which is in disagreement with our observations, Figs. IV.7 and IV.8. Indeed, the typical void morphologies observed in our experiments implies that surface diffusion and the power-law creep are likely the void growth dominant mechanisms.

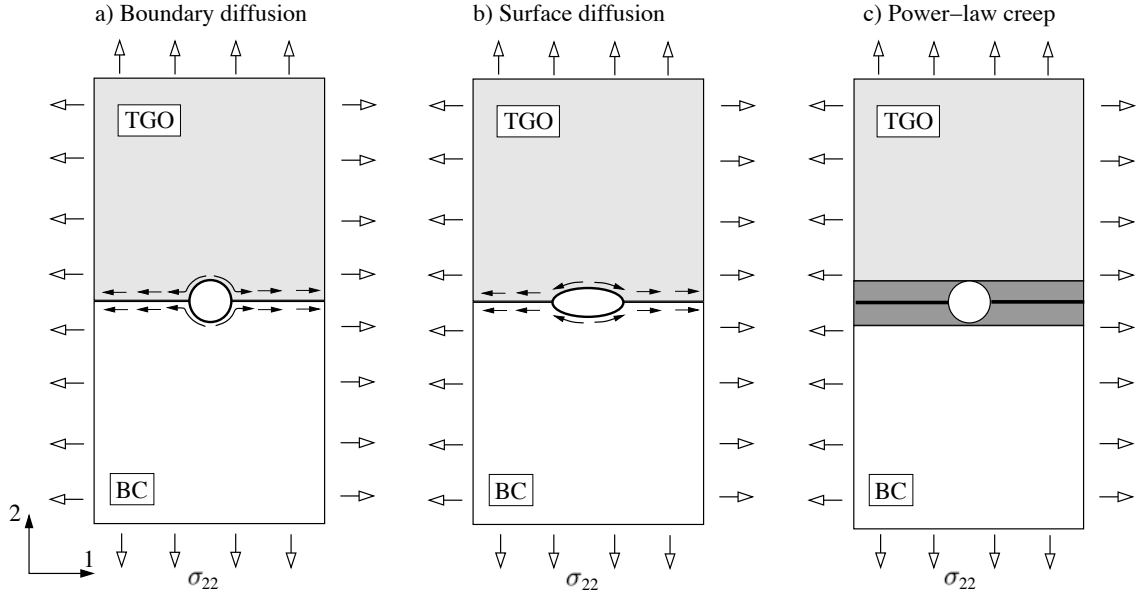

Figure IV.11 : Illustration of the mechanisms controlling void growth: (a) boundary diffusion, (b) surface diffusion and (c) power-creep law (Cocks and Ashby, 1982).

Oxidised species might be transported around the void in regions where a void has nucleated (Smialek, 1978, Hindam and Smeltzer, 1980). This assumption is based on surface porosity observations which suggest that surface diffusion occurs (Théry et al., 2007, Théry et al., 2009). Considering the Cocks and Ashby model, surface diffusion controls void growth for low out-of-plane stress values (σ_{22} in Fig. IV.11), high temperatures and low void sizes. Power-law creep is the dominant mechanism under high stress levels and high void sizes. With time, voids growth can be controlled by a combination of both mechanisms, see Fig. IV.12.

IV.3.4.3 Discussions

The nucleation of nano-porosities ($< 0.1\ \mu$m) at the TGO-BC interface can be associated with the interdiffusion of Al and Ni in the bond coat (Kirkendall effect), resulting from bond coat oxidation. Depending on the void size, stress and temperature, the mechanisms controlling void growth are not the same. To explain the void nucleation and growth mechanism, from a nano-porosity ($< 0.1\ \mu$m) to a large one ($> 3\ \mu$m), the following observations can be made:

- at high temperatures, the Kirkendall phenomenon is the dominant mechanism leading to the nucleation and growth of nano porosities,

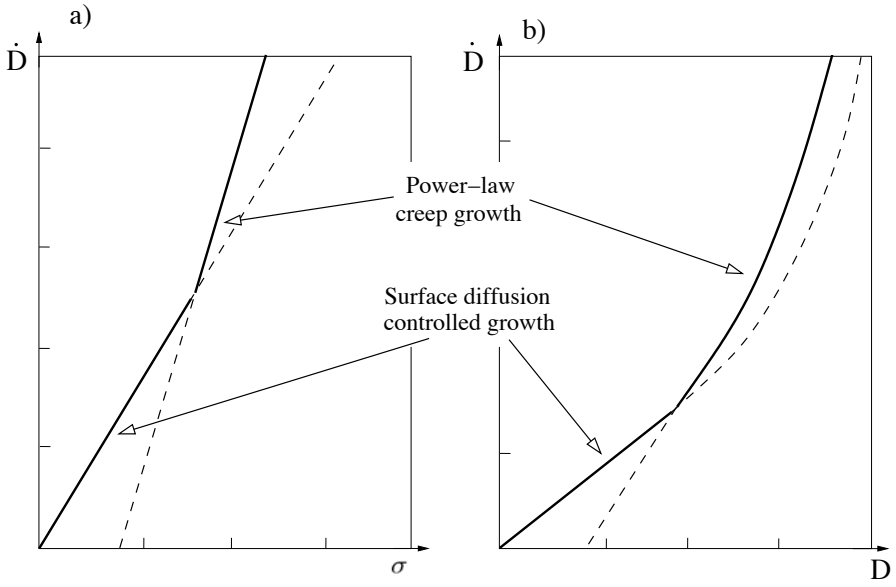

Figure IV.12 : Damage rate as a function of (a) stress and (b) damage, when the void growth is limited by surface diffusion and power-law creep (Cocks and Ashby, 1982).

- coupling to the Kirkendall effect and still at high temperatures, surface diffusion may control void growth. Indeed, the void morphology is ellipsoidal, see Fig. IV.8, its size is still small ($<$ few μm) and stresses are relatively low,
- when stresses develop at high temperatures or when the porosity size is large enough ($>$ few μm), void growth can be controlled by power-law creep. According to Figures IV.7 and IV.8 voids appear in the valley zones, supporting, the assumption that void growth is due to the coupling of physical and mechanical phenomena.

Based on interfacial porosities observations, the model of micro-damage time-evolution at the TGO-BC interface should take into consideration porosity nucleation and growth. The latter assumes to be a function of stress and plastic/creep strains close to the TGO. The model should also be able to distinguish damage generated during cyclic thermal loading and that at high temperatures related to chemical effects and to the growth strains associated with bond coat oxidation.

IV.4 TGO interface toughness

In this section, the recent measurements of oxide interface toughness, G_c, presented in the literature are studied, and more especially for TBC systems based of an EB-PVD YSZ top coat and on a $NiCoCrAlY$ bond coat. There are many different methods to determine the interface stickiness (Volinsky et al., 2002). Based on a fundamental fracture approach, mechanical tests (four-point bent, compressive test, indentation, barbing...) provide measurements of the delamination fracture resistance. A significant mode-dependence of the interface toughness of brittle interfaces has been observed in experimental studies of the interface fracture. G_c increases with the mode mixity parameter, Φ, and the interface toughness is significantly larger in Mode II than in Mode I (Hutchinson and Suo, 1992, Volinsky et al., 2002). For EB-PVD TBC systems, delamination is caused by compressive in-plane stresses and spallation occurs under Mode II loading. The experimental data can be separated into two parts: (1) the TGO interface toughness for as-prepared and undamaged sample (no interfacial microcracks or porosities) and (2) for samples thermally exposed. In both cases, G_c has been determined at room temperature.

IV.4.1 TGO interface toughness for as-prepared specimens

Interface adhesion has been measured for alumina scales bonded to Au substrates. The reported values for G_c range from 80 to 125 J/m^2 (Reimanis et al., 1991) and from 50 to 70 J/m^2 (Mao and Evans, 1997). For Al_2O_3 on $Ni-Cr$ alloy, Gaudette *et al.* (1997) have used experimental values from J. Stolken (unpublished research at UCSB) and G_c was found to be around 100 J/m^2 (Gaudette et al., 1997). More recently, based on a barb pullout method, Guo *et al.* have found that the measured interface adhesion for undamaged TBC system ranges from 60 to 90 J/m^2 (Guo et al., 2005, Guo et al., 2007).

IV.4.2 Time-evolution of the TGO interface toughness

Measurements of the influence of exposure time on TGO interface toughness for $NiCoCrAlY$ bond coats have been reported by Vasinonta and Beuth (2001). Interface toughness results were also obtained from indentation tests. According to the authors, the results would be affected by changes in the TBC system properties. The quantitative results are dependent on the model and the low interface toughness measured in undamaged TBC systems ($G_c = 49$ J/m^2) illustrates the disadvantage of this method. Nevertheless, the results show a significant decrease of the interface toughness with exposure, ranging from 49 to 4.3 J/m^2 after 0 and 56 h of exposure time at 1200°C, see Fig. IV.13.

To improve the quantitative evaluation of interface toughness, Kim *et al.* (2007) have determined experimentally interface adhesion using a push out method, for exposure times ranging from 0 to 200 h at 1150°C. And G_c ranges from 115 to 13 J/m^2, the interface toughness decrease becomes significant after 100 h thermal exposure, see Fig. IV.13. Note that the interface adhesion before thermal exposure does not follow the curve trend. Nevertheless, initial oxide toughness is in agreement with the values previously presented.

A comparison between the methods used to determined G_c and the results obtained for a $NiCoCrAlY$ bond coat leads us to calibrate our lifetime model with the experimental results provide by Kim *et al.* (2007).

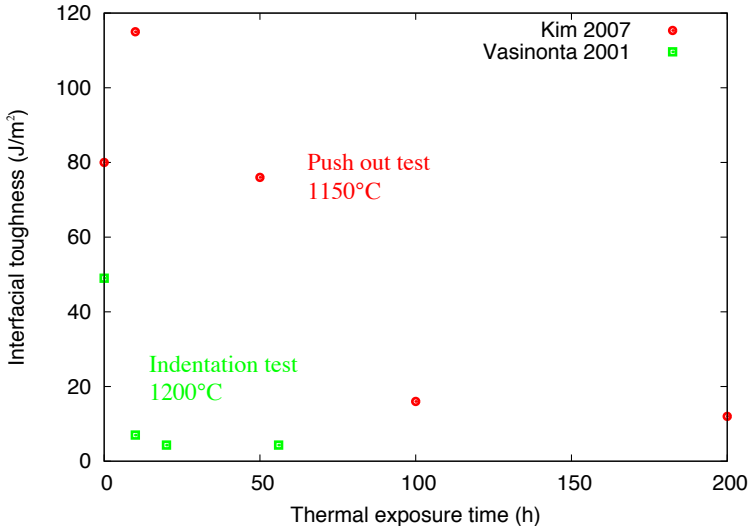

Figure IV.13 : Plots of the interface toughness as a function of thermal exposure time for a $NiCoCrAlY$ bond coat and EB-PVD top coat (Vasinonta and Beuth, 2001, Kim et al., 2007).

IV.5 Concluding remarks

For isothermal loading and for the TBC tested specimens, micrograph observations and analysis show that:

- among all the plausible scenari, top coat buckling is the mechanism retained to explain TBC spallation,
- top coat spallation is associated with the buckling delamination of the TGO-BC interface,
- top coat delamination and spallation may occur simultaneously and suddenly,
- TGO-BC interface delamination, leading to spallation, is a brittle phenomenon,
- EB-PVD TBC system is defined by a binary state: non-spalled or spalled,
- the TGO-BC interface is the weakest one due to the presence of interfacial damage in our system (porosities),
- porosities are observed in the valley regions at the TGO-BC interface,
- interfacial damage initiation could be due to interdiffusion phenomenon (Kirkendall effect) occurring in the bond coat,
- the Kirkdendall effect associated with the stress field could also explain porosity growth,
- porosity growth may be controlled by surface diffusion, or by power-law creep and may generate the observed spherical morphologies of interfacial porosities.

The last chapter of the present thesis will consist in establishing the relationship between the microscopic (porosity) and macroscopic (delamination/spallation) damage observed in the TBC studied and the lifetime model. The latter should be based on the results of the stress and strain fields simulations presented in Chapter III.

Reference

Bi, X., Xu, H., and Gong, S. (2000). Investigation of the failure mechanism of thermal barrier coatings prepared by electron beam physical vapor deposition. *Surface and Coating Technology*, 130:122–127.

Brumm, M. and Grabke, H. (1993). Oxidation behaviour of NiAl. Cavity formation beneath the oxide scale on NiAl of different stoichiometries. *Corrosion Science*, 34:547–561.

Cocks, A. and Ashby, M. (1982). On creep fracture by void growth. *Progress in Material Science*, 27:189–244.

Dalgleish, B., Trumble, K., and Evans, A. (1989). The strength and fracture of alumina bonded with aluminium alloys. *Acta Materialia*, 37:1923–1931.

Evans, A., Crumbley, G., and Demaray, R. (1983). On the mechanical behavior of brittle coatings and layers. *Oxidation of Metals*, 20:193–216.

Evans, H. (1989). Cracking and spalling of protective oxide layers. *J. of Materials Science and Engineering*, 120:139–146.

Gaudette, F., Suresh, S., Evans, A., Dehm, A., and Ruhle, G. (1997). The influence of chromium addition on the toughness of γ-Ni/α-Al_2O_3 interfaces. *Acta Mettal Mater*, 45:3503–3513.

Guo, S., Mumm, D., Karlsson, A., and Kagawa, Y. (2005). Measurement of interface shear mechanical properties in TBC systems by a Barb pullout method. *Scripta Materialia*, 53:1043–1048.

Guo, S., Tanaka, Y., and Kagawa, Y. (2007). Effect of interface roughness and coating thickness on interfacial shear mechanical properties of EB-PVD yttria-partially stabilized zirconia thermal barrier coatings systems. *Journal of European Ceramic Society*, 27:3425–3431.

Harvey, M., Courcier, C., Maurel, V., and Rémy, L. (2008). Oxide and TBC spallation in β-NiAl coated systems under mechanical loading. *Surface and Coating Technology*, 203:432–436.

He, M., Mumm, D., and Evans, A. (2004). Criteria for the delamination of thermal barrier coatings: with application to thermal gradients. *Surface and Coating Technology*, 185:184–193.

Hindam, H. and Smeltzer, W. (1980). Growth and microstructure of α-Al_2O_3 on β-NiAl. *J. Electrochem. Soc.*, 127:1630–1635.

Hutchinson, J. and Suo, Z. (1992). Mixed mode cracking in layererd materials. *Advances in Applied Mechanics*, 29.

Ibégazène-Ouali, F., Mévrel, R., Rio, C., and Renollet, Y. (2000). Microstructure evolution and degradation modes in cyclic and isothermal oxidation of an EB-PVD thermal barrier coating. *Materials at High Temperatures*, 17:205–218.

Kim, G., Yanar, N., Hewitt, E., Pettit, F., and Meier, G. (2002). The effect of the type of thermal exposure on the durability of thermal barrier coatings. *Scripta materialia*, 46:489–495.

Kim, S., Liu, Y., and Kagawa, Y. (2007). Evaluation of interface mechanical properties under shear loading in EB-PVD TBCs by the pushout method. *Acta Materialia*, 55:3771–3781.

Kumar, A., Nasrallah, M., and Douglass, D. (1974). The effect of yttrium and thorium on the oxidation behavior of Ni-Cr-Al alloys. *Oxidation of Metals*, 8:227–263.

Mao, S. and Evans, A. (1997). The influence of blunting on crack growth at oxide/metal interfaces. *Acta Materialia*, 45:4263–4270.

Mumm, D. and Evans, A. (2000). On the role of imperfections in the failure of thermal barrier coating made by electron beam deposition. *Acta Materialia*, 48:1815–1827.

Newaz, G., Nusier, S., and Chaudhury, Z. (1998). Damage accumulation mechanisms in thermal barrier coatings. *Journal of Engineering Material and Technology*, 120:149–156.

Reimanis, I., Dalgleish, B., Brahy, M., Rühle, M., and Evans, A. (1990). Effects of plasticity on the crack-propagation resistance of metal-ceramic. *Acta Metallurgica Materialia*, 38:2645–2652.

Reimanis, I., Dalgleish, B., and Evans, A. (1991). The fracture-resistance of a model metal/ceramic interface. *Acta Metallurgica Materialia*, 39:3133–3141.

Siegler, D. (1993). Adherence behavior of oxide grown in air and synthetic exhaust gas on Fe-Cr-Al alloys containing string sulfide forming elements Ca, Mg, Y, Ce, La, Ti and Zr. *Oxidation of Metals*, 40:555–583.

Smialek, J. (1978). Oxide morphology and spalling model for NiAl. *Metallurgical Transactions A*, 9:309–320.

Spitsberg, I., Mumm, D., and Evans, A. (2005). On the failure mechanisms of thermal barrier coatings with diffusion aluminide bond coatings. *Materials Science Engineering A*, 394:176–191.

Suo, Z. (1995). Wrinkling of the oxide scale on an aluminium-containing alloy at high temperature. *J. of mechanics of physics and solids*, 43:829–846.

Théry, P., Poulain, M., Dupeux, M., and Braccini, M. (2007). Adhesion energy of a YPSZ EB-PVD layer in two thermal barrier coating systems. *Surface and Coating Technology*, 202:648–652.

Théry, P., Poulain, M., Dupeux, M., and Braccini, M. (2009). Spallation of two thermal barrier coating systems: experimental study of adhesion and energetic approach to lifetime during cyclic oxidation. *Journal of Materials Science*, 44:1726–1733.

Tolpygo, V. and Grabke, H. (1994). Microstructural characterization and adherence of the α-Al_2O_3 oxide scale on the Fe-Cr-Al and Fe-Cr-Al-Y alloys. *J. of Oxidation of metals*, 41:343–364.

Vasinonta, A. and Beuth, J. (2001). Measurement of interfacial toughness in TBC systems by indentation. *Acta Materialia*, 48:843–840.

Volinsky, A., Moody, N., and Gerberich, W. (2002). Interfacial toughness measurements for thin films on substrates. *Acta Materialia*, 50:441–466.

Xu, C., Faulhaber, S., Mercer, C., Maloney, M., and Evans, A. (2004). Observations and analyses of failure mechanisms in thermal barrier systems with two phase bond coats based on NiCoCrAlY. *Acta Materialia*, 52:1439–1450.

Yanar, N., Petti, F., and Meier, G. (2006). Failure characteristics during cyclic oxidation of yttria stabilised zirconia TBCs deposited via EB-PVD on platinum aluminide and on NiCoCrAlY bond coats with processing modifications for improved performances. *Metallurgical and materials transactions*, 37A:1563–1580.

Yang, S., Wang, F., and Wu, W. (2001). Effect of microcrystallization on the cyclic oxidation behavior of β-NiAl intermetallics at 1000°C in air. *Intermetallics*, 9:741–744.

Chapter -V-

Multiscale predictive model of EB-PVD TBC lifetime

Contents

V.1 Introduction

The ability to predict the lifetime of TBC systems protecting gas turbine blade is among the highest priorities for gas turbine manufacturers. Despite considerable experimental work, the understanding and the prediction of TBC lifetime is still a demanding task. The main difficulty is to model the relationship between the microscopic mechanical and physical phenomena occurring close to the TGO-BC interface and the high stored energy generated by macroscopic in-plane stresses present in TBCs. Due to their multiple structures (APS or EB-PVD top coats, $NiCoCrAlY$ or $(Pt, Ni)Al$ bond coats) and their complexity, TBCs exhibit multiple failure mechanisms, as discussed in Chapter IV. A lifetime assessment has to be based first on damage observations, related to the TBC system of interest. The second step is to model the observed damage evolution and to take into account the influent parameters of the system such as oxide interface toughness and stored elastic strain energy per unit area. Finally, calibration and validation of the lifetime model are required.

TBCs life assessment has been proposed in the literature for APS top coats based on fracture mechanics approaches (Busso et al., 2001b, Traeger et al., 2003, Aktaa et al., 2005, Arai et al., 2006, Brodin and Eskner, 2004). Damage evaluation takes place in terms of fatigue cracks initiation/growth and its evolution is modelled using a Paris' law (Brodin and Eskner, 2004). Also using rupture concept, microcrack propagation is governed by the buckling of the YSZ ceramic and oxide layers. This approach allows to model the interface delamination (Evans et al., 1983, Hutchinson and Suo, 1992). Taking into consideration that TGO delamination could drive a macroscopic failure, intensive works have been achieved to evaluate interfacial energies using first principles calculations (Evans et al., 1993, Evans et al., 1997, Carling and Carter, 2007). For EB-PVD TBC systems and based on numerical approaches, cracking through or at the TGO interfaces has been described using cohesive zone elements (Qiu et al., 2001, Yuan and Chen, 2003, Caliez et al., 2003, Bialas et al., 2005). This approach has been improved using the partition-of-unity method (Hille et al., 2009a, Hille et al., 2009b). Lifetime model has been proposed based on a local stress criterion (Busso and Qian, 2006, Busso et al., 2007). These numerical approaches allow to model oxide interfacial damage using a numerical simulation of stress fields close to the TGO, where micro-damage is known to appear. Nevertheless, this type of general damage development is not observed in the TBC system studied here. Due to the brittle nature of TGO-BC interface, no crack propagation is observed and thus a rupture approach is not relevant. Furthermore, if the existence of an interfacial micro-damage is a necessary condition for top coat spallation to occur, it is not sufficient to explain TBC spallation.

This final chapter proposes a multi-scale predictive model of the EB-PVD TBCs lifetime. It establishes the relationship between a local approach of the TGO-BC interfacial micro-damage, which leads to its interfacial toughness decrease and an energetic approach which takes into account the effects of macroscopic in-plane stresses. This work brings together all the previous considerations dealing with the TBC microstructure (oxide roughness, YSZ top coat sintering), observation of damage mechanisms and numerical simulations of the local stress/strain fields close to the TGO.

In Section V.2, a TBC spallation predictive method, based on a global energetic approach, is presented. Interface adhesion is defined, as well as the spallation mechanisms and the criterion defining time spallation. Time-evolution of the stored elastic strain energy per unit area is formulated and applied to EB-PVD TBCs. In Section V.3, time-evolution of TGO-BC interface toughness is modelled. A phenomenological definition of interfacial damage, using a standard mesoscopic variable D is presented. D is related to both TGO-BC interface

toughness and to the local damage present along the TGO-BC interface. The interfacial micro-damage rate $\dot{D}_{loc}$ is defined as a function of the stress/strain fields close to the TGO-BC interface using a model previously developed by Lemaitre (1992). The model takes into consideration the interfacial damage evolution along the moving TGO-BC interface. The main challenge in the application of the damage model to a TBC comes from the need to conserve interfacial damage along a moving interface and to integrate the historic effects of thermal loading. Finally, in Section V.4, the relationship between the interfacial micro-damage D_{loc} at each Gauss point and the phenomenological variable, D, is defined. The calibration and validation of the model are carried out using experimental data provided by our database and by the literature.

V.2 Global energetic approach for TBC spallation

This section deals with the approach proposed to predict TBC spallation using a global energetic principle. To this purpose, it is assumed that there are two necessary conditions for spallation of an unstable multi-layer system after cooling: (i) the stored elastic strain energy per unit area, G (J/m^2), must be greater than the TGO-BC interface toughness, noted G_c (*i.e.* macroscopic criterion) and (ii) micro-damage must be present (*i.e.* microscopic criterion). It should also be noted that the stored elastic strain energy per unit area is released during top coat spallation.

First, interface adhesion and the energy available in a multi-layer system is presented in order to define the spallation criterion. In the case of TBC systems, the stored energy or driving force for coating spallation increases with exposure time whereas the critical interfacial energy decreases due to the degradation incurred during service (Smialek et al., 1994). The stored energy takes into account the high in-plane stress levels which arise from thermal loading and the microstructured degradation, such as sintering of the YSZ and the oxide layer growth. Time evolution of the TGO-BC interface toughness, affected by oxide interfacial micro-damage, is studied in the Section V.3.

V.2.1 Global energetic TBC lifetime approach

V.2.1.1 Interface adhesion

The interface toughness is one of the main properties which controls the mechanical integrity of a multilayer system. The interface decohesion resistance, G_c, is defined as the amount of the thermodynamic (W_{ther}) and the dissipated mechanical (W_{diss}) energies (Volinsky et al., 2002, Théry et al., 2007, Théry et al., 2009). The first one is the intrinsic interface resistance and represents the true work of adhesion. Without any dissipative phenomena such as plasticity and interfacial friction, W_{ther} should be equal to the interface decohesion resistance, G_c. With dissipative phenomena, G_c represents the practical work of adhesion and is expressed as:

$$G_c = W_{ther} + W_{diss}. \tag{V.1}$$

In the present study, the oxide interface toughness G_c is taken as the practical work of adhesion and no distinction will be done G_c and W_{ther} or W_{diss}.

V.2.1.2 Spalling criterion

In the presence of micro-damage at the TGO-BC interface and of high in-plane compressive stress states, the oxide and top coat are susceptible to spall, as illustrated in Fig. V.1. In our system, top coat spallation is known to occur by buckling delamination (Evans et al., 1983). As explained in Section IV.2, the delamination and spallation mechanisms occur simultaneously and suddenly. In our approach, we suppose that the TBC is an unstable system defined by two states: the initial one which exists before spallation, with a damaged TGO-BC interface (Step II in Fig. V.1) and a second one where the top coat has already spalled, (Step IV). Because of buckling Step (III) is assumed to be very short in time, it will not be considered in our approach.

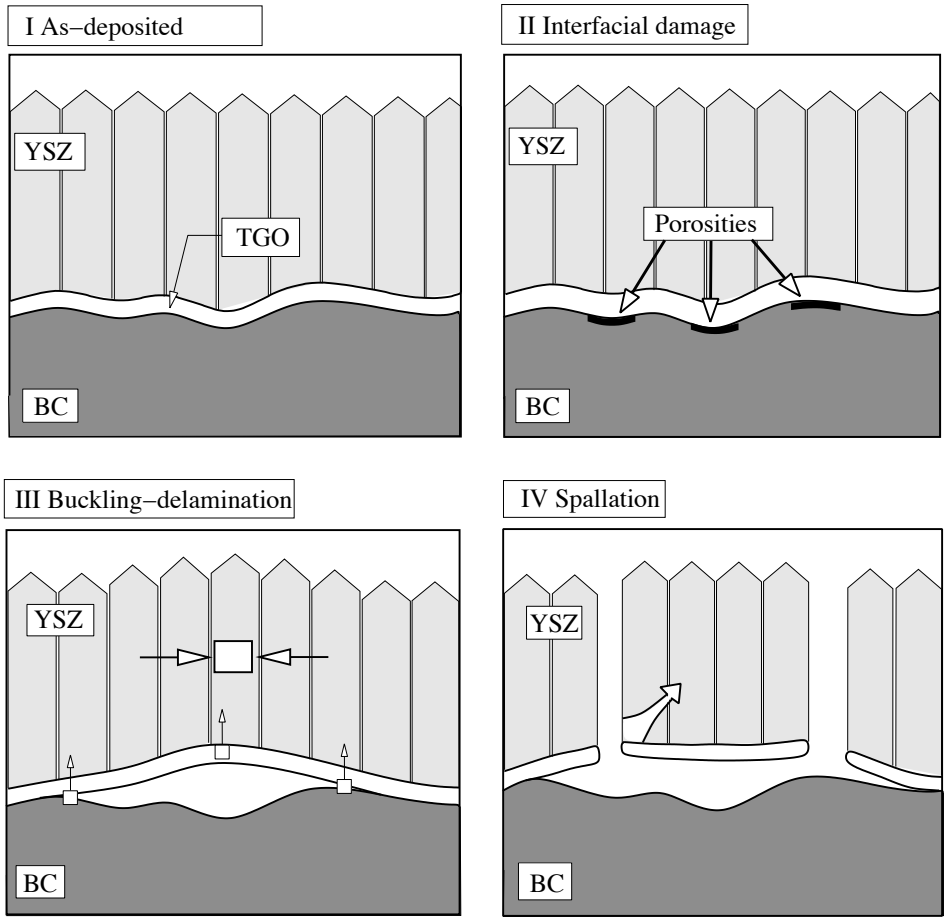

Figure V.1 : Schematics representation of the TBC system spallation mechanism: (I) safe TBC system, (II) damaged TGO-BC interface, (III) buckling-delamination and (IV) top coat spallation.

TBC lifetime can be determined by knowing (i) the evolution of the stored elastic strain energy per unit area, G (J/m^2) and (ii) the critical interfacial TGO energy, G_c, which represents the coating spallation resistance. Top coat spallation occurs when the stored energy reaches the interface oxide energy. Note that the proposed approach assumes the existence of micro-damage prior to final failure and that a complete release of stored energy at the TGO-BC interface occurs during top coat spallation. Thus, the spallation criterion is given by:

$$G_c = G \tag{V.2}$$

The conditions leading to the critical conditions defined by this criterion are illustrated in Fig. V.2.

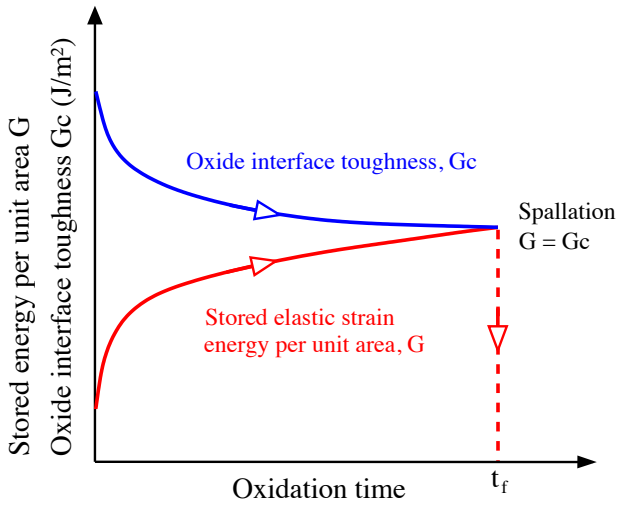

Figure V.2 : Schematic evolution of stored elastic strain energy per unit area and oxide interface toughness with oxidation time, leading to the critical condition, $G = G_c$, for the onset of spallation.

V.2.1.3 Formulation of the stored elastic strain energy per unit area

For an unbuckled and flat TBC system, under plane strain conditions, the stored strain elastic energy per unit area (J/m^2) is defined by:

$$G = \frac{1}{S}\int_V \underset{\sim}{\boldsymbol{\sigma}} : \underset{\sim}{\boldsymbol{\varepsilon}}_{elas} dv = \frac{\sigma_{11}^2(1-\nu^2)}{2E_1}h, \tag{V.3}$$

where σ_{11} is the macroscopic in-plane stress, in the direction X_1 parallel to the macroscopic bond coat and the YSZ ceramic interface. Here, σ_{11} is assumed to be homogeneous inside each TBC layer, ν the Poisson's ratio, E_1 the in-plane Young's modulus and h the thickness.

In a preliminary approach, G is analytically formulated in terms of the oxide and top coat thicknesses, their elastic properties and the macroscopic in-plane stresses. As delamination initiates at the TGO-BC interface, the energy released during spallation is that previously stored in the TGO and YSZ layers. Here, the total stored elastic strain energy per unit area, G_{tot}, can be expressed in terms of the amount of those in the TGO and the top coat, noted G_{TGO} and G_{YSZ}, respectively (Théry et al., 2007, Théry et al., 2009). Thus:

$$G_{tot} = G_{TGO} + G_{YSZ}. \tag{V.4}$$

Using Eq. V.3, Eq. V.4 can be rewritten as:

$$G_{tot} = \frac{\sigma_{TGO}^2(1-\nu^2)}{2E_1^{TGO}}h_{TGO} + \frac{\sigma_{YSZ}^2(1-\nu^2)}{2E_1^{YSZ}}h_{YSZ}. \tag{V.5}$$

Here, E_1^{TGO} and E_1^{YSZ} are the in-plane Young's moduli of the oxide and ceramic, respectively. In TBC systems, the in-plane stresses σ_{11} are generated by thermal and mechanical property mismatch and can reach a few GPa. When TBC constituents are assumed elastic, with plane strain conditions and a flat TBC morphology, compressive in-plane stresses inside each layer are given by:

$$\sigma_{11}^i = \frac{\Delta\alpha^i(T)\Delta T}{(1-\nu)}E_1^i, \tag{V.6}$$

where$\Delta\ ^i\alpha(T)$ is the relative coefficient of thermal expansion between each TBC constituents and the substrate, and formulated as in Section III.3.1. Then:

$$\Delta\varepsilon_{th}^i = \varepsilon_{th}^i - \varepsilon_{th}^{sub} = \Delta\alpha^i(T)\Delta T \text{ with } i = \text{YSZ, TGO and BC}, \tag{V.7}$$

As previously explained in Section III.3.1, two cases need to be distinguished for stress induced by thermal expansion. In equation V.6,$\Delta\ T$ can be the relative temperature (ΔT_a) between that during EB-PVD deposition and the in-service temperature, T_{dep} and T, respectively. Equation V.6 can then be rewritten as:

$$\sigma_{11}^i = \frac{\Delta\alpha^i\Delta T_a}{(1-\nu)}E_1 = \frac{\Delta\alpha^i(T)[T-T_{dep}]}{(1-\nu)}E_1^i \text{ with } i = \text{YSZ and BC}. \tag{V.8}$$

This equation could be applied to all the TBC constituents except for the new oxide which forms at high temperatures, T_h. In such case,$\Delta\ T$ is the relative temperature, noted$\Delta\ T_b$, between the peak temperature T_h and in-service thermal loading temperature T. Then:

$$\sigma_{11}^i = \frac{\Delta\alpha^i\Delta T_b}{(1-\nu)}E_1 = \frac{\Delta\alpha^i(T)[T-T_h]}{(1-\nu)}E_1^i \text{ with } i = \text{TGO}. \tag{V.9}$$

The top coat is expected to spall during cooling when the driving force for spallation reaches its peak value. Nevertheless, damage and toughness degradation can also take place at high temperatures. Thus, the stored elastic strain energy per unit area, $G(J/m^2)$ is (i) a function of the EB-PVD deposition temperature (T_{dep}) and the in-service temperatures (T), (ii) greater at low temperatures, (iii) a function of macroscopic TBC parameters such as high in-plane stress fields and TGO thickness, (iv) made up of contributions from the stored elastic strain energies in each TBC constituents (YSZ and TGO) and (v) takes into account top coat sintering effects via the time-evolution of the YSZ in-plane Young's modulus.

The oxide interface toughness, G_c, is an intrinsic property of the interface and decreases with exposure time due to interfacial micro-damage. It can also be a function of oxide growth, local stress/strain fields at the oxidising temperatures and during thermal transients and may be affected by a fatigue component introduced by thermal cycling.

V.2.2 Time evolution of the stored elastic strain energy per unit area

As a preliminary study, a comparison of the stored strain energy per unit area, obtained by analytical and numerical approaches, has been made for a flat TBC system. The results show that stored energies are similar for both approaches, which implies that G is not affected by the creep and plastic deformation of the bond coat and oxide layer. This result is consistent with the investigation of creep and plastic behaviour influence on in-plane stress states, previously presented in Section III.3.1. The same study has been performed for a rough TGO layer, and the analytical and numerical approaches give identical results.

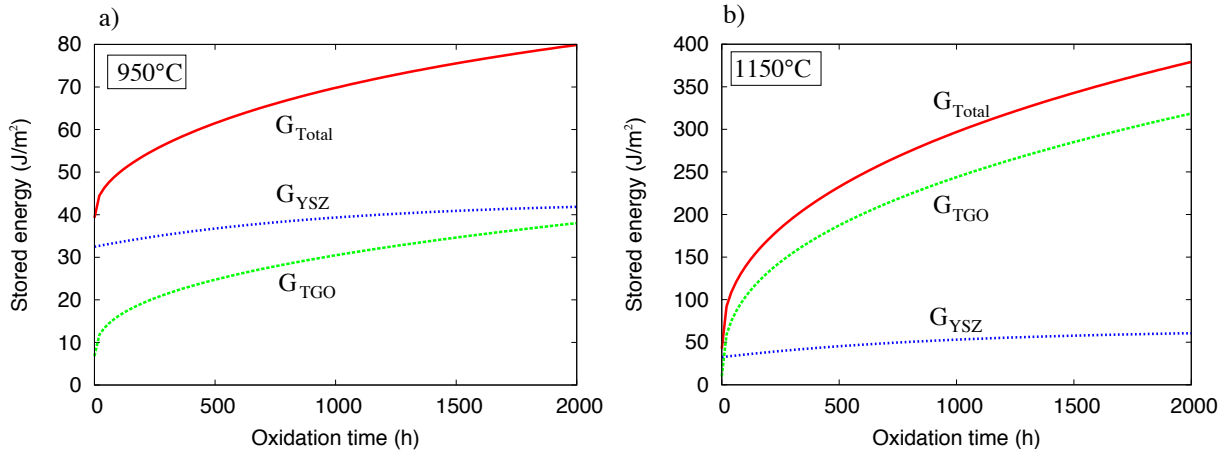

Figure V.3 : Time-evolution of the stored elastic strain energy per unit area at room temperature determined analytically using Eq. V.5, after thermal exposure at (a) 950°C and (b) 1150°C.

To compare the respective influence of the top coat and TGO layer on the total stored energy (Eq. V.4), its evolution inside each layer has been estimated analytically for the EB-PVD TBC system, at 950°C and 1150°C , the results are shown in Fig. V.3. At 950°C, the low effects of YSZ sintering is reflected by the light increase of G_{YSZ}, from 33 to 42 J/m^2 after 2000 h oxidation, see Fig. V.3(a). The TGO layer contribution increases with exposure time, from 8 to 38 J/m^2. G_{TGO} increase from 20% to 47% of the total stored energy after 2000 h oxidation. Despite its small thickness, the high contribution of the TGO layer is due to the difference between the relative temperature ($\Delta T_a < \Delta T_b$, see Eqs. V.8 and V.9) and the low top coat in-plane Young's modulus. In conclusion, at 950°C, the total stored elastic energy per unit area arises mainly from the oxide layer and its relative contribution to the overall driving force increases with oxidation time. At 1150°C, the qualitative results are different than at 950°C. The contribution of the top coat is higher and represents 20% and 84% of the total stored energy per unit area, respectively, after 0 and 2000 h, Fig. V.3(b). The top coat sintering has a light influence on the stored energy evolution, G_{YSZ}, which ranges from 33 to 60 J/m^2.

Figure V.4(a) illustrates the effect of sintering at 950°C and 1150°C. The effects are greater at 1150°C, as expected. The contribution of the YSZ top coat sintering is around 30 J/m^2. In spite of its low relative influence on the stored elastic strain energy per unit area, the top coat sintering behaviour has to be modelled so as to determine not only the local stresses close to the oxide but also the macroscopic stored elastic strain energy.

Figure V.4(b) shows the influence of the in-service temperature on G, taking into account top coat sintering, oxide thickness growth and the thermal loading. The temperature effect

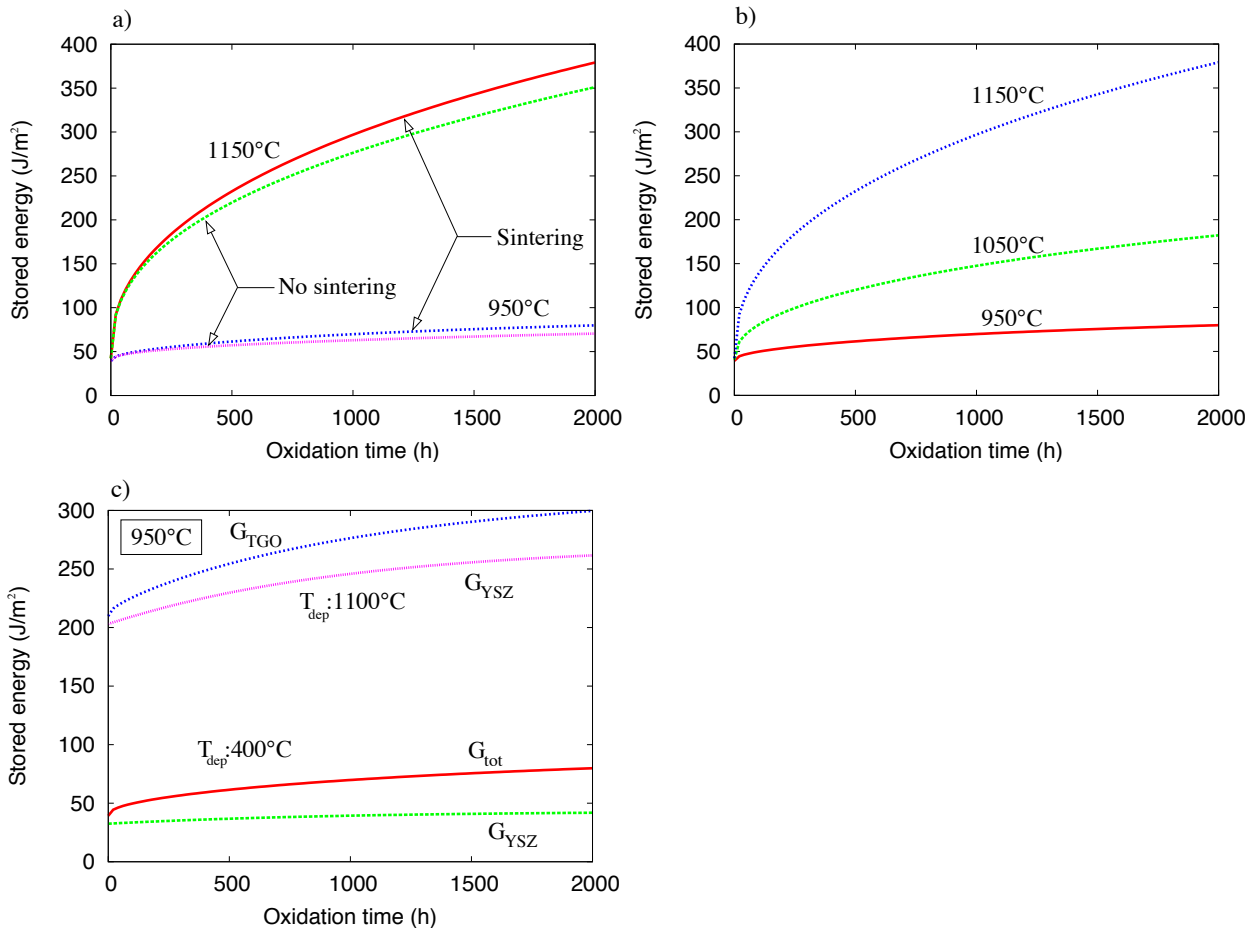

Figure V.4 : Time-evolution of the elastic stored strain energy per unit area showing the influence of (a) sintering at 950°C and 1150°C on G, (b) in-service peak temperature and (c) EB-PVD top coat deposition temperatures, T_{dep}.

is evident and G increases from 80 to 381 J/m^2 when the peak temperature increases from 950°C to 1150°C.

The influence of the EB-PVD deposition temperature, T_{dep}, has also been analysed for an in-service temperature of 950°C, Fig. V.4(c). This parameter affects only G_{YSZ}, and G ranges from 80 to 298 J/m^2 after 2000 h of exposure. Then, the contribution of the top coat represents 96% and 87% of the total stored energy, respectively, after 0 and 2000 h oxidation. This result illustrates the strong influence of the EB-PVD process temperature on the top coat stored energy. Note, that the EB-PVD process temperature has a greater influence than top coat sintering.

In this section, it has been shown that the EB-PVD TBCs lifetime can be modelled following an energy approach, which is in turn based on the description of the coating's driving force for top coat spallation, G, and the oxide interface toughness, G_c. It is important to note that this failure criterion, $G = G_c$ assumes implicitly the existence of interfacial micro-damage.

V.3 Time evolution of the TGO-BC interface toughness

In the previous section, a relation between top coat spallation and oxide interface toughness was proposed following an energetic approach. And the stored elastic strain energy per unit area was analytically predicted. One of the main difficulties to model TBC systems lifetime remains to formulate the relationship between the interfacial TGO micro-damage and the oxide interface toughness. In order to model the oxide interface toughness decrease, local stress/strain fields close to the damaged zone need to be investigated along a representative interface profile, modelling the TGO morphology. Based on the predicted stress and strain fields, a model has been develop to describe the evolution of the critical TGO interface energy needed in the energy-based TBC lifing approach.

From observations of TBC damage evolution and from results published in the literature, it is known that the oxide interface toughness decreases with exposure time. Note that, even if spallation is known to occur at room temperature when the stored energy is maximal, interfacial damage can generally evolve at high temperatures and during cooling. In this section, a formulation of the TGO-BC interface damage model is first proposed. The TGO-BC interface adhesion is linked to a mesoscopic damage variable D, determined on a representative elementary interfacial length (L_{REL}). Here, D is related to both the TGO-BC interface toughness and the local damage D_{loc} present along the TGO-BC interface which is a function of the local stress and strain fields (Lemaitre, 1992). The model distinguishes damage (i) at high temperatures due to the oxide growth strains and (ii) during cyclic thermal loading. Next, the micro-damage evolution following the TGO-BC interface is modelled. Note that D_{loc} is history dependent so as to include the accumulation of the local damage due to the thermal cycling (*i.e.* thermal fatigue).

V.3.1 Formulation of the mesoscopic interfacial damage model

The formulation of the TGO-BC interface toughness could be done following a mesoscopic damage approach expressed in terms of a mesoscopic scalar damage variable D and is defined as:

$$G_c = (1 - D)G_c^0, \tag{V.10}$$

where G_c^0 is the oxide interface toughness in the as-deposited state. Here, it is assumed that the damage is isotropic and represents the relative reduction of the TGO-BC interface area. It can be defined as the ratio between the undamaged and damage surfaces, S_s and S_d:

$$D = \frac{S_d}{S_s}. \tag{V.11}$$

In our study, it is assumed that the TGO-BC interface degradation is generated by porosity growth or by an intrinsic decrease of its interfacial toughness. Let the mesoscopic damage D be defined as the mean value of the local damage, D_{loc}, in an integration surface, S_{int}, close to the TGO-BC interface, as shown in Fig. V.5. The local damage describes the damage in each finite element close to the TGO-BC critical interface. The advantage of this approach is that a relationship between micro and mesoscopic damage can be proposed so as to take into

account the damage along the entire TGO-BC interface and not just close to the peak region, where normal tractions are positives and maximum. Locally, a small part of the TGO-BC interface could fail when $D_{loc} = 1$ without leading to top coat spallation. The integration surface, S_{int}, is a parameter of this model and will be discussed later on. The mesoscopic damage, D, can be expressed in terms of the integration surface, S_{int}, and the local damage, D_{loc}, as:

$$D = \frac{1}{S_{int}} \int_{S_{int}} D_{loc} dS. \tag{V.12}$$

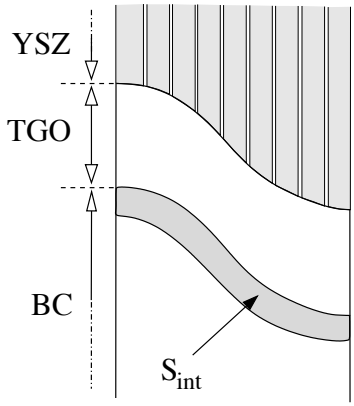

Figure V.5 : Schematic showing the integration surface S_{int} on which D_{loc} is integrated to determine the mesoscopic damage D.

V.3.2 Formulation of the microscopic interfacial damage model

In Section IV.3, porosities have been observed at the TGO-BC interface and a suitable mechanism has been proposed to explain void nucleation and growth. Local damage rate $\dot{D}_{loc}$ can be defined as a combination of the damage rate due to physical ($\dot{D}^{oxi}_{loc}$) and mechanical ($\dot{D}^{mec}_{loc}$) phenomena. Then:

$$\dot{D}_{loc} = \dot{D}^{oxi}_{loc} + \dot{D}^{mec}_{loc}. \tag{V.13}$$

According to the micrograph presented in Chapter IV, the porosities nucleate and grow in the valley regions where the bond coat is submitted to high levels of stress and to plastic and creep deformations. For long exposure times typical of land based gas turbine, the damage induced by chemical phenomena may be assumed to be negligible when compared to porosity growth damage ($D^{oxi}_{loc} \ll D^{mec}_{loc}$). Furthermore, our interest is to predict the TGO-BC interface toughness after long exposure times when the TGO-BC interface is considerably damaged. Gc time evolution in the first hours is not interesting in the present study. It could be relevant to add a term to account the nucleation and growth of interfacial microcracks when the system is cooling down. Nevertheless, according from our observations, no interfacial crack have been observed, except due to the dynamic nature of the top coat spallation and therefore it will not be modelled in the present study.

To simulate damage growth at the TGO-BC interface, a model which accounts for stress and creep/plastic strain fields has been chosen. The local damage rate, $\dot{D}_{loc}$, is determined incrementally at each Gauss point, based on a thermodynamic approach. According to the work of Lemaitre (1992), a thermodynamic approach gives an expression of the local damage rate:

$$\dot{D}_{loc} = \dot{D}_{loc}^{mec} = \left(\frac{Y}{A}\right)^{\beta} \dot{p}, \tag{V.14}$$

where Y (N/m^2) is the energy density release rate associated with the local damage (Eq. V.17), $\dot{p}$ is a scalar representing the equivalent creep and plastic strain rate at the TGO-BC interface (Eq. V.15) A and β are the damage material parameters.

$$\dot{p} = \left(\frac{2}{3}\underset{\sim}{\dot{\varepsilon}}^{i} : \underset{\sim}{\dot{\varepsilon}}^{i}\right)^{\frac{1}{2}}, \text{ with } i = \text{creep or plastic} \tag{V.15}$$

Here, $\dot{p}$ is controlled by the bond coat visco-plastic behaviour. To complete the damage formulation, the concept of an effective stress needs to be recalled. Bearing in mind that the nominal stress $\underset{\sim}{\boldsymbol{\sigma}}$ acts on a damaged interfacial area, then the effective stress $\underset{\sim}{\bar{\boldsymbol{\sigma}}}$ can be defined as:

$$\underset{\sim}{\bar{\boldsymbol{\sigma}}} = \frac{\underset{\sim}{\boldsymbol{\sigma}}}{1 - D_{loc}}. \tag{V.16}$$

The energy density release rate, Y, is a function of the local elastic strain energy density, which can be expressed in terms of both the stress and strain states:

$$Y = \frac{1}{2}\underset{\sim}{\varepsilon} : \underset{\sim}{\bar{\sigma}} = \frac{\underset{\sim}{\bar{\sigma}}_{eq}^2 R_v}{2E}, \tag{V.17}$$

$$\underset{\sim}{\bar{\sigma}}_{eq} = \left(\frac{3}{2}\underset{\sim}{\bar{\sigma}}_D : \underset{\sim}{\bar{\sigma}}_D\right)^{\frac{1}{2}}, \tag{V.18}$$

$$R_v = \frac{2}{3}(1+\nu) + 3(1-2\nu)\frac{\underset{\sim}{\bar{\sigma}}_H}{\underset{\sim}{\bar{\sigma}}_{eq}}, \tag{V.19}$$

where $\underset{\sim}{\bar{\sigma}}_{eq}$ is the von Mises equivalent stress, $\underset{\sim}{\bar{\sigma}}_D$ is the deviatoric part of the stress tensor $(\underset{\sim}{\bar{\sigma}})$, $\underset{\sim}{\bar{\sigma}}_H$ is the hydrostatic stress and Rv is a function that introduces the triaxiality function, $T_x = \underset{\sim}{\bar{\sigma}}_H / \underset{\sim}{\bar{\sigma}}_{eq}$.

In this approach, the global damage rate $\dot{D}$ is assumed to decrease with exposure time in order to be consistent with the expected decrease of the oxide adhesion energy. Thus, it is possible to model the damage at high temperatures (low Y, high $\dot{p}$) and during the cooling or heating transients (high Y, low $\dot{p}$).

Table V.1 summarises the relationships and the relative scale between the different formulations used to model the stored elastic strain energy per unit area G, TGO-BC interface toughness G_c, mesoscopic damage D and microscopic damage D_{loc}.

Table V.1 : Summary of the different formulations used, namely the stored elastic strain energy per unit area G, TGO-BC interface toughness G_c, mesoscopic damage D and microscopic damage D_{loc}.

TGO-BC interface toughness G_c					
Micro scale	Eq.	**Meso scale**	Eq.	**Macro scale**	Eq.
$\dot{D}_{loc} = \left(\frac{Y}{A}\right)^{\beta} \dot{p}$	V.14	$D = \frac{1}{S_{int}} \int_{S_{int}} D_{loc} dS$	V.12	$G_c = (1-D)G_c^0$	V.11
$Y = \frac{1}{2} \underset{\sim}{\boldsymbol{\varepsilon}} : \underset{\sim}{\bar{\boldsymbol{\sigma}}}$	V.17	$D = \frac{S_d}{S_s}$	V.11		
$\underset{\sim}{\bar{\boldsymbol{\sigma}}} = \frac{\underset{\sim}{\boldsymbol{\sigma}}}{1 - D_{loc}}$	V.16				

Stored elastic strain energy per unit area G	
Macro scale	Eq.
$G = \frac{1}{S} \int_V \underset{\sim}{\boldsymbol{\sigma}} : \underset{\sim}{\boldsymbol{\varepsilon}}_{elas} dv$	V.3
$G_{tot} = G_{TGO} + G_{YSZ}$	V.4
$\sigma_{11} = \frac{\Delta\alpha(T)\Delta T}{(1-\nu)} E_1$	V.6

V.3.3 Conservation of micro-damage during the TGO-BC interface motion

An important point to know is whether the TGO-BC interface damage (i) follows the oxidation internal front, (ii) is locally conserved or (iii) is healed at each step at high temperatures due to oxidation (Schutze M., 1991). According to observations on tested samples, the TGO-BC interface damage is seen to follow the inward oxidation front and to increase with oxidation time and temperature. The methodology developed to model the conservation of the microscopic interface damage is presented and illustrated next with a flat TBC interface.

V.3.3.1 Methodology

The formulation of the oxide growth model requires the development of a method to drive the inward oxidation front motion during oxidation in the FE mesh, see Section III.2. This method allows to know the position in the FE mesh of the transition zone between the oxidised and non-oxidised material, see Fig. V.6(a). The FE mesh is generated so as to contain vertical and horizontal rows of finite elements. When the oxide front position reaches a new element, the initial damage of the element to be oxidised is defined as:

$$D^{i+1}_{loc-ini} = D^{i}_{loc-final}, \tag{V.20}$$

where i is the index of the last element fully oxidised, $i+1$ is the index of the next element to be oxidised and the subscripts $final$ and ini correspond, respectively, to the final and initial damage values of the given finite element. The Figure V.6 illustrates this method which takes into account the previous local damage due to the oxide growth strains and thermal loading.

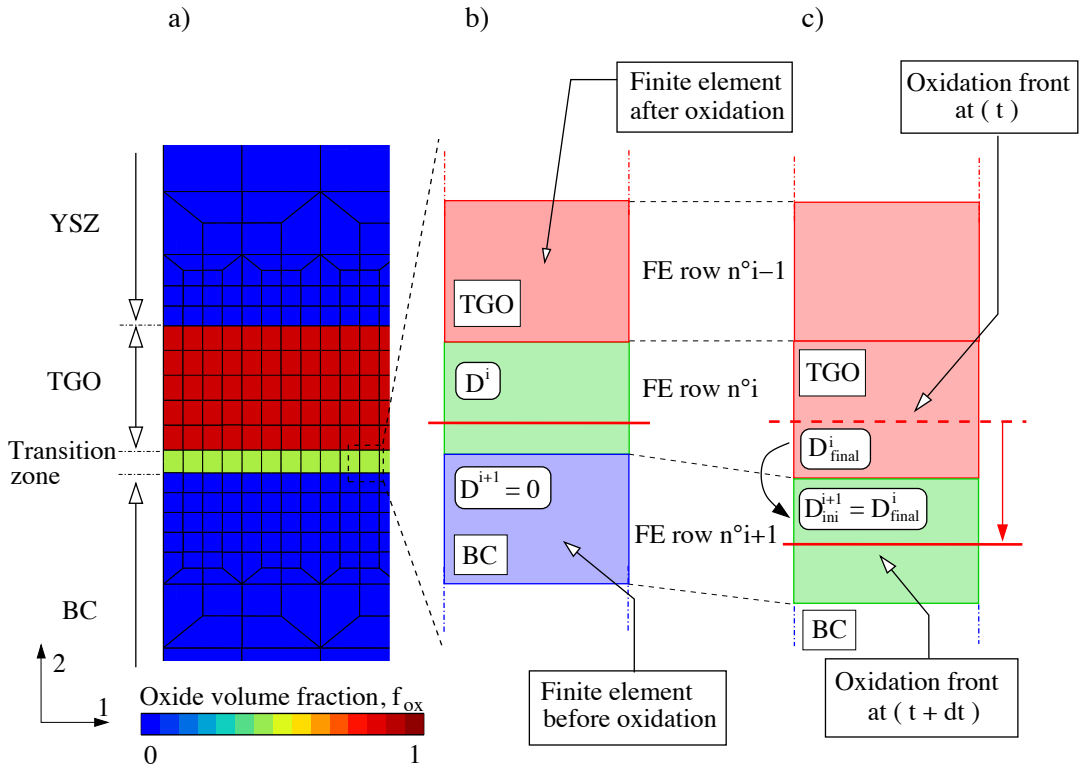

Figure V.6 : (a) Value of the oxide volume fraction (f_{ox}) in a flat 2D FE mesh, and (b), (c) close-up views of the transition zone showing the damage values in the FEs and the damage assigned to the new oxidised FE.

V.3.3.2 Application to a flat TBC system

To illustrate the FE approach to model the moving TGO interfaces, the previous methodology proposed to determine micro and mesoscopic TBC damage has been applied to a flat TBC system, see Fig. V.7. The values of the two parameters A and β in Eq. V.14, which are used to calibrate the damage evolutions, are for the moment arbitrarily chosen, namely $A = 100$ N/M^2 and $\beta = 1$. Their calibrations will be done in the next section.

The thermal history imposed on the TBC consists of 200 day-long cycles, with an in-service temperature of 950°C. Figure V.7 shows the the local damage D_{loc} evaluated at each Gauss point at three different oxidation times. Since the oxide interfaces are flat, D_{loc} is constant in the transition zone of the TGO-BC interface. Here, the mesoscopic damage D, characterising the average damage at the BC-TGO interface, is not presented. Note that, D_{loc} increases with oxidation time, see Eq. V.20 and that its maximal value is located at the

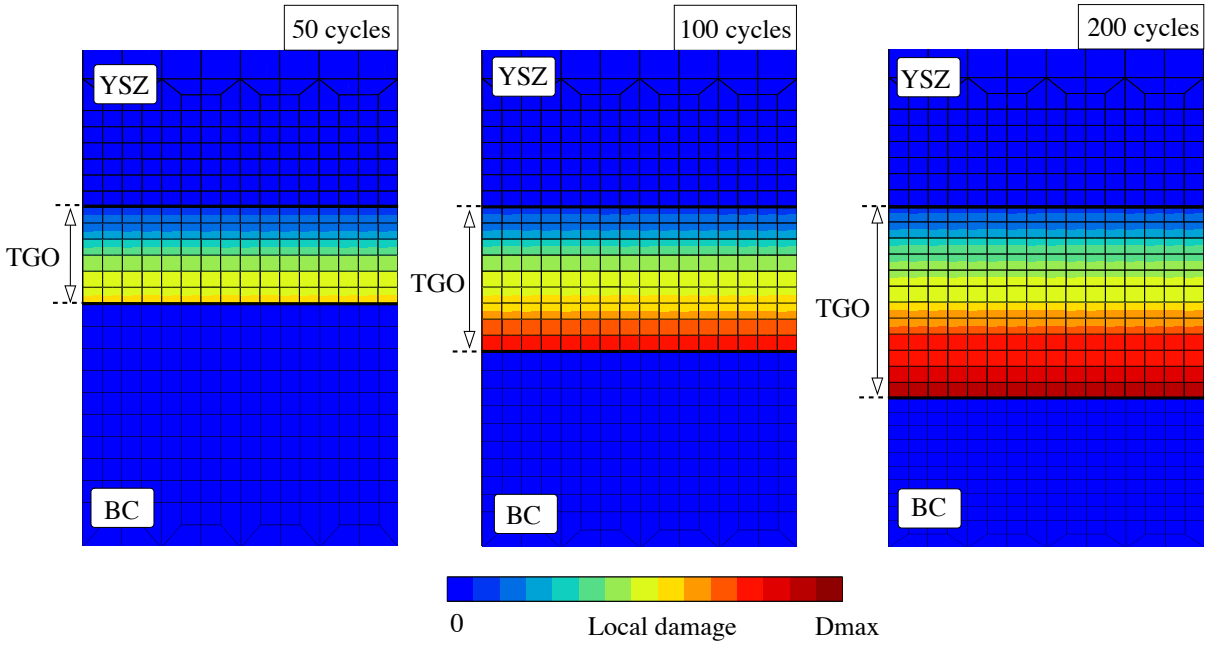

Figure V.7 : Predicted distribution of the local damage, D_{loc}, at 20°C after 50, 100 and 200 day-long cycles at 950°C.

moving BC-TGO interface.

For a given FE belonging to the row i and crossed over by the oxidation front, the time-evolution of the local damage D_{loc} and oxide volume fraction f_{ox} are presented in Fig. V.8. Initially, the FE belongs to the bond coat, that is for $f_{ox} = 0$. When the oxide front begins to cross the given FE row, the initial local damage value $D^i_{loc-ini}$ is set to the final local damage value $D^{i-1}_{loc-fin}$ of the previous oxidised FE belonging to the FE row $i-1$. Then, the growth strains associated with the oxide volume expansion leads to an increase of the local damage. The damage jump seen in Fig. V.8 corresponds to the damage due to a thermal cycle occurring during the motion of the oxide front along this FE row. Finally, the damage continues to grow until $f_{ox} = 1$ at which time D_{loc} reaches its final value, $D^i_{loc-fin}$. This latter value is assigned to the new oxidised FE row, $D^{i+1}_{loc-ini} = D^i_{loc-fin}$.

Note that, the model used to describe the local damage at the moving TGO-BC interface takes into account the damage (i) at high temperatures due to the oxide growth strains associated with the bond coat oxidation and (ii) that due to the thermal cycling during the cooling and heating transients. Furthermore, the local damage remained along the moving TGO-BC interface and models the history-dependence. This approach can be calibrated by setting appropriate values for the parameters A, β and S_{int}.

V.3.3.3 Application to a sinusoidal TGO morphology

The predicted local damage (D_{loc}) defined in Eq. V.14, is shown in Fig. V.9 after 20, 50, 100 and 200 days at 950°C with or without cyclic thermal loading. The prediction of D_{loc} is done for a 2D sinusoidal simulation of the TGO morphology. This periodic unit cell is considered as a representative elementary volume and its geometry is similar to the one used in Section III.3. The lifetime model parameters are still arbitrarily chosen, $A = 100\ N/M^2$

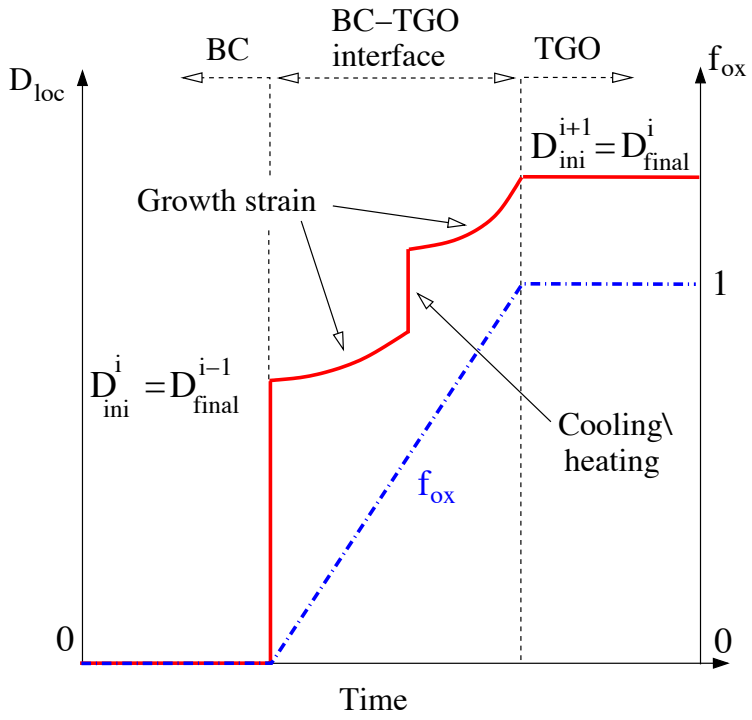

Figure V.8 : Plot of the local damage value D_{loc} and the oxide volume fraction f_{ox} time-evolution for a chosen FE belonging to the FE row i and crossed over by the oxide front.

and $\beta = 1$. Figure V.9 shows that the predicted local damage field increases with exposure time and that it follows the internal oxidation front motion. It is significant in the oxide zone located between the peak and the valley regions for isothermal loading, see Fig. V.9(a) or a low number of thermal cycles Fig. V.9(b). After 100 cycles, damage is observed in the valley region. The local damage field can be separated into two parts: (i) damage due to the growth strains occurring at high temperatures, located between the peak and the valley regions at the TGO-BC interface and (ii) damage due to thermal cycling located in the valley regions. This point is illustrated in Fig. V.10. The predicted damage field is in agreement with the SEM observations presented in Section IV.3. Porosities have been observed to nucleate and grow in the valley regions and between the peak and valley regions, see Figs. IV.7 and IV.8.

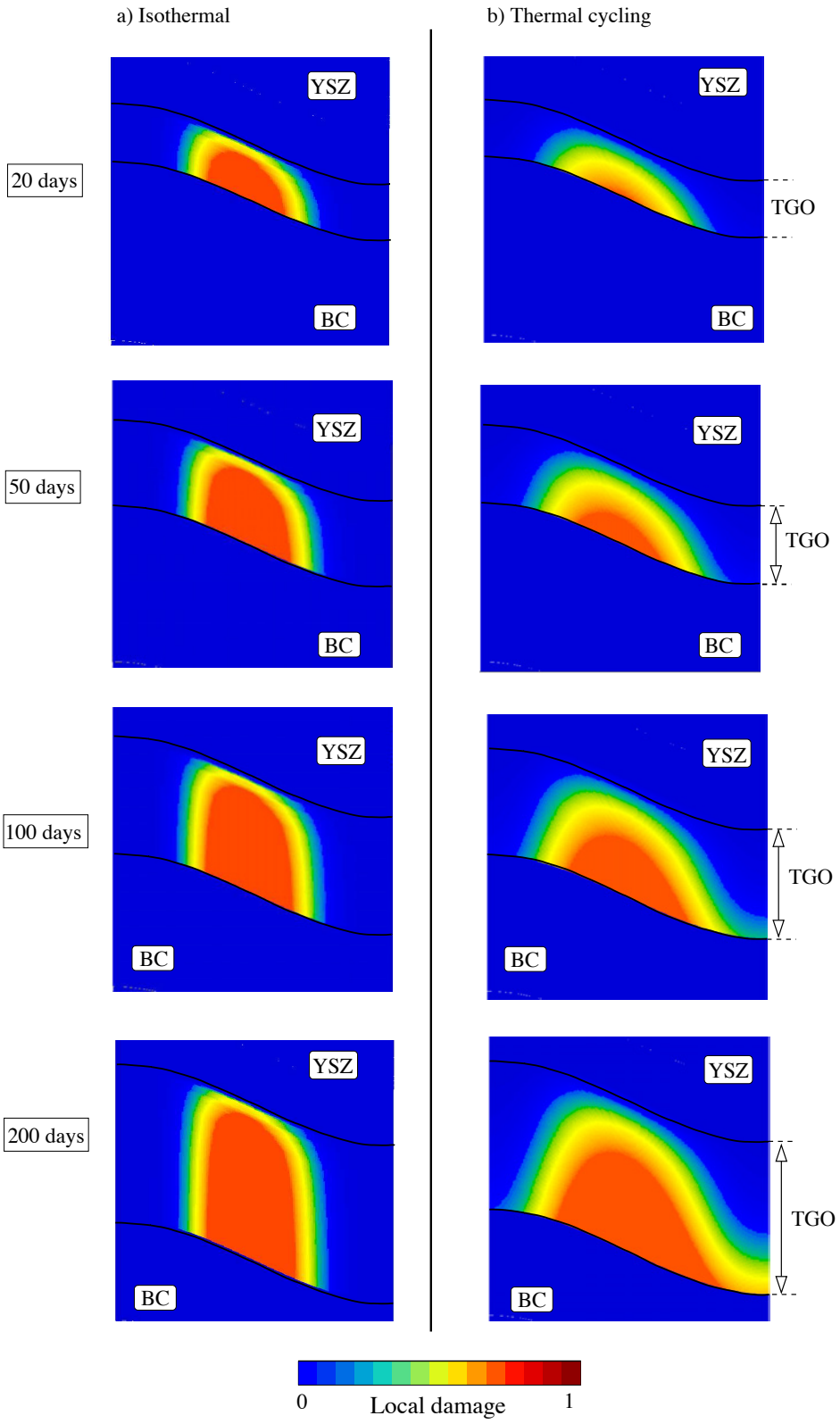

Figure V.9 : Comparison of the Gauss point value plot of the local damage D_{loc} at 20°C after 20, 50, 100 and 200 days for (a) isothermal loading and (b) thermal cycling with day-long cycles at 950°C. A cycle consists of a 22 h-40 min period at high temperatures and of a 40 min cooling/heating transients.

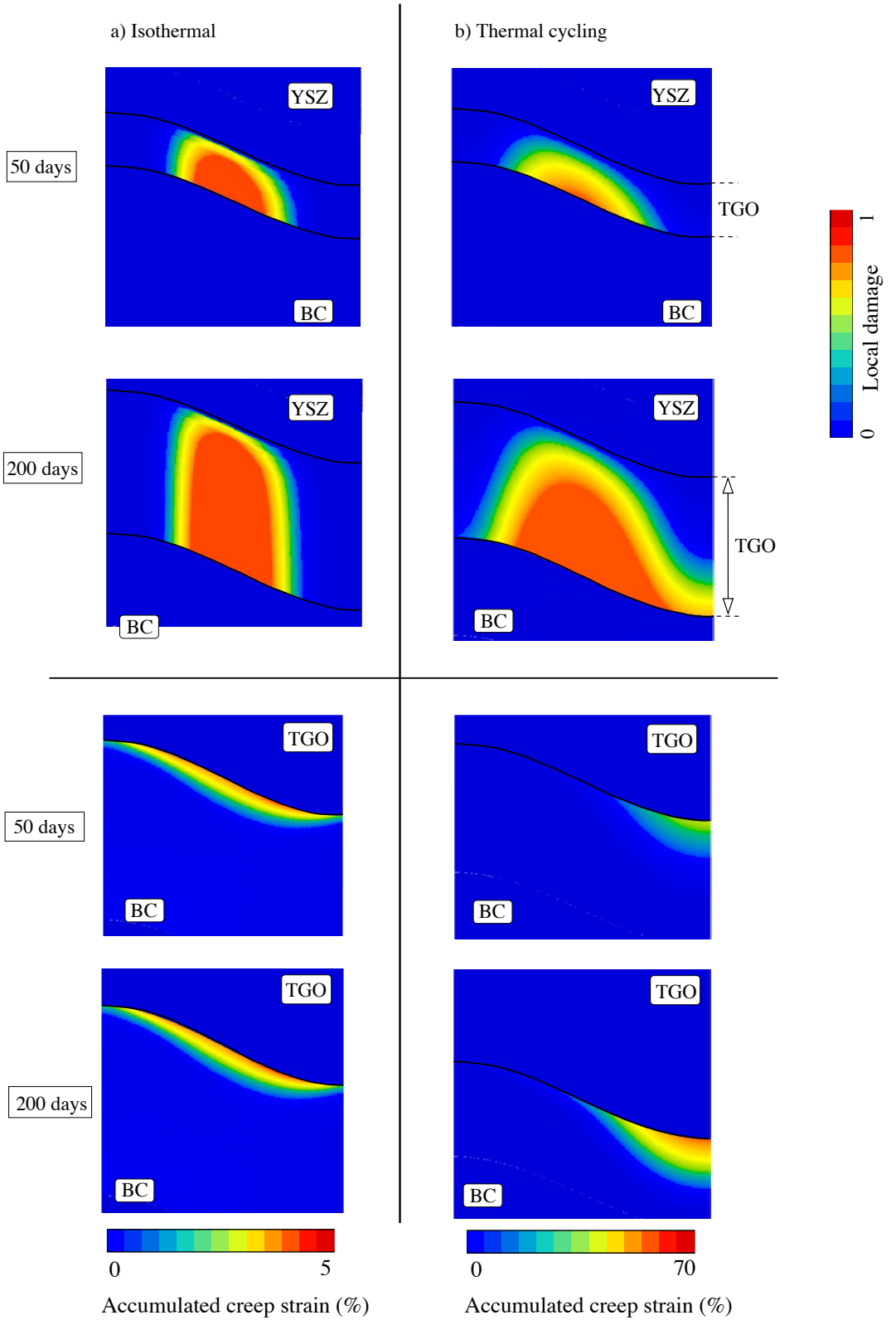

Figure V.10 : Comparison between the Gauss point value plot of the local damage (D_{loc}) and of the accumulated creep strain (ε^c_{acc}) in the bond coat after 50 and 200 days under (a) isothermal loading and (b) thermal cycling with day-long cycles at 950°C. A cycle consists of a 22 h-40 min period at high temperatures and of a 40 min cooling/heating transients.

V.4 TBC lifetime simulation

This section reports the calibration of the lifetime model parameters A, β and S_{int} defining the local damage in Eqs. V.12 and V.14 and the validation of the model using the experimental results previously presented in Section IV.2.4. For the calibration stage, the methodology followed consists in:

- modelling the thermal loading applied experimentally to each TBC samples,
- simulating the predicted stress and strain fields,
- using the post processing approach to calculate the microscopic local damage fields D_{loc} close to the TGO-BC interface, the mesoscopic damage D and the TGO-BC interface toughness G_c.

For the validation stage, the prediction of the stored elastic strain energy per unit area G was performed using the analytical formulation, given by Eq. V.3.

Prediction of the stress, strain and local damage fields was carried out for a 2D sinusoidal profile of the TGO morphology. This periodic unit cell is considered as a representative elementary volume, its geometry is similar to the one used in Section III.3. First, definition of the integration surface, S_{int}, is discussed and is followed by the calibration of the lifetime model parameters (A and β) using experimental data from the literature. Second, the lifetime model is validated based on TBC lifetime results obtained experimentally, see Section IV.2.4 and Fig. IV.5.

V.4.1 Characterisation of the relationship between the micro and mesoscopic interfacial damages

The mesoscopic damage D has been defined as the average value of the local damage (D_{loc}) over the surface S_{int}, see Eq. V.12. To propose a relevant choice of S_{int}, an analysis of the local damage field needs to be done first. Accordingly, the local damage field, only the transition zone localised between the TGO and the bond coat has been retained to determine D. The transition zone (S_{trans}) corresponds to the TGO-BC interface and has been defined in Section III.2.1.1. Eq. V.12 could be rewritten as:

$$D = \frac{1}{S_{int}} \int_{S_{int}} D_{loc} dS = \frac{1}{S_{trans}} \int_{S_{trans}} D_{loc} dS. \tag{V.21}$$

V.4.2 Calibration of the damage model parameters

Calibration of the TBC lifetime model parameters A and β in Eq. V.14 is based on the experimental results reported on a $NiCoCrAlY$ bond coat by Kim *et al.* (2007), presented in Section IV.4.2. The oxide interface toughness has been determined experimentally for exposure times ranging from 0 to 200 h at 1150°C. The heating rate to the exposure temperature (+6°C/min) and the cooling rate (−1°C/min) have been simulated.

To calibrate the model parameters, the criteria used were: (i) to respect the initial and final values of the oxide interface toughness and (ii) to model the significant decrease of G_c in the first hours. The parameter A affects the final value of G_c and β its evolution. The increase

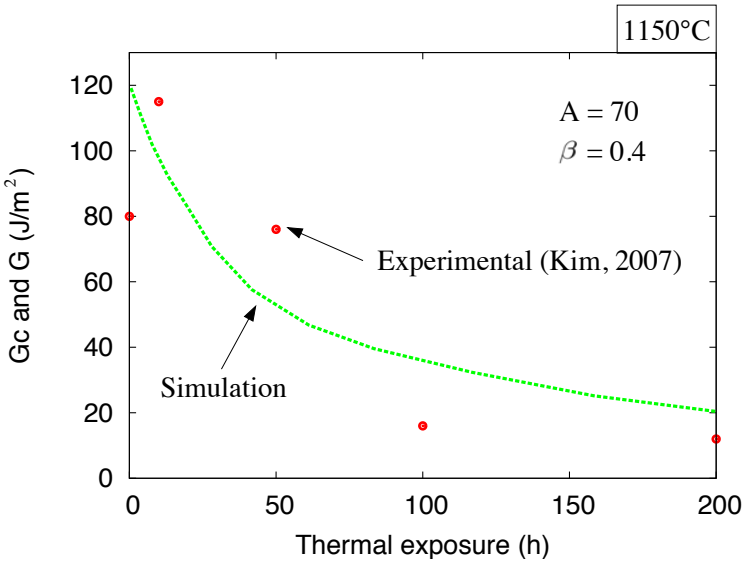

Figure V.11 : Comparison between the experimental (Kim et al., 2007) and simulated TGO-BC interface toughness as a function of exposure time at 1150°C.

of G_c after 10 h exposure time has not been taken into account to calibrate the model. Finally, after a post processing calculation based on the stress and strain fields obtained numerically, the optimum parameters A and β are found to be 70 N/m^2 and 0.4. For this parameter combination, the numerical results are compared to the experimental data in Fig. V.11. Experimental and predictive results of the TGO-BC interface toughness both start from a maximal value, namely 120 J/m^2 which corresponding to the TGO-BC interface toughness of the as-deposited specimen and then decreases to a final value between 15-20 J/m^2 after 200 h.

V.4.3 Validation of the lifetime model

To validate the lifetime model, a comparative study between the experimental results and those obtained by the lifetime model is carried out. For each isothermal loading case ranging from 930 to 1110°C, evolution of the stored elastic strain energy per unit area (G) is analytically determined using Eq. V.3. The oxide interface toughness (G_c) is simulated based on the predicted stress/strain fields and using the post processing tool previously developed in this work and calibrated. Time-evolution of G and G_c are presented in Fig. V.12 for each isothermal loading. As expected, with thermal exposure time, the stored elastic strain energy per unit area G increases and the oxide interface toughness G_c decreases. According to the energy-based TBC lifing approach, the top coat spallation occurs when $G = G_c$, see Fig. V.12(b). According to these predictions, no top coat spallation is expected to occur before 1000 h at 930°C. The top coat is expected to spall after 460 h, 165 h and 34 h isothermal loading at 990°C, 1050°C and 1110°C respectively, see Fig. V.12.

The predicted times to TBC spallation are compared to those experimentally obtained in Fig. V.13. For the isothermal case at 930°C, the spallation time is predicted using the interpolation of the G and G_c time evolution, namely 1600 h. For isothermal loading at 930°C, 990°C and 1050°C, the TBC lifetime model predictions are accurate. Indeed, the predicted spallation times are within the boundaries defined by a spalled or not spalled TBC states, as illustrated Fig. V.13. Nevertheless, at 1110°C, the top coat spallation is

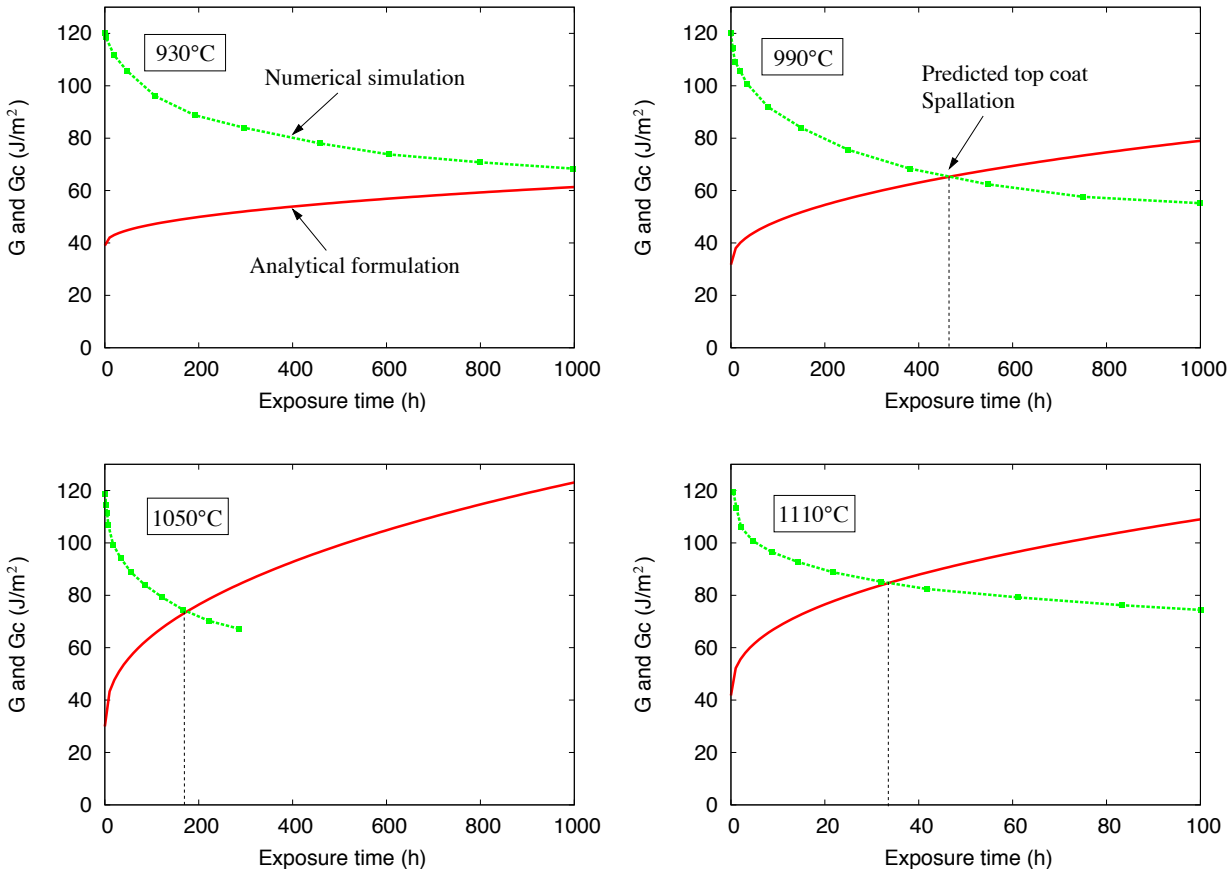

Figure V.12 : Time-evolution of the stored elastic strain energy per unit area G (analytical estimation) and the oxide interface toughness G_c (numerical estimation) at (a) 930°C, (b) 990°C, (c) 1050°C and (d) 1110°C.

predicted at 34 h whereas spallation is observed experimentally before 24 h. This observation was expected since the model calibration was focused on long exposure times. It has been assumed that void nucleation is negligible in comparison with void growth. Nevertheless, for short exposure times and at high temperatures, void nucleation contribution in the TGO-BC interface damage cannot be neglected. In Figure V.13, the predicted boundary between the non-spalled and spalled TBC system is shown. For short oxidation times, a more restrictive hypothetical boundary is proposed, illustrated by the dotted line in Fig. V.13, that is not taken into account by the previous model.

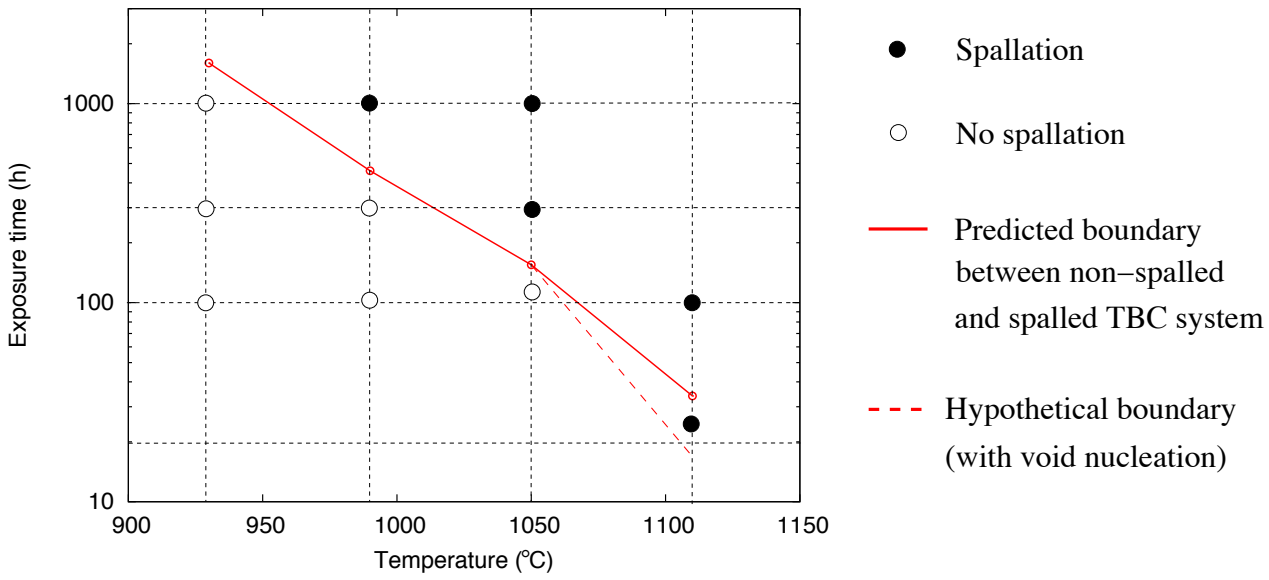

Figure V.13 : Comparison between the predicted TBC lifetime and experimental data.

V.5 Concluding remarks

TBC lifetime can be predicted knowing the time-evolution of the driving force for coating spallation and the degradation of the TGO-BC interface toughness. Here, delamination is assumed to occur at the internal oxide interface, as it has been observed in Chapter IV. The stored elastic strain energy is analytically formulated, considering time-evolution of the ceramic in-plane Young's modulus (sintering effect) and the oxide growth. The stored energy increases mainly due to the TGO growth and is influenced by the EB-PVD process temperature. Our approach provides an improvement in the prediction of the oxide internal interface toughness for long in-service loading. This TGO-BC interface toughness is numerically predicted based on a multi-scale approach of the damage. It requires knowing the relationship between the microscopic interfacial damage and the mesoscopic damage of a unit cell. Based on experimental work and identification of the TBC failure mechanisms, this model allows to link the predicted microscopic interfacial damage to the macroscopic interface toughness. The advantage of the proposed model is that it can account for history effects on the interfacial damage, accumulated locally during cycling.

This approach also allows to simulate the damage at high temperatures due to the TGO growth strains and during cooling. The model is validated for isothermal tests and should be also tested for cyclic thermal loading. In this case, an additional term must be formulated to model the crack propagation which may occur during thermal cycling.

Reference

Aktaa, J., Sfar, K., and Munz, D. (2005). Assessment of tbc systems failure mechanisms using a fracture mechanics approach. *Acta materialia*, 53:4399–4413.

Arai, M., Okajima, Y., and Kishimoto, K. (2006). Mixed-mode interfacial fracture toughness for thermal barrier coating. *Engineering Fracture Mechanics*.

Bialas, M., Majerus, P., Herzog, R., and Mroz, Z. (2005). Numerical simulation of segmentation cracking in tbcs by means of cohesive zone elements. *Materials Science Engineering A*, 412:241–251.

Brodin, H. and Eskner, M. (2004). The influence of oxidation on mechanical and fracture behaviour of an air plasma-sprayed NiCoCrAlY bond coat. *Surface and Coating Technology*, 187:113–121.

Busso, E., Lin, J., Sakurai, S., and Nakamaya, M. (2001b). A mechanistic study of oxydation-induced degradation in a plasma-sprayed thermal barrier coating system. Part II: life prediction model. *Acta Materialia*, 49:1529–1536.

Busso, E. and Qian, Z. (2006). Mechanistic study of microcracking in transversely isotropic ceramic-metal systems. *Acta Materialia*, 54:325–338.

Busso, E., Wright, L., Evans, H., McCartney, L., Saunders, S., Osgerby, S., and Nunn, J. (2007). A physics-based life prediction methodology for thermal barrier coating systems. *Acta Materialia*, 55:1491–1503.

Caliez, M., Chaboche, J., Feyel, F., and Kruch, S. (2003). Numerical investigation of eb-pvd thermal barrier coatings spallation. *Acta Materialia*, 51:1133–1141.

Carling, K. M. and Carter, E. A. (2007). Effects of segregating elements on the adhesive strength and structure of the α-Al_2O_3 β-NiAl interface. *Acta Materialia*, 55(8):2791 – 2803.

Evans, A., Crumbley, G., and Demaray, R. (1983). On the mechanical behavior of brittle coatings and layers. *Oxidation of Metals*, 20:193–216.

Evans, H., Mitchell, G., Lobb, R., and Owen, D. (1993). A Numerical Analysis of Oxide Spallation. *Proceedings of the Royal Society of London Series A-Mathematical Physical and Engineering Sciences*, 440(1908):1–22.

Evans, H., Strawbridge, A., Carolan, R., and Ponton, C. (1997). Creep effects on the spallation of an alumina layer from a NiCrAlY coating. *Materials Science and Engineering: A*, 225(1-2):1 – 8.

Hille, T., Nijdam, T., Suiker, A., Turtelhaub, S., and Sloof, W. (2009a). Damage growth triggered by interface irregularities in thermal barrier coatings. *Acta Materialia*, 57:2624–2630.

Hille, T., Suiker, A., and Turtelhaub, S. (2009b). Microcrack nucleation in thermal barrier coating systems. *Engineering fracture mechanics*, 76:813–825.

Hutchinson, J. and Suo, Z. (1992). Mixed mode cracking in layererd materials. *Advances in Applied Mechanics*, 29.

Kim, S., Liu, Y., and Kagawa, Y. (2007). Evaluation of interface mechanical properties under shear loading in EB-PVD TBCs by the pushout method. *Acta Materialia*, 55:3771–3781.

Lemaitre, J. (1992). *A course of Damage Mechanics*. Springer Verlag.

Qiu, Y., Crisfield, M., and Alfano, G. (2001). An interface element formulation for the simulation of delamination with buckling. *Engineering Fracture Mechanics*, 68:1755–1776.

Schutze M. (1991). *Protective oxyde scales and their breakdown*. D.R Holmes. Wiley Series on Corrosion and Protection.

Smialek, J., Jayne, D., Schaeffer, J., and Murphy, W. (1994). *Thin Solid Films*, 253:285.

Théry, P., Poulain, M., Dupeux, M., and Braccini, M. (2007). Adhesion energy of a YPSZ EB-PVD layer in two thermal barrier coating systems. *Surface and Coating Technology*, 202:648–652.

Théry, P., Poulain, M., Dupeux, M., and Braccini, M. (2009). Spallation of two thermal barrier coating systems: experimental study of adhesion and energetic approach to lifetime during cyclic oxidation. *Journal of Materials Science*, 44:1726–1733.

Traeger, F., Ahrens, M., Vaβen, R., and Stöver, D. (2003). A life time model for ceramic thermal barrier coatings. *Materials Science Engineering A*, 358:255–265.

Volinsky, A., Moody, N., and Gerberich, W. (2002). Interfacial toughness measurements for thin films on substrates. *Acta Materialia*, 50:441–466.

Yuan, H. and Chen, J. (2003). Computational analysis of thin coating layer failure using a cohesive model and gradient plasticity. *Engineering Fracture Mechanics*, 70:1929–1942.

Chapter -VI-

Conclusions and proposal for future work

Lifetime assessment of TBC systems protecting gas turbine blades requires to distinguish firstly the mechanical and physical phenomena responsible for microscopic degradations at the TGO interfaces and secondly the determination of the high level of macroscopic stresses which drive top coat spallation. For long exposure times typical of land based turbine gas (> 50.000 h), ageing effects such as sintering of the YSZ ceramic, evolution of the bond coat microstructure, oxide growth and TGO morphology, have to be taken into consideration.

The present lifetime model is based on an energetic approach applied to a multilayer EB-PVD TBC system. According to observations and analyses of the tested samples, it is assumed that there are two necessary conditions for spallation of an unstable TBC system: (1) the stored elastic strain energy per unit area must be greater than the TGO-BC interface toughness and (2) a local damage has to be present at the delaminated interface. This approach is relevant since it takes into consideration the multi-scale phenomena occurring in TBC system. A critical point in this model is the fact that the stored energy and interface toughness for the TBC system to be considered. In particular, the interface toughness and the failure mechanisms (local interfacial damage or top coat spallation) are related to the TBC system studied and to the thermal loading.

A numerical tool predicting the stress/strain fields and the local damage close to the TGO layer has been developed. Associated to experimental work and identification of the TBC failure mechanisms, this model allows to correlate the predicted microscopic interfacial damage to the macroscopic interface toughness. This model is capable of taking into account the thermal loading history on the interfacial damage evolution.

Main results

The results presented in this work can be divided in four parts related to each chapter: (i) a preliminary work based on the knowledge of each individual TBC constituent, (ii) the numerical prediction of the stress/strain fields close to the TGO and a parametric study, (iii) the observation of TBC failure mechanisms and (iv) the multi-scale predictive model of the EB-PVD TBCs lifetime.

(i) The energy-based TBC lifing approach requires a preliminary work based on the knowledge of each individual constituent material properties and the evolution of the oxide morphology. To this purpose, image-processing analysis has been used to characterise the microstructure of the EB-PVD YSZ ceramic layer. It has been observed that the ceramic is rather compact close to the TGO layer and is not affected by sintering. In contrast, sintering occurs in the porous part of the top coat. The $NiCoCrAlY$ bond coat presents a complex multiphased microstructure which evolves with oxidation time and greatly influences the TGO evolution. Due to the presence of reactive elements in the bond coat such as yttrium, the TGO grows by internal oxidation ($J_{Al^{3+}} \ll J_{O^{2-}}$) and yttrium heterogeneities are observed at the BC-TGO interface. The growth strains associated with the bond coat oxidation reaction are assumed to be anisotropic, and to be influenced by the TGO columnar microstructure and the boundary conditions. The TGO morphology has been characterised using image-processing analysis along a window width enough to be representative. A mean wavelength ($w = 11.72$ μm) and amplitude ($a = 0.864$ μm) have been obtained as well as a representative elementary length ($L_{REL} = 16$ μm). The TGO morphology has been simulated using Fourier analysis.

(ii) The stress and strains fields in the TBC system close to the TGO layer have been predicted using a finite element technique as it is described in Chapter III. The methodology

and the implementation in a FE code of the numerical tool simulate the TGO growth and determine the stress field in the critical oxide TGO-BC interface area have been presented. The proposed methodology uses as input the oxidation front motion for both geometry and kinetics. Hence, mechanical fields could be evaluated incorporating the effect of oxide growth. The results point out that the transition zone, at the TGO-BC interface, is the highest stressed region at high and low temperatures. Only the regions of the bond coat and ceramic layer close to the TGO have an influence on the local stress fields. To improve our knowledge of EB-PVD TBC system behaviour, a parametric study of the TBC system mechanical behaviour has been investigated. It shows that the associated role of the bond coat creep/plastic and the TGO creep behaviour in the stress relaxation at high temperatures and during cooling. Unfortunately the parameters defining the TGO creep behaviour are difficult to obtain experimentally. It is also concluded that the ceramic sintering does not affect the local stress/strain fields at the TGO-BC interface. The TGO morphology was found to be the most critical parameter and its simulation was improved. To this purpose, a 2D simulation of the TGO has been performed, using SEM micrograph and a Fourier decomposition. This approach allows to simulate the roughness heterogeneities observed at the TGO-BC interface. In comparison with the 2D sinusoidal simulation, a difference of 17% of the maximal normal traction is predicted. In the case of a 3D sinusoidal simulation of the oxide morphology, the difference reaches up to 35% and the out-of-plane stress field is strongly different. If these simulations give more information, the time calculation is twenty times higher and should be performed using the method of parallel computation.

(iii) From micrograph observations and analyses of TBC specimens tested under isothermal loading, top coat buckling was identified as the mechanism preceding to TBC spallation. Top coat spallation is associated with the buckling delamination of the TGO-BC interface. Due to the brittle nature of this interface, top coat delamination and spallation occur simultaneously and suddenly. Nevertheless, interfacial damage is assumed to be a progressive mechanism occurring at high temperatures. Porosities observed are assumed to nucleate and to grow due to the interdiffusion phenomenon occurring in the bond coat and due to the high stress level at the TGO-BC interface.

(iv) If the existence of an interfacial micro-damage is a necessary condition, it is not sufficient to explain top coat spallation. The TBC lifetime can be predicted knowing the time-evolution of the driving force for coating spallation and the TGO-BC interface toughness. The stored elastic strain energy has been analytically formulated, taking into account the time-evolution of the ceramic in-plane Young's modulus (sintering effect) and the oxide growth. The TGO-BC interface toughness is numerically predicted, based on a multi-scale approach of the damage, defined by the relationship between the microscopic interfacial damage and the mesoscopic damage of a unit cell. This approach is well adapted to the TBC studied as it gives satisfying results in the lifetime prediction of the top coat spallation. The historic effects of the thermal loading on the interfacial damage is also addressed.

Proposal for future work

The model has been developed to be generic and can be applied to other TBC systems. The analytical formulation of the stored energy allows to determine easily its time evolution knowing parameters such as the TGO and YSZ thicknesses and the elastic properties of the ceramic and oxide layers. The simulation of the oxide interface toughness requires experimental work focus on the identification of the local damage mechanisms.

To improve the model of the TGO interface damage proposed by Lemaitre, it can be

proposed to distinguish the case of a zone under compression or under tensile stress. For this, a microdamage closure parameter can be introduced following Lemaitre and Desmorat(1999). In the presence of microcracks through or at the TGO interfaces, their propagation could be described using cohesive zone elements or the partition-of-unity method. In both cases, a local approach can give satisfying results if it is associated to the macroscopic approach of the stored energy. The advantage of the above approach is to provide a value of the mesoscopic damage, determined for a unit cell as a function of the temperature, time and external boundary conditions. The mesoscopic damage could be input in a numerical approach of the entire blade. Indeed, it should be possible to determine the mesoscopic damage evolution as a function of temperature, time and external stress or strain applied to a unit cell.

For simplicity, we have chosen to directly implement the oxide growth, based on the experimental work. The TGO formation should be modelled through a continuous oxidation process, taking into account the relationship between stress and diffusion. Such approach requires data to describe the complex relationship between stress and diffusion. Phase-field approach could certainly be a suitable method, as long as it is used with an adapted FE mesh. In both cases, these approaches will be able to model the oxide roughness time-dependent generated by the complex bond coat or TGO microstructures.